Synthesis and Catalytic Properties of Binary/Core-Shell Coinage Metal(s) Nanostructures

Thesis Submitted

By

Anila

(Regd. No. 901109001)

In fulfillment of the requirement for the Degree of

Doctor of Philosophy

Under the Supervision of

Dr. Bonamali Pal

(Professor and Head)

School of Chemistry and Biochemistry

Thapar University, Patiala-147004

Punjab (India)

May, 2016

Dedicated

To

My Parents

&

Teachers

Certificate

This is to certify that thesis entitled ***"Synthesis and Catalytic Properties of Binary/Core-Shell Coinage Metal(s) Nanostructures"***, being submitted by Miss Anila in fulfillment of the requirement for the award of the Degree of Doctor of Philosophy in the School of Chemistry and Biochemistry, Thapar University, Patiala, is a record of candidate's own independent and original research work carried out by her under my supervision and guidance. The matter presented in this thesis has not been submitted in part or full for the award of any degree in any other University or Institute.

(Supervisor)

Dr. Bonamali Pal

Professor and Head

School of Chemistry and Biochemistry

Thapar University, Patiala - 147004

Punjab (India)

Candidate's Declaration

I, hereby declare that the work presented in the thesis entitled ***"Synthesis and Catalytic Properties of Binary/Core-Shell Coinage Metal(s) Nanostructures"***, in fulfillment of the requirement for the award of the Degree of Doctor of Philosophy, School of Chemistry and Biochemistry, Thapar University, Patiala, is an authentic record of my own work carried out under the supervision of Dr. Bonamali Pal, Professor and Head, School of Chemistry and Biochemistry, Thapar University, Patiala, India. The matter embodied in this thesis has not been submitted in part or full to any other university or institute for the award of any degree in India or Abroad.

Anila

(Supervisor)

Dr. Bonamali Pal

Professor and Head

School of Chemistry and Biochemistry

Thapar University, Patiala - 147004

Punjab (India)

Acknowledgements

Through this section of the thesis, I would like to convey my heartiest thanks to all those who supported and encouraged me in many ways for the accomplishment of this study and made it an unforgettable journey for me.

First and foremost, praises and thanks to the almighty God, the most merciful and compassionate, for His blessings throughout my research work to complete this project successfully.

I would like to extend my sincerest gratitude to my supervisor, Dr. Bonamali Pal, Professor and Head, School of Chemistry and Biochemistry, Thapar University, Patiala for giving me the valuable opportunity to work under his worthy guidance. His immense knowledge, constructive ideas, and innovative way of teaching, efforts and time for giving me the useful suggestions on manuscript writing and research presentations were priceless. He has always supported, inspired, encouraged and challenged me in many ways for making me confident and enhancing my professional growth. He gave me the opportunities to present my research work in several conferences and other professional gatherings, through which my public speaking skills have improved immensely. I will always remain thankful to him for preparing me for my future career and without his inspiration; I would not be able to achieve so much today. I attribute the level of my doctoral degree to his motivation, encouragement and sustainable effort.

I express my special regards to Dr. Satnam Singh, Professor, School of Chemistry and Biochemistry, Thapar University, Patiala for his ever-helping attitude and good wishes. I would also like to thank the members of my doctoral committee, Dr. Kulvir Singh, Dr. Amjad Ali and Dr. Kamaldeep Paul for their insightful comments, advices and scientific discussions. I am indebted to all my respected teachers who touched my life and enlightened my path with their incredible knowledge. Also, special thanks to the faculty specially Dr. Vijay Luxmi and the other staff of School of Chemistry and Biochemistry for their supportive nature and official help.

I sincerely acknowledge the Council of Scientific and Industrial Research, CSIR for providing me the financial support.

I would also like to thank Dr. B. K. Chudasama and Mrs. Parveer Kaur (School of Physics and Material Science, Thapar University, Patiala) for Zeta potential and Conductance analysis. I would like to extend my thanks to Sophisticated Analytical Instruments (SAI) Laboratories,

Thapar University, Patiala, Sophisticated Analytical Instrumentation Facility (SAIF), Punjab University, Chandigarh, SAIF, IIT Bombay and Central Instrumentation Laboratories (CIL), NIPER, Mohali for SEM and TEM analysis.

This word 'Thank you' seems insufficient for my friends who expressed their constant moral support, care and understanding towards me and providing a stimulating and fun filled environment. I am greatly thankful to my senior labmates Mrs. Rupinder Kaur, Mrs. Nidhi Gupta, Mr. Rohit Singh and Mr. Inderpreet Singh, who extended their support in a special way. I am also thankful to my dear friends Mrs. Jaspreet Kaur, Mr. Bhupender Pal Thakur, Miss Harjot Kaur, Miss Nitika Sharma, Miss Parul Gulati, Miss Tanushree Basu, Mrs. Shweta Sareen, Mr. Rayees Ahmed Rather and Mr. Roopchand Prajapati for their precious friendship and for making this journey easier. I will forever cherish the warmth shown by them, whose smiling faces always inspired me. I would also like to acknowledge Miss Mani Mahajan, Miss Prinka, Miss Richa Rani and Mr. Akul Sen Gupta for their timely help.

Words fail me to express my regards to my family for their encouragement and inspiration throughout my research work, which always kept me lifted up during the hard phases of my life. I would always remain indebted to my loving mother, Mrs. Kiran Monga and father, Mr. Satish Kumar, who always remained beside me as a source of motivation. I owe everything to them. My special thanks to my younger brother, Mr. Sanjay Monga, my grandma and grandpa for their unconditional and support in every aspect. A deep gratitude to my mother-in-law and father-in-law for their sustained encouragement and consistent moral support, throughout and always.

Saving the most important for last, I wish to give my heartfelt thanks to my husband, Mr. Pankaj Gandhi, whose unwavering love, patience and continual support in my academic endeavors enabled me to complete this thesis.

Besides this, I am thankful to the persons who knowingly and unknowingly helped me during the successful completion of this work.

Table of Contents

List of Abbreviations

NPs	Nanoparticles
SPR	Surface Plasmon Resonance
LSPR	Localized Surface Plasmon Resonance
SP band	Surface Plasmon band
TSP band	Transverse Surface Plasmon band
LSP band	Longitudinal Surface Plasmon band
BM	Bimetallic
NCs	Nanocomposites
NS	Nanosphere
NR	Nanorod
M	Metal
UV	Ultraviolet
Vis	Visible
DRS	Diffuse Reflectance Spectrophotometer
PL	Photoluminescence
TCSPC	Time-correlated single photon counting
DLS	Dynamic Light Scattering
EDX	Energy Dispersive X-ray
SEM	Scanning Electron Microscopy
TEM	Transmission Electron Microscopy
HRTEM	High Resolution Transmission Electron Microscopy
SAED	Selected Area Electron Diffraction
JCPDS	Joint committee on powder diffraction standards
HPLC	High-Performance Liquid Chromatography
GC-MS	Gas Chromatography Mass Spectrometry
SERS	Surface Enhanced Raman Spectroscopy
VB	Valence Band
CB	Conduction Band

FCC	Face centered cubic
PVP	Polyvinylpyrrolidone
CTAB	Cetyltrimethylammoniumbromide
TX	Triton X-100
DMF	Dimethyl formamide
EG	Ethylene glycol
Au NS	Au nanospheres
Ag NS	Ag nanospheres
Cu NS	Cu nanospheres
Au NR	Au nanorod
Ag NPs	Ag nanoparticles
NB	Nitrobenzene
AN	Aniline
DNB	1,3-dinitrobenzene
NA	3-nitroaniline
PDA	1,3-phenylenediamine
NT	3-nitrotoluene
AT	3-aminotoluene
CNB	1-chloro-3-nitrobenzene
CAB	1-chloro-3-aminobenzene
NAP	3-nitroacetophenone
AAP	3-aminoacetophenone
PNP	*p*-nitrophenol
PAP	*p*-aminophenol
PNB	*p*-nitrobenzoic acid
PAB	*p*-aminobenzoic acid
SA	Salicylic acid
a.u	Arbitrary Unit
ca.	Calculated amount
wt%	Weight percent
R_t	Retention time

List of Symbols

e^-	Electron
h^+	Hole
C(ƶ)	Autocorrelation function
E_g	Band gap
h	Planck's constant
υ	Frequency
W	Watt
nm	Nanometer
m	Meter
cm	Centimeter
µm	Micrometer
µS	Micro Siemen
mm	Millimeter
µL	Microliter
mL	Milliliter
g	Gram
mg	Milligram
mV	Millivolt
min	Minute
h	Hour
s	Second
ns	Nanosecond
mol	Mole
mM	Millimolar
µM	Micromolar
α	Absorption coefficient
°	Degree
λ	Wavelength

%	Percentage
ζ	Zeta potential
ζ_{av}	Average lifetime
E^{o}	Reduction potential
E_f	Fermi energy
V	Volt
eV	Electron volt
keV	Kiloelectron volt
L	Length
W	Width

Abstracts

The work presented in this thesis enlightens the significance of coinage bimetallic (BM) nanocomposites (NCs) over their monometallic counterparts. Main emphasis has been given to the synthesis of BM NCs in the form of core@shell alloy and hollow nanostructures by varying the nature of core, shell composition and composition, their characterization, and application to catalysis and co-catalysis. This whole work is divided into six chapters which are described below:

Chapter 1: Introduction and Literature: The first chapter provides the brief introduction on the need of BM NCs over monometallic NPs which have been emerging as important catalyst due to the synergistic effects between the two metals. A brief description of preparation strategies for core@shell, alloy and hollow BM NCs and various techniques used for the characterization of optical, electrokinetic, catalytic and co-catalytic properties of BM NCs relative to their monometallic counterparts have also been incorporated.

Chapter 2: Improved Catalytic Activity and Surface Electro-kinetics of Bimetallic Au-Ag Core-Shell Nanocomposites: This chapter demonstrates the preparation of core@shell NCs of Au@Ag and Ag@Au for measuring their catalytic activity and electro-kinetic properties relative to their respective monometallic counterparts. A significant blue-shift (530 to 408 nm) and red-shift (420 to 550 nm) of the surface plasmon (SP) band for Au@Ag and Ag@Au NCs, respectively, was observed due to increased size of binary composites depending on the nature of core and shell material. The thickness of the deposited Ag shells varied from ~3-10 nm on Au core leading to the formation of Au@Ag NCs. On the other hand, the Ag core served as a sacrificial template, where Ag@Au NCs was converted to hollow Ag-Au alloy shells (~15 nm) because of the galvanic reaction between them due to the difference in their redox potential. Further, an increased zeta potential of resulting Au@Ag (+57.8 mV) and hollow Ag-Au alloy shell (-20.13 mV) NCs in comparison to monometallic Au (-6.13 mV) and Ag nanospheres (-5.74 mV) was found due to surface passivation with aqueous $AgNO_3$ and $AuCl_4^-$ solution, respectively. These BM NCs exhibited ~2 times higher catalytic activity than the monometallic

nanoparticles depending on shell thickness and the core of the respective metals for the nitrobenzene and 1,3-dinitrobenzene reduction.

Chapter 3: Preparation and Characterization of Different Shapes of Au-Ag Bimetallic Nanocomposites for Enhanced Physicochemical Properties: This section reports the preparation and characterization of BM Au@Ag NCs consisting, Ag shell of varied thickness (2-20 nm) and Au nanospheres (Au NS) and Au nanorods (Au NR) as cores for the selective catalytic reduction of nitro-organics. A significant blue-shift in the SP band of Au NS (529 nm) and Au NR (700 and 538 nm) to 400 nm, and 522 and 412 nm, respectively, was found with an increased thickness of Ag shell that led to a notable color change. The measured zeta potential of Au NS (+26 mV) and Au NR (+22.4 mV) were also considerably increased due to the surface passivation with an Ag-shell over Au particles. It revealed that the catalytic reduction of 1,3-dinitrobenzene by the anisotropic AuNR@Ag BM NCs produced a highly selective formation of 3-nitroaniline (74%) relative to 1,3-phenylenediamine by bare Au NR (64%), Au NS (45%) and AuNS@Ag NCs (76%). Whereas 53-60% aniline was obtained from the reduction of nitrobenzene by Au@Ag compared to 34-41% yield by bare Au NPs. Thus, it was derived that the surface structural properties for the selective catalytic reduction of nitro-organics could be significantly tuned by varying the shape of the Au-core and Ag-shell thickness.

Chapter 4: Morphological and Physicochemical Properties of Ag-Au Binary Nanocomposites Prepared by Different Surfactants Capped Ag Nanoparticles: This chapter demonstrates the influence of surfactants of different chemical nature passivizing the Ag nanoparticles (Ag NPs) on the morphology and physicochemical properties of Ag-Au BM NCs. The Ag NPs were synthesized using: polyvinylpyrrolidone (PVP), cetyltrimethylammoniumbromide (CTAB) and Triton X-100 (TX), followed by the deposition of Au on their surface. TEM analysis revealed the formation of hollow Ag-Au shells (~15 nm) and mixed solid Ag-Au alloys (~20-25 nm) using PVP and CTAB-Ag NPs, respectively as the reaction template. In contrast, the porous-hollow aggregates of Ag-Au NCs (~16-22 nm) were evolved during the reaction between Au^{3+} and TX-Ag NPs due to the difference in reaction rates between the Au^{3+} ions and various surfactants capped Ag NPs. As a result, these diverse morphologies of BM NCs exhibited a significant variation in SP band, color, hydrodynamic size

and zeta potential as compared to their monometallic Ag NPs. For example, a SP band of PVP-Ag NPs (488 nm) gradually red-shifted to 550 nm with the addition of Au^{3+} with notable color change from green to characteristic blue color indicating the composition change from Ag to Au rich. Therefore, the catalytic activity of various Ag-Au BM NCs was found to be ~2 times higher than the monometallic Ag NPs for the reduction of different nitro-aromatic compounds attributed to the electronic effect at Ag-Au interface and their morphology.

Chapter 5: Comparative Co-catalytic Effect of Monometallic and Bimetallic Core-Shell Nanocomposites on Titania Photocatalysis by Visible Light: This chapter signifies that the BM coinage metal NCs deposited on TiO_2 possess the ability to absorb visible light in a wide wavelength range and are also expected to display the new properties due to synergy between two distinct metals. As a result, they reveal highest level of activity than the monometallics deposited on TiO_2. In this respect, the core@shell, (Cu@Ag and Ag@Cu), inverse core@shell (Cu@Au and Au@Cu) BM NCs and their monometallics modified TiO_2 have been relatively investigated for the optical absorption, emission, charge carrier dynamics, surface structural morphology and photocatalytic activity under visible light irradiation. A significant blue-shift in the SP band of Cu@Ag and Cu@Au and a red-shift in Ag@Cu and Au@Cu with notable color change were observed due to their composition change and morphology. Further, the TEM analysis also revealed the formation of eccentric core-shell Cu@Ag and uniform core@shell Ag@Cu and Au@Cu BM NCs which were deposited on TiO_2, evidenced by diffuse reflectance spectroscopy, EDX, photoluminescence and time resolved spectroscopy. The visible light irradiation on core@shell BM-TiO_2 promoted ~3 times higher reduction of 3-nitroacetophenone and 1-chloro-3-nitrobenzene and ~2 times higher degradation of salicylic acid as compared to monometallic-TiO_2. This can be attributed to decreased work function of resulting Cu-Ag and Cu-Au BM NCs (ca. 3.8-4.6 eV) relative to their individual particles (4.3-5.3 eV) which decreased the height of Schottky barrier created at core@shell BM-TiO_2 heterojunction. As a result, this led to the efficient electron transfer from the BM NCs to TiO_2, resulting in enhanced photocatalytic activity than the monometallic-TiO_2.

Chapter 6: Influence of oxidative etching of Au nanostructures by $KMnO_4$ on its surface morphology, electro-kinetic properties and improved catalytic activity: This section reports the impact of oxidative etching of Au NS and Au NR by $KMnO_4$ on their surface morphology, electro-kinetic properties and catalytic activity. A significant blue-shift of the SP bands for Au NS (536 to 527 nm) and Au NR (679 to 532 nm) were observed, due to their size and shape alterations after oxidative dissolution. TEM analysis also revealed the formation of various irregular Au nano-morphologies such as spheres (~4-7 nm), low aspect ratio rods (2.6) and spheroids (~13 nm) of narrow size distribution after $KMnO_4$ etching. As a result, the hydrodynamic diameter of Au NS (~41 nm) and Au NR (~109 nm) were reduced to ~4 nm and ~34 nm, respectively. The oxidative dissolution of Au^0 by $KMnO_4$ occurred via its oxidation to Au^{3+} ions as confirmed by the measured electrode potential, $E^0(Au^0/Au^{3+})$ = -0.90 V by cyclic voltammetry with significant increase in the zeta potential and conductance values. The etched Au NPs being smaller in size and of higher surface to volume ratio resulted in ~2 fold higher catalytic activities for the reduction of *p*-nitrophenol and *p*-nitrobenzoic acid as compared to bare unetched Au nanostructures.

CHAPTER 1

Introduction and Literature

1.1 Background

1.1.1 Metal Nanoparticles as Catalysts

Metal nanoparticles (NPs) have attracted extensive interest in scientific research as well as industrial applications, owing to their unique electronic [1-4], optical and catalytic properties [5-9], sensing [10-12], and surface enhance d Raman scattering (SERS) [13-15]. In nano size regime, the metal NPs exhibit a large fraction of surface atoms i.e., high surface to volume ratio [16] which increases the surface energy compared to bulk materials. In addition, the continuous band structure of metals becomes discrete and loses their metallic character, as the size of particle decreases due to quantum confinement effect [17]. As a result, the high surface to volume ratio and quantum size effect [18] gives NPs distinctly different properties from their bulk counterparts. *Nanomaterials, therefore, refers to the class of materials having at least one of its dimension in the nanoscale (1-100 nm).* Thus, the metal NPs are considered as the promising materials for catalysis in industries. For instance, the small clusters of Au were found to be catalytically active [19] in contrast to bulk Au because the exposed surface atoms were 50 times more than its bulk material. As a result, the use of NPs as catalysts has increased exponentially as their properties and reactions are recognized. The metal NPs have been considered for both homogeneous (catalyst and reactants are in the same phase) as well as heterogeneous (catalyst and reactant are in different phase) catalysis. The major difference between these two systems is that the homogeneous catalyst is difficult to recover from the reaction medium [20] in contrast to heterogeneous catalyst. However, the homogeneous catalyst is used in a very minute quantity where every single catalytic entity acts as a single activity site [21]. This makes homogeneous catalyst more active and selective compared to traditional heterogeneous catalysts such as oxides or supported metal particles. Besides this, the catalytic performances of NPs are strongly dependent on the morphology i.e., size and shape of the particles.

(a) Influence of Nanoparticles Size

Literature reveals [22] that a particle of size 30 nm has 5% of its atoms on the surface, 10 nm has 20%, and 3 nm has 50% exposed surface atoms which can efficiently participate in a chemical

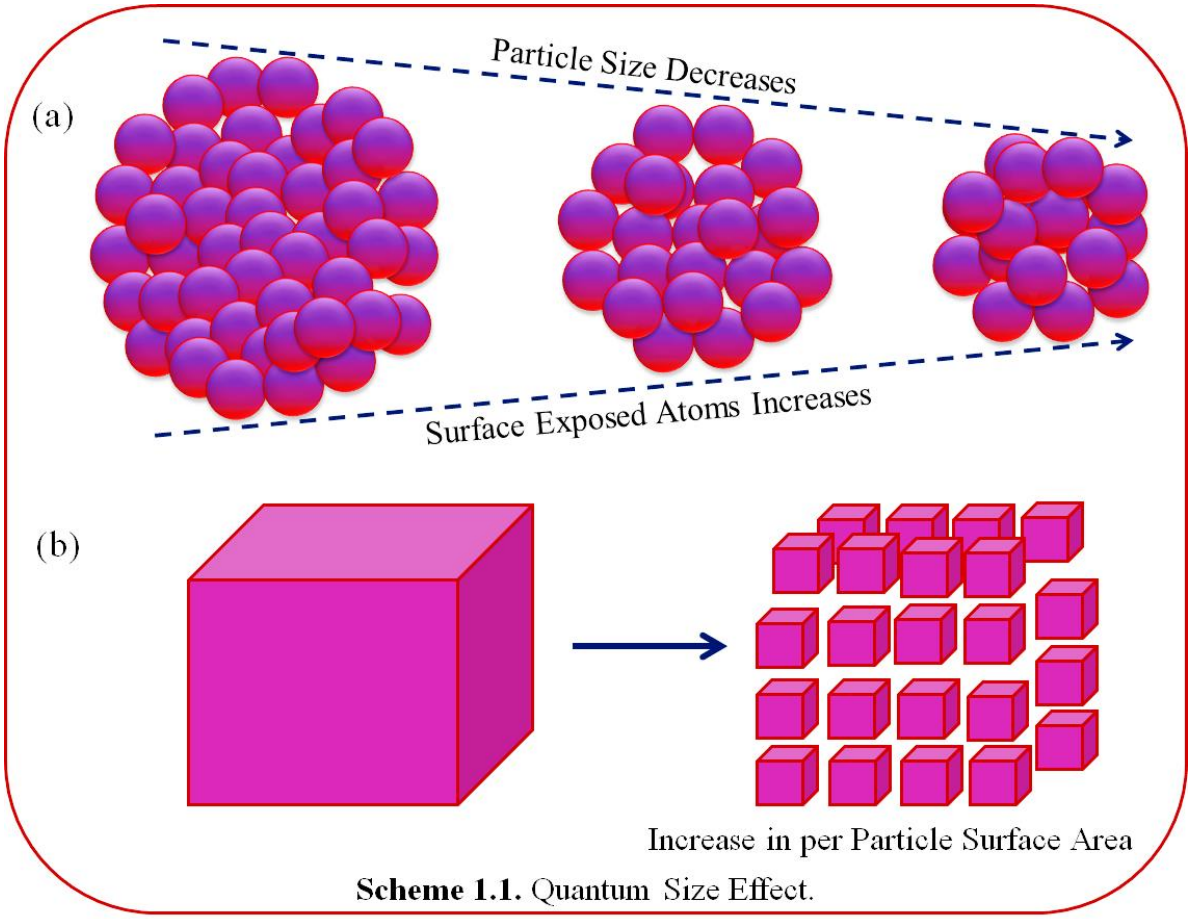

Scheme 1.1. Quantum Size Effect.

reaction as shown in Scheme 1.1a. Scheme 1.1b illustrates that when a bulk material is subdivided into individual NPs, the total volume remains the same, but the collective surface area would greatly increase and hence, intend to show a profound effect on catalytic performances. Therefore, the smaller particles are found to be more active owing to the large numbers of surface active atoms available for catalysis. The catalytic activity of metal NPs was reported [23] to increase with decreasing particle size for the reduction of nitro-aromatic compounds. Furthermore, a large number of coordinatively unsaturated surface atoms are associated with quantum sized particles which have rough surfaces and therefore, exhibit enhanced reactivity due to the effective chemisorption of the reactant molecules [24]. Ornelas et al. reported the higher hydrogenation of styrene using Pd NPs of smaller size due to the presence of uncoordinated sites on the catalyst surface [25].

(b) Influence of Nanoparticles Shape

Another important parameter which plays a key role in catalysis is the geometric shape of the nanocrystal [26-36]. Every shape has its own characteristic property, have varied number of

atoms on the corners and edges, dissimilar surface to volume ratio, high and low index planes, exposed crystallographic facets, etc. as shown in Scheme 1.2. The atomic arrangement within the spherical shape is quite different in comparison to rod or wire and hence, interacts with the substrate in a dissimilar manner and would result in diverse reactivities and selectivities. This gives rise to the possibility that the use of metal NPs of varied geometries could catalyze different reactions with different proficiency. For example, Xu et al. [37] observed that the Ag nanocubes were 14 times more reactive than the nanoplates, and 4 times more active than spherical NPs for the oxidation of styrene. Similarly, Cuenya et al. [38] reported that the Ag nanocubes and nanowires with {100} facets display better selectivities than nanospheres (NS) composed of {111} facets for the selective epoxidation of ethylene. Narayanan et al. [26,30,39] examined the conversion of hexacyanoferrate (III) by thiosulfate ions using various shapes of Pt NPs which follow the sequence as Pt nanocubes < Pt nanospheres < Pt nanotetrahedra. In addition, the different morphologies like hollow or porous NPs tends to exhibit quite distinctive catalytic performances relative to their solid NPs. For example, Au nanocages and nanoboxes were reported [28] to be the superior catalysts than the solid Au NPs for a redox reaction.

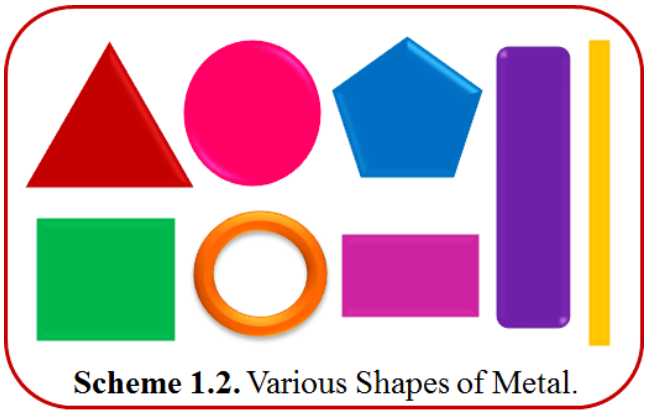

Scheme 1.2. Various Shapes of Metal.

1.1.2 Why Coinage Metal Nanoparticles?

Among the various transition metals, the coinage metal NPs (i.e., Au, Ag and Cu) with fascinating optical, physicochemical and electronic properties [40-42] have become the subject of intense research. These metals owing to their brilliant luster, stability in air and water and anti-fungi and anti-bacterial properties [43-46] were used to make ornaments, utensils, currency coins, medicines, colored window glass etc. since prehistoric times. However, with the advent of nanoscience, the size and shape dependent unique properties of nanoscaled noble metal materials [47] have been investigated for many applications. The study of coinage metal NPs is advantageous because they are noble and stable to oxidation. The colloidal solution of these noble metal NPs, show a very intense color and exhibit a characteristic absorption band in the visible region of the spectrum, called surface plasmon resonance (SPR) band [48-53] which is

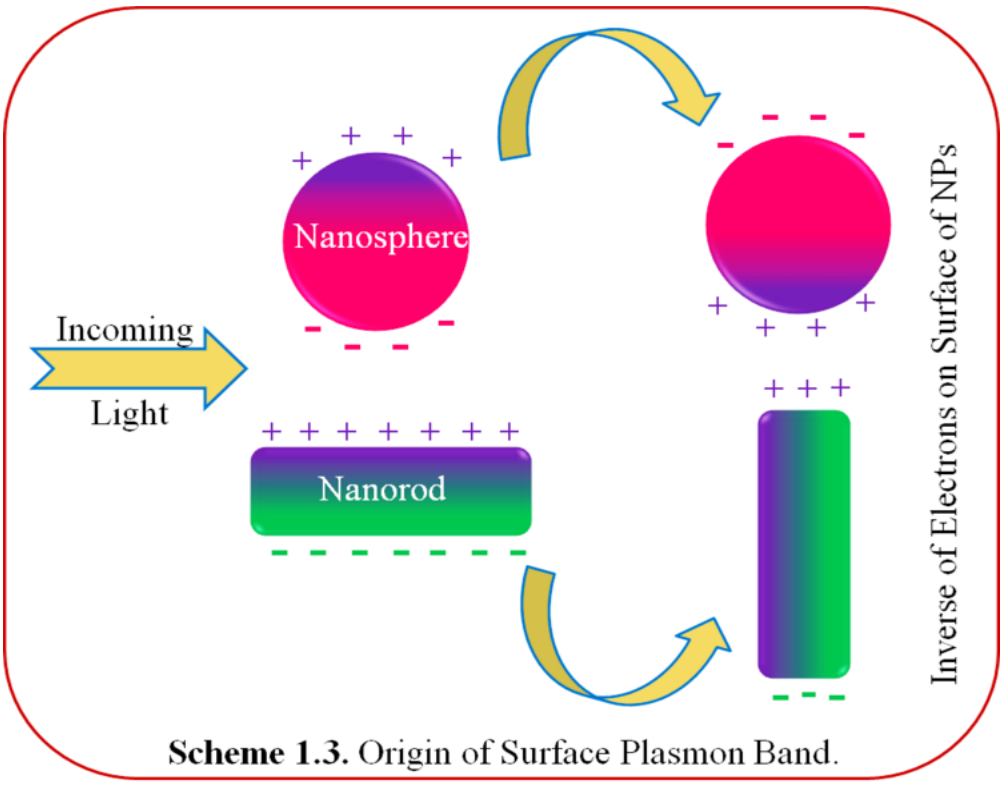

Scheme 1.3. Origin of Surface Plasmon Band.

absent from the bulk material. SPR is the optical feature of metal NPs and can be defined as the resonance energy produced, when the frequency of the incident light comes into resonance with the frequency of the oscillating conduction band electrons (e^-) present on the metal NPs surface (Scheme 1.3). The electric fields of the incoming light polarize the free conduction e^- and hence, they oscillate under the influence of applied fields against the restoring force of the heavier positive core of a NP. As a result, a dipolar oscillation of the e^- is produced which is known as the surface plasmon (SP) band [48]. This resonance frequency can be easily determined from absorption spectroscopy and depends on a few factors such as particle size, shape and nature of the surrounding medium [48-54]. However, the SP band of many metals such as, Pt, Rh, Pb, In, Hg, Cd and Sn etc., lies in the UV part of the spectrum and do not exhibit any special color effects. But the coinage metals such as Au, Ag and Cu are exceptional and are also known e^- banks that lend out e^- at the appropriate time, and store them for chemical species at other times.

1.1.3 Need of Bimetallics over Monometallic Nanoparticles

In recent years, the bimetallic (BM) NPs, composed of two different metal elements, have gained tremendous progress and interest [55-59] than their monometallic counterparts due to their fascinating physical and chemical properties, especially in catalysis. Since the catalysis depend upon the catalyst surface, the precise modification by introducing another metal element on the

catalyst surface could alter their catalytic performances (reactivities, selectivities, etc.). A variety of approaches have been investigated to prepare BM nanocomposites (NCs) including photochemical method, co-reduction of mixed metal ions, electrochemical reduction, successive reduction, galvanic displacement reaction, microwave-polyol method, etc. [60-67]. Malik et al. [60] reported a photochemical approach for the preparation of core@shell, Au@Ag BM NCs. The Au-Ag BM alloy NPs were prepared by the simultaneous reduction of the metal ions in the presence of an appropriate stabilizer, such as sodium citrate [68] whereas the core@shell BM NPs were reported to generate through the sequential reduction of the different metals, with well-defined boundaries between them [69]. Sun et al. [61] reported the formation of Au-Ag nanoboxes due to the galvanic replacement reaction between Ag nanocubes and $HAuCl_4$. The Au@Ag nanorods were synthesized by using Au nanorods (Au NR) as the template [64] with different shell thickness of Ag resulting in color change of the solution from light gray to green to bluish green to purplish red depending upon the amount of Ag. Tsuji at al. synthesized Au-Ag BM NPs under oil-bath heating in ethylene glycol at 150 ºC [66] and Au@Ag [67] and Au@Cu [70] nanocrystals by microwave-polyol method.

The difference in catalytic performances between a BM and monometallic catalyst can be explained through electronic or a ligand effect [71-73], where an electronic charge transfer process takes place at the interface of two metals, resulting in the change of net e^- density at the surface of BM NCs. Besides this, the new geometries of active sites are also formed [74,75] due to the incorporation of second metal on the surface of first metal, called the ensemble or geometric effect. For example, S. Tokonami et al. [76] performed glucose oxidation using Ag-Au BM NPs and reported that the activity was 18 times higher than that of monometallic Au NPs under the same conditions. Zhang et al. [77] reported the higher catalytic activity of Au@Ag having higher rate constant, k= 0.18 min^{-1} than the corresponding monometallic Au (k=0.019 min^{-1}) and Ag NPs (k=0.069 min^{-1}) for the reduction of *p*-nitrophenol to *p*-aminophenol by $NaBH_4$. Similarly, the Au-Ag alloy BM NPs were also observed [78] to be highly active during the reduction of *p*-nitrophenol than their monometallic NPs. The Au-Pd, Au-Pt and Au-Ag [79] BM NPs showed a higher glucose oxidation of 9230, 14200, and 14900 mol glucose h^{-1} mol $metal^{-1}$, respectively, than the monometallic Au NPs (4020 mol glucose h^{-1} mol $metal^{-1}$). The Ag-tipped Au NRs exhibited superior catalytic activity [80] than the Au@Ag NRs and Au NRs, due to their distinctive morphology and electronic effect between the Ag and Au metals. Monga et al.

[81] studied that the core@shell, Au@Ag and inverse core@shell, Ag@Au BM NCs exhibited higher catalytic activity for the reduction of different nitro-aromatic compounds than their monometallic NPs as described in Chapter 2.

The physical and chemical (reactivities, selectivities, etc.) properties of BM NCs can be well tuned by varying the constituting materials, composition, nature of core, shell thickness, morphology (size and shape), the core to shell ratio, etc. For example, the styrene oxide selectivity was reported [82] to be 76.6% using Ag/Cu supported on alumina with molar ratio of 3/1 than 66.9%, 65.6% and 20.4% by Ag/Cu (1/1), Ag/Cu (1/0) and Ag/Cu (0/1), respectively, for the epoxidation of styrene. In the hydrodechlorination of *p*-chlorophenol [83], the $AgPd_x$ (x = 2, 4, 6, 9, 19) showed pronounced composition dependent catalytic activities, leading to the $AgPd_9$ catalyst with excellent activity. Fu et al. [84] studied the impact of shell thickness on Au@Ag NR, where the refractive index sensitivity and figure of merit increased with Ag shell thickness, but decreased when Ag shell became too thick due to the change of shape from rod to non-regular. The Au/Ag-dendrimer NCs with a 1:1 Au/Ag metal ratio showed the highest reactivity [85] as compared to other metal ratios (3:1, 1:3) and to pure Ag and Au. Wang et al. [86] showed that the activity of Ag-Pt NWs was highly enhanced over monometallic nanostructures, and was optimized by a low Pt loading of 1.34 at.%, which indicated a catalytic role of the inter-metallic interface for the e^- transfer. The control of the shape of BM NCs also allows the various physico-chemical properties to be tuned because of the anisotropy effects. The electrochemical activity of Au@Pd of different shapes tetrahexahedra, concave octahedra and octahedral were investigated [87] for the oxidation of ethanol and found that the tetrahexahedra nanocrystals with high index {730} facets exhibited the best electrocatalytic activity. Au-Ag octahedral NPs of size (> 100 nm) with Ag shell-thickness of 22.5-37 nm displayed a higher catalytic reduction [88] of nitroarenes than the nanocubes of the same material. Khlebtsv et al. [89] investigated the better SERS response of the Au@Ag cuboids due to the uniform packing and more efficient generation of electromagnetic hot spots, as compared to the Au@Ag dumbbell. Monga et al. [90] revealed that the catalytic reduction of 1,3-dinitrobenzene by the anisotropic core@shell Au@Ag NR produced a highly selective formation of 3-nitroaniline relative to 1,3-phenylenediamine by bare Au NR, Au nanospheres (Au NS) and Au@Ag NS as explained in Chapter 3.

The introduction of a second metal element on the surface of the first metal element or monometallic NPs leads to the surface modification and hence, changes the functionality, dispersibility and stability of BM NCs. These resulting BM NCs have a distinctive type of binding properties with reactants as compared to the individual metal NPs. As a result, an extra stabilization of the transition state during the bonding between BM NCs and the reactants can be attained in contrast to the respective interaction with the monometallic NP [91]. In addition to the above properties, the cost of the catalyst can also be reduced, by coating a less noble metal with a more noble metal and, thereby, dropping the consumption of expensive metal compared to the same sized pure metal. Colloidal NPs can also act as a sacrificial template for the formation of hollow or porous BM morphologies which possess increased surface area, low densities [92-95] and show promising applications in drug delivery, nanosized chemical reactor, catalysis, and nanomedicine, etc. [94,96-99]. Hollow Pt/Ag nanostructures have been found [100] to catalyze the degradation of Rhodamine B as efficiently in the presence of KBH_4 than that of Ag NS. Rao et al. [101] gave ~2 times higher catalytic efficiency of Ag-Pd hollow NPs embedded in PVA thin films than Ag NPs by its application in Suzuki-Miyaura reaction. Recently, the enhanced localized surface plasma response (LSPR) and SERS response of Ag_{core}-$AgAu_{frame}$ nanocubes was reported [102], where, upon the etching of Ag-core served as an active catalyst for reduction of *p*-nitrophenol. Monga et al. [103] reported the higher catalytic activity of various hollow, porous and alloy Ag-Au BM NCs resulted from the different surfactants capped Ag NPs for the different nitroarenes reduction, ascribed to their morphology as explained in Chapter 4.

1.2 Research gap

BM NCs with controlled morphologies and composition have exhibited superior properties and broader applications in comparison to their monometallic counterparts. In recent years, the research towards the variety of BM NCs with diverse combinations of metals and morphologies have been developing and reported. Despite this fast progress in the exploration of BM NCs, challenges still remain in the following directions:

(a) The synergistic electronic effect at the interface of the two metals in BM NCs enhances its catalytic efficacy. As a result, they have the potential to exhibit higher catalytic activity and other functionalities by continual tuning through the different combinations of metal elements (Au-Ag, Au-Cu, Ag-Cu, etc.) and the composition of the constituents. Therefore, how the nature of

metals, shell-thickness and shape affect the reactivity and selectivity during the catalytic process and TiO_2 photocatalysis is an emerging field of research. The core particle is prepared by the reduction of metal salt (M_1) which acts as a seed for the deposition of shell (M_2) in the presence of suitable stabilizer, and the shell thickness is varied by changing its molar ratio with respect to the core as shown in Scheme 1.4. Similarly, the inverse core@shell structures are prepared by reversing the metal salts (Scheme 1.4). In this way, the functionality of core@shell BM NCs changes by changing the shell thickness and nature of metals due to the change in the electronic or geometric properties of a parent monometallic NPs. Therefore, these nanostructures have potential to exhibit higher catalytic activity and selectivity.

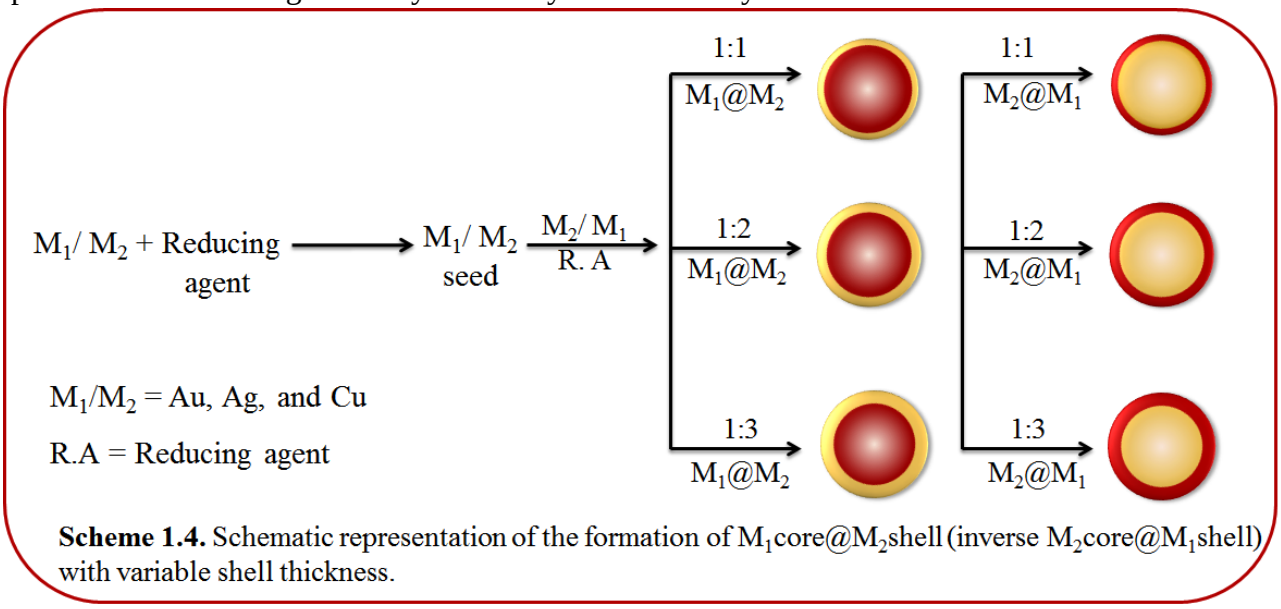

Scheme 1.4. Schematic representation of the formation of M_1core@M_2shell (inverse M_2core@M_1shell) with variable shell thickness.

(b) The monometallic NPs are used as a sacrificial template for the formation of hollow BM NCs which are still under investigation due to their exceptional properties attributed to higher surface areas and lower densities. Infact, the chemical dissolution can lead to the nanochannels formation, which can offer more bonding sites for the transport of reactant and products. So, these metallic hollow NPs can be useful in selective organic transformations. Since the core@shell BM NCs are generally prepared via seed mediated process, therefore, the surfactants capping the monometallic NPs i.e., seed, may affect the coating of second metal on the resulting morphology, which may give rise to solid alloys, hollow or porous BM NCs of unique properties.

(c) The etching of monometallic NPs by chemical or photo-etching process can lead to the narrowing of the NP size by their fragmentation into smaller sizes or transformation into a new

shape. This could result in the formation of particles having a higher surface exposed atoms and, thereby, enhanced optoelectronic and physiochemical properties.

(d) Furthermore, there is a need to explore the surface or interfacial phenomenon (zeta potential) arising due to the electronic effect at the interface across the two metals or the interface of the core and the shell. The variation in the values of zeta potential determines the electrostatic repulsion or attraction between the NPs which decides the stability and net charge on the surface of NPs. The zeta potential measurements for the monometallic NPs have been observed by various research groups. However, there is no report available on the zeta potential measurement of coinage BM NCs. Besides this, the particle size distribution is also expected to vary from monometallic NPs to core@shell BM NCs. Therefore, the zeta potential and particle size distribution as a function of nature of metal, core-size, shell thickness needs to be focused in finding an optimum catalytic activity of BM nanostructures.

1.3 Objectives

Keeping in view the above points, the following objectives have been designed:

(i) Preparation of bimetallic/core@shell of coinage metals (Au, Ag and Cu).

(ii) Optimization of optical properties, electrokinetic parameters (i.e., zeta potential, conductance) and particle size distribution as a function of nature of metal.

(iii) Study of the effect of chemical or photo-etching (laser) on nanostructures and their morphology.

(iv) Study of catalytic activity for reduction of nitro organics.

1.4 Methodology

1.4.1 Preparation of Coinage Bimetallic Nanocomposites

Preparation of coinage (Au, Ag and Cu) BM NCs from their precursor metal salts can be divided into following parts: co-reduction, successive reduction and galvanic displacement reaction. BM NPs can have either core@shell, alloy, or hollow type of morphology depending upon the synthetic method adopted during their preparation.

(a) Co-reduction: This is a relatively simple method that involves the simultaneous reduction of the metal ions in their atomic form in the presence of suitable stabilizer giving rise to alloy BM NPs as shown in Scheme 1.5. For example, BM Au-Ag alloy NPs were prepared by the co-reduction of Au^{3+} and Ag^{+} metals in the presence of sodium citrate [68].

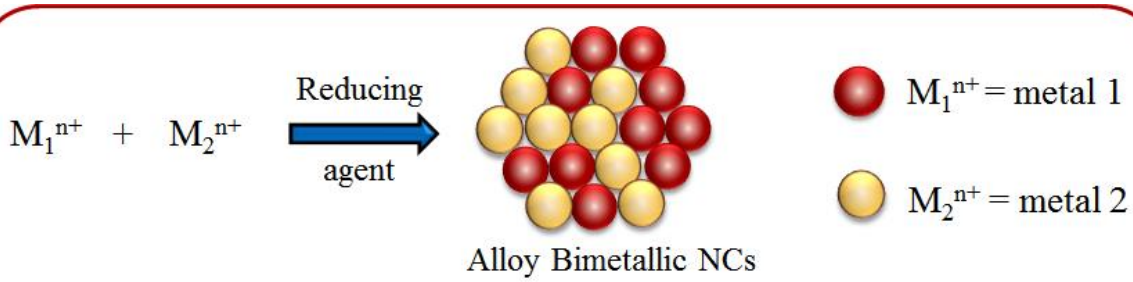

Scheme 1.5. Schematic representation showing the formation of Alloy Bimetallic Nanocomposites via Co-reduction Method.

(b) Successive reduction: This method is usually carried out to prepare core@shell BM nanostructures. The deposition of one metal (referred as shell) on a preformed NP of another metal (referred as core) seems to be very effective. For this purpose, monometallic NP is pre-synthesized and then second metal precursor is introduced into NPs solution which acts as a seed for the deposition of the second element as shown in Scheme 1.6.

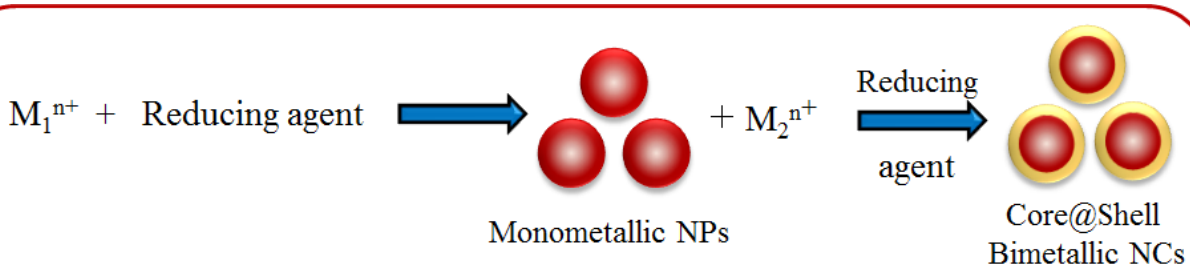

Scheme 1.6. Schematic representation showing the formation of Core@Shell Bimetallic Nanocomposites via Successive Reduction Method.

(c) Galvanic Displacement Reaction: It is a powerful method to produce hollow BM nanostructures. This comprises the usage of metal NPs having lower reduction potential and hence, serve as a sacrificial template for the incoming metal ions with higher reduction potential. As a result, the metal NP template is oxidized with the simultaneous reduction of incoming noble metal ions onto the surface of the template giving rise to hollow NCs (Scheme 1.7). These NCs may form smooth or rough surface depending on the reaction conditions, composition, capping agent used, etc.

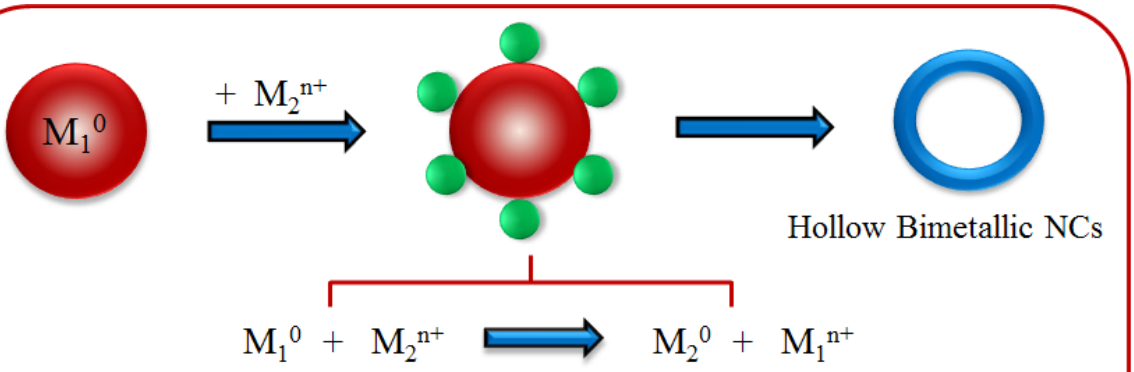

Scheme 1.7. Schematic representation showing the formation of Hollow Bimetallic Nanocomposites via Galvanic Displacement Reaction.

1.4.2 Preparation of Monometallic-TiO_2 and Core@Shell Bimetallic-TiO_2 Nanocomposites

The composites of as-synthesized monometallic as well as BM with TiO_2 were prepared by the wet impregnation method in which the total metal mass percentage of NCs were kept fixed with respect to TiO_2. In this method, TiO_2 was dissolved in an aqueous or organic solution and then, the NPs solution was added to a catalyst support. The catalyst was dried and treated with heat to drive off the volatile components within the solution, depositing the metal NPs on the catalyst surface.

1.5 Characterizations

Various sophisticated instrumental techniques have been used to characterize the NPs and NCs to get an idea of their size, shape, morphology, surface area, physicochemical properties, etc. which are listed below.

1.5.1 UV-Vis Spectrophotometer

UV-Vis spectroscopy is a technique used to quantify the light that is absorbed and scattered by a sample. Coinage metal NPs possess the optical properties that are dependent on their morphology, aggregation, refractive index and the concentration of particles, which makes this technique a valuable method for the identification and characterization of these nanomaterials. The NPs strongly interact with a specific wavelength of light which results in the promotion of an e^- to a higher energy level and hence, an absorption peak. The analysis was done on **Analytikjena Specord 205** instrument by taking ~2.5 mL colloidal NPs solution in a quartz cuvette within the range of 190-1100 nm.

1.5.2 Diffuse Reflectance Spectrophotometer

Diffuse Reflectance Spectrophotometer (DRS) was used to determine the reflectance/absorption of as prepared bare and monometallic and BM NCs modified TiO_2 in the UV-Vis region, and for the determination of the band gap (E_g) between the valence band (VB) and conduction band (CB) of the powdered samples. The analysis was carried on **Avantes Diffuse Reflectance Spectrophotometer.** The sample (2-5 mg) was taken on a glass slide and the light source probe was placed over the sample to record its absorbance/ reflectance spectra by using $BaSO_4$ as a reference. Band gap calculations of as prepared samples were done by using Tauc equation [88,89].

$$\alpha h\nu = A(h\nu - Eg)^n \quad (1.1)$$

A = constant; h = Planck's constant; υ = frequency of light; E_g = band gap; n = type of e^- transition process (n = ½ for direct allowed and n = 2 for indirect allowed transitions); α = absorption coefficient of the material. As TiO_2 is the indirect band gap semiconductor, hence the band gap was determined by extrapolating the linear portion of the plot of $(\alpha h\nu)^2$ versus hν.

1.5.3 Photoluminescence measurement

Photoluminescence (PL) technique deals with the electronic transitions from the excited state to the ground state (relaxation process) complementary to UV-Vis spectroscopy. In other words, PL is a very sensitive method to understand the electron-hole (e^--h^+) recombination property of a particular substance. **Perkin Elmer LS55 Spectrofluorimeter** was used to analyze the recombination properties of photogenerated species of synthesized NCs. For analysis, 1mg/mL aqueous or ethanol dispersion of as-prepared samples were photoexcited at 225-300 nm with the emission range of 300-900 nm and slit width of 2.5:5.

1.5.4 Time Resolved Spectroscopy

Time resolved spectroscopy measures the time that an e^- stays in its excited state following excitation with a laser pulse in bare TiO_2 and monometallic and core@shell BM modified TiO_2 NCs. The time resolved photoluminescence spectra was measured by time-correlated single photon counting (TCSPC) set up by **Edinburgh FL920 model** at room temperature on excitation with diode lasers at 390 nm in ethanol suspension. The sample was prepared by making a thick paste of TiO_2 powder (~50 mg) and monometallic/BM-TiO_2 NCs with a few drops of ethanol to make it as a solid mass. Thereafter, stub having solid mass was suspended vertically for laser pulsation and an average lifetime was recorded and calculated using the following equation [90].

$$\tau_{av} = (a_1\tau_1 + a_2\tau_2)/a_1 + a_2 \quad (1.2)$$

where, a_1 and a_2 denote the amplitude of band edge excitonic and trapping state emission, respectively.

1.5.5 Dynamic Light Scattering

Dynamic Light Scattering (DLS) is a technique used to determine the hydrodynamic size of NPs which have been dissolved in suspension or solution. The particle size distribution was determined by using a **Brookhaven 90 plus Particle Size Analyzer** by taking 2.5-3 mL of dispersed NPs solution in a cuvette. The Brownian motion of small particles in suspension causes the laser light to be scattered at different intensities. By measuring the time scale of these light intensity fluctuations, DLS can yield information regarding the average size or size distribution of particles in solution.

1.5.6 Zeta Potential measurement

When the NPs are suspended in an aqueous medium, the adsorption or ionization of ions takes place on the NPs surface, which leads to the formation of an electrical double layer resulting in the development of net charge, called zeta potential (ζ). Therefore, zeta potential is an important tool for understanding the state of NP surface and also predicts the long term stability of the NPs. The measurements were carried out by means of **Brookhaven Zeta Plus** at 25 ºC using a cuvette comprising a palladium electrode mounted on a machine support immersed in 1.5-2 mL of NCs solution.

1.5.7 Energy Dispersive X-ray Spectroscopy

Energy Dispersive X-ray (EDX) Spectroscopy was used for the elemental analysis or chemical composition of the selected points or areas of the sample qualitatively and semi-quantitatively. This technique was used as an attachment on scanning electron microscopy (SEM) or transmission electron microscopy (TEM) and utilizes the high-energy e^- that are ejected by an elastic collision of an incident e^- with sample's atom nucleus and are referred to as backscattered e^-. The yield of backscattered is in proportional to the atomic number of an element and therefore, the sample composition, elements and compounds, and their relative ratios in the area of one micrometer in diameter are determined using this technique. This EDX analysis was carried on **JEOL JSM-6510LB**.

1.5.8 Transmission Electron Microscopy

Transmission electron microscopy (TEM) is used to identify finest structural details of individual particles and their statistical size and shape distribution in the samples. In this technique, a beam

of e^- is transmitted through the sample and due to this interaction an image is formed, then magnified and focused onto an imaging device. High resolution transmission electron microscopy (HR-TEM) becomes a valuable technique due to its high magnification by which lattice fringes of materials can be clearly seen. The electron diffraction in TEM can be described analogously with X-ray diffraction by Bragg's equation where the selected area electron diffraction (SAED) of a sample area provides information about the lattice constants, crystallographic orientation and lattice type. In this research, low magnification **TEM Hitachi-7500** of 20-200 kV voltage with 2.4 A˚ resolution and High Resolution-TEM (HR-TEM) of 120 kV with 2 A˚ resolution, operating **on JEOL, JEM 2100** was used to investigate the morphology of all the samples. All the samples prepared in an aqueous solution were dropped on copper grids for their analysis, which was carried out at various sophisticated laboratories such as IIT Bombay, Panjab University, Chandigarh, and NIPER, Mohali, Punjab, India.

1.5.9 Cyclic Voltammetry

The cyclic voltammetry (CV) studies are used to determine the electrochemical properties of an analyte in solution, which measures the current in an electrochemical cell when voltage is applied in excess. This was performed with **DY2300 potentiostat (Digi-Ivy)** comprising of Ag/AgCl as the reference electrode, platinum wire and platinum as the counter electrode and the working electrode, respectively, immersed in an analyte solution.

1.5.10 Potentiometer Titration

It is a technique similar to direct titration of a redox reaction, where potential is measured across the analyte with the addition of titrant. The potentiometric titration was performed with an **Equiptronics Eq-602 potentiometer** comprising of calomel electrode and platinum as the reference and working electrode, respectively, immersed in an analyte solution. The overall electrode potential is calculated as:

$$E_{(\text{half equivalence})} = E^0_{(M^+/M)} - E^0_{(\text{calomel})} \quad (1.3)$$

$$E^0_{(M^+/M)} = E_{(\text{half equivalence})} + E^0_{(\text{calomel})} \quad (1.4)$$

where, $E^0_{(M^+/M)}$ = electrode potential of analyte

$E_{(\text{half equivalence})}$ = electrode potential at half equivalence point

$E^0_{(\text{calomel})}$ = electrode potential of calomel electrode

1.6 Catalytic Activity

The catalytic performances of coinage monometallic as well as BM NCs were carried out by the reduction of various nitro-aromatic compounds (Table 1.1). In a typical reaction, the requisite amount of the ice-cold $NaBH_4$ solution was added to an aqueous solution of nitro-aromatic compounds followed by the addition of calculated amount of NCs (Scheme 1.8). The reduction reaction was examined at regular intervals of time by measuring their absorption spectra and the products were further quantified using a high-performance liquid chromatography (HPLC). The reaction intermediates were investigated by gas chromatography mass spectrometry (GC-MS).

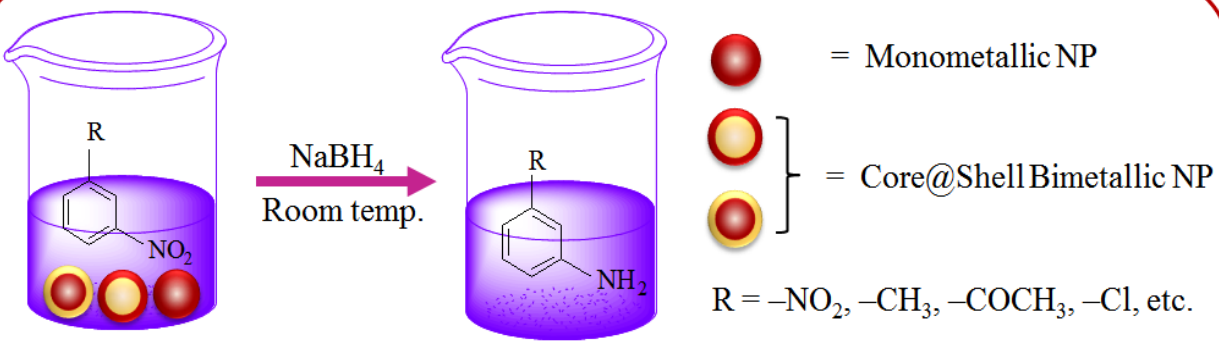

Scheme 1.8. Experimental set up for catalytic reduction reaction using Coinage Mono/ Bimetallic Nanocomposites.

1.7 Photocatalytic Activity

The photocatalytic activity of TiO_2 modified with monometallic and core@shell BM NCs was performed for the reduction of nitro-aromatic compounds (3-nitroacetophenone, 3-nitrobenzoic acid) and degradation of salicylic acid under visible light irradiation. A 250 W halogen lamp served as the visible light source which has high stability and an intense coverage of a wide spectrum in the range of 400-1100 nm. The experiments were carried out in a Pyrex tube containing substrates and catalysts under visible light illumination provided through a probe (0.7 cm) of optical fiber (1 m × 1.4 cm) at a distance of 1 cm over the surface of reaction mixture in the test tube as shown in Scheme 1.9. The reaction mixture was analyzed after filtration withcellulose filter 0.22 μm at fixed time of interval with UV-Visible spectrophotometer and HPLC.

Table 1.1. Nitroaromatics studied for catalytic reduction by monometallic and their bimetallic nanocomposites

S. No.	Substrates Studied	Products Analyzed
1.	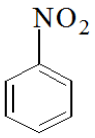	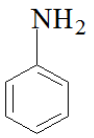
2.	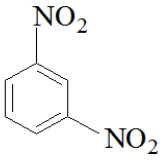	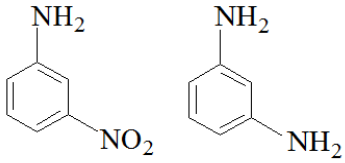
3.	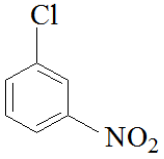	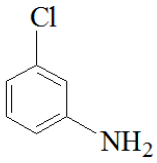
4.	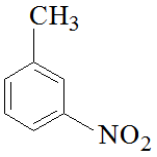	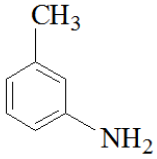
5.	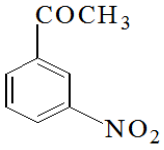	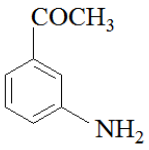
6.	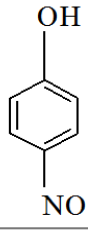	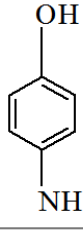
7.	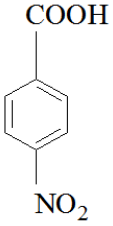	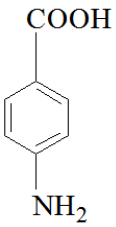

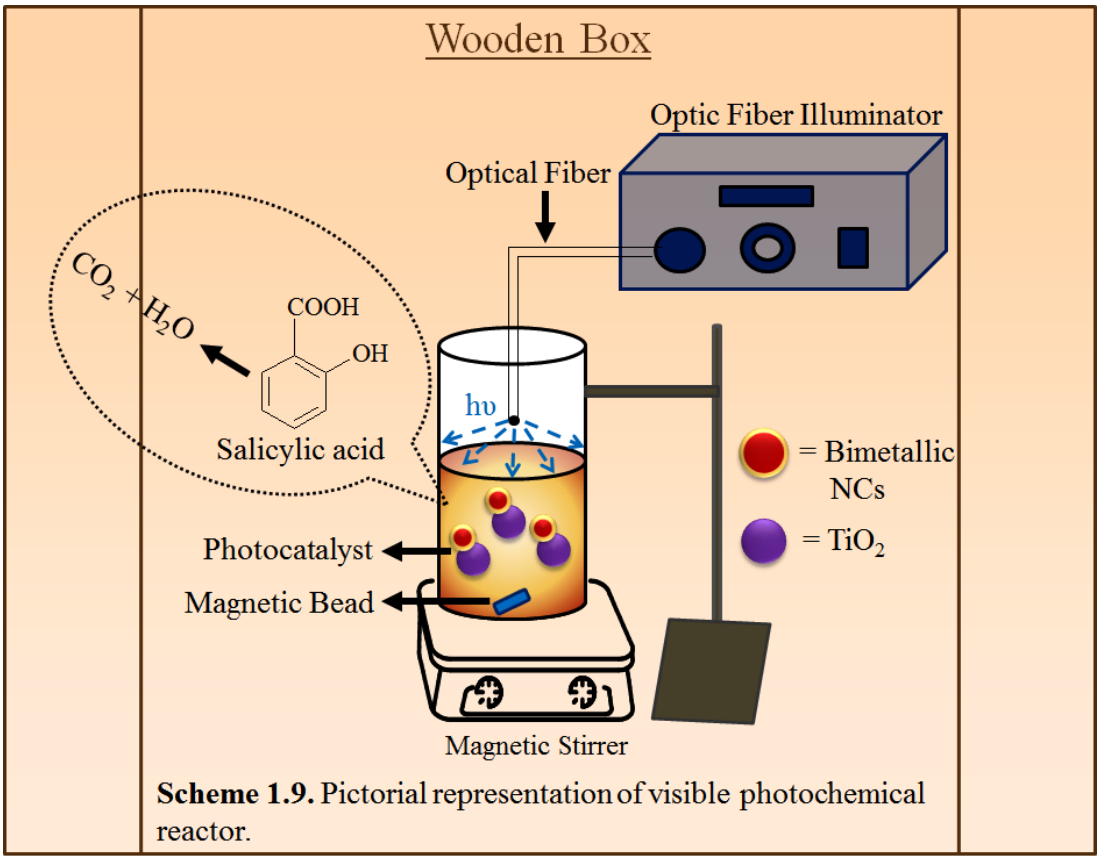

Scheme 1.9. Pictorial representation of visible photochemical reactor.

1.8 Reaction Analysis

1.8.1 UV-Vis Spectrophotometer

The time course studies of the catalytic reactions were monitored by measuring their absorption spectra using **Analytikjena Specord 205** instrument at regular intervals of time by taking 3 mL of filtered reaction sample in a quartz cuvette within the range of 190-1100 nm.

1.8.2 High-Performance Liquid Chromatography

High-performance liquid chromatography (HPLC) is a powerful tool employed to analyze the formation of different compounds during the reaction process. In this research, the analysis or the separation of the components of the reaction mixture were carried out by using **Agilent 1120 Compact LC** equipped with a column of Qualisil BDS C-18 (250 mm × 4.5 mm, 5 µm). The mobile phase used for the analysis was methanol: water (70:30) with a flow rate of 1 mL/min at 254 nm for the detection of the reduced products. 20 µL of the reaction mixture was injected into the loop after filtration by cellulose filter of 0.22 µm. This technique is based on the principle of adsorption in which analyte molecules are separated on the basis of their interaction with the mobile and the stationary phase.

1.8.3. Gas Chromatography Mass Spectrometry

Gas Chromatography Mass Spectrometry (GC-MS) technique was used to get the structural information of the various reaction intermediates and the products formed during the progress of the reaction. The spectra were measured by **Shimadzu GC 2010 and MS QP 2010** Plus equipped with a column of RTX-5 Sil MS (30 m × 0.25 mm i.d.). The reaction solution (5 mL) obtained after reaction, was subjected to centrifugation, filtration (cellulose filter 0.22 μm), and then evaporated to dryness over rota-evaporator. The left residue was dissolved in acetonitrile (5 mL) and then injected (1 μL) by using a 10 μL syringe for GC-MS analysis. The injection temperature was 270 °C, injection mode was split less and electron ionization detector with temperature 310 °C, oven temperature was 100 °C, and carrier gas was helium with flow rate 1 mL/min.

1.9 References

[1] S. Chen and Y. Yang, *J. Am. Chem. Soc.*, 2002, **124**, 5280–5281.

[2] M. A. El-Sayed, *Acc. Chem. Res.*, 2001, **34**, 257–264.

[3] S. A. Maier, M. L. Brongersma, P. G. Kik, S. Meltzer, A. A. G. Requicha and H. A. Atwater, *Adv. Mater.*, 2001, **13**, 1501–1505.

[4] P. V. Kamat, *J. Phys.Chem. B*, 2002, **106**, 7729–7744.

[5] C. J. Murphy and N. R. Jana, *Adv. Mater.*, 2002, **14**, 80–82.

[6] F. Kim, J. H. Song and P. Yang, *J. Am. Chem. Soc.*, 2002, **124**, 14316–14317.

[7] S. R. N. Pena, R. G. Freeman, B. D. Reiss, L. He, D. J. Pena, I. D. Walton, R. Cromer, C. D. Keating and M. J. Natan, *Science*, 2001, **294**, 137–141.

[8] T. S. Ahmadi, Z. L. Wang, T. C. Green, A. Henglein and M. A. El-Sayed, *Science*, 1996, **272**, 1924–1925.

[9] X. Teng, D. Black, N. J. Watkins, Y. Gao and H. Yang, *Nano Lett.*, 2003, **3**, 261–264.

[10] A. G. Tkachenko, H. Xie, D. Coleman, W. Glomm, J. Ryan, M. F. Anderson, S. Franzen and D. L. Feldheim, *J. Am. Chem. Soc.*, 2003, **125**, 4700–4701.

[11] T. A. Taton, C. A. Mirkin and R. L. Letsinger, *Science*, 2000, **289**, 1757–1760.

[12] N. T. K. Thanh and Z. Rosenzweig, *Anal. Chem.*, 2002, **74**, 1624–1628.

[13] P. M. Tessier, O. D. Velev, A. T. Kalambur, J. F. Rabolt, A. M. Lenhoff and E. W. Kaler, *J. Am. Chem. Soc.*, 2000, **122**, 9554–9555.

[14] L. A. Dick, A. D. McFarland, C. L. Haynes and R. P. V. Duyne, *J. Phys. Chem. B*, 2002, **106**, 853–860.

[15] J. B. Jackson, S. L. Westcott, L. R. Hirsch, J. L. West and N. J. Halas, *Appl. Phys. Lett.*, 2003, **82**, 257–259.

[16] S. Eustis and M. A. El-Sayed, *Chem. Soc. Rev.*, 2006, **35**, 209–217.

[17] O. S. Alexeev, S. Y. Chin, M. H. Engelhard, L. O. Soto and M. D. Amiridis, *J. Phys. Chem. B*, 2005, **109**, 23430–23443.

[18] N. Toshima and Y. Shiraishi, *Catalysis by metallic colloids. In: Encyclopedia of Surface and Colloid Science*, 2002, 879–886.

[19] M. Haruta, *Catal. Today*, 1997**, 36**, 153–166.

[20] W. Y. Teoh, J. A. Scott and R. Amal, *J. Phys. Chem. Lett.*, 2012, **3**, 629–639.

[21] E. Farnetti, R. D. Monte and J. Kaspar, *Homogeneous and Heterogeneous Catalysis, Inorganic and Bioinorganic Chemistry- Vol II, Chemical Sciences Engineering and Technology Resources, in Encyclopedia of Life Support Systems*, 2007.

[22] S. Chaturvedi, P. N. Dave and N. K. Shah, *J. Saudi Chem. Soc.*, 2012, **16,** 307–325.

[23] S. Panigrahi, S. Basu, S. Praharaj, S. Pande, S. Jana, A. Pal, S. K. Ghosh and T. Pal, J. *Phys. Chem. C*, 2007, **111**, 4596–4605.

[24] H. Song, R. M. Rioux, J. D. Hoefelmeyer, R. Komor, K. Niesz, M. Grass, P. Yang and G. A. Somorjai, *J. Am. Chem. Soc.*, 2006, **128**, 3027–3037.

[25] C. Ornelas, J. R. Aranzaes, L. Salmon and D. Astruc, *Chem. Eur. J.*, 2008, **14**, 50–64.

[26] R. Narayanan, *Molecules*, 2010, **15**, 2124–2138.

[27] H. Choi, W. T. Chen and P. V. Kamat, *ACS Nano*, 2012, **6**, 4418–4427.

[28] J. Zeng, Q. Zhang, J. Chen and Y. Xia, *Nano Lett.*, 2010, **10**, 30–35.

[29] J. K. Norskov, T. Bligaard, B. Hvolbaek, F. A. Pedersen, I. Chorkendorff and C. H. Christensen, *Chem. Soc. Rev.*, 2008, **37**, 2163–2171.

[30] R. Narayanan and M. A. El-Sayed, *Langmuir*, 2005, **21**, 2027–2033.

[31] A. Primo, A. Corma and H. Garcia, *Phys. Chem. Chem. Phys.*, 2011, **13**, 886–910.

[32] B. R. Cuenya, *Acc. Chem. Res.*, 2013, **46**, 1682–1691.

[33] S. Schauermann, N. Nilius, S. Shaikhutdinov and H. J. Freund, *Acc. Chem. Res.*, 2013, **46**, 1673–1681.

[34] S. E. Allen, R. R. Walvoord, R. P. Salinas and M. C. Kozlowski, *Chem. Rev.*, 2013, **113**,

6234–6458.

[35] X. Yang, Z. Wu, M. M. Debusk, D. R. Mullins, S. M. Mahurin, R. A. Geiger, M. Kidder and C. K. Narula, *J. Phys. Chem. C*, 2012, **116**, 23322–23331.

[36] S. Linic, P. Christopher and D. B. Ingram, *Nat. Mater.*, 2011, **10**, 911–921.

[37] R. Xu, D. Wang, J. Zhang and Y. Li, *Chem. Asian J.*, 2006, **1**, 888–893.

[38] B. R. Cuenya, J. R. Croy, S. Mostafa, F. Behafarid, L. Li, Z. Zhang, J. C. Yang, Q. Wang and A. I. Frenkel, *J. Am. Chem. Soc.*, 2010, **132**, 8747–8756.

[39] M. A. Mahmoud, R. Narayanan and M. A. El-Sayed, *Acc. Chem. Res.*, 2013, **46**, 1795–1805.

[40] N. R. Jana, L Gearheart and C. J. Murphy, *Langmuir*, 2001, **17**, 6782–6786.

[41] I. O. Sosa, C. Noguez and R. G. Barrera, *J. Phys. Chem. B*, 2003, **107**, 6269–6275.

[42] L. M. L. Marzan, *Langmuir*, 2006**, 22**, 32–41.

[43] P. K. Jain, X. Huang, I. H. El-Sayed and M. A. El-Sayed, *Plasmonics*, 2007, **2**, 107–118.

[44] M. C. Daniel and D. Astruc, *Chem. Rev.*, 2004, **104**, 293–346.

[45] R. Brayner, *Nano Today*, 2008, **3**, 48–55.

[46] T. Maneerung, S. Tokura and R. Rujiravanit, *Carbohydr. Polym.*, 2008, **72**, 43–51.

[47] P. C. Ray, *Chem. Rev.*, 2010, **110**, 5332–5365.

[48] S. K. Ghosh and T. Pal, *Chem. Rev.*, 2007, **107**, 4797–4862.

[49] S. T. Kochuveedu, Y. H. Jang and D. H. Kim, *Chem. Soc. Rev.*, 2013, **42**, 8467–8493.

[50] X. Zhou, G. Liu, J. Yu and W. Fan, *J. Mater. Chem.*, 2012, **22**, 21337–21354.

[51] K. L. Kelly, E. Coronado, L. L. Zhao and G. C. Schatz, *J. Phys. Chem. B*, 2003, **107**, 668–677.

[52] K. P. Rice, E. J. Walker Jr, M. P. Stoykovich and A. E. Saunders, *J. Phys. Chem. C*, 2011, **115**, 1793–1799.

[53] M. Abdulla-Al-Mamun, Y. Kusumoto, T. Zannat and M. S. Islam, *Appl. Catal. A: Gen.*, 2011, **398**, 134–142.

[54] M. Achermann, *J. Phys. Chem. Lett.*, 2010, **1**, 2837–2843.

[55] D. S. Wang and Y. D. Li, *Adv. Mater.*, 2011, **23**, 1044–1060.

[56] R. Ferrando, J. Jellinek and R. L. Johnston, *Chem. Rev.*, 2008, **108**, 845–910.

[57] D. Wang, A. Villa, F. Porta, L. Prati and D. Su, *J. Phys. Chem. C*, 2008, **112**, 8617–8622.

[58] A. Lehoux, L. Ramos, P. Beaunier, D. B. Uribe, P. Dieudonne, F. Audonnet, A. Etcheberry, M. J. Yacaman and H. Remita, *Adv. Funct. Mater.*, 2012, **22**, 4900–4908.

[59] A. K. Singh and Q. Xu, *ChemCatChem*, 2013, **5**, 652–676.

[60] M. Kaushik, M. Mandal, N. Pradhan and T. Pal, *Nano Lett.*, 2001, **1**, 319–322.

[61] Y. Sun and Y. Xia, *J. Am. Chem. Soc.*, 2004, **126**, 3892–3901

[62] B. R. Gonzalez, A. Burrows, M. Watanabe, C. J. Kiely and L. M. L. Marzan, *J. Mater. Chem.*, 2005, **15**, 1755–1759.

[63] M. Tsuji, N. Miyamae, S. Lim, K. Kimura, X Zhang, S. Hikino and M. Nishio, *Cryst. Growth Des.*, 2006, **6**, 1801–1807.

[64] M. Liu and P. G. Sionnest, *J. Phys. Chem. B*, 2004, **108**, 5882–5888.

[65] Y. Xiang, X. Wu, D. Liu, Z. Li, W. Chu, L. Feng, K. Zhang, W. Zhou and S. Xie, *Langmuir*, 2008, **24**, 3465–3470.

[66] M. J. Alam and M. Tsuji, *CrystEngComm.*, 2011, **13**, 6499–6506

[67] M. Tsuji, N. Nakamura, M. Ogino, K. Ikedo and M. Matsunaga, *CrystEngComm.*, 2012, **14**, 7639–7647.

[68] M. P. Mallin and C. J. Murphy, *Nano Lett.*, 2002, **2**, 1235–1237.

[69] L. Rivas, S. S. Cortes, J. V. G. Ramos and G. Morcillo, *Langmuir*, 2000, **16**, 9722–9728.

[70] M. Tsuji, D. Yamaguchi, M. Matsunaga and M. J. Alam, *Cryst. Growth Des.*, 2010, **10**, 5129–5135.

[71] J. Liao, Y. Zhang, W. Yu, L. Xu, C. Ge, J. Liu and N. Gu, *Colloids Surf. A: Physiochem. Eng. Aspects*, 2003, **223**, 177–183.

[72] S. E. Skrabalak, L. Au, X. Li and Y. Xia, *Nat. Protoc.*, 2007, **2**, 2182–2190.

[73] J. P. Juste, I. P. Santos, L. M. L. Marzan and P. Mulvaney, *Coord. Chem. Rev.*, 2005, **249**, 1870–1901.

[74] Y. Sun, B. T. Mayers and Y. Xia, *Nano Lett.*, 2002, **2**, 481–485.

[75] Q. Zhao, L. Hou, R. Huang and S. Li, *Mater. Chem. Phys.*, 2004, **85**, 180–183.

[76] S. Tokonami, N. Morita, K. Takasaki and N. Toshima, *J. Phys. Chem. C*, 2010, **114**, 10336–10341.

[77] X. Zhang and Z. Su, *Adv. Mater.*, 2012, **24**, 4574–4577.

[78] W. G. Menezes, B. Neumann, V. Zielasek, K. Thiel and M. Baumer, *ChemPhysChem*, 2013, **14**, 1577–1581.

[79] N. Toshima and H. J. Zhang, 14th IUPAC International Symposium on MacroMolecular Complexes (MMC-14), Helsinki, Finland, 2011, Aug 15.

[80] X. Guo, Q. Zhang, Y. Sun, Q. Zhao and J. Yang, *ACS Nano*, 2012, **6**, 1165–1175.

[81] A. Monga and B. Pal, *New J. of Chem.*, 2015, **39**, 304–313.

[82] H. Wang, C. Y. Yi, L. Tian, W. J. Wang, J. Fang, J. H. Zhao and W. G. Shen, *J. Nanomater.* 2012, **2012,** 1–8.

[83] H. Rong, S. Cai, Z. Niu and Y. Li, *ACS Catal.*, 2013, **3**, 1560–1563.

[84] Q. Fu, D. G. Zhang, M. F. Yi, X. X. Wang, Y. K. Chen, P. Wang and H. Ming, *J. Opt.*, 2012, **14**, 085001.

[85] R. Ricciardi, J. Huskens and W. Verboom, *J. Flow Chem.*, 2015, doi:10.1556/1846.2015.00018.

[86] Y. Wang, X. Wang, B. Sun, S. Tang and X. Meng, *J. Mater. Sci. Tech.*, 2015, doi:10.1016/j.jmst.2015.10.015.

[87] C. L. Lu, K. S. Prasad, H. L. Wu, J. A. A. Ho and M. H. Huang, *J. Am. Chem. Soc.*, 2010, **132**, 14546–14553.

[88] Y. C. Tsao, S. Rej, C. Y. Chiu and M. H. Huang, *J. Am. Chem. Soc.*, 2014, **136**, 396–404.

[89] B. N. Khlebtsov, Z. Liu, J. Ye and N. G. Khlebtsov, *J. Quant. Spectrosc. Radiat. Transfer*, 2015, **167**, 64–75.

[90] A. Monga and B. Pal, *Colloids Surf. A: Physiochem. Eng. Aspects*, 2015, **481**, 158–166.

[91] R. G. Chaudhuri and S. Paria, *Chem. Rev.*, 2011, **112**, 2373–2433.

[92] C. L. Lee and C. M. Tseng, *J. Phys. Chem. C*, 2008, **112**, 13342–13345.

[93] H. M. Chen, R. S. Liu, M. Y. Lo, S. C. Chang, L. D. Tsai, Y. M. Peng and J. F. Lee, *J. Phys. Chem. C*, 2008, **112**, 7522–7526.

[94] S. E. Skrabalak, J. Y. Chen, Y. G. Sun, X. M. Lu, L. Au, C. M. Cobley and Y. N. Xia, *Acc. Chem. Res.*, 2008, **41**, 1587–1595.

[95] Q. Zhang, W. S. Wang, J. Goebl and Y. D. Yin, *Nano Today*, 2009, **4**, 494–507.

[96] E. Mathlowitz, J. S. Jacob, Y. S. Jong, G. P. Carino, D. E. Chickering, P. Chaturvedl, C. A. Santos, K. Vijayaraghavan, S. Montgomery, M. Bassett and C. Morrell, *Nature*, 1997, **386**, 410–414.

[97] S. W. Kim, M. Kim, W. Y. Lee and T. Hyeon, *J. Am. Chem. Soc.*, 2002, **124**, 7642–7643.

[98] M. S. Yavuz, Y. Y. Cheng, J. Y. Chen, C. M. Cobley, Q. Zhang, M. Rycenga, J. W. Xie, C. Kim, K. H. Song, A. G. Schwartz, L. V. Wang and Y. Xia, *Nat. Mater.*, 2009, **8**, 935–939.

[99] G. D. Moon, S. W. Choi, X. Cai, W. Y. Li, E. C. Cho, U. Jeong, L. V. Wang and Y. N. Xia, *J. Am. Chem. Soc.*, 2011, **133**, 4762–4675.

[100] M. R. Kim, D. K. Lee and D. J. Jang, *Appl. Catal. B: Environ.*, 2011, **103**, 253–260.

[101] V. K. Rao and T. P. Radhakrishnan, *J. Mater. Chem. A*, 2013, **1**, 13612–13618.

[102] X. Sun and D. Qin, *J. Mater. Chem. C*, 2015, **3**, 11833–11841.

[103] A. Monga and B. Pal, *RSC Adv.*, 2015, **5**, 39954–39963.

Chapter 2

Improved Catalytic Activity and Surface Electro-kinetics of Bimetallic Au-Ag Core-Shell Nanocomposites

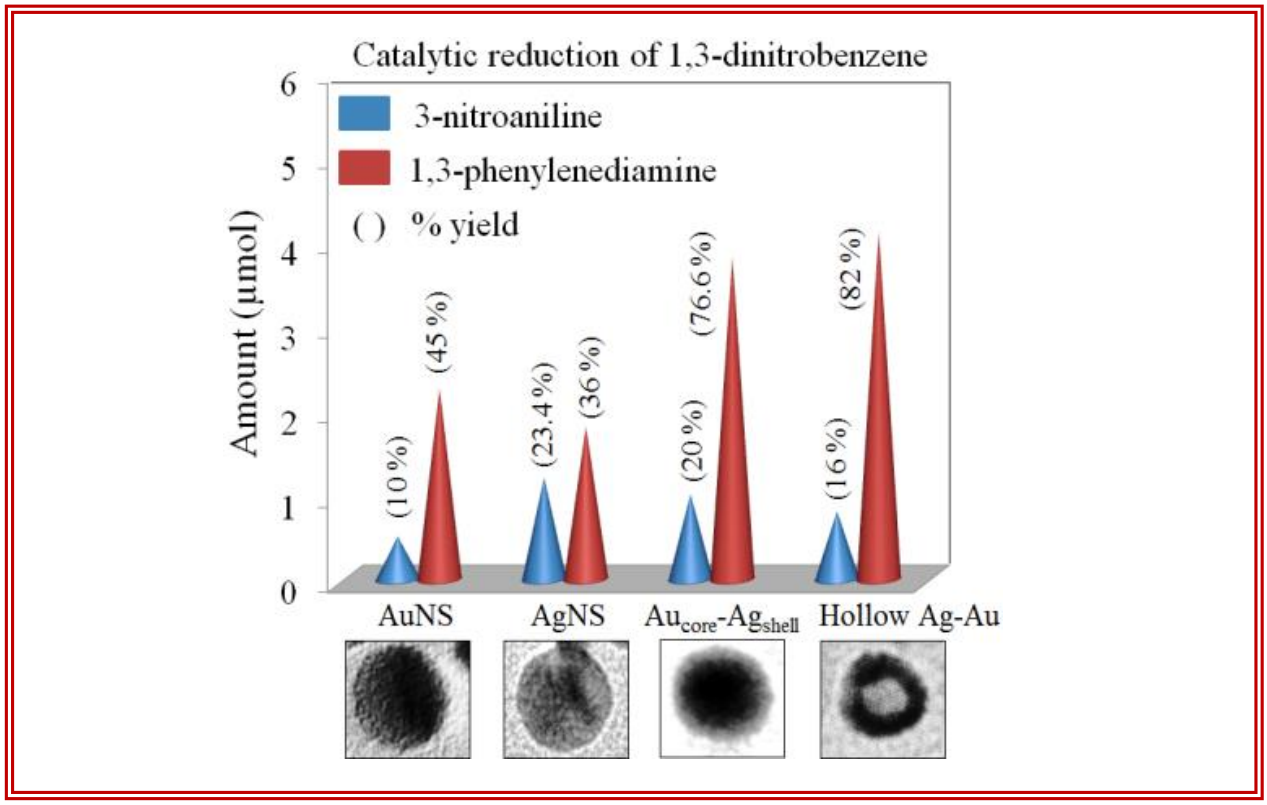

2.1 Introduction

The bimetallic (BM) nanocomposites (NCs) composed of two different metals are more significant than the monometallic ones due to their distinctive electronic and optical properties, superior catalytic activity, high selectivity and stability emanating from bi-functional or synergistic effects [1-4]. The unique properties of BM NCs over monometallic counterparts can be attributed to the; (i) electronic effect or ligand effect [5-7], where the electronic property of surface atoms in the host metal element can be varied by charge transfer between two metals, and (ii) an ensemble or geometric effect [8], where the substrate interact with both the metal elements and result in a new catalytic property. In the past, much progress has been made in the synthesis of BM NCs following a range of synthetic strategies, including co-reduction, galvanic replacement, thermal decomposition, seeded growth, photochemical, successive reduction, microwave, template, and electrochemical deposition methods [3,9-16]. They can adopt either core@shell or alloy structures depending upon the synthetic approach employed [17,18]. The core@shell NCs are more attractive owing to the ability to increase the functionality and stability of NPs by monitoring the nature of core and shell and compositions. Moreover, the lattice mismatch between the core and shell material may induce the interfacial strain which has been shown to enhance catalytic rates in dual-metal systems. For example, core@shell Au@Pt exhibited enhanced electrocatalysis for oxygen reduction reaction [19]. The Au@Pd heterostructures served as effective catalysts for catalyzing a Suzuki-coupling reaction [20].

Among BM systems, the coinage metals (Au/Ag) nanostructures have been extensively explored due to their facile synthesis techniques, tunable surface plasmon (SP) band in the visible region, similar face centered cubic (FCC) crystal structure and lattice constants (a = 0.479 nm; Au and 0.486 nm; Ag), where Ag shells can be epitaxially formed in Au cores or vice-versa. Many NCs of Au-Ag, Au-Cu, Ag-Cu, Au-Pd, Cu-Au, and Cu-Pd, etc. [13,14,21-26] of different morphologies have been reported. Xia et al. recently synthesized core@shell nanocubes of Au@Ag with controllable shell thicknesses [27]. The Au@Ag NCs of different shapes e.g., octahedron, cube, decahedron, rod, wire, and icosahedrons using microwave-polyol method [12,28,29] were prepared. Pal et al. reported [30] the surface enhanced Raman spectroscopy (SERS) activity of core@shell (Au@Ag) and reverse core@shell (Ag@Au) NCs using β-Cyclodextrin. By changing the nature of the core, shell-thicknesses and the core/shell ratio, the surface properties and catalytic activity of Au@Ag NCs can be manipulated to be a consequence

of different work functions of two metals. Since, the electronic distribution of both Au and Ag is different; the catalytic activity of shell atoms (Ag) can be electronically affected by the core atoms (Au) and vice-versa. Moreover, the coating of Au nanoparticles (NPs) core by Ag (shell) or reverse alters the surface properties of NPs surface and hence its dispersion in liquid which governs the electro-kinetic properties i.e., Zeta-potential. Consequently, this work demonstrates the influence of Au@Ag and Ag@Au NCs on the optical properties, surface electro-kinetics and catalytic activity for model organic synthesis, as a function of their morphology, the nature of the core and shell thickness relative to their monometallic counterparts.

2.2 Experimental

2.2.1 Materials

Chloroauric acid ($HAuCl_4.3H_2O$), sodium borohydride ($NaBH_4$), ascorbic acid ($C_6H_8O_6$), sodium hydroxide (NaOH), polyvinylpyrrolidone (PVP, $(C_6H_9NO)_n$), trisodium citrate ($Na_3C_6H_5O_7$), nitrobenzene ($C_6H_5NO_2$) and 1,3-dinitrobenzene ($C_6H_4N_2O_4$) were obtained from Loba Chemie, India. Silver nitrate ($AgNO_3$) was purchased from Fischer Scientific, India. All the chemicals were used as-received without any further purification. De-ionized water was obtained using an ultra-filtration system (Milli-Q, Millipore) with a measured conductivity above 35 mho cm^{-1} at 25 ºC.

2.2.2 Preparation of Core@Shell Au@Ag and Inverse Core@Shell Ag@Au Nanocomposites

The citrate-stabilized Au nanospheres (Au NS) and Ag nanospheres (Ag NS) were prepared as reported [31-33] elsewhere. In brief, a solution of $HAuCl_4.3H_2O$ or $AgNO_3$ (70 µL, 0.1 M) dissolved in water was injected into pre-heated aqueous solution of trisodium citrate (14 mL, 1.6 mM) at 100 ºC. After 20 min, the solution turned wine-red for Au and yellow for Ag, indicating the formation of corresponding metal NPs in the solution (pH = 6.1-6.2). The resulting washed citrate-capped Au NS (0.8 mL) solution was diluted with PVP (4 mL, 1 wt%) into which different amounts of $AgNO_3$ aqueous solution (10-30 µL, 0.01 M) were added. This was followed by adding ascorbic acid (0.1 mL, 0.1 M) and then NaOH (0.2 mL, 0.1 M) to initiate the deposition of the Ag shell at alkaline pH (pH = 10.0-10.2) resulting in the formation of Au@Ag NCs [11,13]. Similarly, the inverse core@shell NCs (Ag@Au) were synthesized by taking pre-synthesized citrate-capped Ag NS as the core (demonstrated above). For each set of Ag NS (0.8 mL) mixed with PVP (4 mL, 1 wt%) and ascorbic acid (0.1 mL, 0.1 M), different amounts of

$HAuCl_4^-$ aqueous solution (10-30 µL, 0.01 M) were added with simultaneous stirring resulting in the formation of Ag@Au NCs (pH = 4.7-5.0). The prepared BM NCs were then washed with distilled water by centrifugation (8000 rpm for 5 min) and re-dispersed in water.

2.2.3 Characterization

The core@shell NCs were characterized using a UV-Vis spectrophotometer (Analytica Jena Specord 205), transmission electron microscope (TEM, Hitachi 7500, 2 Å, 120 kV), and an energy dispersive X-ray (EDX). High-resolution TEM images and selected area electron diffraction (SAED) patterns were taken using a FEI Technai F20 transmission electron microscope. The hydrodynamic size distribution of different NCs dispersed in water was determined using a Brookhaven 90 plus Particle Size Analyzer at 25 ºC using cumulant fitting. The zeta potential (ζ) was studied by taking 1.5 mL of NCs solution in a cuvette consisting of the palladium electrode mounted on a machined support using Brookhaven zeta plus at 25 ºC.

2.2.4 Catalytic Activity

The comparative study of catalytic activity of core@shell BM (Au@Ag and Ag@Au) NCs and their monometallic NPs was carried out by the reduction of nitrobenzene (NB) and 1,3-dinitrobenzene (DNB). In a typical reaction, ice-cold $NaBH_4$ solution (100 µL, 0.01 M) was added to 5 mL nitro-organic compounds (1 mM) and then a calculated amount of NCs was added. The reaction was monitored by measuring the absorption spectra at regular intervals of time (λ_{max} of NB = 270 nm and λ_{max} of DNB = 240 nm) and the products were further quantified using HPLC and GC-MS analysis.

2.3. Results and Discussion

The monometallic Au NS and Ag NS were prepared by reducing Au and Ag metal ions with citrate ions and then, their BM core@shell Au@Ag and Ag@Au NCs were obtained by deposition of varying amount Ag and Au ions over these as-prepared Au and Ag nanospheres, respectively. The resultant change in their surface structural morphology and various physicochemical properties including catalytic activity were comparatively investigated by different characterization techniques as below.

2.3.1 Optical Properties

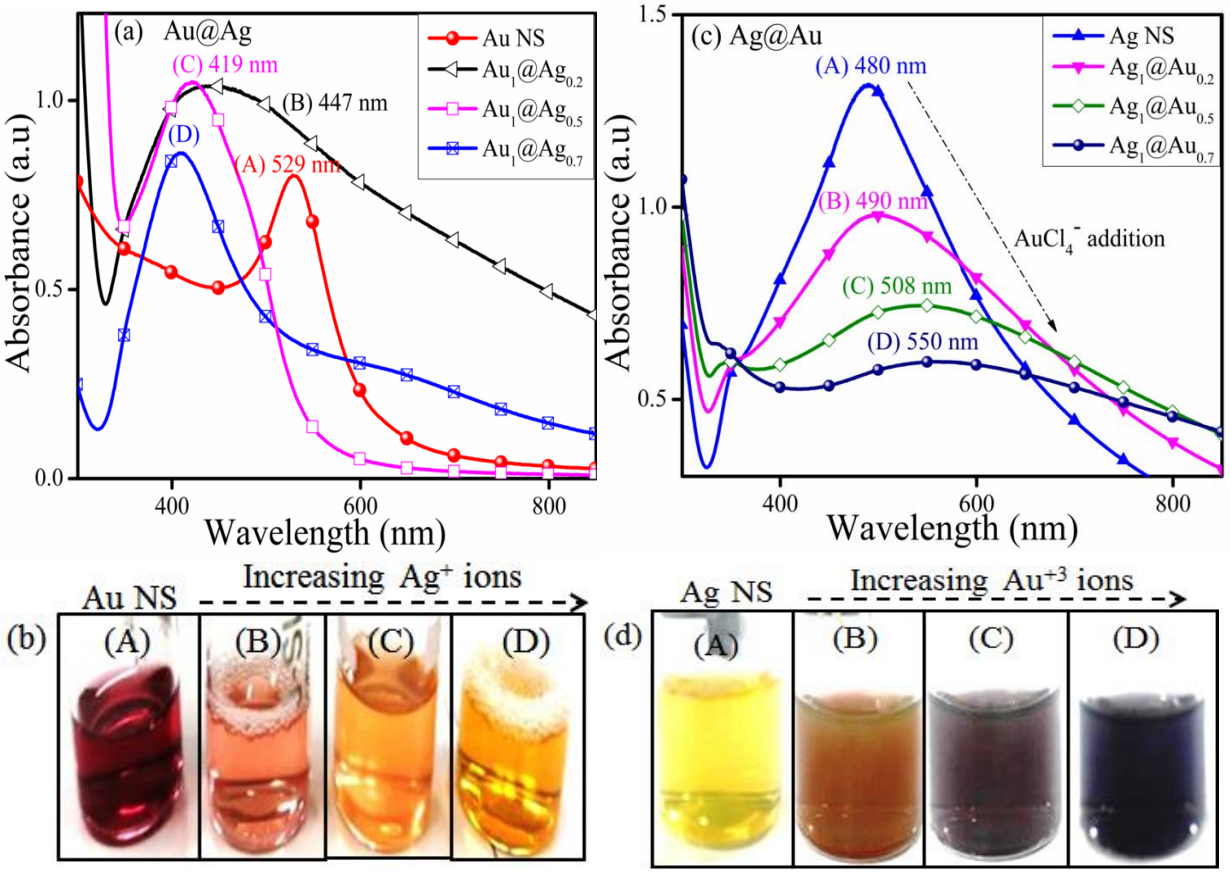

Fig. 2.1. Effect of **(a-b)** $AgNO_3$ (10-30 µL, 0.01 M) deposition onto Au nanospheres, and **(c-d)** $HAuCl_4.3H_2O$ (10-30 µL, 0.01 M) deposition onto Ag nanospheres for the observed variation in the surface plasmon band and their respective color changes.

The characteristic surface plasmon (SP) band of Au NS (529 nm) blue-shifted to a broad peak at 447 nm and 419 nm of increased intensity upon addition of Ag^+ ions (10-20 µL, Fig. 2.1a) accompanied by the color change from wine red to pink to orange as seen in Fig. 2.1b. This indicated some morphological change in which Au NS was used as a seed for the controlled reduction of Ag^+ and, thereby, deposition of Ag-shell over the Au-core as observed from the absorbance measurements. With the progressive addition of Ag^+ ions (30 µL), a sharp absorption band corresponding to 408 nm having a yellow color appeared. At this point, the incident light could only penetrate Ag shell of a certain thickness and could not reach Au cores to excite its e^- [27]. The atomic ratio for the deposition of varying amount of Ag^+ ions (10-30 µL, 0.01 M) on the surface of Au NS were calculated to be 0.2-0.7 as shown in Table 2.1. Therefore, it is

Table 2.1. Calculations of the amount of Au and Ag atoms in core@shell Au@Ag nanocomposites.

Elements	Amount of element (mg)	No. of atoms	Atomic ratio (Au:Ag)
Au NS (800 µL)	0.077	2.3×10^{17}	1:0
Ag^+ (0.01M, 10 µL)	0.0107	0.6×10^{17}	1:0.2
Ag^+ (0.01M, 20 µL)	0.0213	1.2×10^{17}	1:0.5
Ag^+ (0.01M, 30 µL)	0.032	1.8×10^{17}	1:0.7

presumed that Au NS are completely covered by Ag giving rise to core@shell, Au@Ag NCs of different shell-thickness. These results are in good conformity with the reported blue shifting of the SP band for Au NS from 520 nm to 438 nm and 402 nm with increasing Ag-shell thickness. In contrast to Au NS, the SP band of Ag NS (480 nm) gradually decreased and became broader with a peak position shifting to longer wavelengths, 490 nm to 508 nm and 550 nm, through the increasing addition of $HAuCl_4^-$ ions (Fig. 2.1c). This observation is consistent with the report where, the formation of hollow Ag-Au NCs takes place via replacement of Ag by Au [34]. Due to the progressive galvanic replacement reaction, Au is deposited on NPs surface and the cavity size in hollow particles increases with reaction resulting in a red-shift [35] in the SP band of hollow Ag-Au NCs. This morphological transformation was further evidenced by the color change from yellow to light orange to purple and blue as shown in Fig. 2.1d. Similarly, the calculated atomic ratios for the deposition of $HAuCl_4^-$ ions (10-30 µL, 0.01 M) on the surface of Ag NS were 0.2-0.7.

2.3.2 Electro-kinetic Parameters

When NPs are dispersed in an aqueous solution, there is adsorption or surface ionization of cations or anions, which results in the formation of electrical double layer leading to the development of new surface charge measured by Zeta potential (ζ). Here, the measured zeta potential of unwashed citrate-capped Au NS (-22.5 mV) and Ag NS (-28.79 mV) was found to be negatively charged probably due to the presence of surface adsorbed and free citrate ions in their aqueous suspension. However, after washing with de-ionized water, the zeta potential of bare Au NS (-6.13 mV) and Ag NS (-5.74 mV) was notably reduced (Fig. 2.2) [36]. The citrate capped-Au NS and Ag NS are probably stabilized through steric repulsions as reported [37-40],

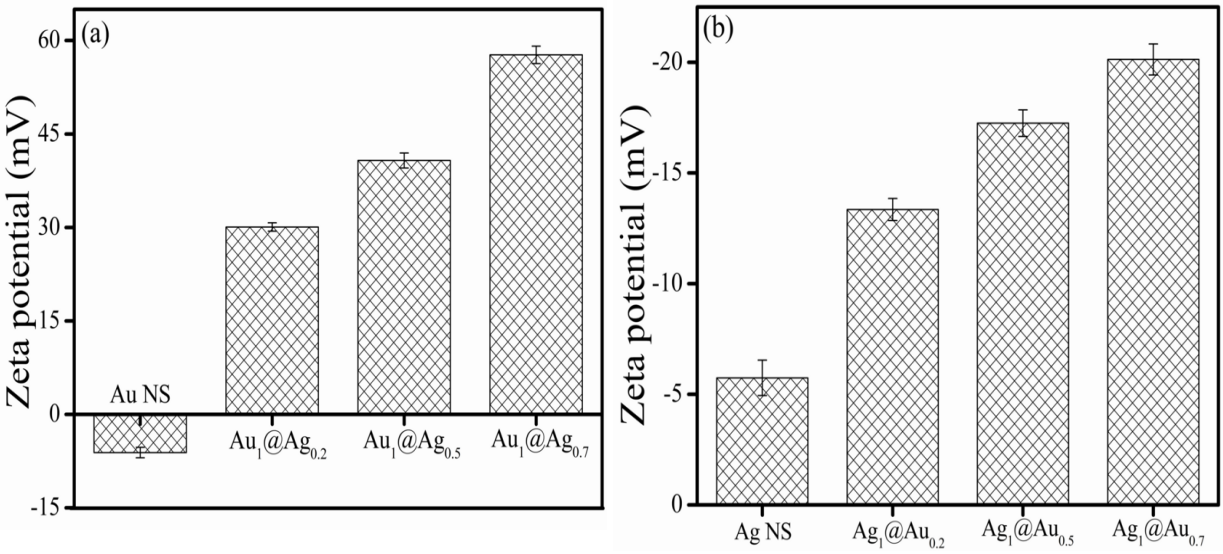

Fig. 2.2. Electro-kinetic parameters of **(a)** Au nanospheres, and **(b)** Ag nanospheres after deposition of $AgNO_3$ and $HAuCl_4.3H_2O$ (10-30 µL, 0.01 M), respectively.

due to the presence of coordinated/adsorbed citrates along with dangling citrate species which are not in direct contact with the metal surface of Au or Ag NPs. As a result, intermolecular interactions take place between the absorbed citrate and dangling citrate anion by –COOH hydrogen bonds and hence forms citrate multilayer on the NPs surface. This provides steric repulsion [37] between citrate layers present on the adjacent NPs, and help in NPs dispersion stability in solution.

The zeta potential for BM Au@Ag and Ag@Au NCs was measured in their aqueous medium having core: shell atomic ratio = 1:0.2, 1:0.5, and 1:0.7 as calculated in Table 2.1. The Ag^+ deposition on the Au NS surface led to the positive (+30.3 mV) surface charge indicating the bare Au NS are chemically modified through the absorbed charged Ag-shell as shown in Fig. 2.2a. Further, it was observed that the zeta potential became more positive (+40.7 mV to +57.8 mV), probably due to the increasing Ag-shell thickness with gradual addition of Ag^+. In case of Ag NS, the surface charge became more negative [36] (-13.35 mV to -20.13 mV) after progressive addition of $HAuCl_4^-$ as shown in Fig. 2.2b. This charge alteration might be due to the electron (e^-) charge donation from Ag with low ionization potential (7.58 eV) to Au with high ionization potential (9.22 eV) [41-43] as depicted in Scheme

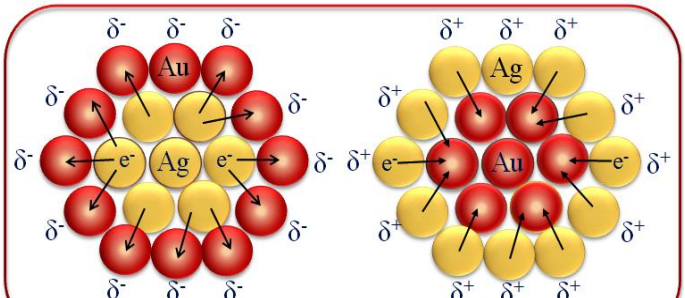

Scheme 2.1. Schematic illustration of electron transfer process.

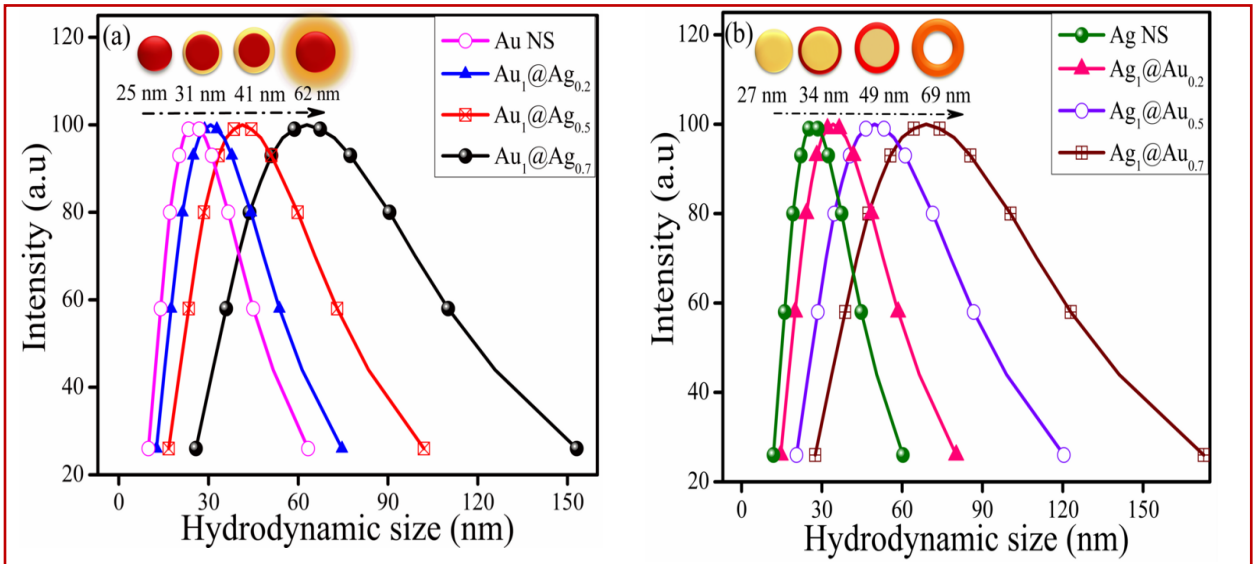

Fig. 2.3. DLS particle size distribution after deposition of 10-30 µL (0.01 M) **(a)** $AgNO_3$ over Au nanospheres, and **(b)** $HAuCl_4.3H_2O$ over Ag nanospheres.

2.1. This results in the accumulation of positive charge on Ag-shell and negative charge on Au-shell in case of Au@Ag and Ag@AuNCs, respectively, as evidenced by the above results in agreement with the previous report [43].

2.3.3 Particle Size Distribution

The coating or deposition of second metal (shell) on core NPs may lead to the change in the particle size of bare NPs. Therefore, the measurement of hydrodynamic size distribution of different BM NCs dispersed in water was carried out where; the samples were lighted with 635 nm solid state laser ranged between 15 to 150 mW. The scattered light was detected at an angle of 90° with an avalanche photodiode detector. Here, the Au-core of particular size (25 nm) was

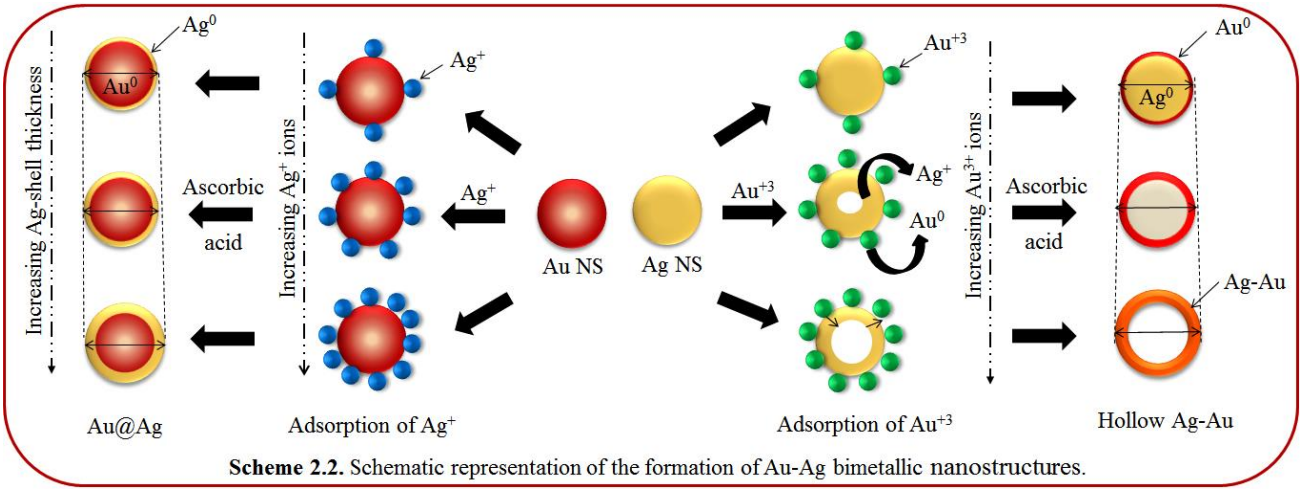

Scheme 2.2. Schematic representation of the formation of Au-Ag bimetallic nanostructures.

used for the deposition of an Ag layer of varying thickness as a function of concentration of Ag^+ ions. The Ag^+ ions are first adsorbed on the surface of Au NS, which then undergoes reduction in the presence of a weak reducing agent, ascorbic acid, so that the reduction takes place on the surface of existing metallic surfaces. Subsequently, the resultant NCs may lead to the increment of size compared to bare NPs (Scheme 2.2) due to the growing thickness of Ag-shell irrespective of the Au-core size which can be evidenced by the DLS particle size distribution [44]. It revealed that the average hydrodynamic diameter of Au NS (25 nm) upon addition of Ag^+ exhibited an increase in particle diameter (31 nm) signifying the successful coating of Ag layer on Au NS as shown in Fig. 2.3a. Further, the successive addition of Ag^+ onto Au NS, resulted in a progressive increase in particle diameter (41 nm to 62 nm) indicating the Ag-shell growth of higher thickness depending upon its added concentration. Similarly, Fig. 2.3b shows that the average hydrodynamic diameter of Ag NS (21 nm) upon addition of different amount of $HAuCl_4^-$ led to the gradual increase in particle diameter (33 nm to 58 nm). The Ag NS acts as a sacrificial template for the growth of Au layer and resulted in the formation of hollow Ag-Au alloy of increased cavity size due to the galvanic displacement reaction as depicted in Scheme 2.2. The observed hydrodynamic diameter was found to be greater than the TEM size due to the adherence of the hydration layer on the NPs surface while estimating the size by DLS. The NPs in liquid undergoes a random Brownian motion which

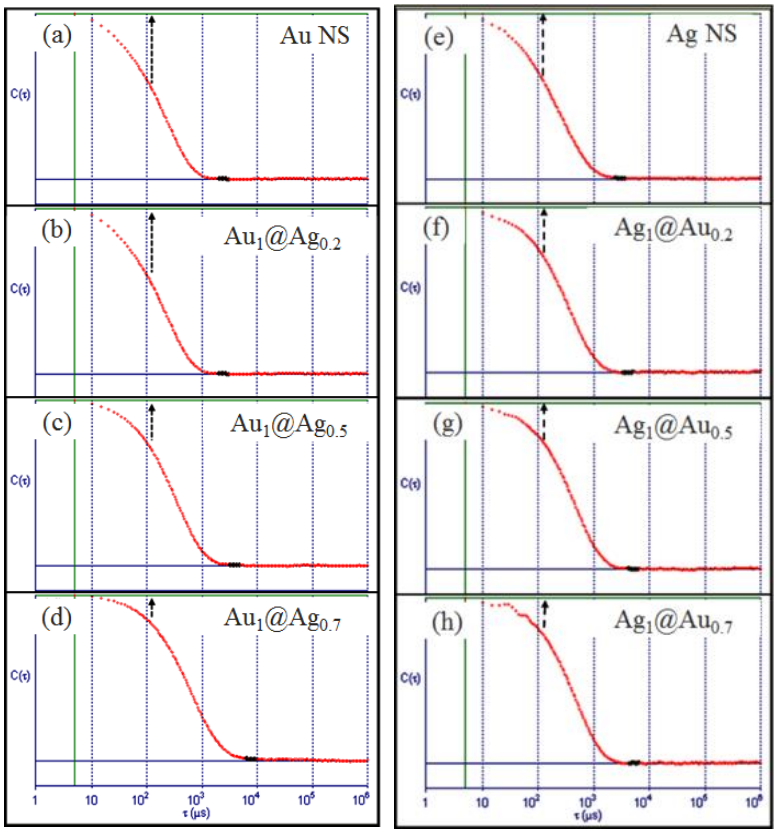

Fig. 2.4. Autocorrelation functions, C(ζ) of **(a)** bare Au nanospheres, **(b-d)** core@shell Au@Ag nanocomposites, **(e)** bare Ag nanospheres, and **(f-h)** core@shell Ag@Au nanocomposites.

fluctuate the scattered light of the DLS with respect to time intensity and this fluctuating signal is converted to autocorrelation function, C(ζ), where, ζ is the time delay. As depicted in Fig. 2.4, the C(ζ) decayed more rapidly for small particles than for the larger particles. This is because the larger size of the diffusing particle corresponds to slower diffusion and hence, the larger width in the autocorrelation function [45-47]. It was observed that the C(ζ) broadened (Fig. 2.4) with the increase in the Ag/Au shell thickness with respect to bare monometallic Au/Ag NS corresponding to an increase in the hydrodynamic size (25 to 62 nm in case of Au@Ag NCs and 21 to 58 nm in case of Ag@Au NCs).

2.3.4 Morphological Studies

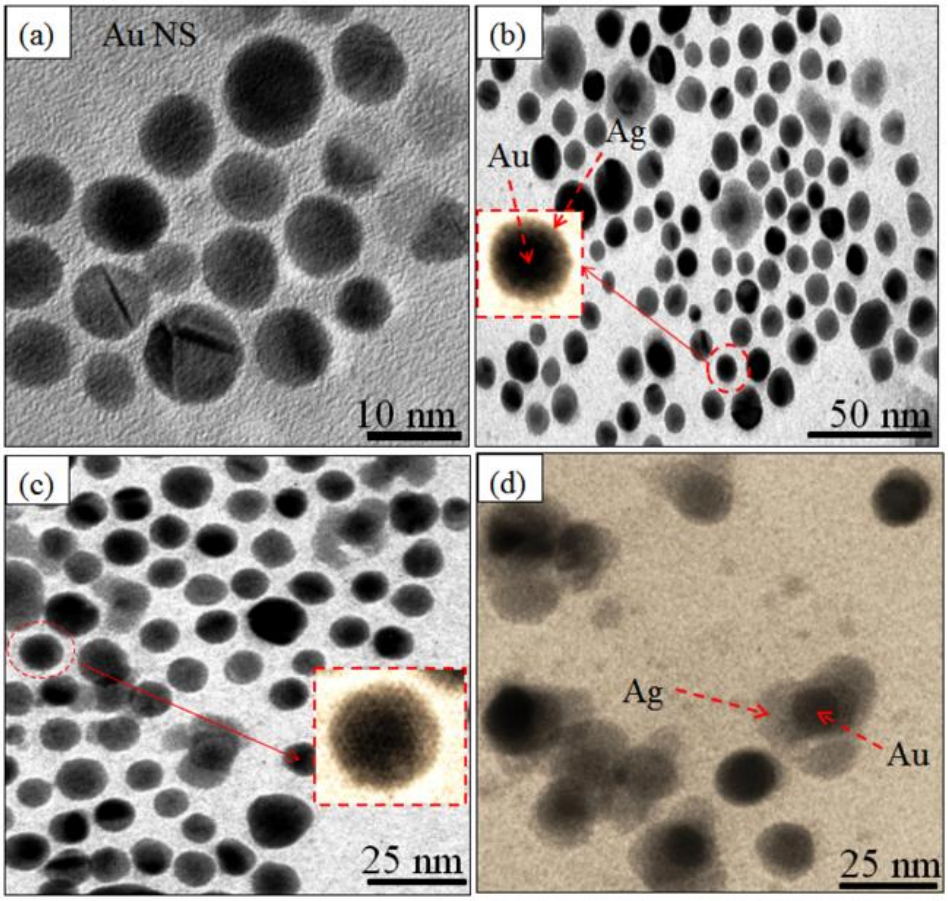

Fig. 2.5. TEM images of **(a)** Au nanospheres, and **(b-d)** core@shell Au@Ag nanocomposites of varying Ag-shell thickness (ca. ~3-10 nm).

TEM analysis revealed that the bare Au NS of diameter = 10-16 nm (Fig. 2.5a) served as a seed for Ag growth on its surface. The gradual addition of Ag^{+} on pre-synthesized Au NS led to a coating of an Ag layer of thickness ~3-4 nm as shown in Fig. 2.5b,c. This is in good agreement

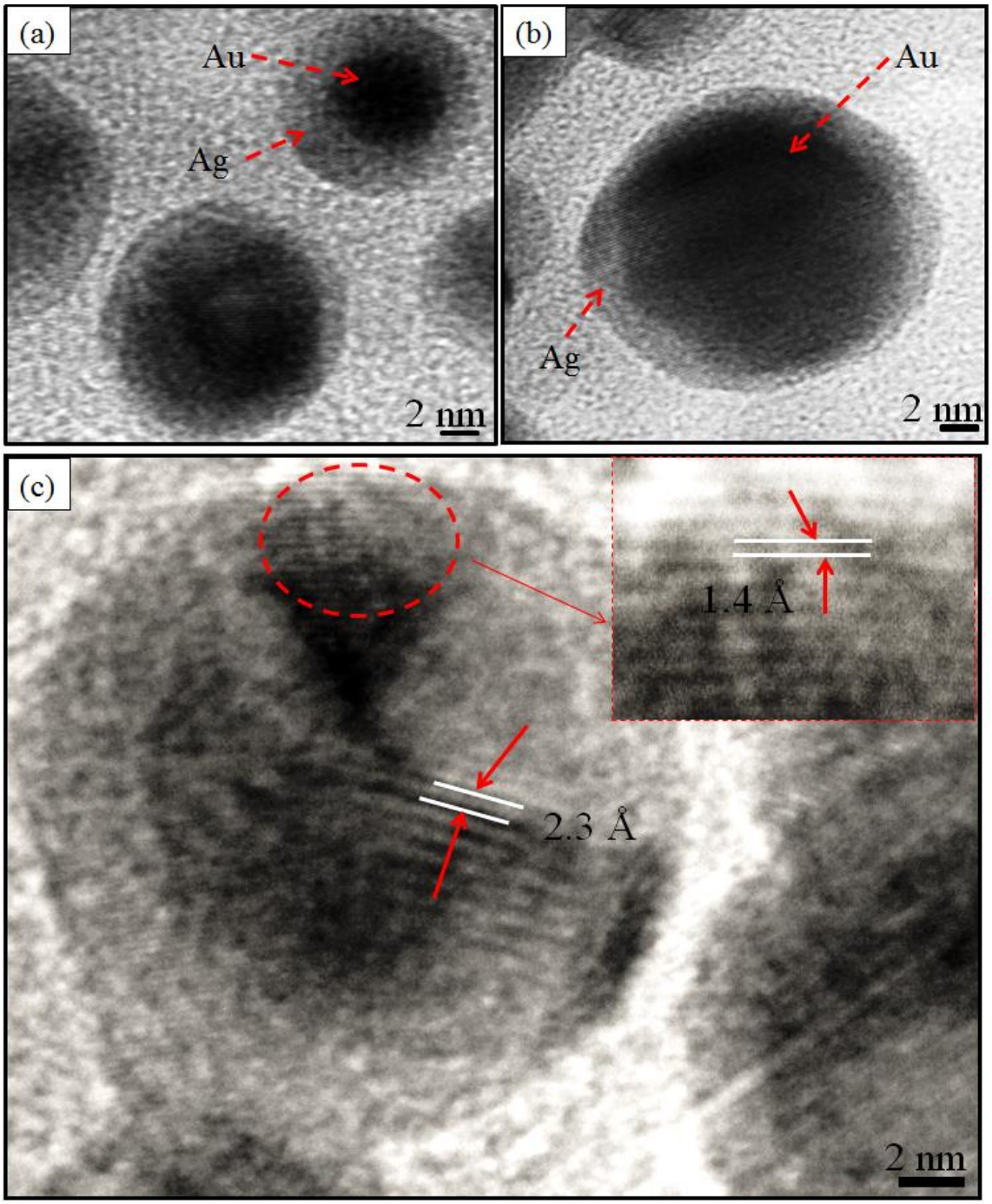

Fig. 2.6. HRTEM image of core@shell Au@Ag nanocomposites.

with the structural configuration of core@shell, i.e., Au@Ag NCs where the dark core is attributed to Au and light shell corresponds to Ag. The Ag shell was observed to become thicker (~8-10 nm), diffused and non-uniform with the addition of higher amount of Ag^{+} ions giving rise

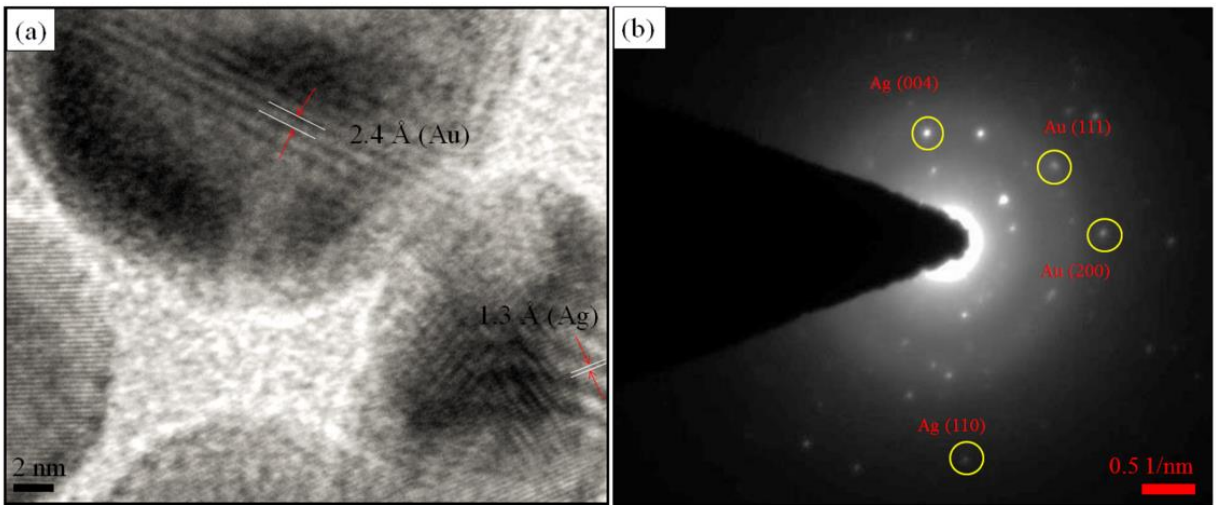

Fig. 2.7. (a) HRTEM image, and **(b)** SAED pattern of core@shell Au@Ag nanocomposites.

to irregular shape (diameter ~20 nm) as seen in Fig. 2.5d. These observations are in accordance with the reports, where Ag coating becomes anisotropic with increasing thickness of Ag shell and the shape of Au nanorods approached being a non-regular [14,48]. The HRTEM image of the as- prepared Au@Ag NCs of size ~14-19 nm with a thickness of Ag shell ~2-3 nm is shown in Fig. 2.6a,b. The measured fringes spacing are 2.3 Å and 1.4 Å, which corresponded well with the (111) plane of the FCC Au (2.355 Å, Fig. 2.6c) and (110) plane of Ag (1.44 Å, JCPDS card no. 04-07484, inset of Fig. 2.6c), respectively. Similarly, another HRTEM and the SAED pattern (Fig. 2.7) of the Au@Ag NCs confirmed the planes (110) of Ag and (111) of Au NPs. These results indicated the presence of both Au and Ag supporting the formation of Au core with Ag shell as suggested by the previous report [49]. Further, the elemental analysis also confirmed that both the Au and Ag are present in Au@Ag NCs as shown in EDX spectra, Fig. 2.8a.

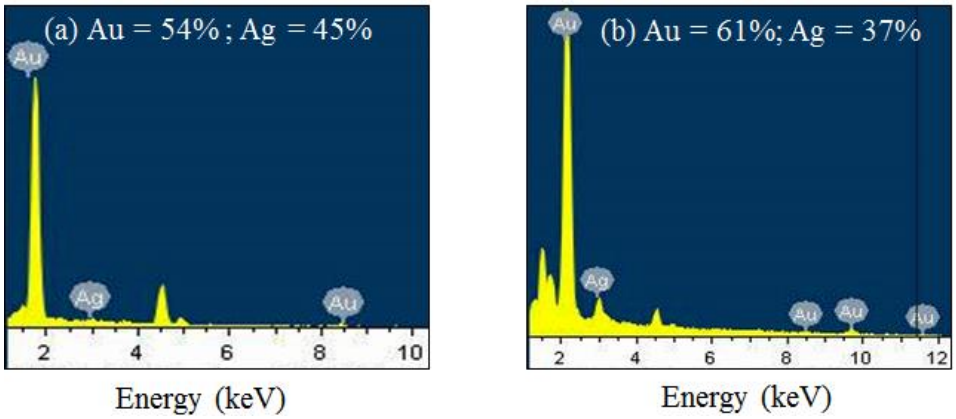

Fig. 2.8. EDX pattern of core@shell **(a)** Au@Ag, and **(b)** Ag@Au nanocomposites.

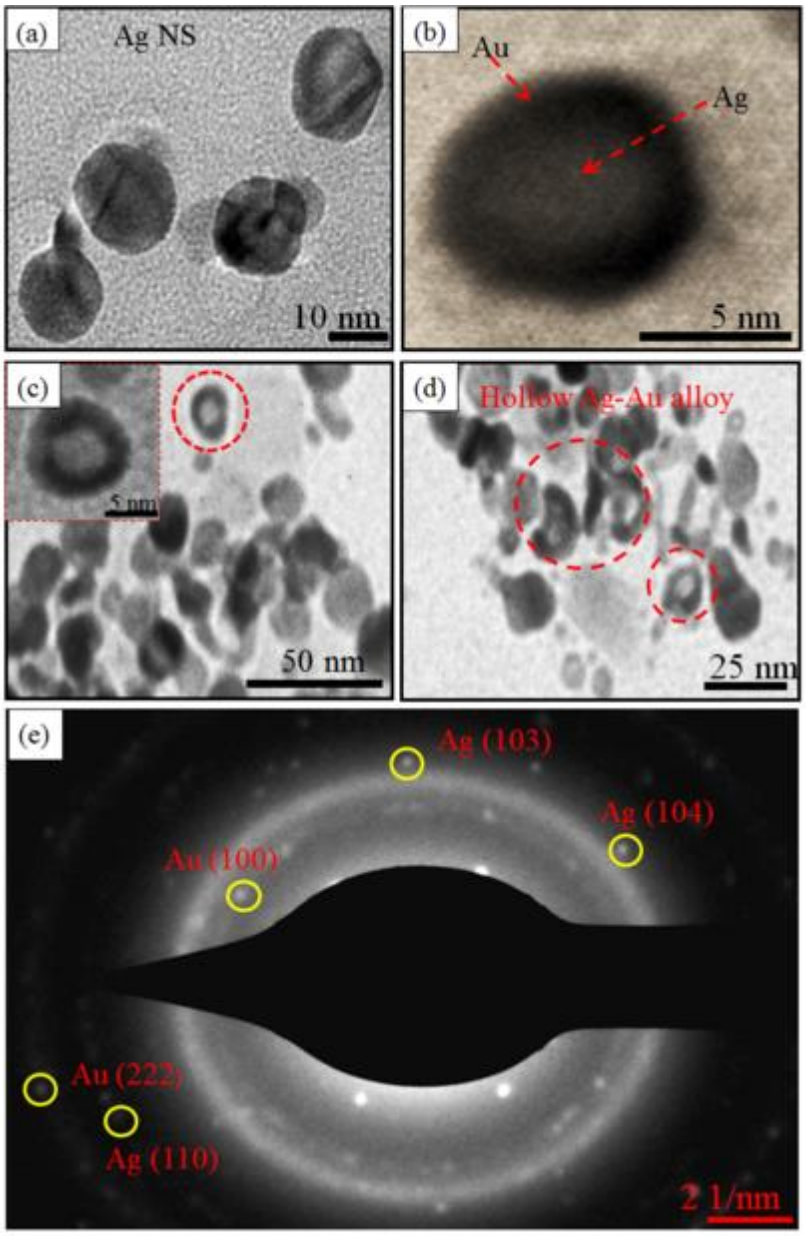

Fig. 2.9. TEM images of **(a)** Ag nanospheres, **(b-d)** core@shell Ag@Au nanocomposites obtained by deposition of $HAuCl_4.3H_2O$ (10-30 µL, 0.01 M), and **(e)** SAED pattern obtained from image-**(c)**.

On the other hand, the different morphology of Ag NS was observed via the galvanic displacement reaction between Ag NS and $HAuCl_4^-$ as seen in Fig. 2.9. The bare Ag NS (diameter = 10-11 nm, Fig. 2.9a) was uniformly coated with an Au-layer (thickness = ~2.9 nm) upon treatment with lower amount (10 µL) of $HAuCl_4^-$ as noted in Fig. 2.9b. With increasing Au content, the Ag particles are oxidized into Ag^+ ions due to the higher reduction potential of Au^{+3}/Au (0.99 V) than Ag^+/Ag (0.80 V). As a result, the growth of Au layer on the surface of Ag

template takes place leading to the formation of Ag-Au alloys (Fig. 2.9c) of diameter ~10-12 nm. The difference in the rates of diffusion of Ag atoms outward and that of $AuCl_4^-$ ions inward started the formation of hollow spaces (~5 nm) to produce Ag-Au alloy nanorings (diameter = 13-15 nm, Fig. 2.9d) with increased cavity size as reported by many groups [10,35,50] in which the different shapes (cubes, spheres, wires, etc.) of Ag-Au BM NCs are prepared. The resulting hollow NCs were observed to compose of both metals as evidenced by the presence of Ag and Au in EDX analysis (Fig. 2.8b). Further, the SAED pattern supported the existence of the planes (111) of Au and (110) of Ag particles as depicted in Fig. 2.9e [51].

2.3.5 Catalytic Activity

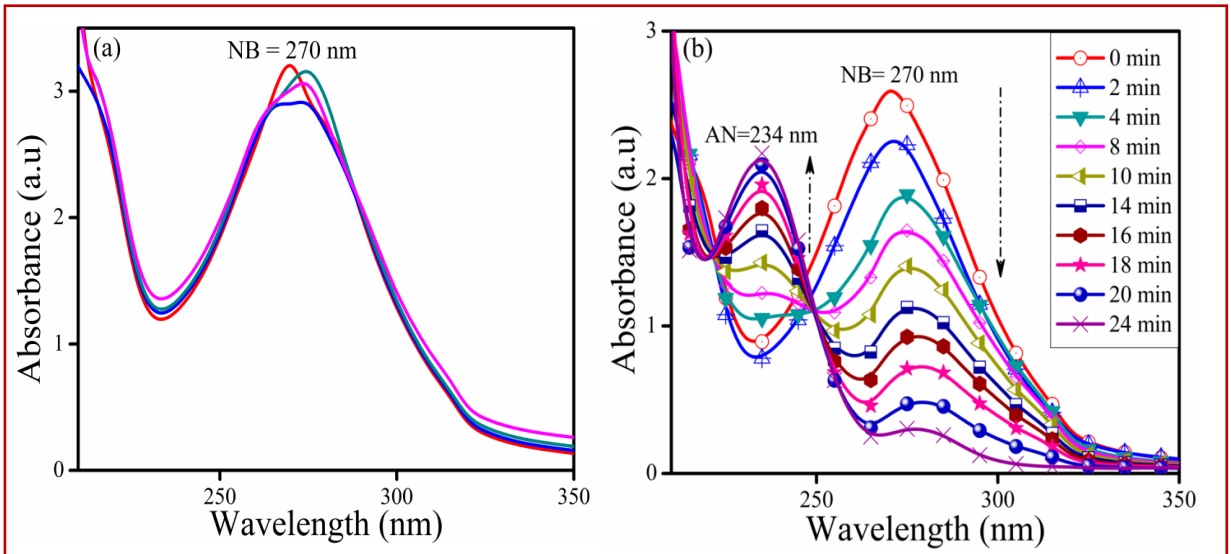

Fig. 2.10. Changes in absorption spectra of nitrobenzene (0.2 mM) reduction by $NaBH_4$ **(a)** in the absence of nanoparticles, and **(b)** in the presence of Au nanospheres.

The absorption spectra for the reduction of NB (270 nm) to aniline (AN) by $NaBH_4$ exhibited insignificant changes in the absence of Au NS up to 120 min as shown in Fig. 2.10a. However, with the addition of Au NS (size = 10-16 nm), the reaction rate was accelerated and the absorption band intensity corresponding to NB at 270 nm was gradually reduced with the simultaneous evolution of new absorption band at 234 nm, characteristic of the AN formation (Fig. 2.10b). The time course studies (Fig. 2.11a) displayed that the Au@Ag and hollow Ag-Au alloy NCs exhibited higher yield of AN i.e., 50% and 72%, respectively, within 15-30 min as compared to bare Au NS (42%) and Ag NS (20%) within 40-50 min. The superior catalytic activity of BM NCs can be explained due to the modification of the electronic structures

[2,52,53] in two metals which results in broader d-band shifted towards the Fermi-level. This is in agreement with the report [54] where the polyelectrolyte multilayer supported Au@Ag (k= 0.18 min^{-1}) NCs showed higher catalytic activity for the reduction of *p*-nitrophenol to *p*-aminophenol by $NaBH_4$ than the corresponding monometallic Au NS (k=0.019 min^{-1}) and Ag NS (k=0.069 min^{-1}) due to synergistic effect. BM synergistic effect exhibits a dramatic improvement in catalytic activity and selectivity in contrast to monometallic counterparts [3,48]. The introduction of second metal (shell) over the surface of another metal NP core leads to the structural change and formation of boundaries two metal atoms. Consequently, an electronic charge transfer occurs between two metals leading to a change in the e^- density on the resultant BM NPs which may promote the reduction process more efficiently [41,42].

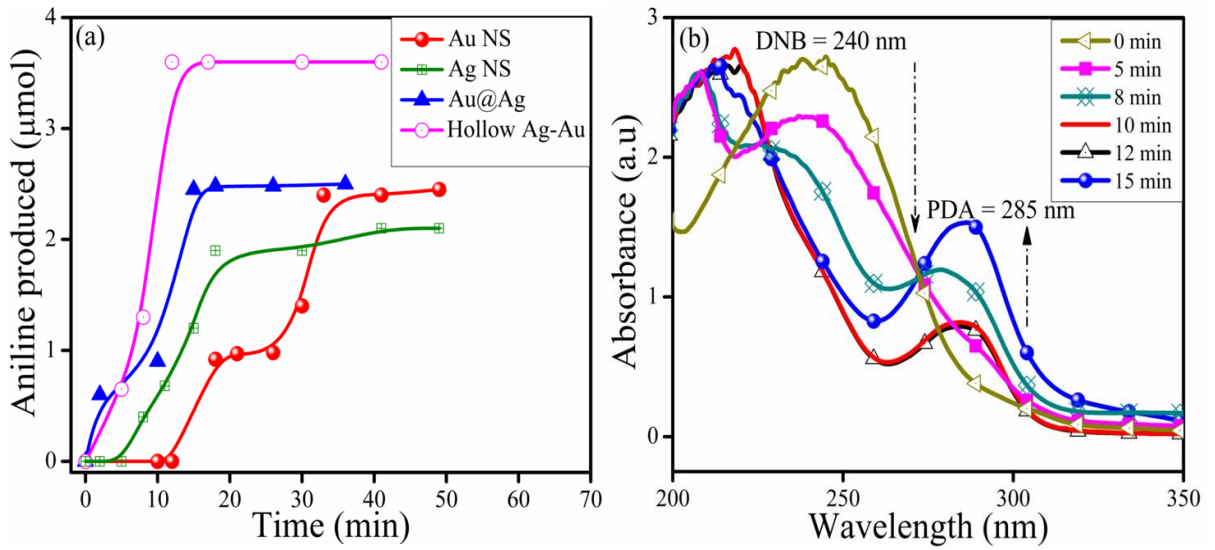

Fig. 2.11. (a) Time course graph of aniline formation from the reduction of nitrobenzene by different monometallic and core@shell bimetallic nanocomposites, and **(b)** Changes in absorption spectra during the reduction of 1,3-dinitrobenzene by $NaBH_4$ in the presence of Au nanospheres.

The effect of e^- withdrawing group on rate of reduction was studied by carrying out the reduction of DNB to 3-nitroaniline (NA) and phenylenediamine (PDA) by core@shell NCs of varying shell-thickness. The reduction process led to the decrease in absorption spectra of DNB (240 nm) with the progressive rise of peak at 285 nm corresponding to a PDA (Fig. 2.11b). But the quantitative analysis (HPLC, Fig. 2.12) revealed the formation of other minor product also i.e., NA along with PDA. Fig. 2.13a shows that the yield of PDA was increased to 70% with the addition of Ag^+ (10 µL) to Au NS ($Au_1@Ag_{0.2}$) in contrast to monometallic Au NS (45%). However, the further increase in the Ag amount (20 and 30 µL) on Au-core i.e., $Au_1@Ag_{0.5}$

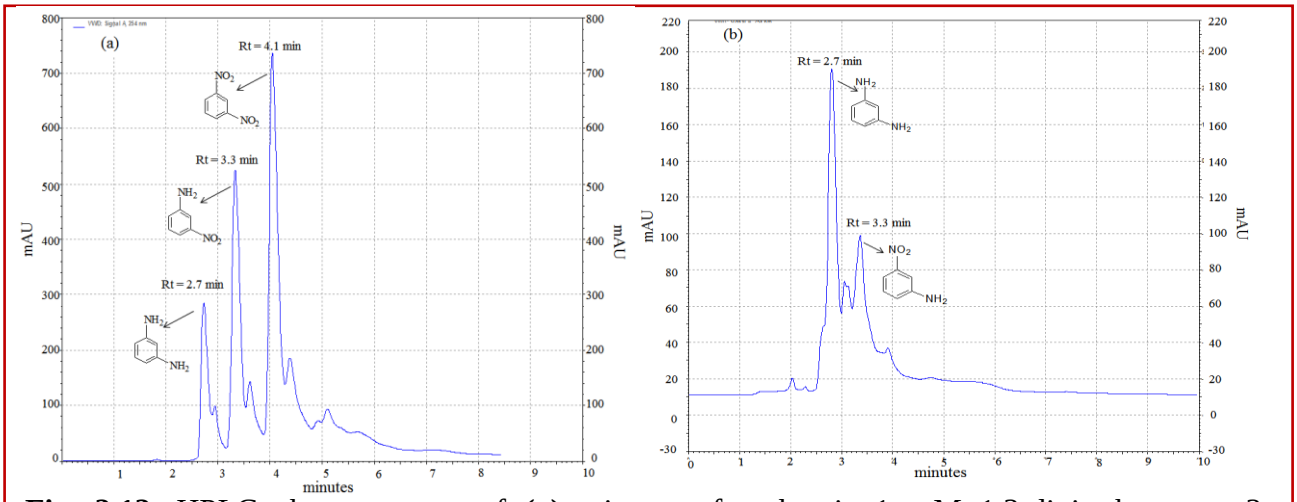

Fig. 2.12. HPLC chromatogram of **(a)** mixture of authentic 1 mM 1,3-dinitrobenzene, 3-nitroaniline and phenylenediamine, and **(b)** reaction product obtained after 10-18 min of reduction of 1,3-dinitrobenzene by core@shell $Au_1@Ag_{0.2}$ nanocomposites.

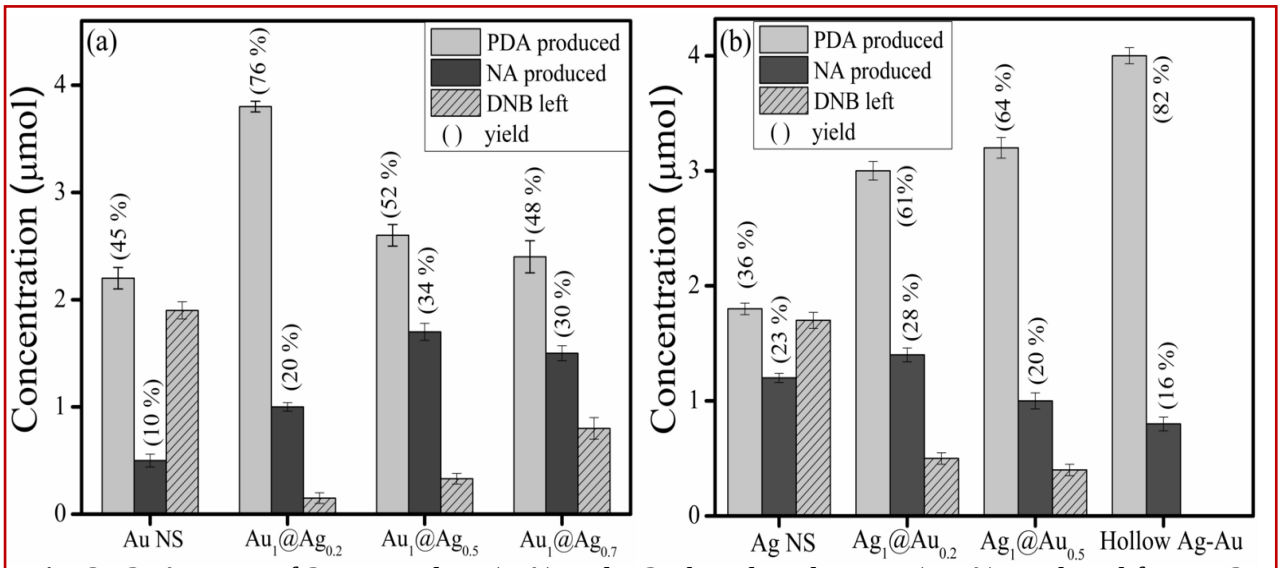

Fig. 2.13. Amount of 3-nitroaniline (NA) and 1,3-phenylenediamine (PDA) produced from 1,3-dinitrobenzene (DNB) reduction by Au and Ag nanospheres and core@shell **(a)** Au@Ag, and **(b)** Ag@Au nanocomposites.

(PDA = 52%) and $Au_1@Ag_{0.7}$ NCs (PDA = 48%), respectively, dramatically decreased the catalytic activity. This can be ascribed to the weaker electronic effect between distant Au-core and Ag-shell, resulting from growing Ag-shell thickness. Ataee-Esfahani et al. [55] even reported that the Pt surface cannot work well as an electro-active surface for methanol oxidation with higher Pt/Au molar ratio or without an Au core. On the other hand, the catalytic reduction by Ag NS to the growing amount of $HAuCl_4^-$ (10-30 µL) showed progressive increase in PDA yield as seen in Fig. 2.13b. The hollow Ag-Au alloy (PDA = 82%) exhibited highest catalytic

activity among the various core@shell Ag@Au NCs (PDA = 61-64%) and bare Ag NS (PDA = 36%) due to their increased surface areas and reduced densities. In this, the inner surface of the hollow shell may provide more bonding sites for the chemical reaction [56-59]. In addition, the different arrangement of Ag and Au in the catalysts (either as core or shell) also played a role in affecting the catalytic efficiency due to which Ag@Au NCs exhibited better catalytic activity than Au@Ag NCs [38]. This is because the electronic charge could transfer from Ag-core to Au-shell in view of their ionization potential, leading to an increase in e^- density on directly exposed Au NPs surface to the solution promoting the reduction more efficient as reported earlier [42,53]. Further, GC-MS analysis of reaction product obtained after reduction of DNB with NCs, qualitatively evidences the formation of PDA, R_t = 11.4 and 12.1 min (1 and 2) and NA, R_t =14.6 and 15.3 min (4 and 6) from DNB, R_t = 14.0 and 14.7 min (3 and 5) as noted in Fig. 2.14. The mass spectrum (Fig. 2.15) showed the peak at m = 108 for 1 and 2 and m = 138 for 4 and 6 compounds confirming the PDA and NA formation. The other peak at m = 168 for 3 and 5 compounds corresponding to DNB was also observed due to its incomplete conversion. Among DNB and NB, the higher reduction rate was found in DNB probably due to the reason that the insertion of the second $–NO_2$ group (e^- withdrawing group) into NB might lower the e^- density on other $–NO_2$ group favoring rapid conversion of $–NO_2$ into $–NH_2$ group. Hence, the conversion of

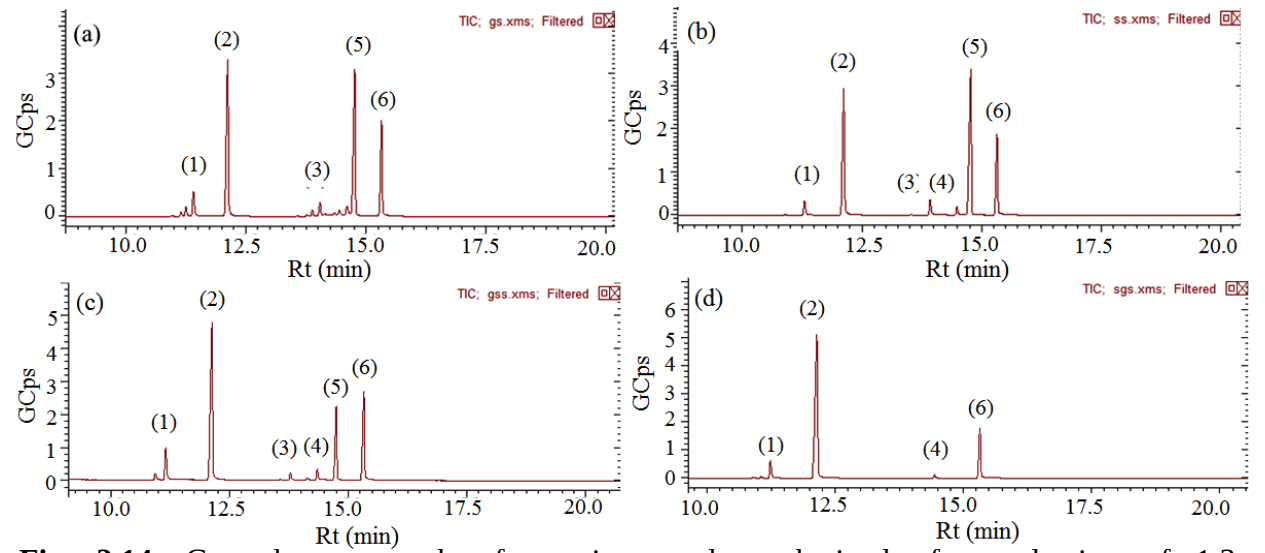

Fig. 2.14. Gas chromatograph of reaction product obtained after reduction of 1,3-dinitrobenzene by **(a)** Au nanospheres, **(b)** Ag nanospheres, **(c)** Au@Ag nanocomposites, and **(d)** hollow Au-Ag alloy.

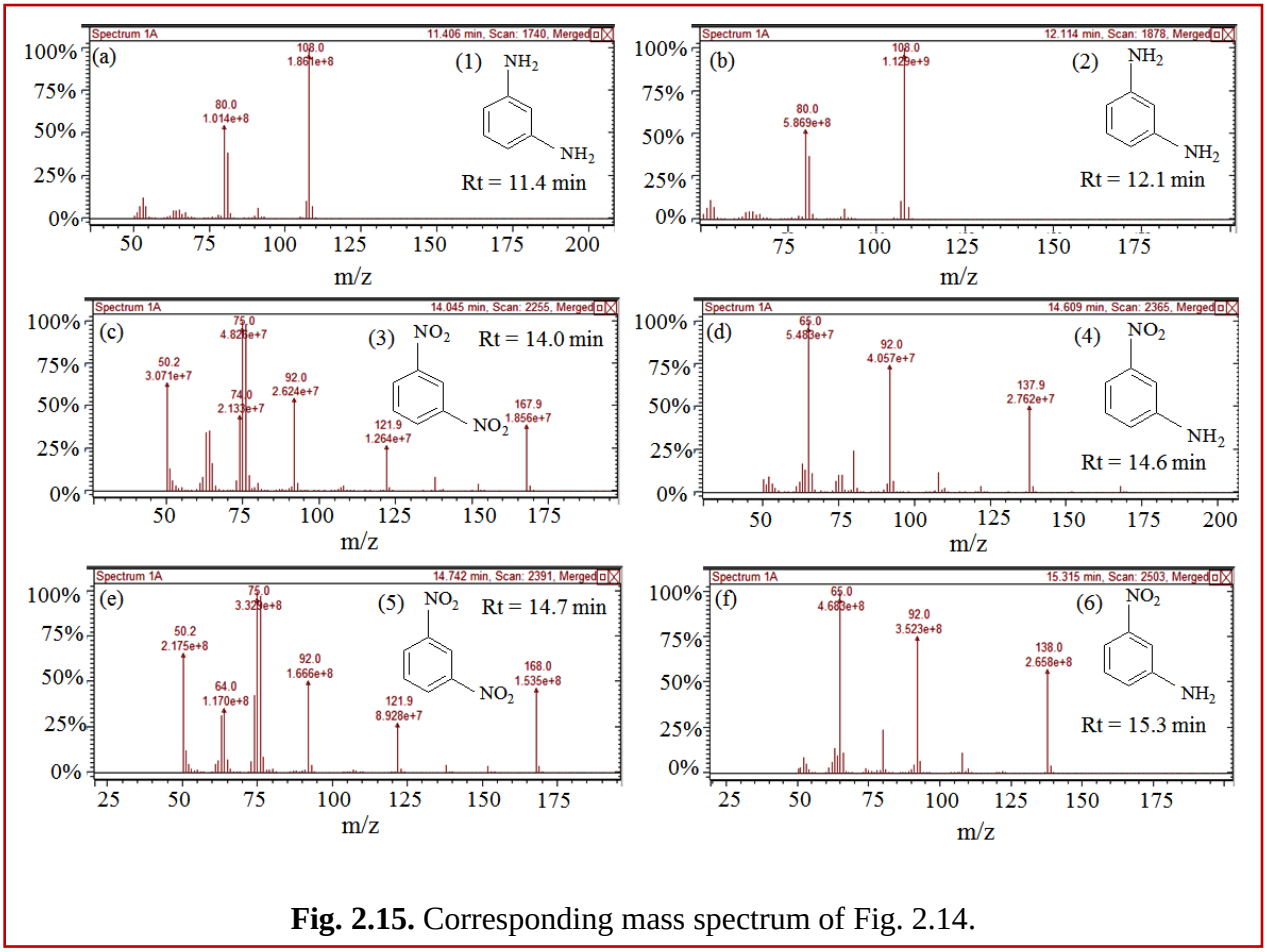

Fig. 2.15. Corresponding mass spectrum of Fig. 2.14.

nitro-aromatic compounds to their respective products enhanced by ~2 times using BM NCs in contrast to their monometallic counterparts. Therefore, through the optimization of shell-thickness and nature of the core, the catalytic efficiency can be enhanced for the other reduction processes.

2.4 Conclusions

In summary, the variation of optical, surface electro-kinetics and catalytic properties of BM NCs relative to their monometallic counterparts have been studied as a function of the nature of coinage metal core as well as shell-thickness. The shell thickness on core NPs can be easily tuned by controlling the concentration of starting precursor solutions. These prepared BM NCs always exhibited significantly higher catalytic activity than their monometallic counterparts attributed to the synergism and the e^- charge transfer at the interface of two metals. However, by changing the morphology from solid Au@Ag to hollow Ag-Au BM NCs displayed the higher catalytic performance due to their more bonding sites available for the chemical reaction.

Therefore, the selectivity and yield of the products for the reduction of nitro-aromatic compounds can be tuned as a function of metal composition and morphology of the coinage BM NCs.

2.5 References

[1] N. Toshima and T. Yonezawa, *New J. Chem.*, 1998, **22**, 1179−1201.

[2] D. S. Wang and Y. D. Li, *Adv. Mater.*, 2011, **23**, 1044−1060.

[3] H. L. Jiang and Q. Xu, *J. Mater. Chem.*, 2011, **21**, 13705−13725.

[4] R. Ferrando, J. Jellinek and R. L. Johnston, *Chem. Rev.*, 2008, **108**, 845−910.

[5] F. Tao, *Chem. Soc. Rev.*, 2012, **41**, 7977–7979.

[6] C. C. Tyson, A. Bzowski, P. Kristof, M. Kuhn, R. Sammynaiken and T. K. Sham, *Phy. Rev. B*, 1992, **45**, 8924–8928.

[7] S. Nishimura, A. T. N Dao, D. Mott, K. Ebitani and S. Maenosono, *J. Phys. Chem. C*, 2012, **116**, 4511−4516.

[8] S. Sakong, C. Mosch and A. Gross, *Phys. Chem. Chem. Phys.*, 2007, **9**, 2216–2225.

[9] M. Kaushik, M. Mandal, N. Pradhan and T. Pal, *Nano Lett.*, 2001, **1**, 319–322.

[10] Y. Sun and Y. Xia, *J. Am. Chem. Soc.*, 2004, **126**, 3892–3901.

[11] B. R. Gonzalez, A. Burrows, M. Watanabe, C. J. Kiely and L. M. L. Marzan, *J. Mater. Chem.*, 2005, **15**, 1755–1759.

[12] M. Tsuji, N. Miyamae, S. Lim, K. Kimura, X. Zhang, S. Hikino and M. Nishio, *Cryst. Growth Des.*, 2006, **6**, 1801–1807.

[13] M. Liu and P. G. Sionnest, *J. Phys. Chem. B*, 2004, **108**, 5882–5888.

[14] Y. Xiang, X. Wu, D. Liu, Z. Li, W. Chu, L. Feng, K. Zhang, W. Zhou and S. Xie, *Langmuir*, 2008, **24**, 3465–3470.

[15] M. J. Alam and M. Tsuji, *Cryst. Eng. Comm.*, 2011, **13**, 6499–6506.

[16] M. Tsuji, N. Nakamura, M. Ogino, K. Ikedo and M. Matsunaga, *Cryst. Eng. Comm.*, 2012, **14**, 7639–7647.

[17] M. P. Mallin and C. J. Murphy, *Nano Lett.*, 2002, **2**, 1235–1237.

[18] L. Rivas, S. S. Cortes, J. V. G. Ramos and G. Morcillo, *Langmuir*, 2000, **16**, 9722–9728.

[19] L. Chen, L. Kuai and B. Geng, *Cryst. Eng. Comm.*, 2013, **15**, 2133–2136.

[20] C. W. Yang, K. Chanda, P. H. Lin, Y. N. Wang, C. W. Liao and M. H. Huang, *J. Am. Chem. Soc.*, 2011, **133**, 19993–20000.

[21] M. Sakamoto, T. Tachikawa, M. Fujitsuka and T. Majima, *Adv. Funct. Mater.*, 2007, **17**, 857–862.

[22] T. Nakamura, Y. Tsukahara, T. Yamauchi, T. Sakata, H. Mori and Y. Wada, *Chem. Lett.*, 2007, **36**, 154–155.

[23] M. Tsuji, S. Hikino, R. Tanabe, M. Matsunaga and Y. Sano, *Cryst. Eng. Comm.*, 2010, **12**, 3900–3908.

[24] Y. Ding, F. Fan, Z. Tian and Z. L. Wang, *J. Am. Chem. Soc.*, 2010, **132**, 12480−12486.

[25] J. Xu, A. R. Wilson, A. R. Rathmell, J. Howe, M. Chi and B. J. Wiley, *ACS Nano*, 2011, **5**, 6119−6127.

[26] S. Chen, S. V. Jenkins, J. Tao, Y. Zhu and J. Chen, *J. Phys. Chem. C*, 2013, **117**, 8924−8932.

[27] Y. Ma, W. Li, E. C. Cho, Z. Li, T. Yu, J. Zeng, Z. Xie and Y. Xia, *ACS Nano*, 2010, **4**, 6725–6734.

[28] M. Tsuji, R. Matsuo, P. Jiang, N. Miyamae, D. Ueyama, M. Nishio, S. Hikino, H. Kumagae, K. S. N. Kamarudin and X. L. Tang, *Cryst. Growth Des.*, 2008, **8**, 2528−2536.

[29] M. Tsuji, M. Ogino, M. Matsunaga, N. Miyamae, R. Matsuo, M. Nishio and M. J. Alam, *Cryst. Growth Des.*, 2010, **10**, 4085−4090.

[30] S. Pande, S. K. Ghosh, S. Praharaj, S. Panigrahi, S. Basu, S. Jana, A. Pal, T. Tsukuda and T. Pal, *J. Phys. Chem. C*, 2007, **111**, 10806−10813.

[31] N. G. Bastus, J. Comenge and V. Puntes, *Langmuir*, 2011, **27**, 11098–11105.

[32] G. Kawamura, Y. Yang and M. Nogami, *J. Phys. Chem. C*, 2008, **112**, 10632–10636.

[33] I. O. Jimenez and V. Puntes, *J. Am. Chem. Soc.*, 2009, **131**, 13320–13327.

[34] X. Zhang, G. Zhang, B. Zhang and Z. Su, *Langmuir*, 2013, **29**, 6722−6727.

[35] C. Shankar, A. T. N. Dao, P. Singh, K. Higashimine, D. M. Mott and S. Maenosono, *Nanotechnology*, 2012, **23**, 245704.

[36] S. H. Wang, C. W. Lee, A. Chiou and P. K. Weil, *J. Nanobiotechnology*, 2010, **8**, 33−45.

[37] J. W. Park and J. S. S. Parry, *J. Am. Chem. Soc.*, 2014, **136**, 1907−1921.

[38] S. Biggs, P. Mulvaney, C. F. Zukoski and F. Grieser, *J. Am. Chem. Soc.*, 1994, **116**, 9150−9157.

[39] P. Wagener, A. Schwenke and S. Barcikowski, *Langmuir*, 2012, **28**, 6132−6140.

[40] C. H. Munro, W. E. Smith, M. Garner, J. Clarkson and P. C. White, *Langmuir*, 1995, **11**, 3712−3720.

[41] H. Zhanga and N. Toshima, *Catal. Sci. Technol.*, 2013, **3**, 268−278.

[42] S. Tokonami, N. Morita, K. Takasaki and N. Toshima, *J. Phys. Chem. C*, 2010, **114**, 10336−10341.

[43] S. Nishimura, A. T. N. Dao, D. Mott, K. Ebitani and S. Maenosono, *J. Phys. Chem. C*, 2012, **116**, 4511−4516.

[44] M. Kahraman, O. Aydin and M. Culha, *Plasmonics*, 2009, **4**, 293−301.

[45] J. Lim, S. P. Yeap, H. X. Che and S. C. Low, *Nanoscale Res. Lett*., 2013, **8**, 1−14.

[46] D. Ray and V. K. Aswal, *Nanosci. Nanotechnol. Lett.*, 2011, **3**, 603−611.

[47] P. Pallavicini, G. Chirico, M. Collini, G. Dacarro, A. Dona, L. D. Alfonso, A. Falqui, Y. D. Fernandez, S. Freddi, B. Garofalo, A. Genovese, L. Sironib and A. Tagliettia, *Chem. Commun.*, 2011, **47**, 1315−1317.

[48] Q. Fu, D. G. Zhang, M. F. Yi, X. X. Wang, Y. K. Chen, P. Wang and H. Ming, *J. Opt.*, 2012, **14**, 085001.

[49] H. F. Zarick, W. R. Erwin, J. Aufrecht, A. Coppola, B. R. Rogers, C. L. Pint and R. Bardhan, *J. Mater. Chem. A*, 2014, **2**, 7088–7098.

[50] S. W. Hsu, K. On, B. Gao and A. R. Tao, *Langmuir*, 2011, **27**, 8494–8499.

[51] T. Ghosh, B. Satpati and D. Senapati, *J. Mater. Chem. C*, 2014, **2**, 2439–2447.

[52] P. Venkatesan and J. Santhanalakshmi, *Langmuir*, 2010, **26**, 12225–12229.

[53] X. Guo, Q. Zhang, Y. Sun, Q. Zhao and J. Yang, *ACS Nano*, 2012, **6**, 1165–1175.

[54] X. Zhang and Z. Su, *Adv. Mater.*, 2012, **24**, 4574–4577.

[55] H. A. Esfahani, L. Wang, Y. Nemoto and Y. Yamauchi, *Chem. Mater.*, 2010, **22**, 6310–6318.

[56] H. Wu, P. Wang, H. He and Y. Jin, *Nano Res.*, 2012, **5**, 135–144.

[57] M. R. Kim, D. K. Lee and D. J. Jang, *Appl. Catal. B: Environ.*, 2011, **103**, 253–260.

[58] H. M. Chen, R. S. Liu, M. Y. Lo, S. C. Chang, L. D. Tsai, Y. M. Peng and J. F. Lee, *J. Phys. Chem. C*, 2008, **112**, 7522–7526.

[59] J. Zeng, Q. Zhang, J. Chen and Y. Xia, *Nano Lett.*, 2010, **10**, 30–35.

Chapter 3

Preparation and Characterization of Different Shapes of Au-Ag Bimetallic Nanocomposites for Enhanced Physicochemical Properties

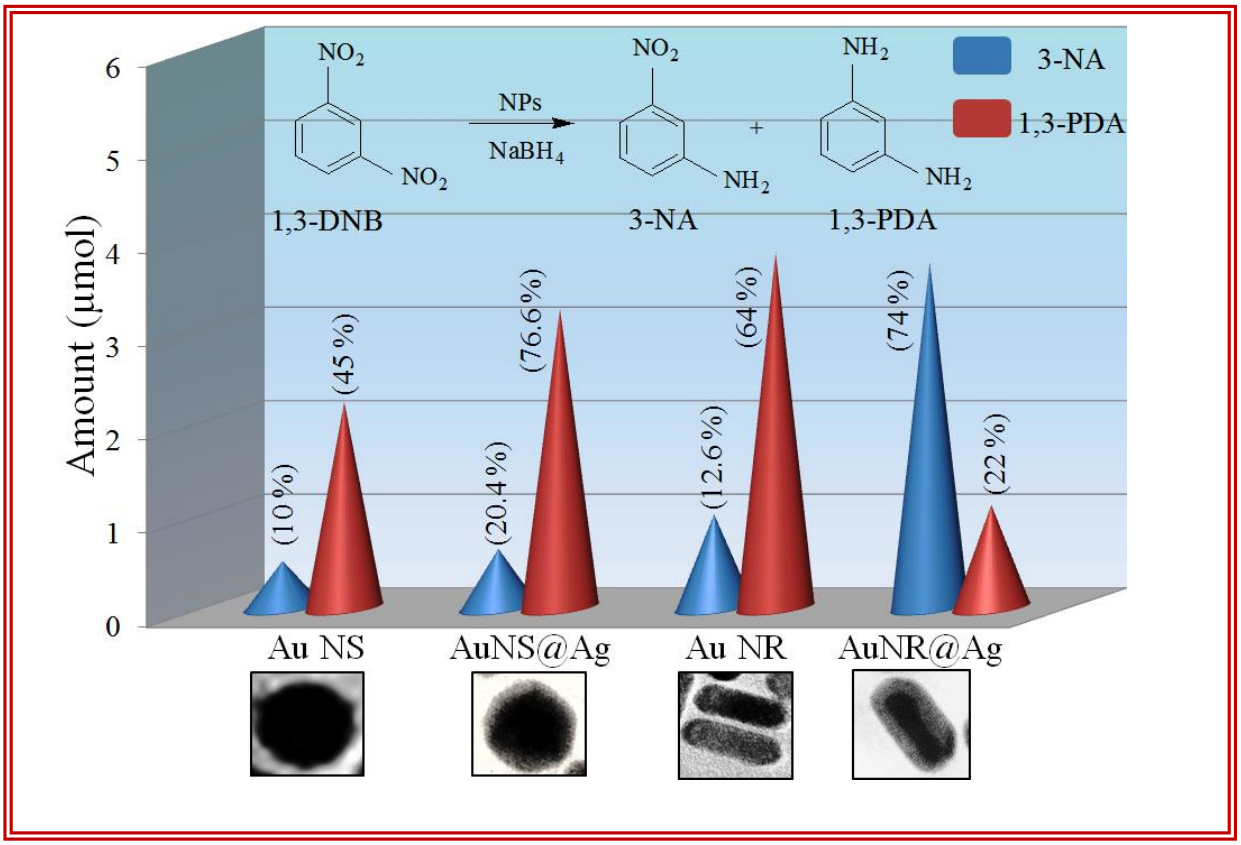

3.1 Introduction

Bimetallic (BM) alloys and core@shell nanocomposites (NCs) composed of two different metals, have received considerable attention [1-4] as compared to their respective monometallic nanoparticles (NPs) due to superior physicochemical, optical and catalytic properties. These are attributed to the synergistic effects [5] which include electronic [6,7] and an ensemble effect [8], induced by the interaction of two metals. Since the catalytic activity is highly dependent on the catalyst surface structure, the deposition of another metal on the surface of another could alter the interface energetic and electron (e^-) transfer process; hence influencing the selectivity and yield of a catalytic reaction. Among BM systems, Au-Ag BM NCs have been widely investigated [3,9-18] because of their strong absorption in the visible region, stability, easy synthesis and similar crystal structure. Moreover, the interaction of the atomic energy level of the Au ($6s^1\ 4f^{14}\ 5d^{10}$) and Ag ($5s^1\ 4d^{10}$) at the Au-Ag interface may result in the formation of wider d-band, moved towards the Fermi-level due to the atomic re-hybridization. It was reported that the spherical Ag/Au BM NCs exhibited ~18 times higher activity than Au NPs for glucose oxidation [19] and a higher rate constant for the reduction of *p*-nitrophenol was found [20] for core@shell Au@Ag ($k= 0.18\ min^{-1}$) than their monometallic NPs ($k = 0.019\text{-}0.069\ min^{-1}$). Hence, the chemical and physical properties of BM NCs can be tuned as a function of the nature of metals, composition, shape, size and shell thickness to be a consequence of the different electronic and chemical properties of Au as well as Ag.

As the anisotropic shapes, i.e., nanorods, triangular and cubical NPs are known to offer a distinct fraction of atoms at the edges and corners that are more active than symmetric shapes and hence, can be be better suited [21-23] for a selective catalytic reaction. The catalytic reduction of aromatic nitro compounds gives aromatic amines, which are used in the synthesis of many fine chemicals, herbicides, pesticides, dyes and pigments [24,25]. One of the industrially important reduction reactions is the conversion of 1,3-dinitrobenzene (DNB) to the products of nitroaniline (NA) and 1,3-phenylenediamine (PDA). The reduction of DNB is generally carried out by disulfides [26], metal acid systems [27], Fe, Zn, Sn, Au-Ni alloy, Au/Pt-Al_2O_3, Pt/TiO_2, Fe_2O_3 and ZrO_2 etc. catalysts [28-31] under harsh experimental conditions such as high pressure (23-24 atm) and temperature (373-473 K) and toxic solvents. However, this paper deals with the usage of homogeneous catalysts in a very minute quantity which offers the effective utilization of atoms. Therefore, a distinct selectivity [32] was exhibited as a function of

specific modification of the catalyst in aqueous medium under ambient temperature and pressure conditions. The coating of Au nanospheres/nanorods core by the Ag shell of different thickness could change the interfacial property and effective electronic charge [33,34]. This may affect the interaction of reactants over the nanocatalyst's surface and, thereby, tailoring the catalytic performances of Au-Ag binary NCs. Consequently, this work signifies the influence on optical, surface electro-kinetics, and catalytic properties of different shapes of Au-core and varying thickness of Ag-shell relative to monometallic Au nanostructures.

3.2 Experimental

3.2.1 Materials

Chloroauric acid ($HAuCl_4.3H_2O$), ascorbic acid ($C_6H_8O_6$), sodium borohydride ($NaBH_4$), sodium hydroxide (NaOH), polyvinylpyrrolidone (PVP, $(C_6H_9NO)_n$), nitrobenzene ($C_6H_5NO_2$) and 1,3-dinitrobenzene were ($C_6H_4N_2O_4$) attained from Loba Chemie, India. cetyltrimethylammoniumbromide (CTAB, $C_{19}H_{42}BrN$) and Silver nitrate ($AgNO_3$) were purchased from Sigma Aldrich and Fischer Scientific, India, respectively. All the chemicals were used without any further purification. De-ionized water was obtained using a Milli-*Q*, Millipore ultra-filtration system with a measured conductivity of above 35 mho cm^{-1} at 25° C.

3.2.2 Preparation of Au Nanospheres and Au Nanorods

The Au nanospheres (Au NS) and Au nanorods (Au NR) were synthesized by a seed-mediated method as reported [35,36] elsewhere. The Au seed solution was prepared by reducing the aqueous mixture (8 mL) containing $HAuCl_4.3H_2O$ (500 µL, 0.01 M) and trisodium citrate (1.47 mg, 2.5×10^{-4} M) by $NaBH_4$ (600 µL, 0.1 M). Then, the Au seeds (ca. 5 mL) were added into the growth solution comprising CTAB (9.5 mL, 0.08 M), $HAuCl_4.3H_2O$ (1.5 mL, 0.01 M) and ascorbic acid (50 µL, 0.1 M) which gave rise to wine-red color of spherical Au NPs. However, for the preparation of Au NR, 500 µL of above seed solution was added into 25 mL of the growth solution containing CTAB (920 mg), $HAuCl_4.3H_2O$ (1.25 mL, 0.01 M), $AgNO_3$ (225 µL, 5 mM) and ascorbic acid (200 µL, 0.1 M). This resulted in the appearance of violet colored solution indicating the formation of Au NR. These Au NPs were repeatedly washed with de-ionized water using centrifugation machine at 8500 rpm for 5-10 min and re-dispersed in de-ionized water.

3.2.3 Preparation of Core@Shell Au@Ag Bimetallic Nanocomposites

The resulting CTAB-capped Au NS and Au NR solution (0.8 mL) was dispersed into an aqueous solution of PVP (4 mL, 1 wt. %) separately into which varying amount of Ag^+ ions (10-30 µL, 0.01 M) were added. After this, a weak reducing acid i.e., ascorbic acid (0.1 mL, 0.1 M) in the presence of NaOH (0.2 mL, 0.1 M) was added in order to start the coating of the Ag shell at the alkaline pH (pH = 10.2-10.4) giving rise [11,13] to Au nanospheres@Ag (AuNS@Ag) and Au nanorods@Ag (AuNR@Ag) NCs. The prepared core@shell NCs of different shapes i.e., NS and NR obtained by adding different amounts (10, 20 and 30 µL) of Ag^+ ions are abbreviated as AuNS@Ag10/20/30 and AuNR@Ag10/20/30 NCs, respectively, and were washed with de-ionized water under centrifugation (8000 rpm for 5 min) and re-dispersed in water.

3.2.4 Characterization

The as-prepared BM NCs were characterized by UV-Vis spectrophotometer (Analytica Jena Specord 205), Transmission electron microscopy, TEM (Hitachi 7500, 2Å, 120 KV) and an energy dispersive X-ray (EDX) analysis. High-resolution TEM (HRTEM) and selected area electron diffraction (SAED) analysis of BM NCs were done by using a FEI Technai F20 transmission electron microscope. The hydrodynamic diameter of different BM NCs was measured by using a Brookhaven 90 plus Particle Size Analyzer using cumulant fitting. The zeta potential (ζ) measurement was done by taking 1.5 mL of NCs solution in a cuvette using Brookhaven zeta plus at 25 $^{\circ}$C.

3.2.5 Catalytic Activity

The catalytic activity of different shapes of Au@Ag NCs in comparison to their monometallic NPs was carried out by the reduction of nitrobenzene (NB) and 1,3-dinitrobenzene (DNB) at room temperature by keeping the number of particles and other conditions same in all cases. In a typical reaction, $NaBH_4$ solution (100 µL, 0.01 M) was added into nitro-organic compound solution (5 mL, 1 mM) and then, calculated or fixed amount of different NPs (6.75×10^{15} atoms) were added. The reaction process was monitored by measuring the absorption spectra ($\lambda_{max.}$ of NB ~ 270 nm and $\lambda_{max.}$ of DNB ~ 240 nm) at regular intervals of time and the products were further quantified by HPLC.

3.2.6 Calculation of the amount of Au atoms in Au Nanospheres

For the preparation of Au NS, 1.5 mL of the Au^{+3} (0.01 M, $HAuCl_4.3H_2O$) in growth solution and 5 mL of the seed solution that contains 2.9 mg and 0.58 mg of Au, respectively, was reduced to Au NPs. These NPs were washed and finally dispersed in 25 mL of water that contain 3.4 mg

of Au. Hence, 1 µL of Au NP solution contains 1.4×10^{-4} mg Au that was converted to number of Au atoms. Similarly, further calculations are given below:

25 mL (25,000 µL) of Au NS solution contains	3.4 mg Au
2 mL (2000 µL) of Au NS solution contains	0.27 mg Au
2 mL Au NS contains	6.75×10^{17} atoms
1 µL Au NS contains	1.3×10^{-4} mg Au
1 µL Au NS contains	3.36×10^{14} atoms
20 µL Au NS contains	6.75×10^{15} atoms

Similarly, the number of atoms for the other NCs (Au NR, AuNS@Ag and AuNR@Ag) was calculated. The number of atoms was fixed to 6.75×10^{15} atoms in order to determine the catalytic activity under the same conditions.

3.3 Results and Discussion

3.3.1 Optical Properties

The typical SP band of Au NS at 529 nm was blue-shifted to broader peaks at 500 nm and 419 nm of higher intensity, after the addition of Ag^+ ions (10 and 20 µL, Fig. 3.1a), respectively, accompanied by the color variation from wine red to pink to orange as displayed in Fig. 3.1b. This specified the modification of the surface of Au NS due to the partial encapsulation of Ag-layer on the Au-core. Further, increasing the Ag^+ ions (30 µL) addition, a sharp SP band at 400 nm appeared and the color changed to yellow. Here, the photons of incident light could only reach the outer Ag shell of a certain thickness [37] and could not penetrate the Au cores to stimulate its e^-. Therefore, it was assumed that the Au NS were completely enclosed by Ag coating forming the core@shell AuNS@Ag NCs of different shell-thickness in good conformity with the report [38], where the SP band of Au NS (520 nm) was gradually blue-shifted to 438 nm and 402 nm with growing thickness of Ag-shell. The atomic ratio for the coating of different amount of Ag^+ ions (10-30 µL, 0.01 M) on the surface of Au NS was calculated to be 0.2-0.6.

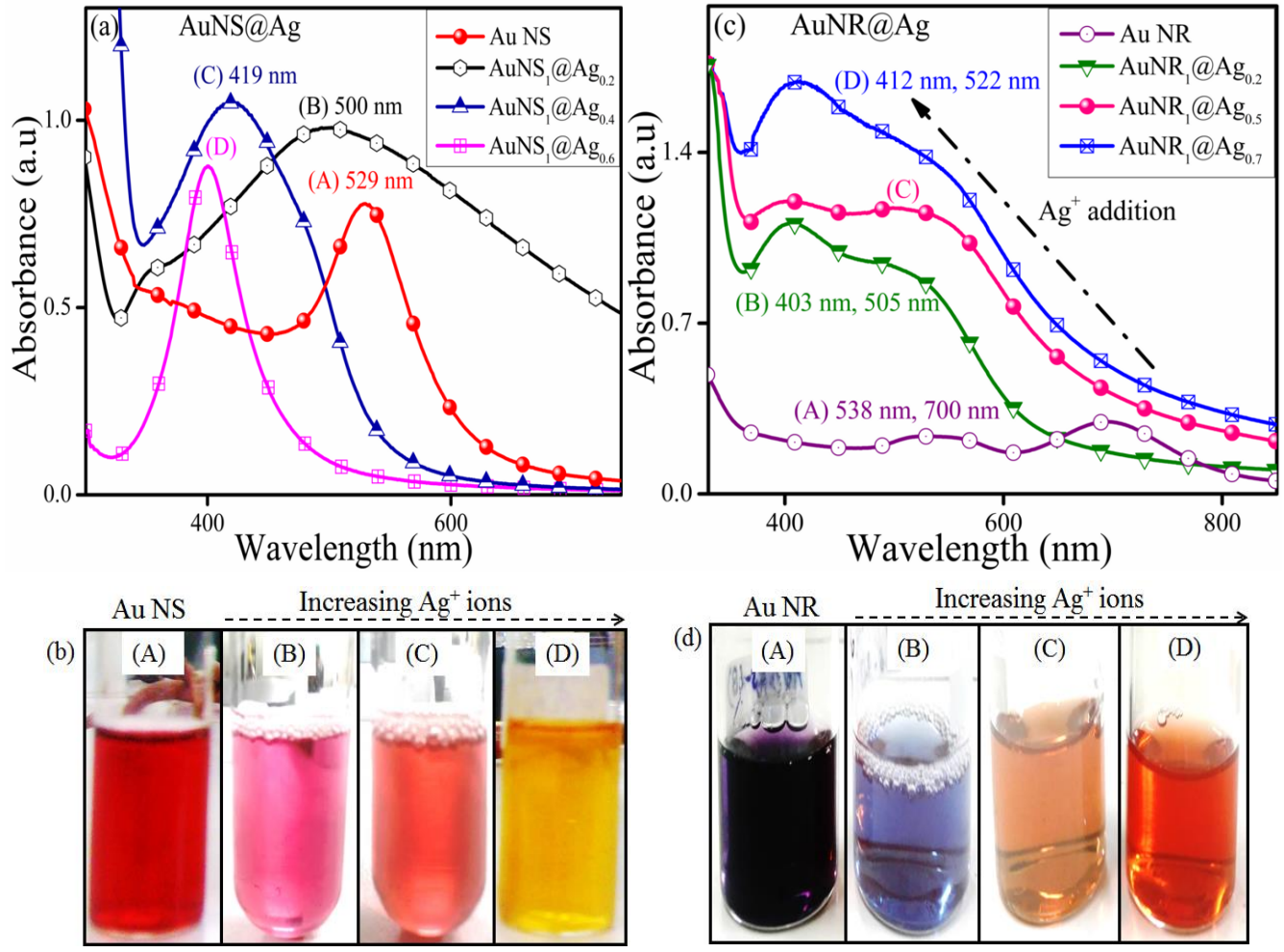

Fig. 3.1. Effect of different amounts of $AgNO_3$ (10-30 µL, 0.01 M) deposition onto **(a-b)** Au nanospheres, and **(c-d)** Au nanorods for the variation in the surface plasmon band and their respective color changes.

Table 3.1. Calculations for the amount of Au and Ag atoms in bare Au nanorods and core@shell AuNR@Ag nanocomposites.

Elements	Amount of element (mg)	No. of atoms (atoms)	Atomic ratio (Au:Ag)
Au NR (800 µL)	0.079	2.4×10^{17}	1:0
Ag^+ (0.01M, 10 µL)	0.0107	0.6×10^{17}	1:0.2
Ag^+ (0.01M, 20 µL)	0.0213	1.2×10^{17}	1:0.5
Ag^+ (0.01M, 30 µL)	0.032	1.8×10^{17}	1:0.7

Similarly, the characteristic longitudinal surface plasmon (LSP) band at 700 nm and transverse surface plasmon (TSP) band at 538 nm of Au NR gradually blue-shifted to 505 nm and 403 nm, respectively, after Ag^+ (10-20 µL) deposition as shown in Fig. 3.1c. With the increasing amount of deposited Ag^+ (30 µL) ions, a new peak at 412 nm appeared along with a shoulder peak at 522 nm probably due to non-uniform and unsymmetrical deposition of Ag layer on Au NR particles. This finding was consistent with the reported results [14] where coating of Ag^+ on the anisotropic Au NR led to the formation of orange like-shape. Here, the calculated atomic ratios for the deposition of Ag^+ ions (10-30 µL, 0.01 M) on the surface of Au NR were 0.2-0.7 (Table 3.1). Further, this morphological change was evidenced by a notable color transformation from violet to blue to brown and orange as seen in Fig. 3.1d verifying the core@shell AuNR@Ag NCs formation.

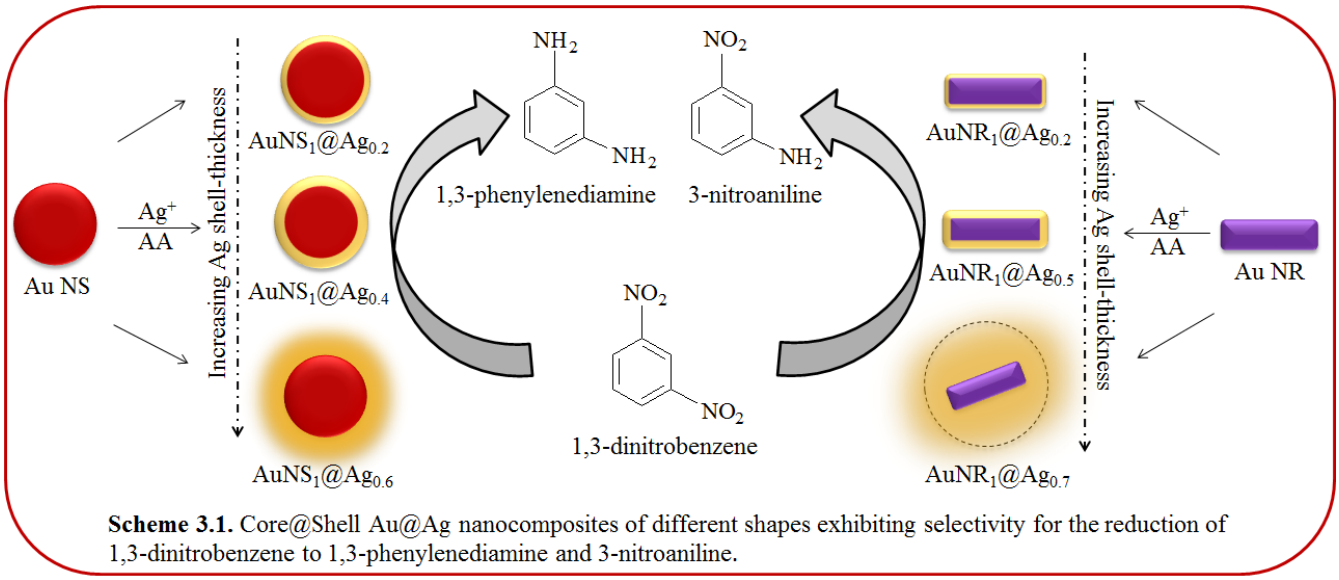

Scheme 3.1. Core@Shell Au@Ag nanocomposites of different shapes exhibiting selectivity for the reduction of 1,3-dinitrobenzene to 1,3-phenylenediamine and 3-nitroaniline.

3.3.2 Particle Size Distribution

The deposition of second metal on the surface of monometallic NPs may modify the overall particle size distribution of BM NCs which can be measured by the DLS particle size distribution [39]. It was found that the hydrodynamic diameter of Au NS (28 nm) changed to 30 nm after coating of 10 µL Ag^+ ions. Further coating of Ag^+ ions (20-30 µL) caused a gradual increment in the particle diameter from 36 nm to 42 nm due to the gradual growth of Ag-shell thickness on Au NS (Scheme 3.1) as shown in Fig. 3.2a. Similarly, the hydrodynamic diameter of Au NR (49 nm) subsequently increased to 52 nm to 55 nm and 69 nm with 10-30 µL of Ag^+ ions (Fig. 3.2b) coating. The measured hydrodynamic diameter was observed to be larger than the TEM size due

to the adherence of the hydration layer on the surface of NCs during the size measurement by DLS.

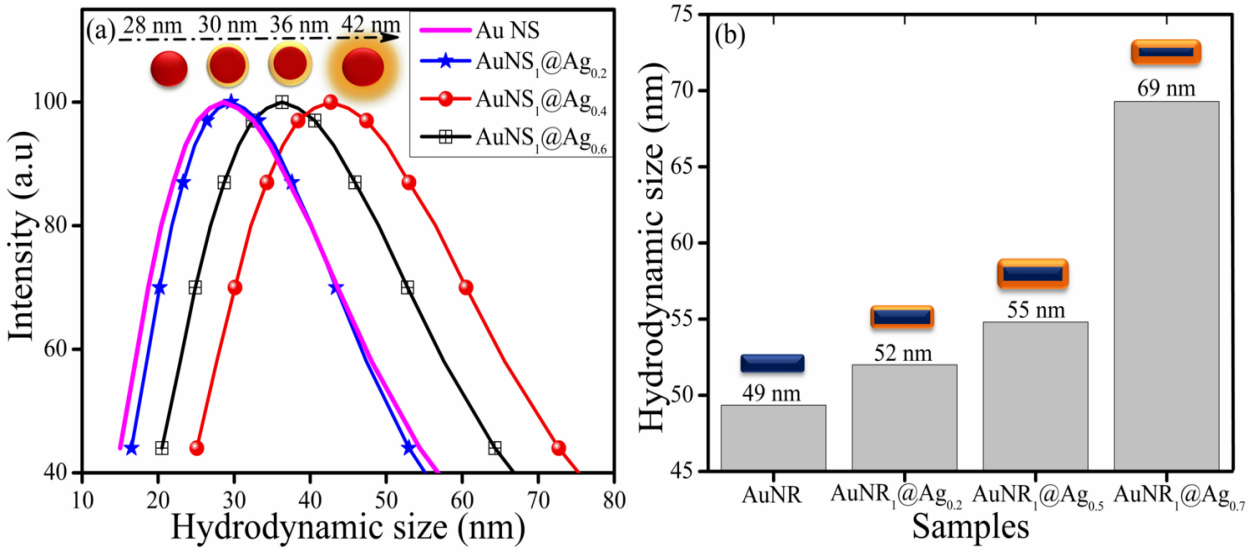

Fig. 3.2. DLS particle size distribution after different amount of $AgNO_3$ (10-30 µL, 0.01 M) deposition onto **(a)** Au nanospheres, and **(b)** Au nanorods.

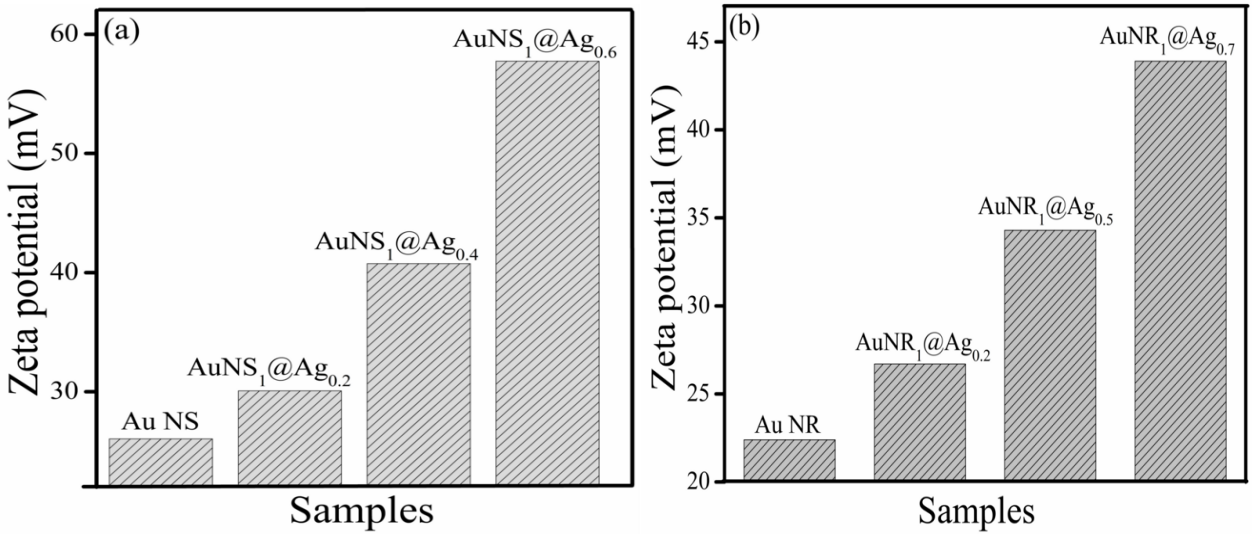

Fig. 3.3. Variation of electro-kinetic parameters after different amount of $AgNO_3$ (10-30 µL, 0.01 M) deposition onto **(a)** Au nanospheres, and **(b)** Au nanorods.

3.3.3 Electro-kinetic Parameters

When the NPs are dispersed in an aqueous solution, the formation of electrical double layer at the NPs surface takes place owing to the surface adsorbed cationic or anionic species, leading to the development of new surface charge called Zeta potential (ζ). As a result, ζ value of a bare Au NS (+26.04 mV) and Au NR (+22.4 mV) were measured to be positive [40,41] due to the

presence of cationic surfactant, CTAB on their surfaces. The deposition of Ag^+ on the Au NS surface made the surface more positive (ζ = +30.07 mV) indicating that the bare Au NS are chemically transformed through the absorption of Ag layer as in Fig. 3.3a. Further, the zeta potential of AuNS@Ag was measured to be more positive (+40.7 mV to +57.7 mV) with the increasing Ag^+ ions addition. Similarly, in case of AuNR@Ag, the zeta potential enhanced (+22.4 mV to +43.9 mV) [42] after an increased amount of Ag^+ deposition as revealed in Fig. 3.3b. This charge variation might be ascribed to the e^- charge transfer from Ag having low ionization potential (7.58 eV) to Au having high ionization potential (9.22 eV) [7,19]. Consequently, the electronic charge transfer takes place from Ag in the shell to Au in the core, leading to the increase of positive charges on the Ag-shell as supported by the above results as reported [7].

3.3.4 Morphological Studies

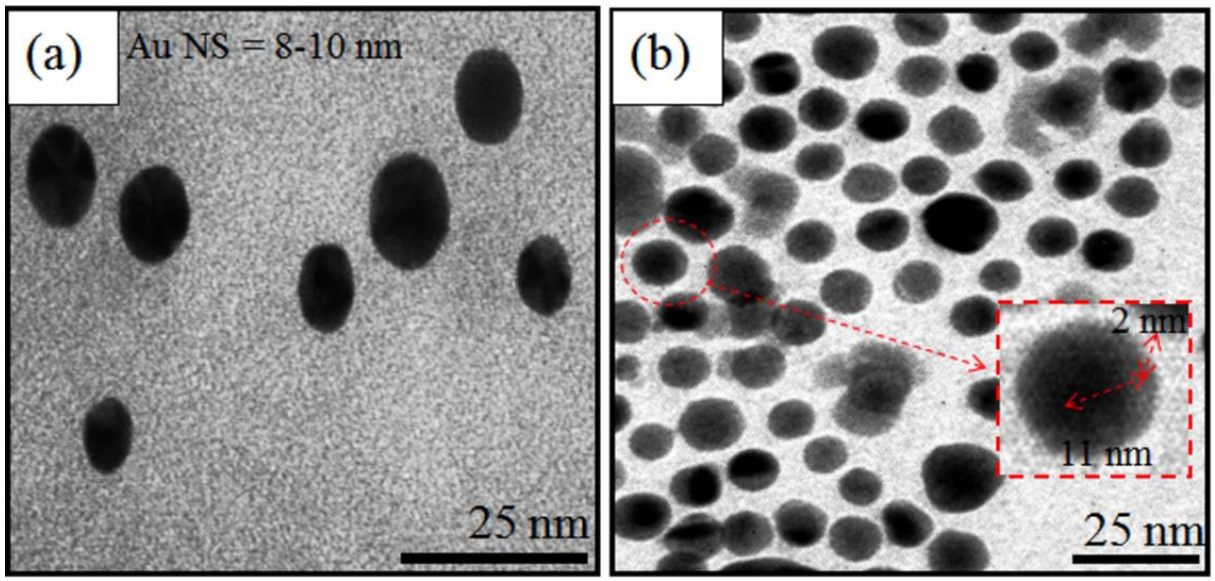

Fig. 3.4. TEM images of **(a)** bare Au nanospheres, and **(b)** core@shell bimetallic AuNS@Ag nanocomposites.

TEM analysis showed that the bare Au NS of size = 8-10 nm (Fig. 3.4a) acted as a seed for the deposition of Ag on its surface and gradually gave rise to a homogeneous formation of a Ag layer (AuNS@Ag NCs) having thickness of ~2 nm (Fig. 3.4b). This result was in conformity with the reported [38,43] core@shell AuNS@Ag NCs, where the darker portion corresponds to the Au core and lighter shell is ascribed to Ag metal. With the addition of higher amount of Ag^+ ions, the Ag shell became thicker (~8-11 nm), asymmetric, diffused and non-uniform (Scheme

3.1), giving an irregular shape to the NCs of size ~20-25 nm (Fig. 3.5a and b). The HRTEM image of AuNS@Ag NCs of size ~20-25 nm with a Ag shell thickness of ~2-3 nm is shown in Fig. 3.5c and the observed fringe spacing, 1.4 Å and 2.3 Å, corresponded well with the (110) plane of the FCC Ag (1.44 Å) and the (111) plane of the FCC Au (2.355 Å, JCPDS card no. 04-07484) respectively. Further, the SAED pattern (inset, Fig. 3.5d) of AuNS@Ag NCs evidenced the planes (111) and (200) of Au and (201) and (100) of Ag NPs. These results strongly support the formation of core@shell AuNS@Ag as proposed by the previous report [44].

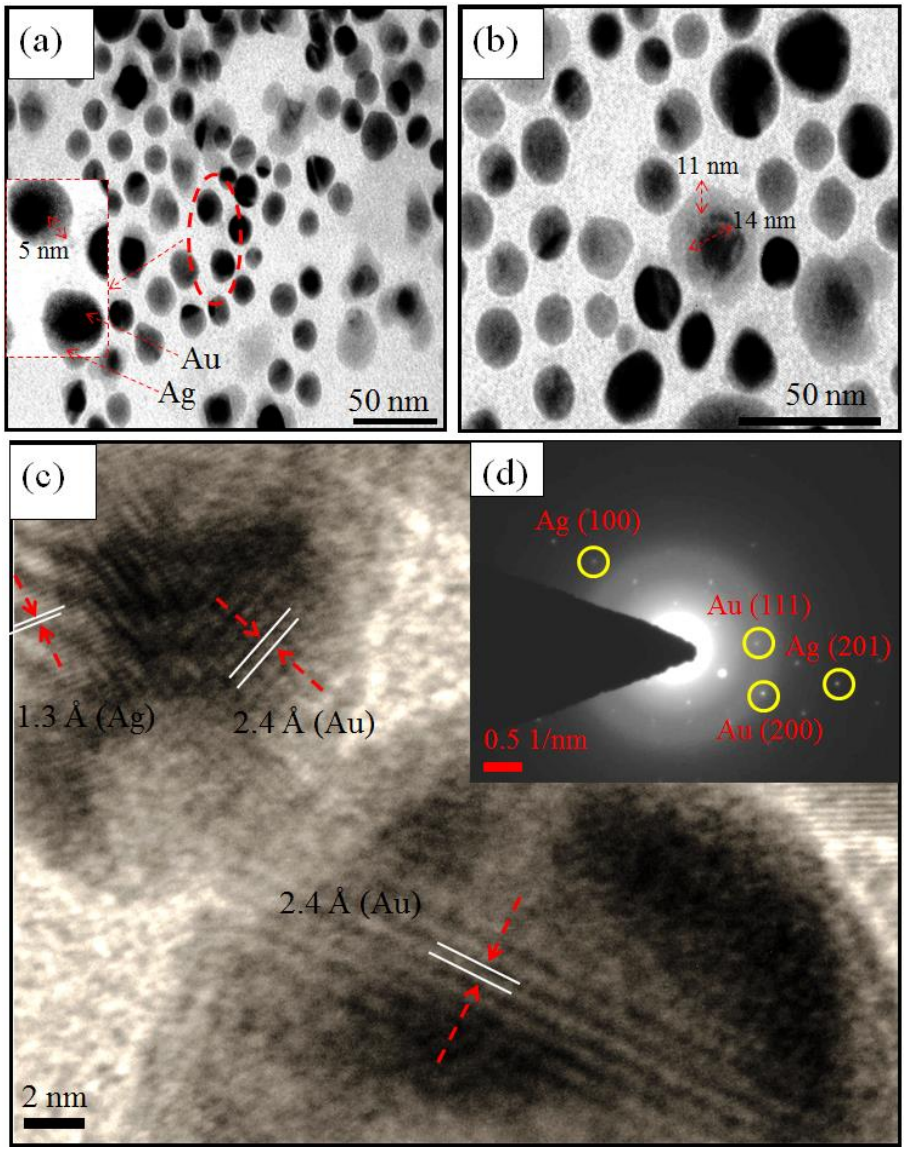

Fig. 3.5. TEM images of **(a-b)** core@shell bimetallic AuNS@Ag nanocomposites of different Ag-shell thickness (~2-11 nm), **(c)** HRTEM of core@shell bimetallic AuNS@Ag nanocomposites, and **(d)** SAED patterns obtained from image **(c)**.

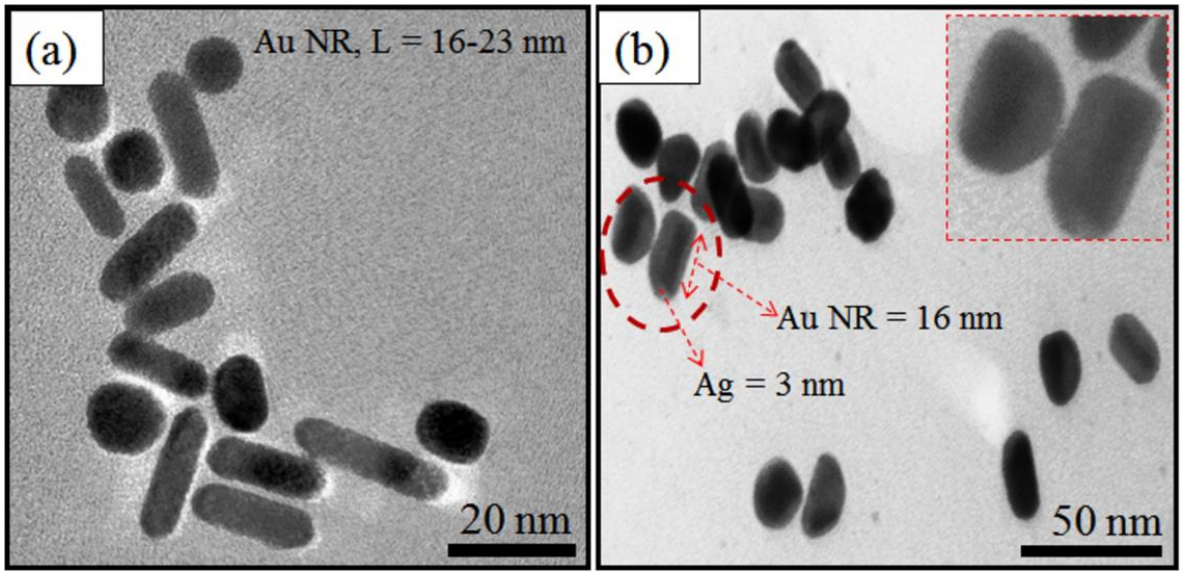

Fig. 3.6. TEM images of **(a)** bare Au nanorods, and **(b)** core@shell bimetallic AuNR@Ag nanocomposites.

It displayed that the bare Au NR (Fig. 3.6a) of size = 15-23 nm × 6 nm was coated with a semi-transparent layer of Ag (~3 nm), after addition of Ag^+ ions (10 µL) (Fig. 3.6b). The thickness of Ag shell was further increased to ~6-20 nm toward the lengthy direction with the increased amount (20-30 µL) of Ag^+ addition (Fig. 3.7a-e). As a result, the shape of the NR approached to the spherical form of size = ~20-25 nm (Scheme 3.1) as observed in Fig. 3.7b-e. Similar report [14,33] was also found, where the Ag coating became diffused with growing Ag shell-thickness, and the shape of Au NR grew into an irregular and asymmetric nature. Further, the SAED pattern evidenced the presence of both the Au and Ag particles corresponding to the planes of (111), (200) and (110), (004) and (104), respectively, as depicted in Fig. 3.7f.

3.3.5 Catalytic Activity

The relative catalytic activity of Au NS, Au NR and their core@shell (Au@Ag) BM NCs was carried out for the reduction of nitrobenzene (NB) to aniline (AN) by $NaBH_4$. The time course graph (Fig. 3.8a) displayed that the reduction of NB to AN formation was increased to 53% (within 25 min) by Ag layer deposition on Au NS ($AuNS_1@Ag_{0.2}$) in comparison to monometallic Au NS (34%, within 55 min). In contrast, the yield of AN was increased to 60% (within 20 min) by $AuNR_1@Ag_{0.2}$ as compared to bare Au NR (41%, within 35 min) due to the

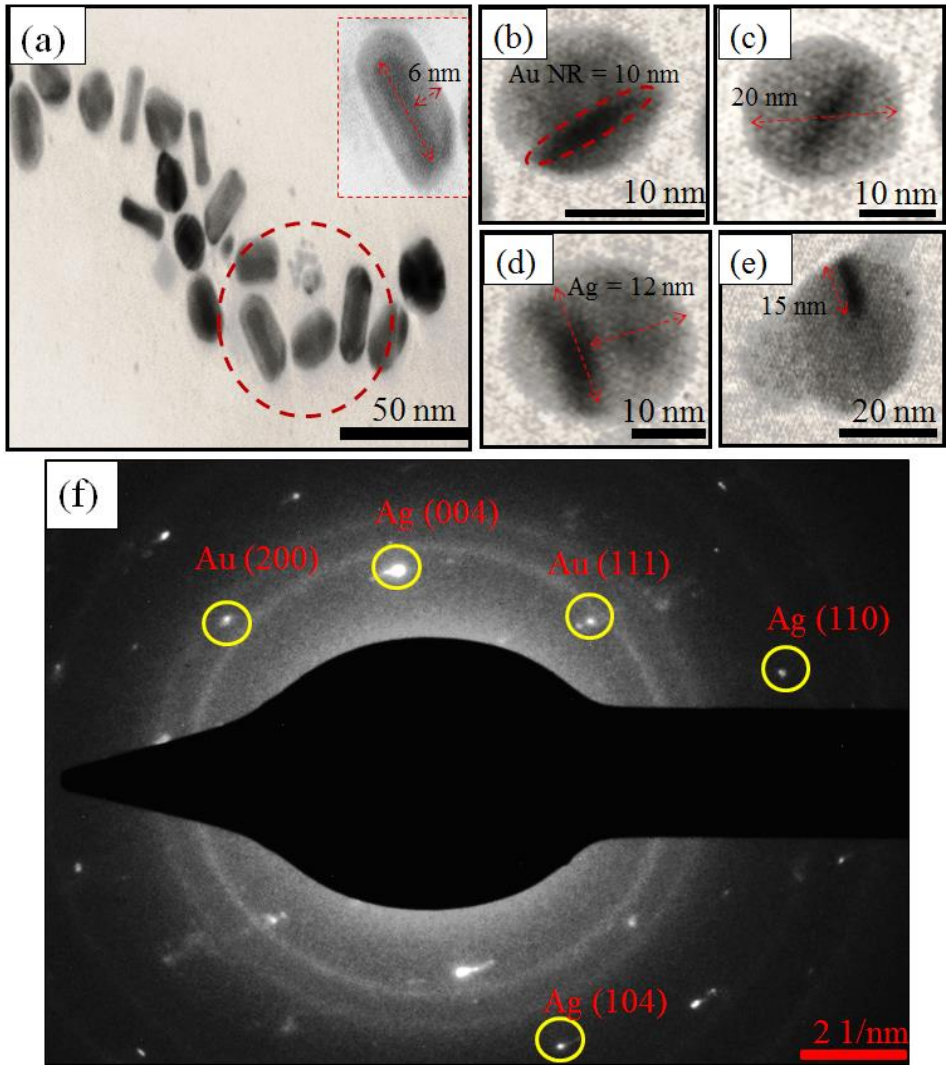

Fig. 3.7. TEM images of **(a-e)** core@shell bimetallic AuNR@Ag nanocomposites of varying Ag-shell thickness (~6-20nm), and **(f)** SAED patterns obtained from image **(a)**.

BM synergistic effect as depicted in Fig. 3.8b. However, the NB reduction significantly decreased with further growth of Ag layer over Au NPs (from 47% to 14%) as seen in Fig. 3.8. It revealed that the thickness of Ag-shell deposited on Au NPs core i.e., composition plays an important role in reduction efficiency and lengthy Au NR exhibits higher catalytic activity than spherical Au NPs.

In addition, the reduction of DNB to NA and PDA by different Au@Ag NCs of different shapes and Ag layer thickness was carried out. The absorption maximum of DNB at 241 nm was decreased after the reduction process, with the simultaneous increase in peak at 285 nm corresponding to the PDA formation (Chapter 2, Fig. 2.14). However, the HPLC quantitative analysis (Fig. 3.9) showed the formation of NA along with PDA. Fig. 3.10 displays that the

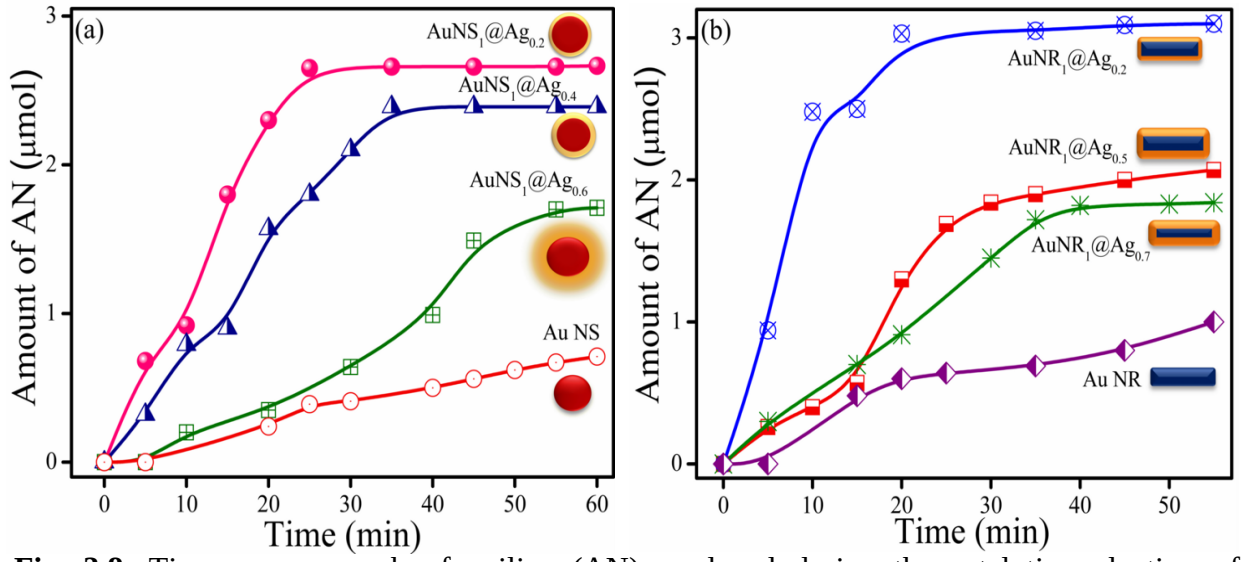

Fig. 3.8. Time course graph of aniline (AN) produced during the catalytic reduction of nitrobenzene (NB) by **(a)** bare Au nanospheres and core@shell AuNS@Ag nanocomposites, and **(b)** bare Au nanorods and core@shell AuNR@Ag nanocomposites.

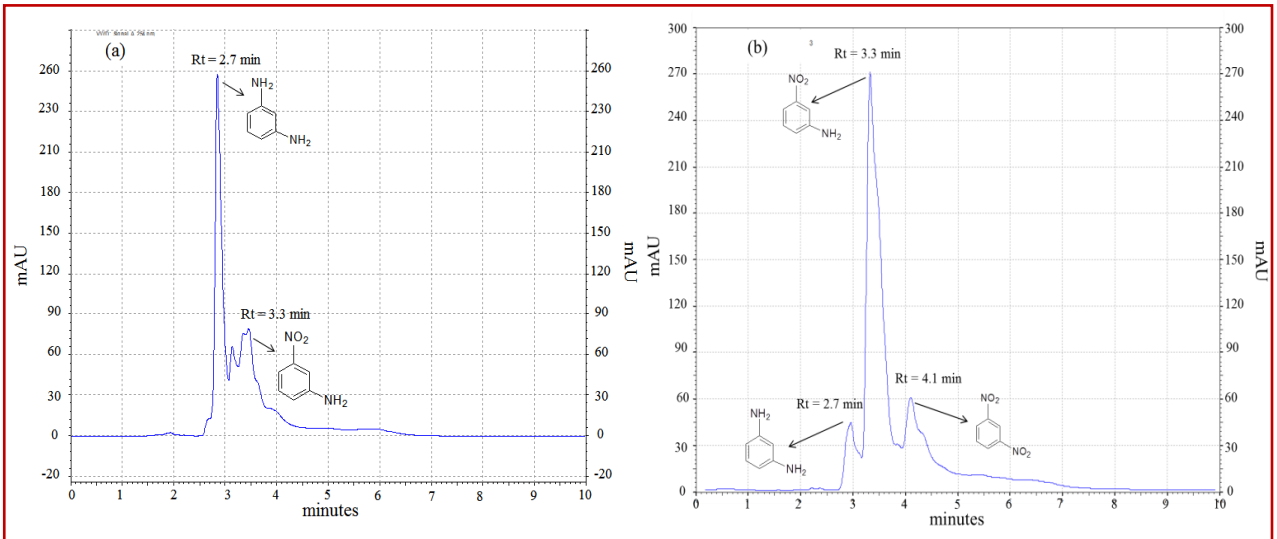

Fig. 3.9. HPLC chromatogram of reaction product obtained after reduction of 1,3-dinitrobenzene (1mM) by **(a)** $AuNS_1@Ag_{0.2}$, and **(b)** $AuNR_1@Ag_{0.2}$ nanocomposites.

distribution of DNB reduction products i.e., NA and PDA and their yield and selectivity varied as a function of the shape of the monometallic NPs core and the Ag-shell thickness on Au NS and Au NR catalysts. It revealed that the PDA was obtained as a major product having yield 76% during DNB reduction by $AuNS_1@Ag_{0.2}$ NCs catalyst relative to monometallic Au NS (45%) and Ag NS (16%), and further, PDA yield decreased to 52-48% because of increasing Ag shell layer thickness (Fig. 3.10a). However, the lengthy elongated Au NR exhibited a considerable

amount of PDA formation (64%) as compared to Au NS (45%) under the same reaction conditions as observed in Fig. 3.10b. Interestingly, when Ag layers of different thickness (3-6 nm) was deposited over the Au NR surface, the selectivity and yield of DNB reduction products significantly altered in contrast to bare Au NR and AuNS@Ag NCs. Fig. 3.10b showed that NA formation (65-74%) was always a major product obtained by AuNR@Ag NCs as compared to the PDA formation (Fig. 3.10a) by bare Au NS (45%), bare Au NR (64%) and $AuNS_1@Ag_{0.2}$ NCs (76%) as is seen in Scheme 3.1 demonstrating the essential role of synergistic effect of Au-Ag interface [3,45,46] on the catalytic activity of BM nanocatalyst.

Generally, the reduction of $–NO_2$ to $–NH_2$ occurs by the hydride ions transfer from BH_4^- to nitro-aromatic compounds adsorbed over the NCs surface [47-49], which in turns depends upon the available surface area of NCs [21,50]. Therefore, the selectivity of NA formation for the reduction of DNB by AuNR@Ag relative to PDA formation as the major product by AuNS@Ag, Au NS and Au NR could be attributed to the per-particle surface area and rate of hydride ions transfer [51,52].

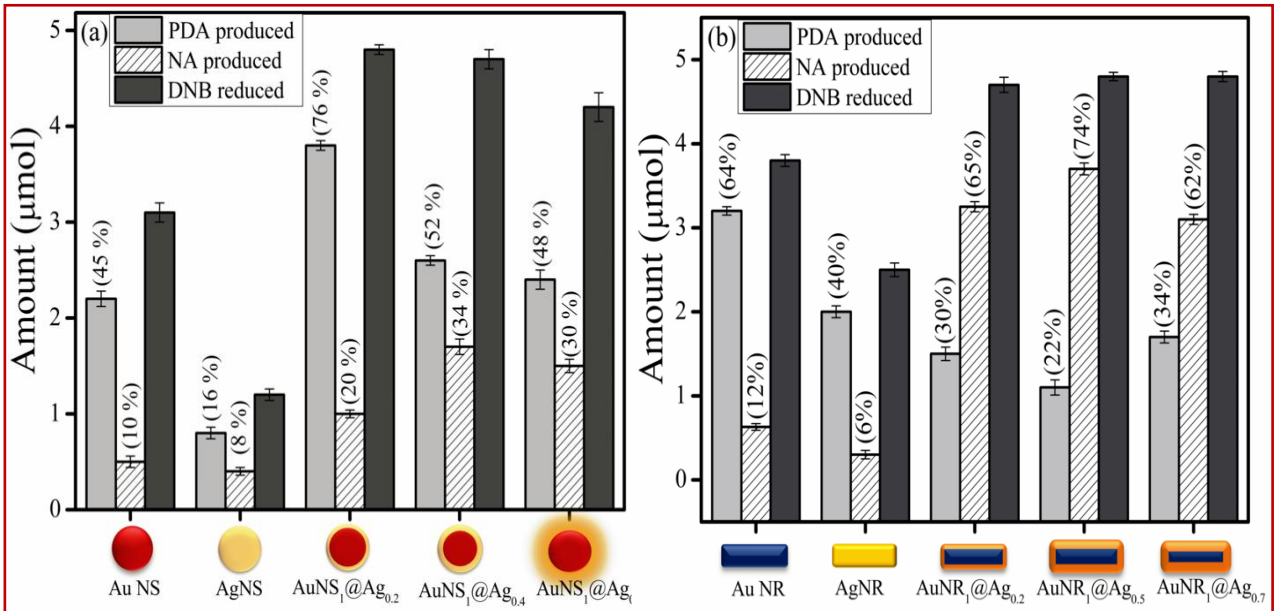

Fig. 3.10. Amount of 3-nitroaniline (NA), 1,3-phenylenediamine (PDA) produced from reduction of 1,3-dinitrobenzene (DNB) by **(a)** bare Au and Ag nanospheres and core@shell AuNS@Ag nanocomposites, and **(b)** bare Au and Ag nanorods and core@shell AuNR@Ag nanocomposites.

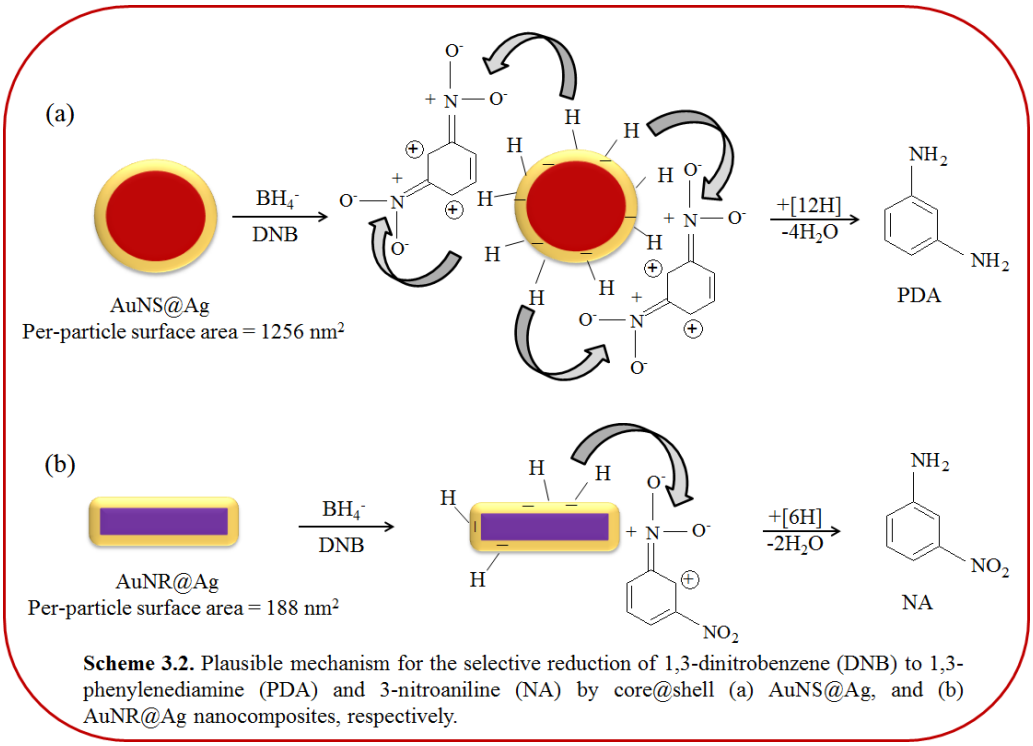

Scheme 3.2. Plausible mechanism for the selective reduction of 1,3-dinitrobenzene (DNB) to 1,3-phenylenediamine (PDA) and 3-nitroaniline (NA) by core@shell (a) AuNS@Ag, and (b) AuNR@Ag nanocomposites, respectively.

Table 3.2. Calculations for surface area of bare Au nanospheres and core@shell AuNS@Ag.

S. No.	Diameter (nm)	Radius (nm)	Surface Area of Spheres, $4\pi r^2$ (nm^2)
		Bare Au NS	
1.	8	4	200
2.	10	5	314
		AuNS@Ag	
3.	13	6.5	1149
4.	20	10	1256
5.	25	12.5	1962

Table 3.3. Calculations for surface area of bare Au nanorods and core@shell AuNR@Ag.

S. No.	Length (nm)	Width (nm)	Radius (nm)	Surface area of cylinder, $2\pi r^2+2\pi rh$, (nm^2)
		Bare Au NR		
1.	15	6	3	339
2.	23	6	3	433
		AuNR@Ag		
3.	16	3	1.5	165
4.	18.5	3	1.5	188
5.	22.2	4	2	303

The per-particle surface area [21,53] of AuNR@Ag (188 nm^2) was found to be ~6 times lower than the AuNS@Ag (1256 nm^2) and ~2 times lower than the Au NR (433 nm^2) and Au NS (314 nm^2) (calculated from TEM images, Table 3.2 and 3.3). As a result, the extent of hydride ions and DNB molecule adsorption over AuNR@Ag might be lesser than the other NCs (Scheme 3.2), which is the rate determining step [54]. Therefore, inadequate transfer of hydride ions takes place to DNB molecules over AuNR@Ag NCs leading to the partial reduction to NA formation as the major product (Scheme 3.2). The other plausible reason for the difference in selectivity of NA and PDA over AuNR@Ag and AuNS@Ag, respectively, can be ascribed to the exposed crystallographic orientation of planes (Fig. 3.5d and 3.7f) determined by the shape of the catalyst [55]. The (100)-bounded AuNS@Ag exhibited complete reduction of DNB to PDA to the maximum extent due to its more reactivity than the AuNR@Ag enclosed by (110), which gave rise to NA as the major product in agreement with the previous report [56]. The literature revealed the selectivity of NA over Pt/C [57] and PDA over Ni/SiO_2 [58,59] and Ni-Pt/C [60] at 323-393 K and 26-34 atm pressure. Saha and Ranu [61] also reported the reduction of DNB to NA catalyzed by Cu NPs, but it required high ratio of Cu NPs and excess reductant, long reaction time (8-12 h) and argon protection. However, in the present study, Au@Ag NCs of different shapes (NS and NR) exhibited a quite distinct selective response in aqueous medium, at room temperature in contrast to the catalysts used at high temperatures and high pressures. In addition, a very small amount and fixed particles of monometallic or BM NCs i.e., 6.75×10^{15} atoms were used to carry out the catalytic reduction under similar conditions, which offers the effective utilization of atoms. As a result, every single catalytic entity act as an active site that imparted more activity and selectivity [32] as compared to supported metal oxide catalysts. Thus, the desired yield and selective products could be achieved by tuning surface morphology, core@shell composition, and nature of metal-metal interface in composite systems.

However, the superior or enhanced catalytic performances of core@shell NCs (Au@Ag) than their respective monometallic Au NPs might result from the modification of the electronic structure [62] through the interaction of two kinds of metals at their interface, a phenomenon called ligand effect or synergistic effect [3]. The incorporation of atoms of second metal on the surface atoms of other metal NP result in the morphological change and formation of interface between the two metal elements. Thus, an electronic charge transfer occurs across the interface of two metals leading to net e^- density change on the surface of BM NP which promote the

reduction reaction more effectively [19,63]. Menezes et al. [4] reported the enhanced catalytic activity of Au NPs for *p*-nitrophenol reduction with the addition of Ag and similar results were also obtained by other groups due to the different work functions of two metals [64]. This interfacial interaction between the two metals decreased with further increase in the Ag layer thickness (~9-20 nm) on the Au-core of different shapes, which largely reduced the catalytic activity. The core@shell structure with optimum and thin shell layer is readily activated for catalysis [65,66] due to lower activation barrier energy. For example, Pt surface was not an electro-active surface [67] with higher Pt/Au molar ratio or in the absence of Au core for the methanol oxidation. Hence, the reduction of nitro-aromatic compounds to their respective amines enhanced almost by ~2 times using BM NCs as compared to their individual counterparts due to synergistic effect. The atomic re-hybridization between Au ($6s^1\ 4f^{14}\ 5d^{10}$) and Ag ($5s^1\ 4d^{10}$) and their close Fermi energy level (Au = -5.1 eV and Ag = -4.7 eV) might favor rapid e^- transfer at the Au-Ag interface for improved catalytic activity. Therefore, the optimization of shell-thickness and core shape for the selected product yield is highly desired for organic syntheses.

3.4 Conclusions

In summary, the effect on catalytic performances was investigated as a function of shape (nanospheres and nanorods) of BM NCs comprising Au and Ag. Interestingly, the selectivity for the formation of NA from the reduction of DNB by AuNR@Ag was obtained, in contrast to PDA by AuNS@Ag ascribed to their lower surface area, without using any toxic solvents and harsh experimental conditions. However, the catalytic performances of core@shell BM NCs dramatically decreased after a certain shell-thickness due to the reduced electronic effect among the distant core and shell. Therefore, the strong Au-Ag interfacial interaction along with geometric effects can effectively tune the yield and selectivity of the products for the reduction of nitro-organic compounds.

3.5 References

[1] N. Toshima and T. Yonezawa, *New J. Chem.*, 1998, **22**, 1179−1201.

[2] D. S. Wang and Y. D. Li, *Adv. Mater.*, 2011, **23**, 1044−1060.

[3] H. L. Jiang and Q. Xu, *J. Mater. Chem.*, 2011, **21**, 13705−13725.

[4] R. Ferrando, J. Jellinek and R. L. Johnston, *Chem. Rev.*, 2008, **108**, 845−910.

[5] F. Tao, *Chem. Soc. Rev.*, 2012, **41**, 7977−7979.

[6] C. C. Tyson, A. Bzowski, P. Kristof, M. Kuhn, R. Sammynaiken and T. K. Sham, *Phy. Rev. B*, 1992, **45**, 8924−8928.

[7] S. Nishimura, A. T. N. Dao, D. Mott, K. Ebitani and S. Maenosono, *J. Phys. Chem. C*, 2012, **116**, 4511−4516.

[8] S. Sakong, C. Mosch and A. Gross, *Phys. Chem. Chem. Phys.*, 2007, **9**, 2216−2225.

[9] M. Kaushik, M. Mandal, N. Pradhana and T. Pal, *Nano Lett.*, 2001, **1**, 319−322.

[10] Y. Sun and Y. Xia, *J. Am. Chem. Soc.*, 2004, **126**, 3892−3901.

[11] B. R. Gonzalez, A. Burrows, M. Watanabe, C. J. Kiely and L. M. L. Marzan, *J. Mater. Chem.*, 2005, **15**, 1755−1759.

[12] M. Tsuji, N. Miyamae, S. Lim, K. Kimura, X. Zhang, S. Hikino and M. Nishio, *Cryst. Growth Des.*, 2006, **6**, 1801−1807.

[13] M. Liu and P. G. Sionnest, *J. Phys. Chem. B*, 2004, **108**, 5882−5888.

[14] Y. Xiang, X. Wu, D. Liu, Z. Li, W. Chu, L. Feng, K. Zhang, W. Zhou and S. Xie, *Langmuir*, 2008, **24**, 3465−3470.

[15] M. J. Alam and M. Tsuji, *Cryst. Eng. Comm.*, 2011, **13**, 6499−6506.

[16] M. Tsuji, N. Nakamura, M. Ogino, K. Ikedo and M. Matsunaga, *Cryst. Eng. Comm.*, 2012, **14**, 7639−7647.

[17] M. P. Mallin and C. J. Murphy, *Nano Lett.*, 2002, **2**, 1235−1237.

[18] L. Rivas, S. S. Cortes, J. V. G. Ramos and G. Morcillo, *Langmuir*, 2000, **16**, 9722−9728.

[19] S. Tokonami, N. Morita, K. Takasaki and N. Toshima, *J. Phys. Chem. C*, 2010, **114**, 10336−10341.

[20] X. Zhang and Z. Su, *Adv. Mater.*, 2012, **24**, 4574−4577.

[21] S. Kundu, S. Lau and H. Liang, *J. Phys. Chem. C*, 2009, **113**, 5150−5156.

[22] J. Zeng, Q. Zhang, J. Chen and Y. Xia, *Nano Lett.*, 2010, **10**, 30−35.

[23] M. A. Mahmoud, R. Narayanan and M. A. El-sayed, *Acc. Chem. Res.*, 2013, **46**, 1795−1805.

[24] P. F. Vogt and J. J. Gerulis, *Aromatic Amines Ullmann's Encyclopedia of Industrial Chemistry, Wiley-VCH, Weinheim*, 2005, **2**.

[25] L. Yingxin, C. Jixiang and Z. Jiyan, *Chin. J. Chem. Eng.*, 2007, **15**, 63−67.

[26] P. H. Groggins, *Unit Process in Organic Synthesis, 5th ed.; McGraw-Hill: New York*, 1958.

[27] D. S. Wulfmann and C. F. Cooper, *Synthesis*, 1978, **12**, 924−925.

[28] F. C. Lizana, S. G. Quero, N. Perret and M. A. Keane, *Catal. Lett.*, 2009, **127**, 25−32.

[29] A. Corma and P. Serna, *Science*, 2006, **313**, 332−334.

[30] H. Zhu, X. Ke, X. Yang, S. Sarina and H. Liu, *Angew. Chem.*, 2010, **122**, 9851−9855.

[31] F. C. Lizanaa, S. G. Queroa, C. J. Baddeleyb and M. A. Keanea, *Appl. Cata. A: Gen.*, 2010, **387**, 155−165.

[32] E. Farnetti, R. D. Monte and J. Kaspar, *Homogeneous and Heterogeneous Catalysis, Inorganic and Bioinorganic Chemistry- Vol II, Chemical Sciences Engineering and Technology Resources, in Encyclopedia of Life Support Systems*, 2007.

[33] Q. Fu, D. G. Zhang, M. F. Yi, X. X. Wang, Y. K. Chen, P. Wang and H. Ming, *J. Opt.*, 2012, **14**, 085001.

[34] W. G. Menezes, B. Neumann, V. Zielasek, K. Thiel and M. Baumer, *Chem. Phys. Chem.*, 2013, **14**, 1577−1581.

[35] N. R. Jana, L. Gearheart and C. J. Murphy, *Langmuir*, 2001, **17**, 6782−6786.

[36] G. Kawamura, Y. Yang and M. Nogami, *J. Phys. Chem. C*, 2008, **112**, 10632−10636.

[37] Y. Ma, W. Li, E.C. Cho, Z. Li, T. Yu, J. Zeng, Z. Xie and Y. Xia, *ACS Nano*, 2010, **4**, 6725−6734.

[38] S. Pande, S. K. Ghosh, S. Praharaj, S. Panigrahi, S. Basu, S. Jana, A. Pal, T. Tsukuda and T. Pal, *J. Phys. Chem. C*, 2007, **111**, 10806−10813.

[39] M. Kahraman, O. Aydin and M. Culha, *Plasmonics*, 2009, **4**, 293−301

[40] X. Guo, Q. Zhang, Y. Sun, Q. Zhao and J. Yang, *ACS Nano*, 2012, **6**, 1165−1175.

[41] C. J. Orendorff, P. L. Hankins and C. J. Murphy, *Langmuir*, 2005, **21**, 2022−2026.

[42] A. Monga and B. Pal, *J. Clust. Sci.*, 2014, **25**, 1085−1098.

[43] S. H. Wang, C. W. Lee, A. Chiou and P. K. Wei, *J. Nanobiotechnology*, 2010, **8**, 33−45.

[44] H. F. Zarick, W. R. Erwin, J. Aufrecht, A. Coppola, B. R. Rogers, C. L. Pint and R. Bardhan, *J. Mater. Chem. A*, 2014, **2**, 7088−7098.

[45] A. Groß, *Top Catal.*, 2006, **37**, 29−39.

[46] H. C. Ham, G. S. Hwang, J. Han, S. W. Nam and T. H. Lim, *J. Phys. Chem. C*, 2010, **114**, 14922−14928.

[47] S. Praharaj, S. Nath, S. K. Ghosh, S. Kundu and T. Pal, *Langmuir*, 2004, **20**, 9889−9892.

[48] N. Pradhan, A. Pal and T. Pal, *Langmuir*, 2001, **17**, 1800−1802.

[49] S. Wunder, F. Polzer, Y. Lu, Y. Mei and M. Ballauff, *J. Phys. Chem. C*, 2010, **114**, 8814−8820.

[50] M. Haruta, *Cattech.*, 2002, **6**, 102−115.

[51] S. Panigrahi, S. Basu, S. Praharaj, S. Pande, S. Jana, A. Pal, S. K. Gosh and T. Pal, *J. Phys. Chem. C*, 2007, **111**, 4596−4605.

[52] S. C. Romero, J. P. Juste, P. Heves, L. L. Marzan and P. Mulvaney, *Langmuir*, 2010, **26**, 1271−1277.

[53] R. Kaur and B. Pal, *J. Mol. Catal. A: Chem.*, 2012, **355,** 39−43.

[54] G. Guella, B. Patton and A. Miotello, *J. Phys. Chem C*, 2007, **111,** 18744−18750.

[55] Y. Li and W. Shen, *Chem. Soc. Rev.*, 2014, **43**, 1543−1574.

[56] J. Wang, J. Gong, Y. Xiong, J. Yang, Y. Gao, Y. Liu, X. Lu and Z. Tang, *Chem. Commun.*, 2011, **47**, 6894–6896.

[57] F. Zhao, S. I. Fujita, J. Suna, Y. Ikushima and M. Arai, *Catal. Today*, 2004, **98**, 523−528.

[58] Y. X. Liu, Z. J. Wei and J. Y. Zhang, *Korean J. Chem. Eng.*, 2006, **23**, 902−907.

[59] Y. X. Liu, J. X. Chen and J. Y. Zhang, *Chin. J. Chem. Eng.*, 2007, **15**, 63−67.

[60] M. M. Telkar, J. M. Nadgeri, C. V. Rode and R. V. Chaudhari, *Appl. Catal. A: Gen.*, 2005, **295**, 23−30.

[61] A. Saha and B. C. Ranu, *J. Org. Chem.*, 2008, **73**, 6867−6870.

[62] H. R. Gong, *Mater. Chem. Phy.*, 2010, **123,** 326−330.

[63] H. Zhanga and N. Toshima, *Catal. Sci. Technol.*, 2013, **3**, 268−278.

[64] T. Endo, T. Yoshimura and K. Esumi, *J. Colloid Interface Sci.*, 2005, **286,** 602−609.

[65] H. L. Jiang, T. Akita, T. Ishida, M. Haruta and Q. Xu, *J. Am. Chem. Soc.*, 2011, **133,** 1304−1306.

[66] A. U. Nilekar, S. Alayoglu, B. Eichhorn and M. Mavrikakis, *J. Am. Chem. Soc.*, 2010, **132**, 7418−7428.

[67] H. A. Esfahani, L. Wang, Y. Nemoto and Y. Yamauchi, *Chem. Mater.*, 2010, **22**, 6310−6318.

Chapter 4

Morphological and Physicochemical Properties of Ag-Au Binary Nanocomposites Prepared by Different Surfactants Capped Ag Nanoparticles

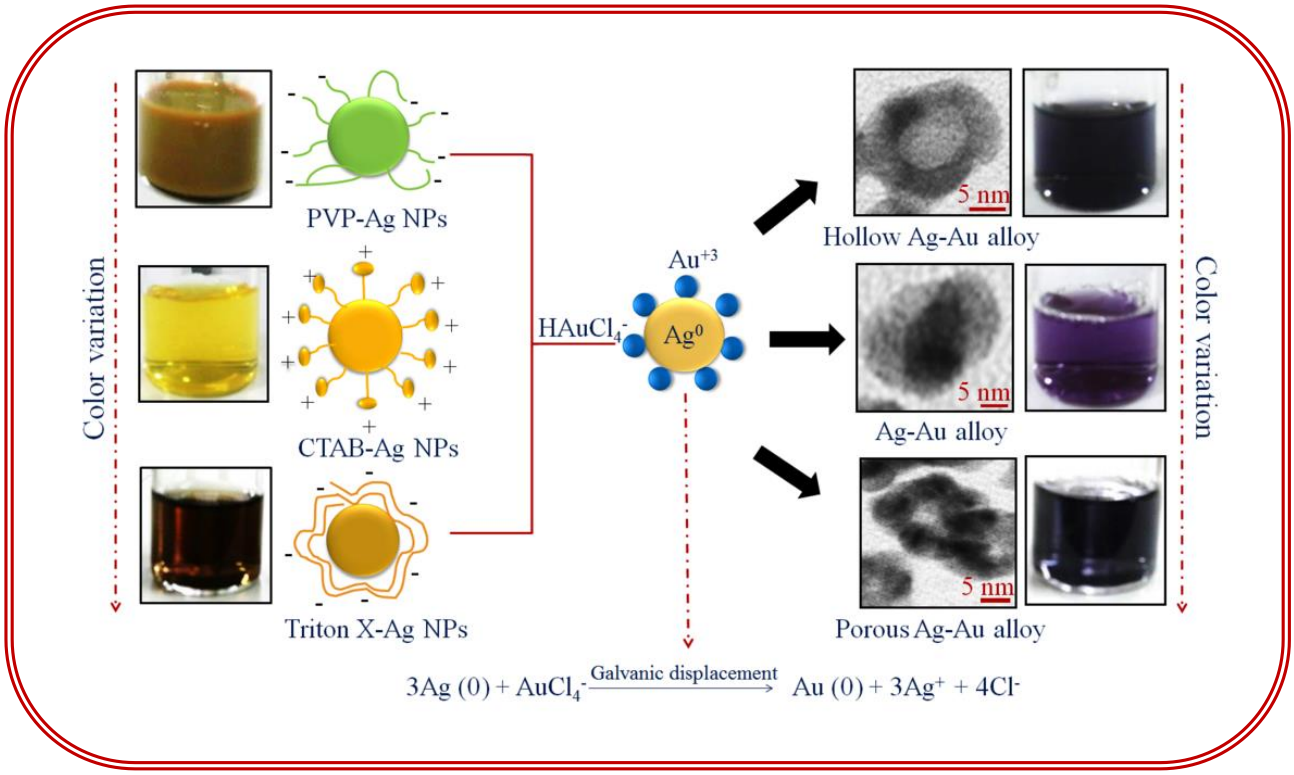

4.1 Introduction

Coinage metal (Au, Ag and Cu) nanoparticles (NPs) are of great research interest due to their fascinating optical, electronic and catalytic properties in various types of chemical transformations [1-4], such as hydrogenation of nitro-aromatic compounds, oxidation, carbon-carbon bond formation, etc. In comparison to Ag and Cu, Au NPs have been extensively studied because of their facile synthesis, homogeneity, high resistance to oxidation and tunable surface plasmon (SP) band in the visible region [5-7]. The Ag NPs also have the exceptional extinction coefficient than any metal that lead to its use as a sensing agent and for antimicrobial treatment [5,8-10]. However, monometallic Ag NPs have been found to be of limited practical use because of its severe susceptibility to oxidation [11-12], which makes the optical and catalytic results for these particles non-reproducible. An extensive number of capping agents such as polymers, ligands, dendrimers and surfactants have been used to enhance NPs suspension stability to prevent their aggregation through electrostatic repulsion, steric repulsion or both [13]. The mechanism and functional groups involved in colloid stabilization differs with the chemical structure of capping agents, which may lead to varying particle size and stability [14]. But these stabilizing agents block or hinder the true optical and catalytic properties to a certain extent.

Therefore, another helpful attempt has been employed to coat Ag NPs with a layer of Au which imparts chemical stability and protects the Ag core against oxidation due to the electron (e^-) transfer process [12,15,16] between the two metallic elements. This gives rise to the formation of bimetallic (BM) nanocomposites (NCs) which exhibit unique superior activity, high selectivity, and stability, interesting electronic, optical, chemical, and biological properties as compared to their monometallic counterparts. This can be attributed to [17-21], (i) the electronic effect, in which the electronic charge transfer takes place between the interface of two metal elements leading to a change in the e^- density on the resultant BM structures; (ii) synergistic effect, in which the new property arises due to the interaction between two metals. For example, the reduction of *p*-nitrophenol to *p*-aminophenol by $NaBH_4$ was found [22] to be higher with core@shell Au@Ag NCs due to the synergistic effect than the bare Au and Ag nanospheres as depicted by their rate constants. The colloidal Ag NPs are known to serve as a versatile substrate or sacrificial templates for the material deposition (Au) or displacement reactions, respectively, leading to the formation of core@shell Ag@Au [21,23-25], hollow [26-29], cage-like [30,31], porous [32] or alloyed [33] nanostructures. These different morphologies play an important role

in catalysis where the hollow/porous NPs exhibit superior catalytic activities than their solid counterparts. For example, Xia et al. demonstrated that the Au nanocages and nanoboxes are better catalysts than the solid Au NPs for a redox reaction [31]. The previous studies [30-32] showed that the replacement reaction between silver nanostructures and an aqueous $HAuCl_4$ solution can be used as a versatile method for generating metal nanostructures with hollow interiors. However, the role of capping agents, polymers, or surfactants adsorbing the Ag NPs (core) surface during these transformation reactions remain unexplored, as the coating of the shell-metal is a surface-driven charge transfer process. Therefore, the chemical species bound to the Ag NPs surface might alter the deposition rate of incoming metal, mechanism, and subsequently alloy formation. In the present study, we investigated the adsorbed surfactants on the Ag NPs surface, used during their synthesis can play a key role in the galvanic deposition mechanism. This chemical strategy allows controlling the morphological transformation of solid Ag NPs via the surface modification and presents the opportunity for the systematic study of optical, electro-kinetic parameters and catalytic properties of BM NCs.

4.2 Experimental

4.2.1 Materials

Chloroauric acid ($HAuCl_4.3H_2O$), ascorbic acid ($C_6H_8O_6$), sodium hydroxide (NaOH), polyvinylpyrrolidone (PVP, $(C_6H_9NO)_n$), dimethyl formamide (DMF, C_3H_7NO), nitrobenzene ($C_6H_5NO_2$), 3-nitrotoluene ($C_7H_7NO_2$) and 1-chloro-3-nitrobenzene ($C_6H_4ClNO_2$) were obtained from Loba Chemie, India. Sodium borohydride ($NaBH_4$), trisodium citrate ($Na_3C_6H_5O_7$), Silver nitrate ($AgNO_3$), cetyltrimethylammoniumbromide (CTAB, $C_{19}H_{42}BrN$) and Triton X-100 (TX, $C_{14}H_{22}O(C_2H_4O)_n$) were purchased from Rankem, SDFCL, Fischer Scientific, Sigma Aldrich and Merck, India, respectively. All the chemicals were used as-received without any further purification. Deionized water was obtained using an ultra-filtration system (Milli-Q, Millipore) with a measured conductivity above 35 mho cm^{-1} at 25 ˚C.

4.2.2 Preparation of Ag Nanoparticles using Different Surfactants

The Ag NPs modified with different capping agents were prepared by using various surfactants viz., cetyltrimethylammoniumbromide (CTAB), Triton X-100 (TX) and polyvinylpyrrolidone (PVP). An aqueous solution (10 mL) containing $AgNO_3$ (0.25 mM)

and trisodium citrate (0.25 mM) followed by reduction with $NaBH_4$ (0.6 mL, 0.01 M) gave rise to the formation of Ag seeds [34,35]. This seed solution (ca. 0.0125 mL) was introduced at room temperature into the mixture of $AgNO_3$ (1 mL, 0.01 M), CTAB (10 mL, 80 mM), ascorbic acid (0.5 mL, 0.1 M) and NaOH (0.2 mL, 1M) resulting in the formation of CTAB-capped Ag NPs (CTAB-Ag NPs). The TX capped Ag NPs (TX-Ag NPs) was prepared by the addition of above prepared seed solution (ca. 0.25 mL) at room temperature to the aqueous mixture containing TX (25 mL, 0.015 M), $AgNO_3$ (1 mL, 0.01 M) and ascorbic acid (0.5 mL, 0.1 M) giving rise to brown color. On the other hand, the Ag NPs employing PVP (PVP-Ag NPs) were prepared through one-step seedless, solvo-thermal reduction route [36,37], by refluxing $AgNO_3$ (0.0017 g) and PVP (42 mM) in DMF (20 mL) at 120 ˚C for 30 min in a round bottom flask yielding muddy-green color.

4.2.3 Preparation of Ag-Au Bimetallic Nanocomposites

The Ag-Au BM NCs were prepared by taking pre-synthesized Ag NPs coated with different surfactants (as demonstrated above). Each set of Ag NPs (0.8 mL) diluted with deionized water (4 mL) was treated with different amount of $AuCl_4^-$ aqueous solution (15-35 µL, 0.01 M) for its deposition on the surface of Ag NPs. This resulted in the formation of Ag-Au NCs of different color depending on the amount of Au^{3+} ions added [38,39]. The prepared BM NCs were then washed with distilled water by centrifugation (8000 rpm for 5 min) and re-dispersed in deionized water.

4.2.4 Characterization

The optical properties of various Ag-Au BM NCs were analyzed by UV-Vis spectrophotometer (Analytik Jena Specord-205) and spectrofluorometer (Perkin-Elmer LS55) using xenon lamp as an excitation source. Transmission electron microscope (TEM) photographs and selected area diffraction pattern (SAED) were taken on the Hitachi 7500 model with resolution 2˚A operating at voltage 120 kV. The hydrodynamic size distribution of different NCs dispersed in water was determined by using Brookhaven 90 plus Particle Size Analyzer at 25 ˚C. The zeta potential (ζ) was studied by taking 1.5 mL of NCs solution in a cuvette consisting of the palladium electrode mounted on a machined support using Brookhaven zeta plus at 25 ˚C.

4.2.5 Catalytic activity

The catalytic activity of various Ag-Au NCs relative to monometallic Ag NPs was evaluated for the reduction of (5 mL, 0.2 mM) nitrobenzene (NB), 3-nitrotoluene (NT) and 1-chloro-3-nitrobenzene (CNB) containing ice-cold $NaBH_4$ solution (100 µL, 0.01 M) and calculated amounts of different NCs (5.99×10^{16} atoms) under similar conditions. The reaction samples were analyzed by UV-Vis spectrophotometer ($\lambda_{max.}$ of NB ~270 nm, NT ~272 nm and CNB ~265 nm) and the products were further quantified by HPLC.

4.3 Results and Discussions

4.3.1 Optical Properties

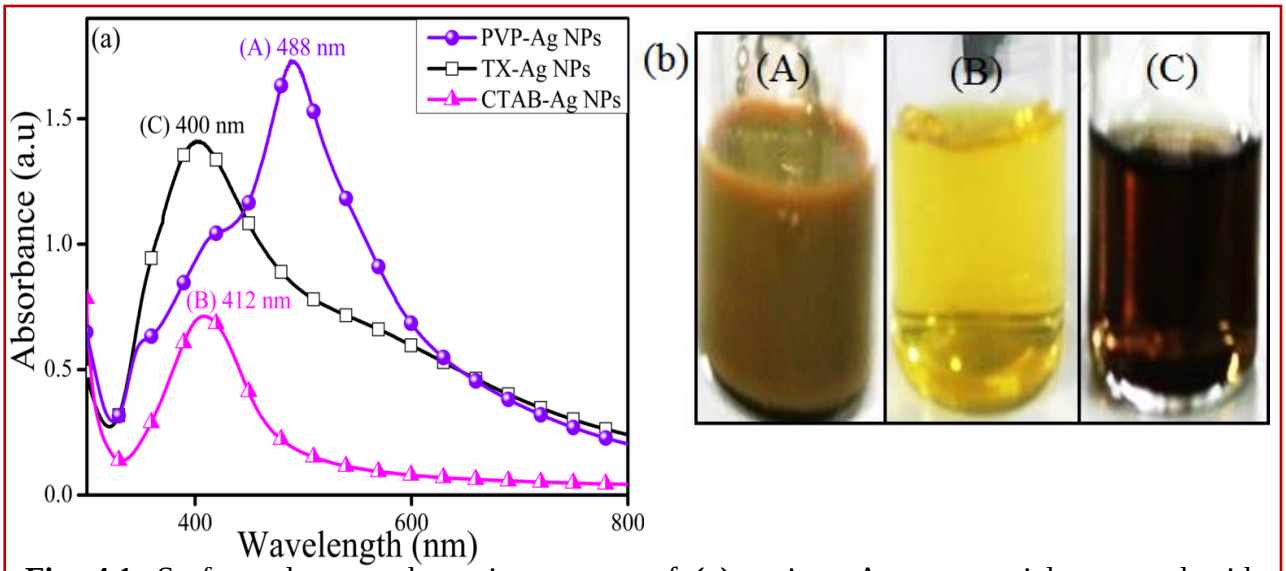

Fig. 4.1. Surface plasmon absorption spectra of **(a)** various Ag nanoparticles capped with different surfactants, and **(b)** their corresponding colors.

The absorption studies revealed an intense surface plasmon (SP) band at maximum wavelength, 488 nm and a sharp SP band at 412 nm (Fig. 4.1a) corresponding to PVP-Ag NPs and CTAB-Ag NPs, respectively. On the other hand, TX-Ag NPs showed a blue-shifted and broader absorption peak at 400 nm as depicted in Fig. 4.1a. This suggested the formation of different sizes of Ag NPs of spherical shape as the plasmon frequencies are highly dependent on the morphology of NPs [40] and as a result, the Ag NPs capped with various surfactants exhibited different colors as seen in Fig. 4.1b. The optical properties of Ag NPs can be facilely adjusted by adding Au^{3+} ions of varying amounts (15-35 µL, 0.01 M) and the atomic ratio for their deposition on the surface of Ag NPs is calculated to be 0.2-0.4 (Table 4.1). Fig. 4.2a shows that the SP band intensity of PVP-Ag NPs (488 nm) gradually decreased and became broader with a peak position red-shifted

to, 500 nm and 592 nm, through the addition of aqueous solution of $HAuCl_4^-$ ion (15-25 µL), which further broadened and decreased by an increased amount of Au^{3+} ions (35 µL). These observations are consistent with the report [35] where the hollow Ag-Au NCs were obtained via replacement of Ag by Au. In the progressive galvanic replacement reaction, Au is deposited on the NPs surface with the Ag consumption from the core and it gave rise to the formation of hollow particles resulting in a red-shift [41] in the SP band of hollow Ag-Au NCs. This morphological change was further supported by the color change from green to red to light purple and blue as shown in Fig. 4.2b.

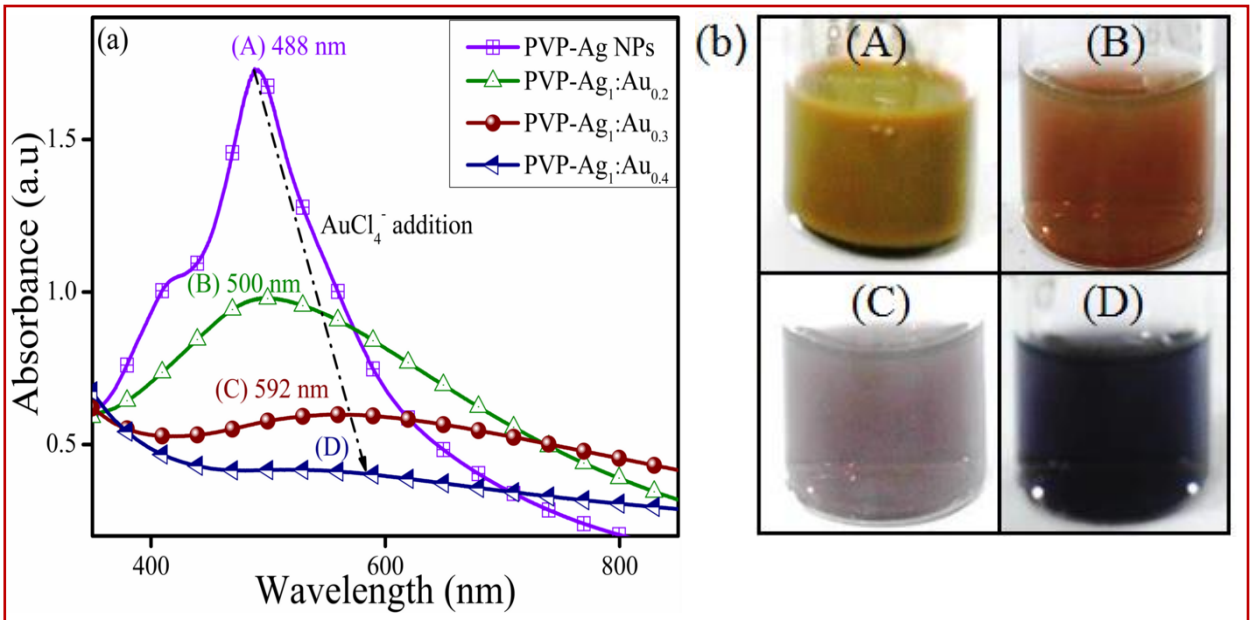

Fig. 4.2. Effect of different amounts of $HAuCl_4.3H_2O$ (15-35 µL, 0.01 M) deposition onto PVP-Ag nanoparticles for the **(a)** variation in the surface plasmon band, and **(b)** their respective color changes.

The SP band of CTAB-Ag NPs (412 nm) red-shifted to a broad peak at 546 nm of decreased intensity upon addition of Au^{3+} ions (15 µL) accompanied by the color change from yellow to light blue (Fig. 4.3a,b). However, with the higher addition of Au^{3+} ions (25-35 µL), the intensity of absorption band corresponding to 565 nm increased, exhibiting a purple color solution. In case of the TX-Ag NPs, the characteristic SP band at 400 nm red-shifted in the range of 411 nm to 500 nm (Fig. 4.3c) of almost the same intensity after Au^{3+} deposition (15-35 µL) along with a notable color change as shown in Fig. 4.3d. The red shifting in absorption peaks of Ag NPs with comparatively higher intensity and the color change from yellow/brown to light blue and finally to intense blue during the reaction process indicated the composition change of

CTAB-Ag NPs or TX-Ag NPs from Ag to Au rich. These SP band variations in CTAB-Ag NPs and TX-Ag NPs were not similar to the observations in PVP-Ag NPs suggesting probably the formation of solid Ag-Au in the alloy structure form rather than the hollow interiors.

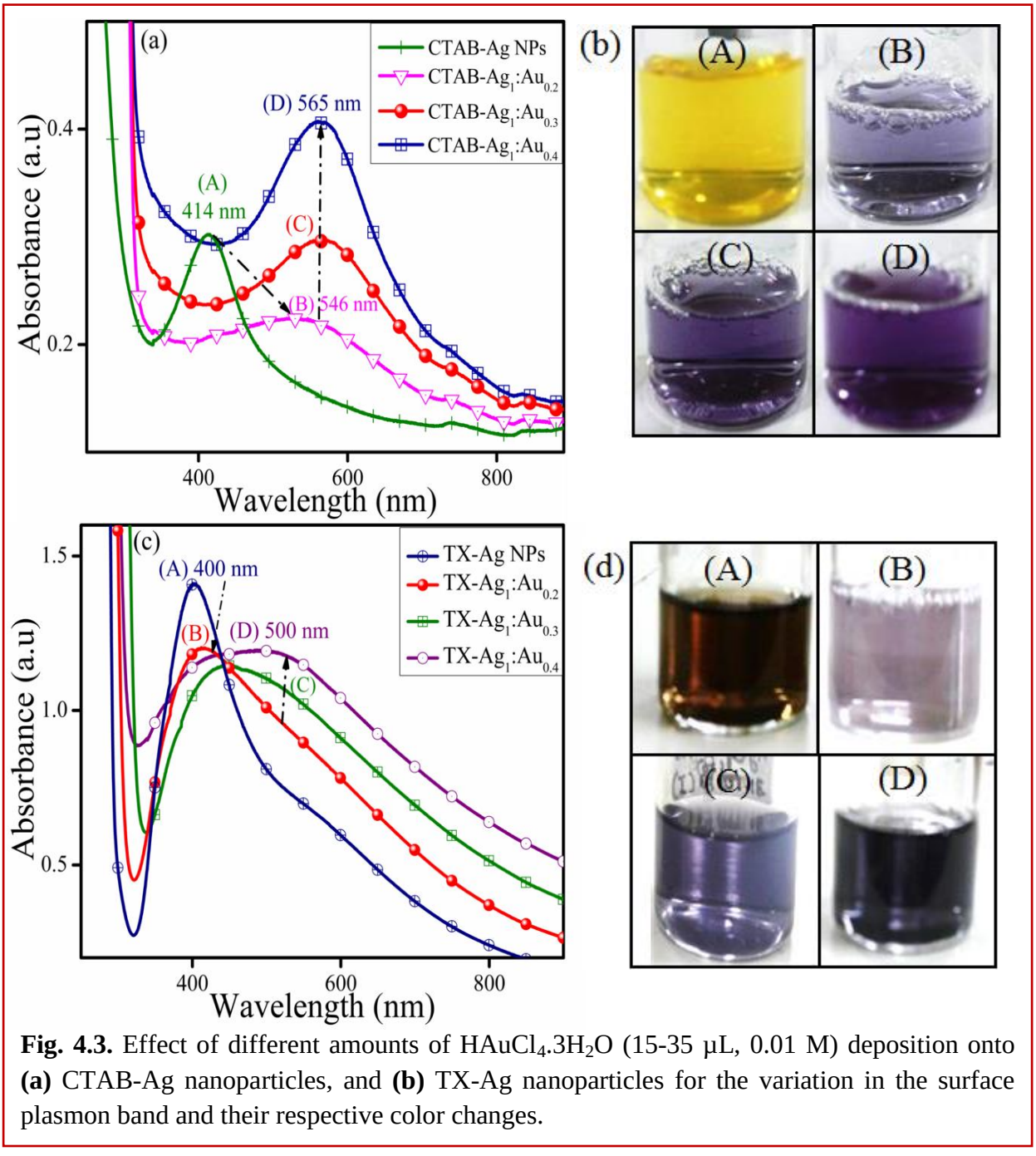

Fig. 4.3. Effect of different amounts of $HAuCl_4.3H_2O$ (15-35 µL, 0.01 M) deposition onto **(a)** CTAB-Ag nanoparticles, and **(b)** TX-Ag nanoparticles for the variation in the surface plasmon band and their respective color changes.

Table 4.1. Calculations for the amount of Ag and Au atoms in Ag-Au bimetallic nanocomposites.

Elements	Amount of element (mg)	No. of atoms (atoms)	Atomic ratio (Ag:Au)
Ag NPs (800 µL)	0.0427	2.4×10^{17}	1:0
Au^{+3} (0.01 M, 15 µL)	0.0147	0.45×10^{17}	1:0.2
Au^{+3} (0.01 M, 25 µL)	0.0246	0.75×10^{17}	1:0.3
Au^{+3} (0.01 M, 35 µL)	0.0344	1.05×10^{17}	1:0.4

4.3.2 Electro-kinetic Parameters

The observed red-shifts in the SP bands as noted in Fig. 4.2-4.3 is attributed to, (i) the changing dielectric function and composition of resulting alloy, and (ii) an increase in NCs size due to the deposition of Au on the Ag NPs surface [42] which can be measured by dynamic light scattering (DLS) particle size distribution. It showed that the average hydrodynamic diameter of PVP-Ag NPs (27 nm) displayed a gradual increase in particle diameter from 34 to 69 nm (Fig. 4.4a) after the deposition of Au on the surface of Ag NPs. Similarly, the hydrodynamic diameter of CTAB-Ag NPs (24 nm) and TX-Ag NPs (20 nm) subsequently increased to 32-58 nm with progressive addition of Au^{3+} ions (15-35 µL) signifying the coating of Au on Ag NPs (Fig. 4.4b, 4.4c). In addition, the zeta potential measurements specified that the as-synthesized PVP-Ag NPs (-3.5 mV), CTAB-Ag NPs (+33.02 mV) and TX-Ag NPs (-12.4 mV), were negatively and positively charged confirming the presence of a weakly adsorbed layer of PVP (-6.59 mV), CTAB (+33.45 mV) and TX-100 (-7.6 mV) capping agents, respectively, on their surfaces. However, the deposition of Au^{3+} ions on PVP-Ag NPs led to the increase in magnitude of negative surface charge (-5.6 to -11.9 mV) as shown in Fig. 4.4d. This charge alteration was probably due to the e^- charge donation from Ag with low ionization potential (7.58 eV) to Au with high ionization potential (9.22 eV) [12,43,44] resulting in accumulation of negative surface charge which was evidenced by XPS measurements and density functional theory in the previous report [12]. Similarly, the net effective charge of BM Ag-Au NCs arising from CTAB-Ag NPs and TX-Ag NPs were also measured to be negative (Fig. 4.4e,f) as explained above.

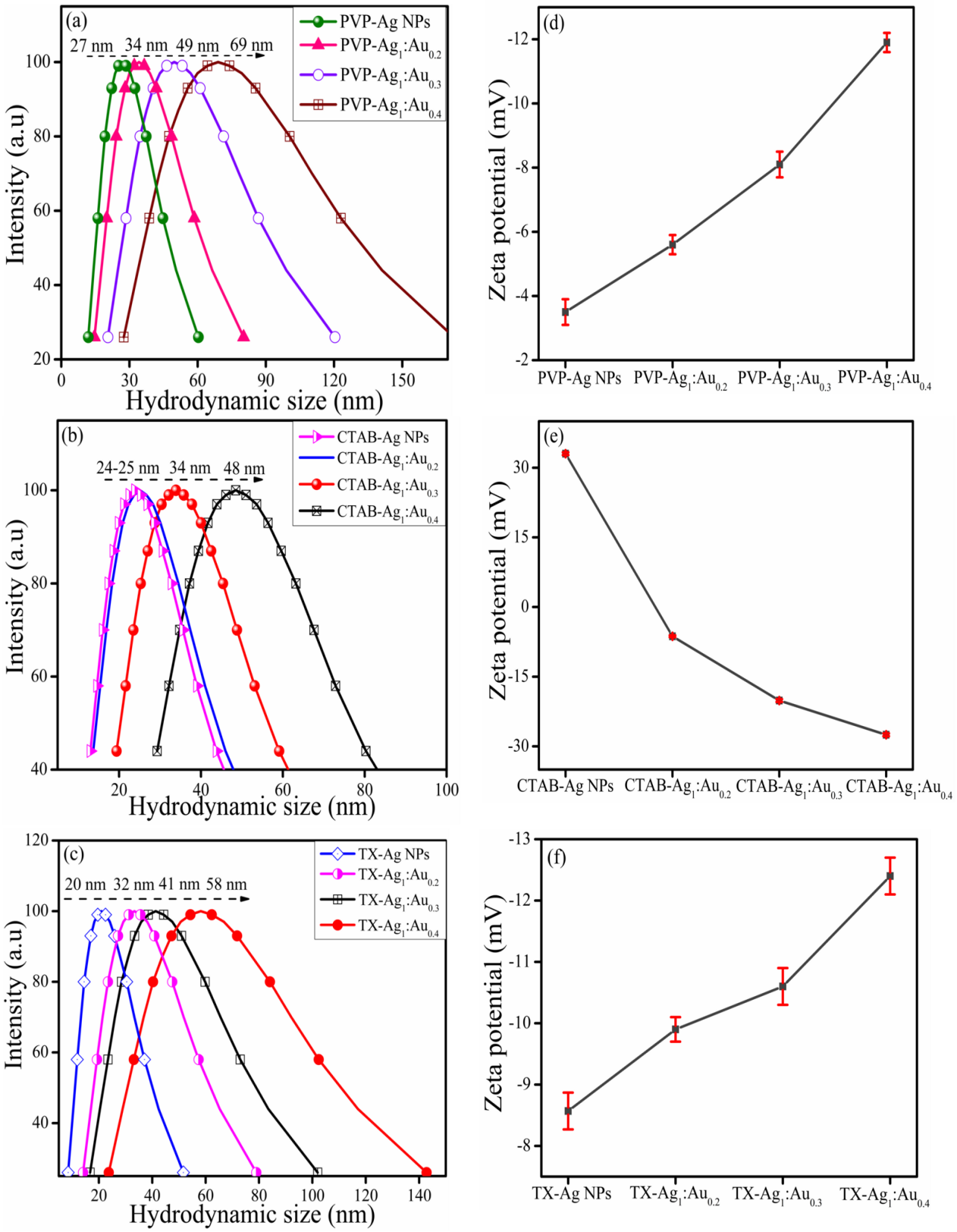

Fig. 4.4. (a-c) DLS particle size distribution and **(d-f)** Zeta potential of different Ag nanoparticles after deposition of $HAuCl_4.3H_2O$ of different amounts (15-35 µL, 0.01 M) onto its surface.

4.3.3 Fluorescence Properties

The change in the photoluminescent behavior of Ag NPs after Au coating on its surface was studied by measuring their fluorescence emission spectra (Fig. 4.5). The emission maximum of PVP-Ag NPs was observed at 305 nm and 600 nm on excitation at 225 nm. The strong emission band at 305 nm can probably be assigned to the Ag-Ag interactions, as reported by other authors [45,46]. However, the weak emission band at 600 nm might be due to the radiationless recombination of the charge species at the surface defect sites. On the addition of Au^{3+} to the surface of PVP-Ag NPs, the fluorescence intensity of pure Ag metal was considerably reduced due to the quenching by Au with an increase in its concentration (Fig. 4.8), which was similar to an observation made in the earlier report [47]. This effect was due to the blocking of superficial surface traps of the Ag NPs by the thick Au layer formation which strongly evidenced the change in morphology resulting from surface capping of Ag NPs by Au.

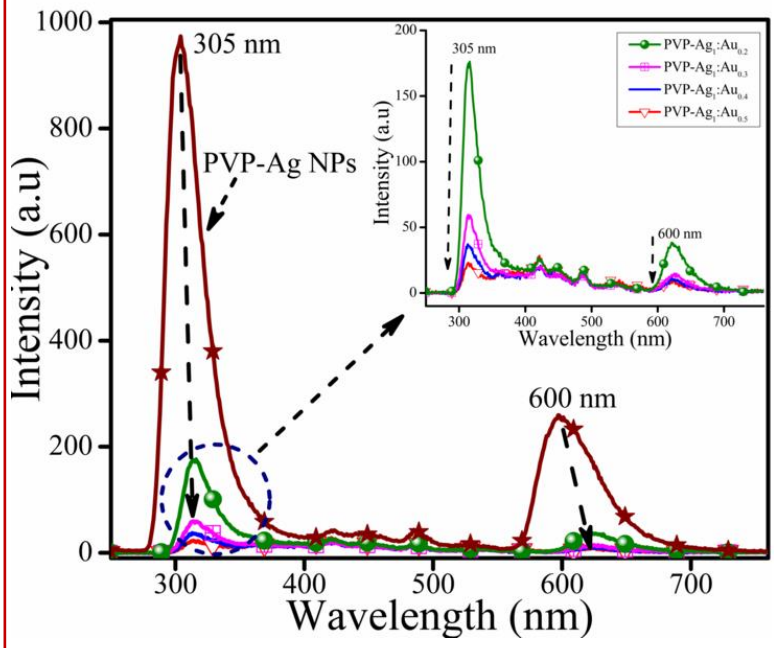

Fig. 4.5. Influence of different amounts (15-35 µL, 0.01 M) of $HAuCl_4.3H_2O$ deposition on the emission spectra of PVP-Ag nanoparticles (λ_{max} = 225 nm).

4.3.4 Morphological Studies

Using the PVP-Ag NPs (~10-11 nm) as the reaction template, the galvanic replacement with Au resulted in the formation of hollow Ag-Au shell (~15 nm) as shown in Fig. 4.6. With the incoming Au^{3+} ions, the Ag NPs were oxidized into Ag^{+} ions due to the higher reduction potential of Au^{3+}/Au (0.99 V) than Ag^{+}/Ag (0.80 V) [48,49]. As a result, a galvanically reduced layer of Au atoms was formed on the surface of Ag NPs, while oxidized Ag^{+} ions diffused out continuously across the boundaries of the Au-shell during the reaction giving rise to hollow Ag-Au shells with cavity size ~8 nm (Fig. 4.6b).

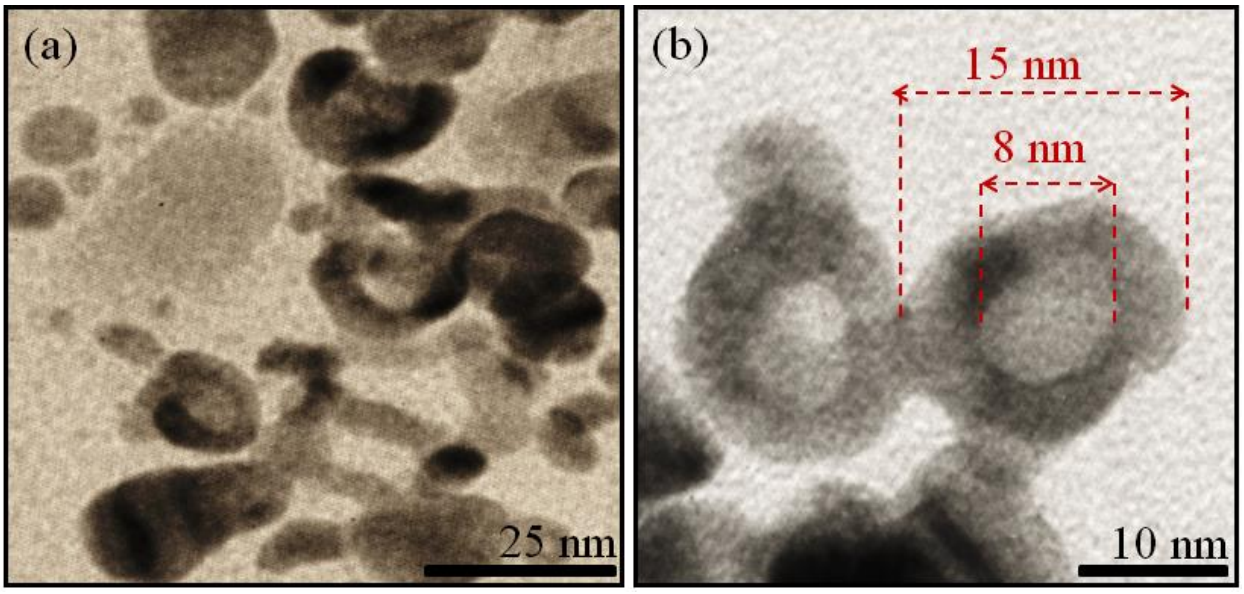

Fig. 4.6. TEM images of Au deposited PVP-Ag nanoparticles

On the other hand, CTAB-Ag NPs used as a seed for the deposition of Au furnished mixed solid Ag-Au alloy morphology of size ~20-25 nm rather than hollow shells. Due to the similar lattice constant (2.35 Å for Au and 2.36 Å for Ag), the two metal elements are miscible in all proportions [50,51] and thus, facilitated the alloy formation (Fig. 4.7). In this context, the TEM images clearly show the dense and light particles corresponding to Au and Ag nanoparticles, respectively, fashioned in non-uniform or irregular manner.

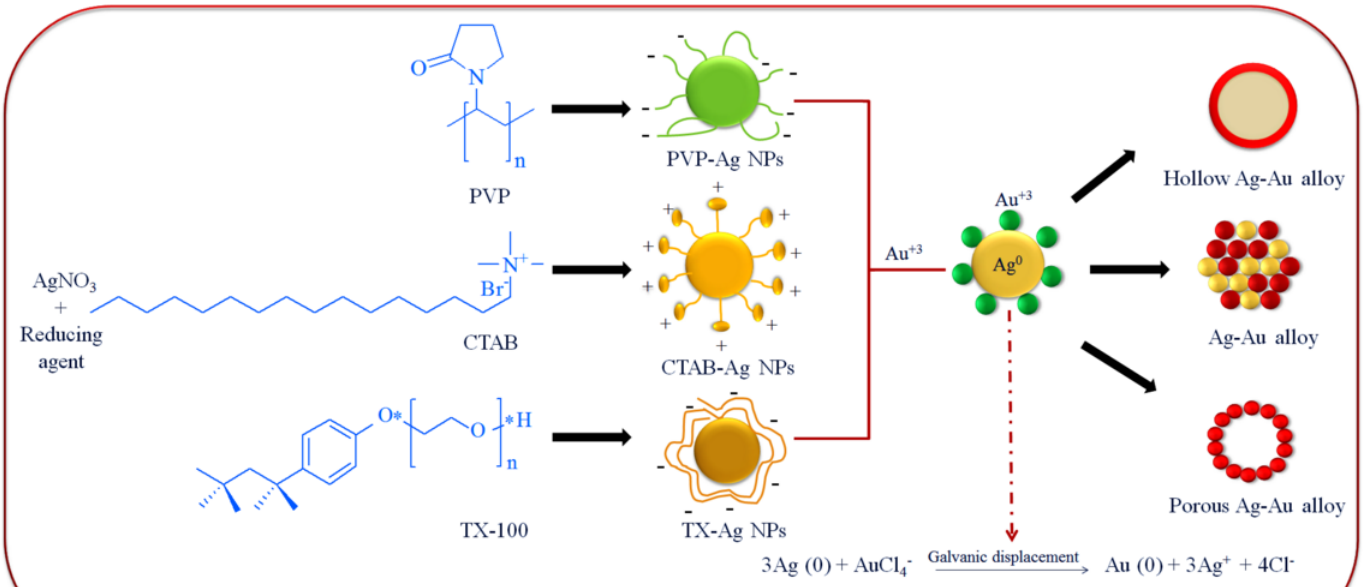

Scheme 4.1. Schematic representation showing the effect of different surfactants capping Ag nanoparticles for the formation Ag-Au bimetallic nanocomposites.

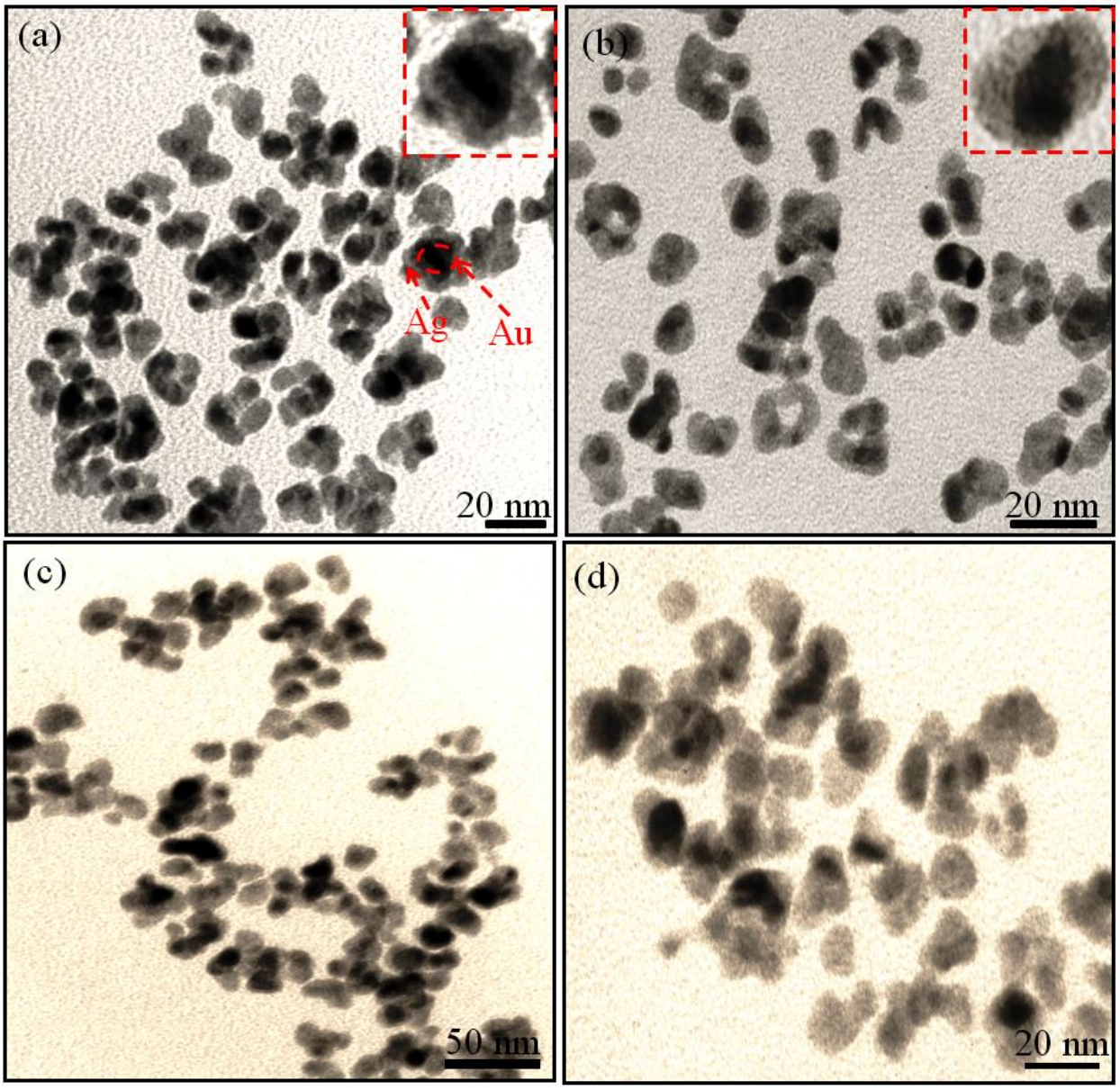

Fig. 4.7. TEM images of Au deposited CTAB-Ag nanoparticles.

In contrast, the porous-hollow aggregates of Ag-Au nanostructures were evolved after the reaction between Au^{3+} and TX-Ag NPs. The resulting NCs appeared to be composed of a number of smaller metal NPs that are interconnected to form a porous and hollow morphology (size = ~16-22 nm) as seen in Fig. 4.8. As a result of the displacement reaction, the Au atoms underwent nucleation on the surface of Ag NPs along with the formation of the hole due to the consumption of Ag [32]. This continues until the whole Ag NPs template is etched with $AuCl_4^-$ and subsequently developed into larger BM lobes (Fig. 4.8a,b). In addition, the SAED pattern of

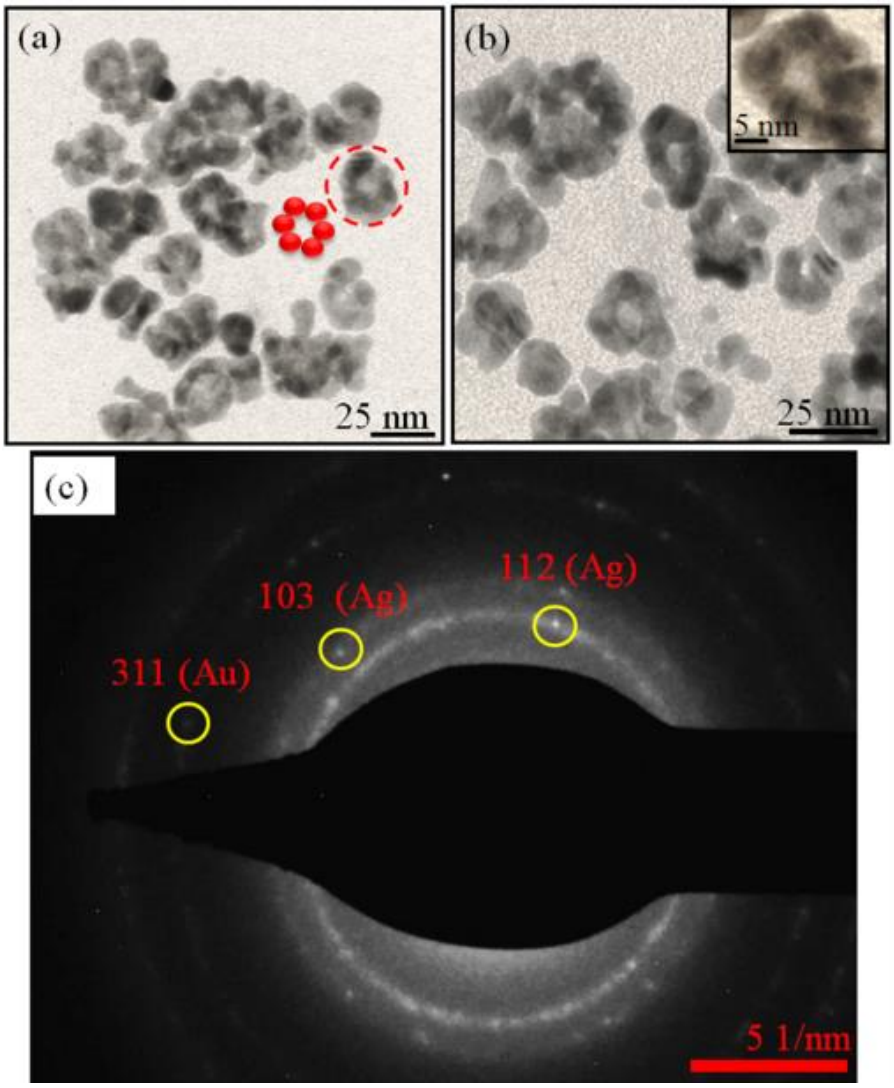

Fig. 4.8. (a-b) TEM images of Au deposited TX-Ag nanoparticles, and **(c)** SAED pattern obtained from image **(b)**.

porous-hollow Ag-Au aggregates showed the presence of both Au and Ag corresponding to the planes (311) and (103), respectively, as depicted in Fig. 4.8c.

Therefore, the diverse morphologies of BM NPs were obtained using Ag NPs absorbed with various surfactants of different chemical nature to template the galvanic reaction as evidenced by UV-Vis absorption studies and TEM images. This can be attributed to the difference in reaction rates between the Au^{3+} ions and the surfactants passivizing the Ag NPs surface and hence, altering the galvanic Au deposition rate. The strong electrostatic interaction between the PVP/ TX-Ag NPs and the incoming Au^{3+} ions promotes faster Au deposition and

thereby displacing the Ag atoms from its core, which resulted in the formation of hollow spaces in contrast to CTAB-Ag NPs as seen in Scheme 4.1.

4.3.5 Catalytic Activity

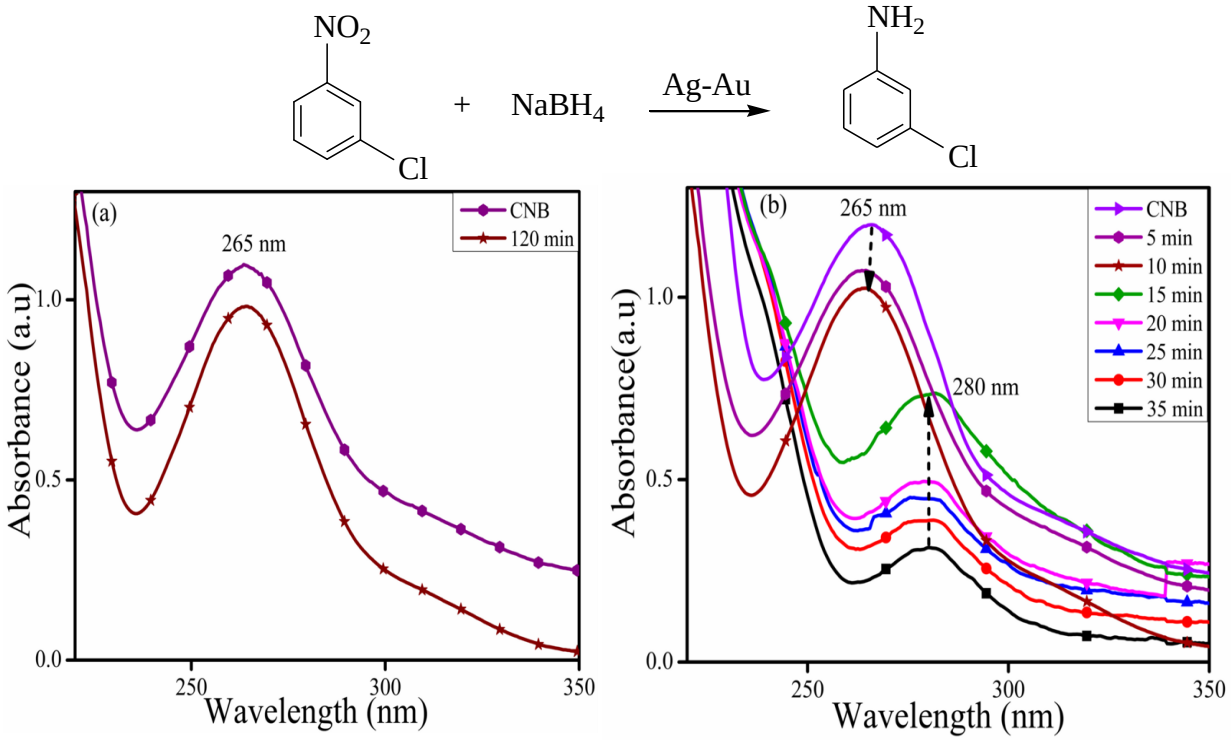

Fig. 4.9. Changes in absorption spectra of 1-chloro-3-nitrobenzene reduction by $NaBH_4$ **(a)** in the absence of nanoparticles, and **(b)** in the presence of Ag nanoparticles.

The comparative catalytic activity of Ag NPs as well as Ag-Au BM NCs was investigated for the reduction of 1-chloro-3-nitrobenzene (CNB) to 1-chloro-3-aminobenzene (CAB) by $NaBH_4$ as shown in the scheme of Fig. 4.9. The absorption spectra for the reduction of CNB (265 nm) by $NaBH_4$ exhibited insignificant changes in the absence of Ag NPs up to 120 min (Fig. 4.9a). However, with the addition of Ag NPs, the reaction rate was accelerated and the absorption band intensity corresponding to CNB at 265 nm was gradually reduced and a new absorption band evolved at 280 nm for the formation of the CAB (Fig. 4.9b). The time course studies (Fig. 4.10a) displayed that the PVP-Ag_1:$Au_{0.2}$ NCs exhibited the higher reduction of CNB, (CNB left = ~37%) with higher yield of CAB (71%) within 60 min as compared to monometallic PVP-Ag NPs (63%, within 70 min) as depicted in Fig. 4.10b. With the growing atomic ratio of Au (0.3 to 0.4) on PVP-Ag NPs, the progressive increase in CAB yield (83-93%) within 50-55 min was observed in Fig. 4.10b. This is due to the fact that the increasing percentages of Au atoms have a

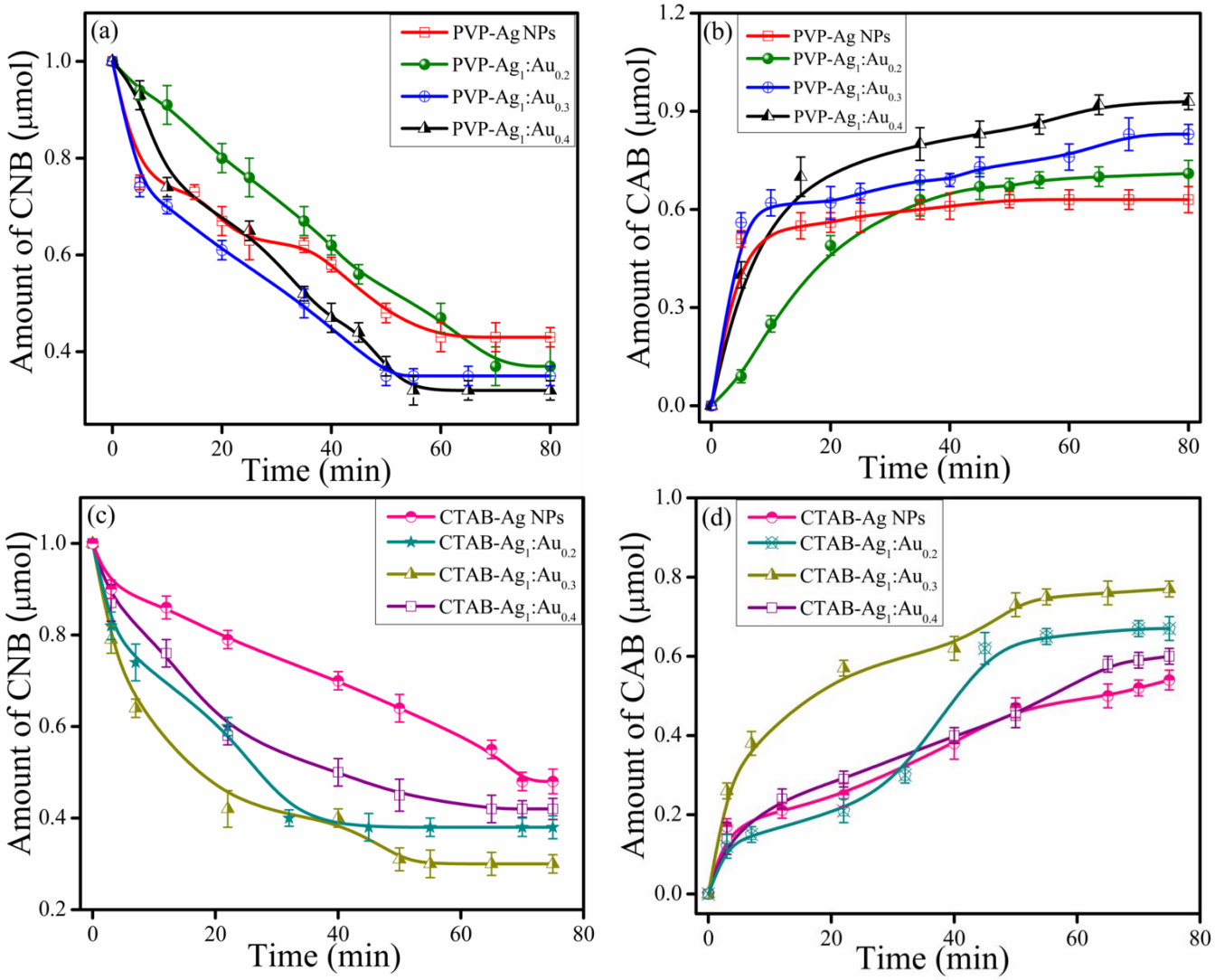

Fig. 4.10. Time course graph for the catalytic reduction of 1-chloro-3-nitrobenzene to 1-chloro-3-aminobenzene by mono and bimetallic of **(a-b)** PVP-Ag nanoparticles, and **(c-d)** CTAB-Ag nanoparticles.

critical effect on the morphology of Ag NPs which resulted in the formation of hollow Ag-Au BM NCs dictating major influence on the catalytic activity. The hollow Ag-Au alloy could possess larger surface areas, reduced densities and may provide more bonding sites for the chemical reaction exhibiting higher catalytic performances [52-54]. From Fig. 4.10c-d, the CTAB capped Ag_1-$Au_{0.3}$ alloy BM NCs showed higher yields (77%, 45 min) for the CAB formation as compared to bare CTAB-Ag NPs (54%, 75 min). The superior catalytic activity can be related to the Ag/Au interface undergoing electronic effect, where Ag has a lower work function than Au [55].

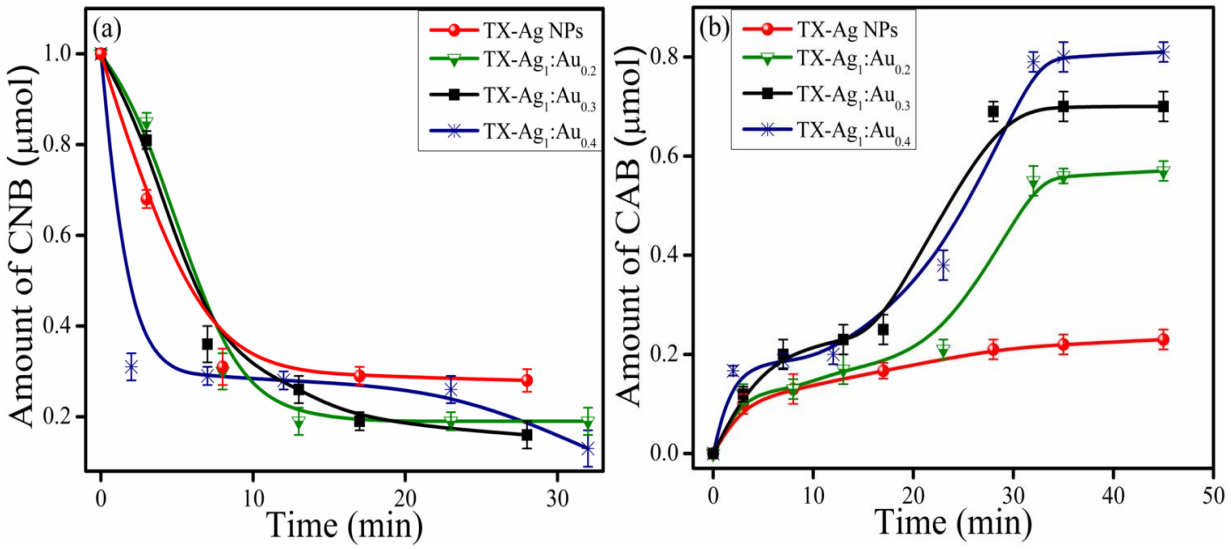

Fig. 4.11. Time course graph showing catalytic activity for the reduction of 1-chloro-3-nitrobenzene to 1-chloro-3-aminobenzene by TX-Ag nanoparticles and their Ag-Au bimetallic nanocomposites.

Therefore, e^- transfer takes place from Ag to Au near an Ag/Au interface and this ends up with an e^- enriched region inside the Au, facilitating the uptake of e^- by adsorbed CNB molecules on the surface of such region. However, further increase in the Au, atomic ratio (0.4) on CTAB-Ag NPs comparatively decreased the product yield to 60% within 65 min reduction time. This can be ascribed to the decrease in accessible interfaces, as the increased addition of Au might start covering the Ag/Au interface which makes them inaccessible for the efficient electronic effect. Similarly, the hollow porous aggregates of Ag-Au alloy evolved from the galvanic replacement reaction between the TX-Ag NPs and varying the atomic ratio of Au^{3+} ions displayed better catalytic performances (57-

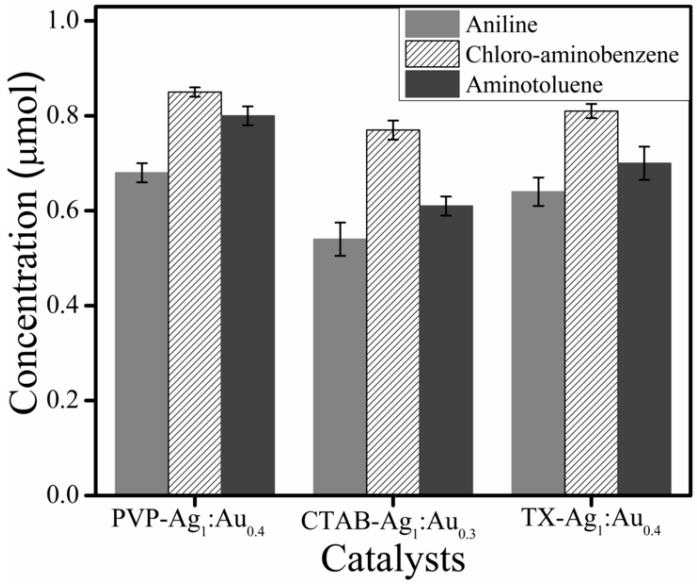

Fig. 4.12. Amount of aniline, 1-chloro-3-aminobenzene and 3-aminotoluene produced during reduction of nitrobenzene, 1-chloro-3-nitrobenzene and 3-nitrotoluene, respectively, by different Ag-Au bimetallic nanocomposites.

80%) than monometallic TX-Ag NPs (23%) as shown in Fig. 4.11a,b. The porosity in a frame-structured Ag-Au nanostructure might have larger surface areas (both inner and outer) and an improved electrical connection between NPs [31] to accommodate the higher reduction of CNB.

The different Ag-Au BM nanostructures obtained from variously capped Ag NPs with a particular Au atomic ratio, exhibited highest catalytic performances as discussed above and was further used as a catalyst for the reduction of nitrobenzene (NB) and 3-nitrotoluene (NT) as shown in Fig. 4.12. Overall, the different BM nanocatalyst can be ordered as follows, PVP-Ag_1:$Au_{0.4}$ > TX-Ag_1:$Au_{0.4}$ > CTAB-Ag_1:$Au_{0.3}$ attributed to their respective morphology. Among NB, CNB and NT, the compound with an e^- withdrawing group ($–Cl^-$) reflects higher catalytic activity relative to the compound with an e^- donating group ($–CH_3$), as can be seen in Fig. 4.12. The higher inductive (+0.34) and lower resonance stabilization value (-0.07) of chloro group relative to low inductive (-0.04) and high stabilization parameters (-0.11) of methyl group reflected faster rate of reduction for chloro group [56]. Hence, the conversion of nitro-aromatic compounds to their respective products was seen to be enhanced by BM NCs as compared to their monometallic counterparts. Therefore, through the optimization of the composition of these two metals (Ag and Au), the catalytic efficiency can be improved for the purpose of other reduction processes.

4.4 Conclusions

In summary, a simple technique has been demonstrated to control the morphology of Ag-Au BM NCs using Ag template capped with surfactants of different chemical nature. A significant variation in the optical properties of Ag NPs can be obtained at a desired level as a function of concentration of Au, which is essential for the application in surface-enhanced Raman spectroscopy (SERS) and optical sensing. Upon galvanic displacement reaction with $AuCl_4^-$ ions, the Ag NPs templates are converted either to solid, hollow or porous Au-Ag alloy NPs depending on the adsorbed surfactants on the Ag NPs surface. Therefore, the surfactants passivizing the Ag NPs surface play an important role in tailoring the NPs morphology, which allows the systematic studies of the synergistic role of Au and Ag for the evaluation of these BM NCs as potential nanocatalysts for various organic syntheses.

4.5 References

[1] A. Roucoux, J. Schulz and H. Patin, *Chem. Rev.*, 2002, **102**, 3757–3778.

[2] M. M. Manas and R. Pleixats, *Acc. Chem. Res.*, 2003, **36**, 638–643.

[3] Y. Zhang, X. Cui, F. Shi and Y. Deng, *Chem. Rev.*, 2012, **112**, 2467–2505.

[4] Y. Mikami, A. Dhakshinamoorthy, M. Alvaro and H. Garcia, *Catal. Sci. Technol.*, 2013, **3**, 58–69.

[5] Y. Cui, B. Ren, J. L. Yao, R. A. Gu and Z. Q. Tian, *J. Phys. Chem. B*, 2006, **110**, 4002–4006.

[6] R. G. Freeman, M. B. Hommer, K. C. Grabar, M. A. Jackson and M. J. Natan, *J. Phys. Chem.*, 1996, **100**, 718–724.

[7] N. R. Jana, *Analyst*, 2003, **128**, 954–956.

[8] Y. W. Cao, R. Jin and C. A Mirkin, *J. Am. Chem. Soc.*, 2001, **123,** 7961–7962.

[9] Y. Yang, J. Liu, Z. W. Fu and D. Qin, *J. Am. Chem. Soc.*, 2014, **136**, 8153–8156.

[10] L. Lu, A. Kobayashi, K. Tawa and Y. Ozaki, *Chem. Mater.*, 2006, **18**, 4894–4901.

[11] C. Shankar, A. T. N. Dao, P. Singh, K. Higashimine, D. M. Mott and S. Maenosono, *Nanotechnology*, 2012, **23**, 245704.

[12] S. Nishimura, A. T. N. Dao, D. Mott, K. Ebitani and S. Maenosono, *J. Phys. Chem. C*, 2012, **116**, 4511–4516.

[13] Y. J. Nam and J. R. Lead, *Sci. Total Environ.*, 2008, **400**, 396–414.

[14] M. E. Badawy, T. P. Luxton, R. G. Silva, K. G. Scheckel, M. T. Suidan, and T. M. Tolaymat, *Environ. Sci. Technol.*, 2010, **44**, 1260–1266.

[15] D. T. N. Anh, P. Singh, C. Shankar, D. Mott and S. Maenosono, *Appl. Phys. Lett.*, 2011, **99**, 073107.

[16] D. Mott, N. T. B. Thuy, Y. Aoki and S. Maenosono, *Phil. Trans. R. Soc. A*, 2010, **368**, 4275–4292.

[17] N. Toshima and T. Yonezawa, *New J. Chem.*, 1998, **22**, 1179–1201.

[18] D. S. Wang and Y. D. Li, *Adv. Mater.*, 2011, **23**, 1044–1060.

[19] H. L. Jiang and Q. Xu, *J. Mater. Chem.*, 2011, **21**, 13705–13725.

[20] R. Ferrando, J. Jellinek and R. L. Johnston, *Chem. Rev.*, 2008, **108**, 845–910.

[21] A. Monga and B. Pal, *New J. Chem.*, 2015, **39**, 304–313.

[22] X. Zhang and Z. Su, *Adv. Mater.*, 2012, **24**, 4574–4577.

[23] B. E. Brinson, J. B. Lassiter, C. S. Levin, R. Bardhan, N. Mirin and N. J. Halas, *Langmuir*, 2008, **24**, 14166–141771.

[24] Y. Xiang, X. Wu, D. Liu, Z. Li, W. Chu, L. Feng, K. Zhang, W. Zhou and S. Xie, *Langmuir*, 2008, **24**, 3465–3470.

[25] H. F. Zarick, W. R. Erwin, J. Aufrecht, A. Coppola, B. R. Rogers, C. L. Pint and R. J. Bardhan, *Mater. Chem. A*, 2014, **2**, 7088–7098.

[26] N. R. Sieb, N. C. Wu, E. Majidi, R. Kukreja, N. R. Branda and B. D. Gates, *ACS Nano*, 2009, **3**, 1365–1372.

[27] L. H. Pu, W. L. Jun, B. C. Li and J. Li, *J. Phys. Chem. B*, 2005, **109**, 7795–7800.

[28] A. M. Schwartzberg, T. Y. Olson, C. E. Talley and J. Z. Zhang, *J. Phys. Chem. B*, 2006, **110**, 19935–19944.

[29] Y. D. Yin, R. M. Rioux, C. K. Erdonmez, S. Hughes, G. A. Somorjai and A. P. Alivisatos, *Science*, 2004, **304**, 711–714.

[30] S. E. Skrabalak, J. Chen, L. Au, X. Lu, X. Li and Y. Xia, *Adv. Mater.*, 2007, **19**, 3177–3184.

[31] J. Zeng, Q. Zhang, J. Chen and Y. Xia, *Nano Lett.*, 2010, **10**, 30–35.

[32] S. W. Hsu, K. On, B. Gao and A. R. Tao, *Langmuir*, 2011, **27**, 8494–8499.

[33] J. H. Liu, A. Q. Wang, Y. S. Chi, H. P. Lin and C. Y. Mou, *J. Phys. Chem. B*, 2005, **109**, 40–43.

[34] N. R. Jana, L. Gearheart and C. J. Murphy, *Langmuir*, 2001, **17**, 6782–6786.

[35] G. Kawamura, Y. Yang, and M. Nogami, *J. Phys. Chem. C*, 2008, **112**, 10632–10636.

[36] P. Y. Silvert, R. H. Urbina and K. T. Elhsissena, *J. Mater. Chem.*, 1997, **7**, 293–299.

[37] Y. Yang, S. Matsubara, L. Xiong, T. Hayakawa and M. Nogami, *J. Phys. Chem. C*, 2007, **111**, 9095–9104.

[38] B. R. Gonzalez, A. Burrows, M. Watanabe, C. J. Kiely and L. M. L. Marzan, *J. Mater. Chem.*, 2005, **15**, 1755–1759.

[39] M. Liu and P. G. Sionnest, *J. Phys. Chem. B*, 2004, **108**, 5882–5888.

[40] S. Eustis and M. A. El-Sayed, *Chem. Soc. Rev.*, 2006, **35**, 209–217.

[41] I. O. Jimenez and V. Puntes, *J. Am. Chem. Soc.*, 2009, **131**, 13320–13327.

[42] M. Kahraman, O. Aydin and M. Culha, *Plasmonics*, 2009, **4**, 293–301.

[43] H. Zhanga and N. Toshima, *Catal. Sci. Technol.*, 2013, **3**, 268–278.

[44] S. Tokonami, N. Morita, K. Takasaki and N. Toshima, *J. Phys. Chem. C*, 2010, **114**, 10336–10341.

[45] F. X. Xie, H. Y. Bie, L. M. Duan, G. H. Li, X. Zhang and J. Q. Xu, *J. Solid State Chem.*, 2005, **178**, 2858–2861.

[46] A. Zhanga, J. Zhanga and Y. Fang, *J. Lumin.*, 2008, **128**, 1635–1640.

[47] M. Ganguly, A. Pal, Y. Negishi and T. Pal, *Langmuir*, 2013, **29**, 2033–2043.

[48] Y. Choi, S. Hong, L. Liu, S. K. Kim and S. Park, *Langmuir*, 2012, **28**, 6670–6676.

[49] T. Ghosh, B. Satpati and D. Senapati, *J. Mater. Chem. C*, 2014, **2**, 2439–2447.

[50] Z. Peng, B. Spliethoff, B. Tesche, T. Walther and K. Kleinermanns, *J. Phys. Chem. B*, 2006, **110**, 2549–2554.

[51] S. Liu, G. Chen, P. N. Prasad and M. T. Swihart, *Chem. Mater.*, 2011, **23**, 4098–4101.

[52] H. Wu, P. Wang, H. He and Y. Jin, *Nano Res.*, 2012, **5**, 135–144.

[53] M. R. Kim, D. K. Lee and D. Jang, *J. Appl. Catal. B*, 2011, **103**, 253–260.

[54] H. M. Chen, R. S. Liu, M. Y. Lo, S. C. Chang, L. D. Tsai, Y. M. Peng and J. F. Lee, *J. Phys. Chem. C*, 2008, **112**, 7522–7526.

[55] J. Huang, S. Vongehr, S. Tang, H. Lu, J. Shen and X. Meng, *Langmuir*, 2009, **25**, 11890–11896.

[56] C. Bougheloum and A. Messalhi, *Phys. Procedia*, 2009, **10**, 1055–1058.

Chapter 5

Comparative Co-catalytic Effect of Monometallic and Bimetallic Core-Shell Nanocomposites on Titania Photocatalysis by Visible Light

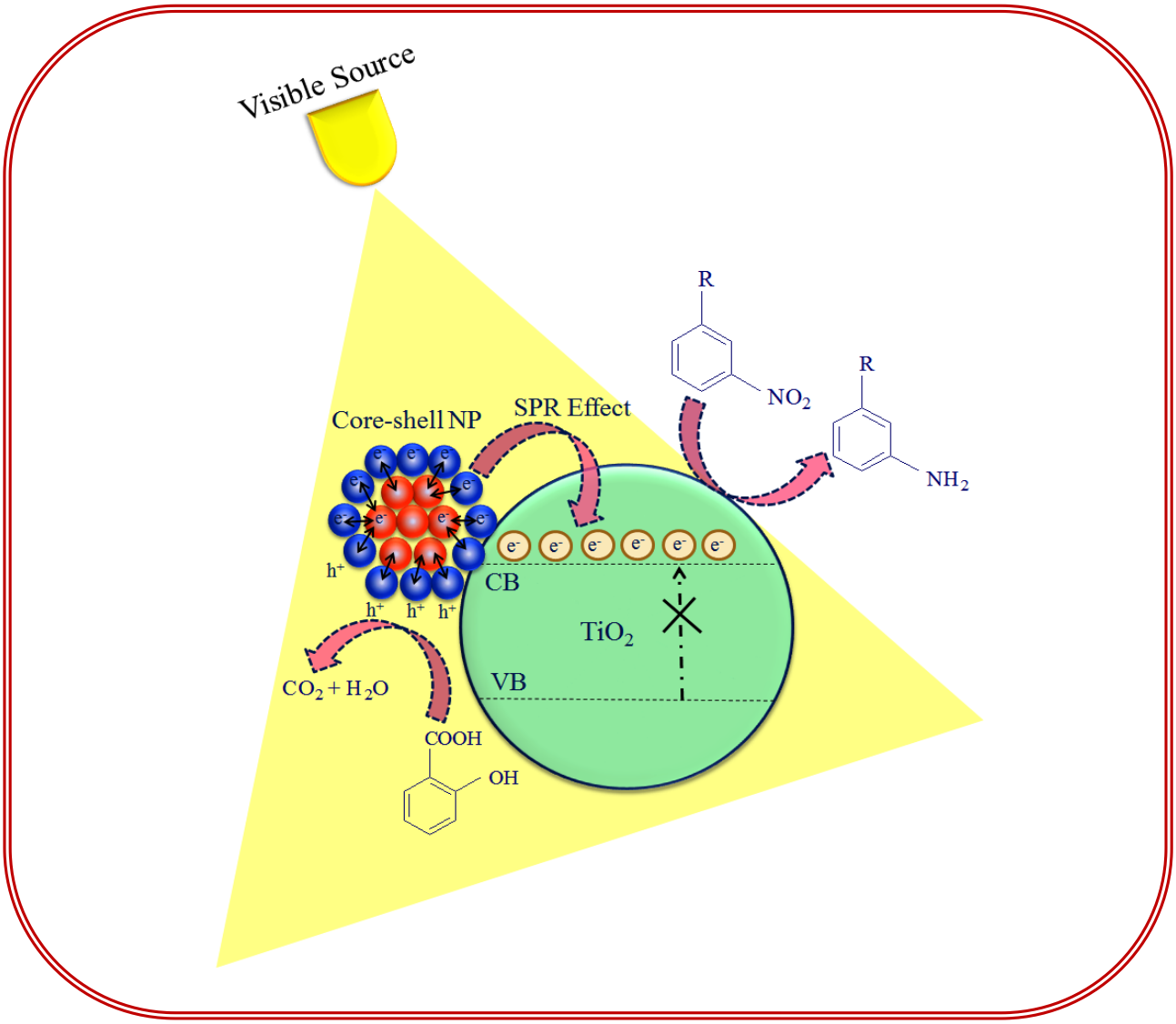

5.1 Introduction

Titania (TiO_2) -metal composites have been widely employed in photocatalysis, where the metal in contact with TiO_2 prolongs the interfacial charge-transfer process [1-4] enhancing the overall photocatalytic efficiency. There are many reports on preparation of Au/TiO_2, Ag/TiO_2, Pt/TiO_2, Cu/TiO_2, etc., nanocomposites (NCs) [5-9] with different morphological forms, which are progressively increasing with focus on enhancing the photocatalytic efficiency in oxidation and reduction processes. This not only results in improved photo-conversion, quantum yield, but also extends the absorption of UV-light active TiO_2 semiconductor in the visible light. For example, Zheng et al. [8] reported the photocatalytic properties of noble-metal photocatalysts, $M@TiO_2$ (M = Au, Pt, Ag) for the oxidation of benzene to phenol under visible light. The plasmonic nanoparticles (NPs) i.e., Au, Ag and Cu have the strong ability to absorb visible light due to their surface plasmon resonance (SPR) [10,11] effect. As a result, they act as an antenna to concentrate light and convert it to heat, that enables them to serve for photovoltaic, photochromic, surface-enhanced Raman spectroscopy, photocatalysis, etc. [7,8,12-22]. Therefore, the deposition of plasmonic nanomaterials onto TiO_2 exhibits an effective transfer of the photoexcited electrons (e^-) from the surface of metal NPs to the conduction band (CB) of TiO_2 [23-27] under visible light. As a result, the metals become e^- deficient and TiO_2 turn out to be e^- enriched, leading to the occurrence of photooxidation reaction on the surface of metal NPs rather than on TiO_2. The fast transference of e^- (less than 240 fs) was reported [28-30] into the TiO_2 support in the presence of Au NPs. However, the use of bimetallic (BM) nanostructures composed of two different metals can further enhance the photocatalytic performance [31-35], particularly with respect to activity and selectivity as compared to their monometallic counterparts. BM NPs deposited on TiO_2 are expected to display not only the combination of the properties associated with two individual metals, but also the new properties due to synergy between two metals. But, there are only few reports on TiO_2 modified with BM NPs. Recently, bimetallization of Pt with Au on TiO_2 has been reported to improve the catalytic activity of Pt clusters for visible light-induced hydrogen generation and degradation of organic dyes or phenol [36]. In addition, the TiO_2 modified with BM Ag-Au NPs prepared by microemulsion method [31] also showed an improved photoactivity under the visible light illumination. Horiguchi et al. [32] investigated the photocatalytic activity of trilayered $Au/Ag/TiO_2$ nanorods for the oxidation of propanol and checked the effect of Au/Ag composition and TiO_2 shell on the same.

BM nanostructures have fascinated increasing attention due to their unique optoelectronic and physicochemical properties owing to strong synergistic effects between two metals, which differ from their respective monometallic counterparts [37-39]. The physicochemical properties of noble metal NPs improve significantly by encapsulation with second suitable metal. Besides this, the consumption of expensive metal can also be reduced by coating with an inexpensive metal while maintaining the characteristics of outer shell metal. Although much progress has been made in the preparation of BM NCs based on Au-Ag [40-45], but still reports on Cu/Ag, Cu/Au BM particles have been rare so far. In fact, Cu NPs have been known to possess high electrical conductivity and is cheap compared to that of Au and Ag, but the easy oxidation of Cu strongly limits its use [46-49]. However, the protection of Cu NPs with an Ag or Au shell has been regarded as an alternative method to prevent spontaneous Cu oxidation due to the electronic effect between the two metals [50,51]. Moreover, the Cu alloying with Ag or Au might decrease the work function of resulting BM NPs and can probably decrease the Schottky barrier height formed at the BM NCs-TiO_2 interface [52,53]. This might promotes the proficient e^- transfer from the surface of photoactivated NCs to the CB of TiO_2 and hence, enhanced photocatalysis. Consequently, the present chapter deals with the synthesis of different core@shell (Cu@Ag and Cu@Au) and inverse core@shell (Ag@Cu and Au@Cu) BM NCs and their impregnation on TiO_2 to address their comparative photo-reduction and photo-degradation reactions relative to their monometallics-TiO_2 under the visible light.

5.2 Experimental

5.2.1 Materials

Cupric sulfate ($CuSO_4.5H_2O$), Aurochloric acid ($HAuCl_4.3H_2O$), ascorbic acid ($C_6H_8O_6$), sodium hydroxide (NaOH), polyvinylpyrrolidone (PVP, $(C_6H_9NO)_n$,), hydrazine (N_2H_4), ethylene glycol (EG, $C_2H_6O_2$) and salicylic acid ($C_7H_6O_3$), were obtained from Loba Chemie, India. The 3-nitroacetophenone ($C_8H_7NO_3$), 1-chloro-3-nitrobenzene ($C_6H_4ClNO_2$) and cetyltrimethylammoniumbromide ($C_{19}H_{42}BrN$, CTAB) were procured from Spectrochem and CDH, respectively. Sodium borohydride ($NaBH_4$), trisodium citrate ($Na_3C_6H_5O_7$) and Silver nitrate ($AgNO_3$) were purchased from Rankem, SDFCL and Fischer Scientific, India, respectively. P25-TiO_2 photocatalyst (size = ~30-50 nm, 70% anatase and 30% rutile) was provided as a gift sample from Degussa Company, Germany. All the chemicals were used as-

received without any further purification and de-ionized water was obtained using an ultra-filtration system (Milli-Q, Millipore) with a measured conductivity of above 35 mho cm^{-1} at 25° C.

5.2.2 Preparation of Monometallic Nanoparticles

(a) Cu Nanospheres

The synthesis of homogenous and stable Cu nanospheres (Cu NS) was achieved by mixing the solution of PVP (0.3 M, 10 mL), $CuSO_4$ (0.1 M, 6 mL) and ascorbic acid (0.25 M, 3 mL) in EG at 25˚C [54]. The appearance of dark reddish-brown color indicated the formation of Cu NS.

(b) Ag Nanospheres

The Ag nanospheres (Ag NS) was prepared by a seed-mediated method as reported [55,56] elsewhere. An aqueous mixture (7.5 mL) of CTAB (0.272 g) and $AgNO_3$ (250 µL, 0.01 M) was reduced by $NaBH_4$ (600 µL, 0.01 M) solution, which gave rise to the Ag seeds formation. This was followed by the addition of prepared seed solution (ca. 1.6 mL) into the growth mixture of $AgNO_3$ (1.25 mL, 0.01 M), CTAB (1.5 g, 50 mL) and ascorbic acid (250 µL, 0.1 M) in the presence of NaOH (1 mL, 1M). The solution turned yellow indicating the formation of Ag NS in the solution.

(c) Au Nanospheres

The Au seed solution was prepared by the reduction of an aqueous solution (7.5 mL) containing CTAB (0.272 g) and $HAuCl_4.3H_2O$ (250 µL, 0.01 M) using $NaBH_4$ (600 µL, 0.01 M) solution. The prepared Au seeds (1.6 mL) were added to the growth solution (50 mL) containing CTAB (1.5 g), $HAuCl_4.3H_2O$ (1.25 mL, 0.01 M) and ascorbic acid (250 µL, 0.1 M). The solution turned to wine-red color indicating the formation of Au nanospheres (Au NS) in the solution.

These resulting monometallic NPs were then repeatedly washed with deionized water using centrifugation (8000 rpm for 5-10 min) and were re-dispersed in water.

5.2.3 Preparation of Core@Shell Bimetallic Nanocomposites

For the preparation of different core@shell BM NCs, the number of atoms for core was fixed to 0.8, whereas the number of atoms for the shell was varied to 0.05, 0.1 and 0.2 by adding a certain amount of the metal elements which are given in Table 5.1.

Table 5.1. Amount of core nanospheres and 0.01 M of metal ions (shell) used for a particular atomic ratio and their respective surface plasmon bands obtained.

No. of atoms of core@shell (A_x@B_y)	Amount of A_x nanospheres and 0.01 M B_y^+ used (µL)	Surface Plasmon Band (nm)
$Cu_{0.8}$@$Ag_{0.05}$	426@53	595
$Cu_{0.8}$@$Ag_{0.1}$	426@100	376
$Cu_{0.8}$@$Ag_{0.2}$	426@200	382
$Ag_{0.8}$@$Cu_{0.05}$	520@213	419
$Ag_{0.8}$@$Cu_{0.1}$	520@427	422
$Ag_{0.8}$@$Cu_{0.2}$	520@854	435
$Cu_{0.8}$@$Au_{0.05}$	426@49	587
$Cu_{0.8}$@$Au_{0.1}$	426@98	563
$Cu_{0.8}$@$Au_{0.2}$	426@197	559
$Au_{0.8}$@$Cu_{0.05}$	610@213	550
$Au_{0.8}$@$Cu_{0.1}$	610@427	560
$Au_{0.8}$@$Cu_{0.2}$	610@854	580

(a) Preparation of Core@Shell Cu@Ag and Cu@Au Bimetallic Nanocomposites

The pre-synthesized Cu NS was used as a seed for the coating of Ag or Au to give rise to the core@shell BM type of nanostructures [57,58]. Each set of Cu NS (426 µL) diluted with an aqueous solution of PVP (4 mL, 1 wt %) was treated with different volumes of $AgNO_3$ or $HAuCl_4.3H_2O$ aqueous solution (49-197 µL, 0.01 M, Table 5.1). After this, ascorbic acid (0.1 mL, 0.1 M) and NaOH (0.2 mL, 0.1 M) was added to initiate the reduction of Ag or Au on the surface of Cu NS resulting in the formation of Cu@Ag or Cu@Au NCs.

(b) Preparation of Inverse Core@Shell Ag@Cu and Au@Cu Bimetallic Nanocomposites

The inverse core@shell NCs was prepared by taking 520 µL of pre-synthesized CTAB-capped Ag NS or 610 µL of Au NS solution in an aqueous solution of PVP (4 mL, 1 wt %). Then different volumes of aqueous solution of $CuSO_4.5H_2O$ (213-854 µL, 0.01 M, Table 5.1) were

added, followed by NaOH (11 µL, 1 M) and hydrazine (5 µL) to start the coating of the Cu shell [59] on Ag or Au surface, giving rise to Ag@Cu or Au@Cu NCs.

The prepared core@shell BM NCs was then washed with deionized water using centrifugation (8000 RPM for 5 min) and re-dispersed in water.

5.2.4 Preparation of Monometallic-TiO_2 and Core@Shell Bimetallic-TiO_2 Nanocomposites

The composites of monometallic as well as core@shell BM with TiO_2 were prepared by the wet impregnation method in which the total metal mass percentage of metal NPs was kept at 1 wt % with respect to TiO_2. The Cu NS, Ag NS, Au NS, $Cu_{0.8}@Ag_{0.1}$, $Cu_{0.8}@Au_{0.1}$, $Ag_{0.8}@Cu_{0.1}$ and $Au_{0.8}@Cu_{0.1}$ NCs was added to 500 mg of TiO_2 separately in an aqueous medium under magnetic stirring at room temperature for 2 h. The solid mass was separated using centrifugation by repeated washings with deionized water and then, the sample was dried in an oven overnight at 50 ºC followed by a heat treatment in a muffle furnace at 500 ºC for 2 h.

5.2.5 Characterization

The optical properties of monometallic and core@shell BM NCs were characterized using a UV-Vis spectrophotometer (Analytica Jena Specord 205). The morphology and composition were analyzed by transmission electron microscope (TEM) and energy dispersive X-ray (EDX) analysis and selected area electron diffraction (SAED) patterns using a FEI Technai F20 TEM. The hydrodynamic diameter of different NCs was determined by using a Brookhaven 90 plus Particle Size Analyzer. The optical properties of M-TiO_2 samples were measured with a diffuse reflectance spectrophotometer (DRS) by Avantes using $BaSO_4$ as a reflectance standard. Photoluminescence (PL) spectra were measured on excitation with xenon lamp at 320 nm by Perkin-Elmer LS5 in ethanolic medium.

5.2.6 Photocatalytic Activity

Irrespective of the morphology of nanostructures, the photocatalytic activity was performed by keeping the atomic ratio of different NCs constant. The photoactivity of various above prepared mono-/BM-TiO_2 was examined by mixing 5 mL of 0.2 mM nitro-aromatic compounds (3-nitroacetophenone, 1-chloro-3-nitrobenzene), 20 mg monometallic /core@shell BM-TiO_2 in 50% isopropanol suspension and Argon atmospheres under visible light (Halogen lamp, 400-1100 nm) illumination. The reaction was examined at regular interval of time by UV-Vis spectrophotometer after filtration with 0.22 µm cellulose filter. Similarly, the photodegradation

of salicylic acid (5 mL, 0.5 mM) was carried out in a pyrex tube by the desired amount of catalyst under the visible light for different time periods.

5.3 Results and Discussion

5.3.1 Optical properties

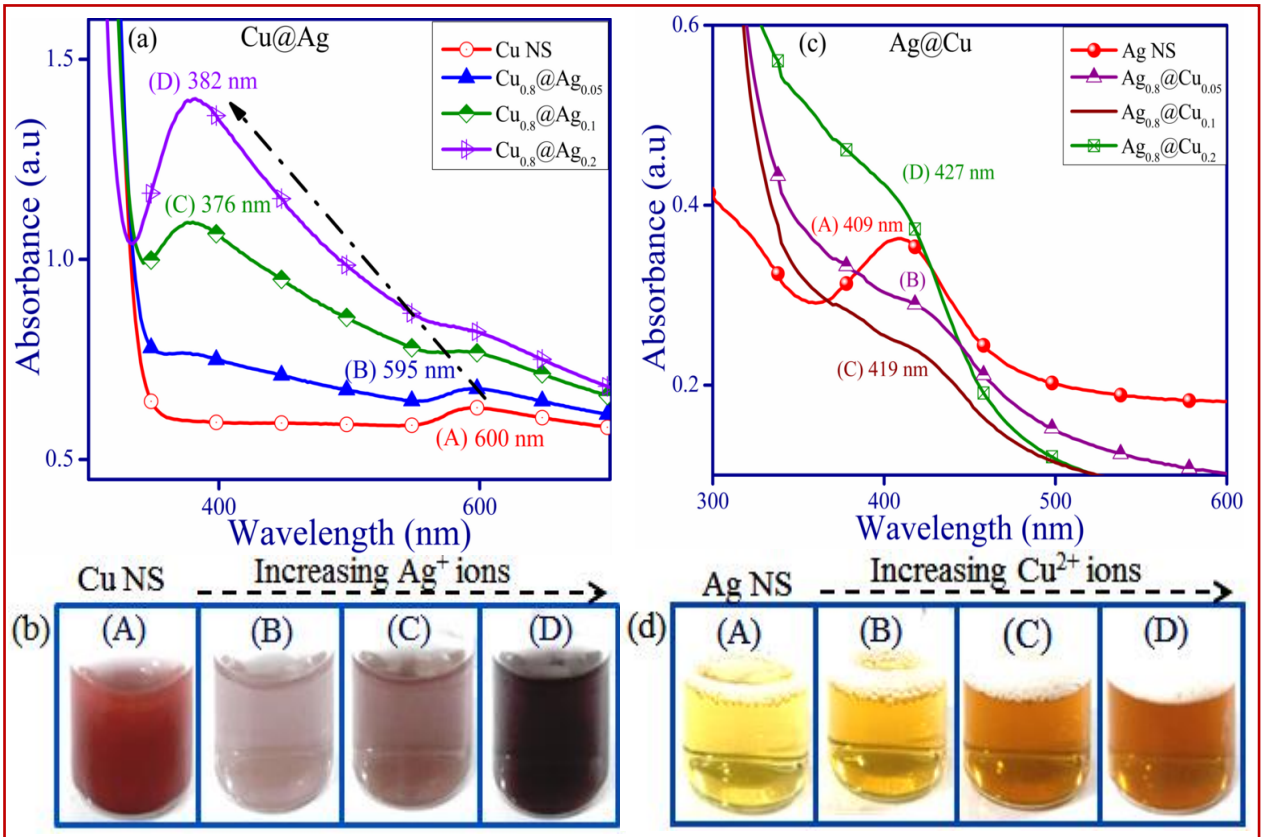

Fig. 5.1. Effect of different amounts of **(a-b)** $AgNO_3$ (0.01 M) deposition onto Cu nanospheres, and **(c-d)** $CuSO_4.5H_2O$ (0.01 M) deposition onto Ag nanospheres for the variation in the surface plasmon band and their respective color changes.

(a) Cu@Ag and Ag@Cu Bimetallic Nanocomposites

In this context, the pre-synthesized Cu NS and Ag NS was used as the seed for the deposition of Ag and Cu, respectively, to give rise to core@shell BM NCs. Owing to the SPR effect, metal NPs possess the collective oscillation of surface e^- and absorb the visible light. As a result, the reddish colored aqueous suspension of Cu NS exhibited a characteristic surface plasmon (SP)

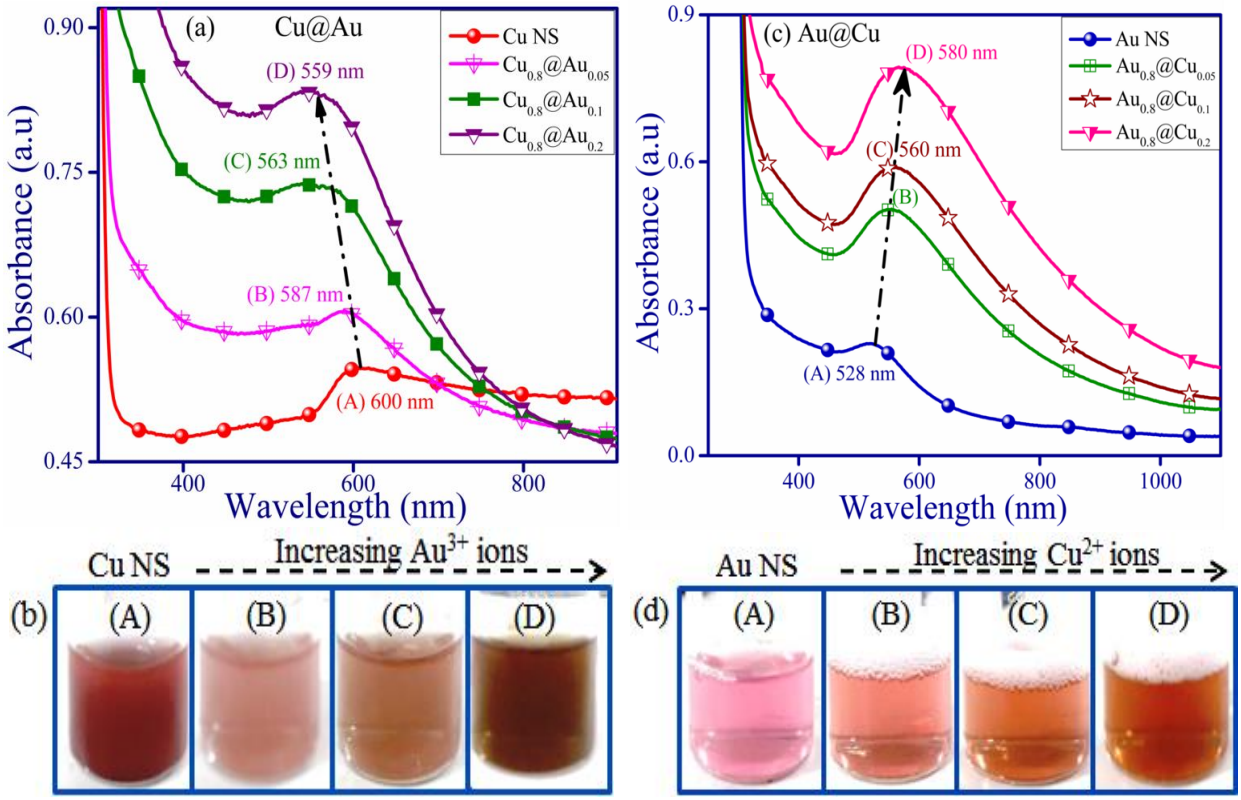

Fig. 5.2. Effect of different amounts of **(a-b)** $HAuCl_4.3H_2O$ (0.01 M) deposition onto Cu nanospheres, and **(c-d)** $CuSO_4.5H_2O$ (0.01 M) deposition onto Au nanospheres for the variation in the surface plasmon band and their respective color changes.

band at 600 nm corresponding to their spherical shape [60] as displayed in Fig. 5.1a. A huge shift in the absorption peak of Cu NS was found with the addition of different amounts of Ag precursor on its surface. It was observed that the SP band of Cu NS blue-shifted to 595 nm of higher intensity (Fig. 5.1a) on addition of Ag^+ (53 µL, 0.01 M), along with the color change from red to light blue as seen in Fig. 5.1b. With the progressive increase of Ag^+ (100-200 µL, 0.01 M), the intensity of new peak at 376-382 nm increased and became sharp having deep blue color (Fig. 5.1a,b). This result was in agreement with the previous report, where on addition of $AgNO_3$ to Cu NPs solution, a strong absorption peak was observed at 402 nm due to formation of Cu@Ag NPs [61]. Therefore, the above result indicated the co-existence of two elements (Cu and Ag) in one particle and assumed that Cu NS are completely encapsulated with a layer of Ag giving rise to Cu@Ag NCs. As a result, the incident light could not reach the Cu-core to excite their electrons due to the certain thickness of Ag shell and hence a peak, 382 nm corresponding to Ag NPs appeared. On the other hand, the characteristic absorption band of pure Ag NS of light yellow was located at 409 nm in Fig. 5.1c. When the Cu^{+2} ions (213 µL, 0.01 M) were reduced

on the surface of the Ag-core, the SP band was red-shifted, showing a shoulder peak at 419-422 nm of decreased absorbance. However, the plasmon intensity at 427 nm increased with successive addition of Cu^{+2} ions (427-854 µL, 0.01 M) due to its changes in the shell thickness as well as its composition. This observation was in agreement with the literature, where the absorption band of the Ag@Cu was red-shifted to 469 nm from 433 nm corresponding to bare Ag NPs [62]. In addition, the coating of the Cu-shell on the Ag-core caused the color transformation from light yellow of Ag NS to dark yellow color and consequently to orange as displayed in Fig. 5.1d.

(b) Cu@Au and Au@Cu Bimetallic Nanocomposites

The SP band of Cu NS (600 nm) was blue-shifted to 587 nm of higher absorbance on adding Au^{3+} ions (49 µL, 0.01 M) on its surface along with the color variation from dark red to light purple as seen in Fig. 5.2a,b. With the progressive addition of Au^{3+} ions (98-197 µL, 0.01 M), the SP band further blue shifted to 563 nm and finally to 559 nm of increased intensity (Fig. 5.2a). This process was supplemented with drastic color change from light purple to light brown and to dark brown (Fig. 5.2b) indicating a prompt growth of the Au shell onto the Cu NPs core. Literature [63] also revealed that with the addition of $AuCl_4^-$ to the Cu core, a new absorbance peak at 520 nm featuring Au SP band suggesting a complete coverage of Au atoms on Cu NPs. In case of Au core, the SP band observed at 528 nm shifted to longer wavelengths, 550-580 nm of higher intensity on treatment with Cu^{2+} ions (213-854 µL, 0.01 M) as shown in Fig. 5.2c. This red shifting in the plasmon band of Au NS with relatively increased intensity and the color change from light pink to red and finally to deep orange (Fig. 5.2d) indicated the formation of Au@Cu NCs. In the same way, Tsuji et al. [64] reported the SP band at 580 nm due to the coverage of Cu shell on Au nanorods.

5.3.2 Particle Size Distribution

The observed changes in these SP bands can be ascribed to the change in composition, dielectric function and size of NCs due to the coating of shell on the surface of core [65] which can be evidenced by DLS particle size distribution measurements. It revealed that the average hydrodynamic diameter of the Cu NS (21 nm) increased to 33 nm after the deposition of Ag (0.1) on the surface of Cu NS (Fig. 5.3a). Similarly, the hydrodynamic diameter of the Ag NS (27 nm) consequently increased to 41 nm with the addition of Cu^{2+} ions (0.1) signifying the coating of Ag

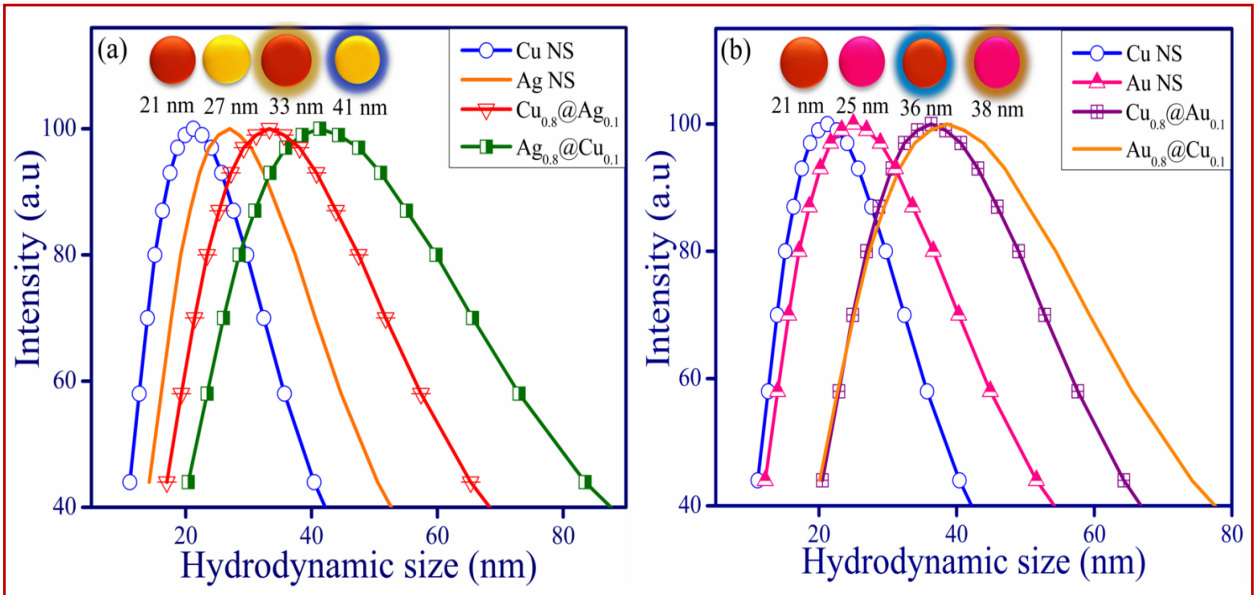

Fig. 5.3. DLS particle size distribution of **(a)** Cu nanospheres and Ag nanospheres after deposition of $AgNO_3$ and $CuSO_4.5H_2O$, respectively, and **(b)** Cu nanospheres and Au nanospheres after deposition of $HAuCl_4.3H_2O$ and $CuSO_4.5H_2O$, respectively.

on Cu NS. Fig. 5.3b also shows the increased hydrodynamic diameter of $Cu_{0.8}@Au_{0.1}$ and $Au_{0.8}@Cu_{0.1}$ NCs to be 36 nm and 38 nm, respectively, as compared to monometallic Cu NS (21 nm) and Au NS (25 nm).

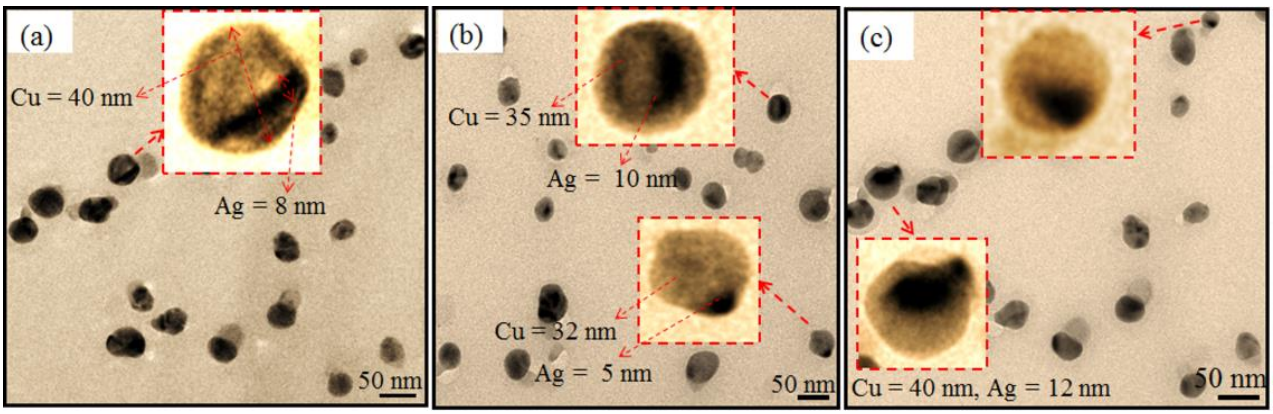

Fig. 5.4. TEM images of Ag deposited Cu nanospheres.

5.3.3 Morphological Studies

To confirm the formation of different core@shell BM NCs, TEM measurements were conducted. Fig. 5.4 reveals the TEM image of Cu-Ag BM NCs, where, when Cu NS was used as a core for the deposition of Ag^+ ions, they were observed to encapsulate the Cu core in a partial manner.

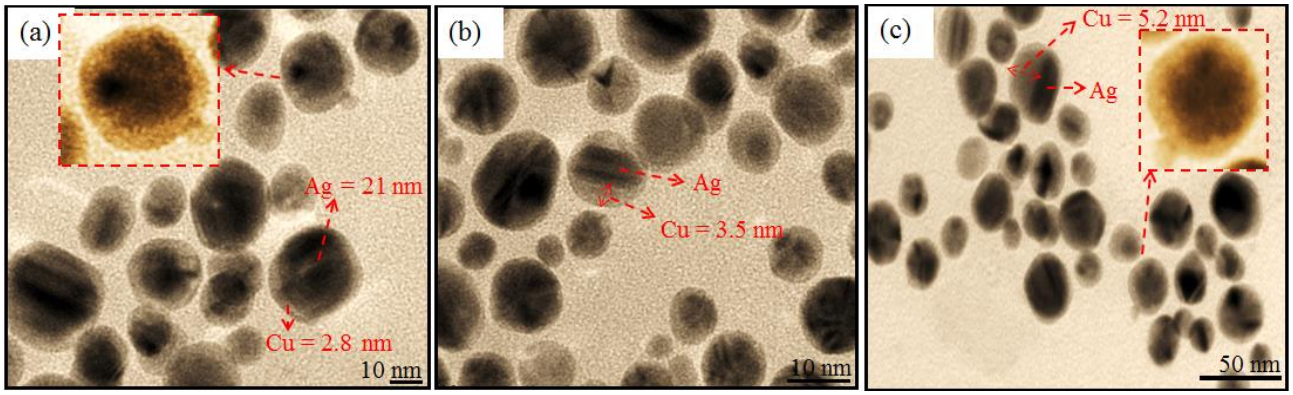

Fig. 5.5. TEM images of Cu deposited Ag nanospheres.

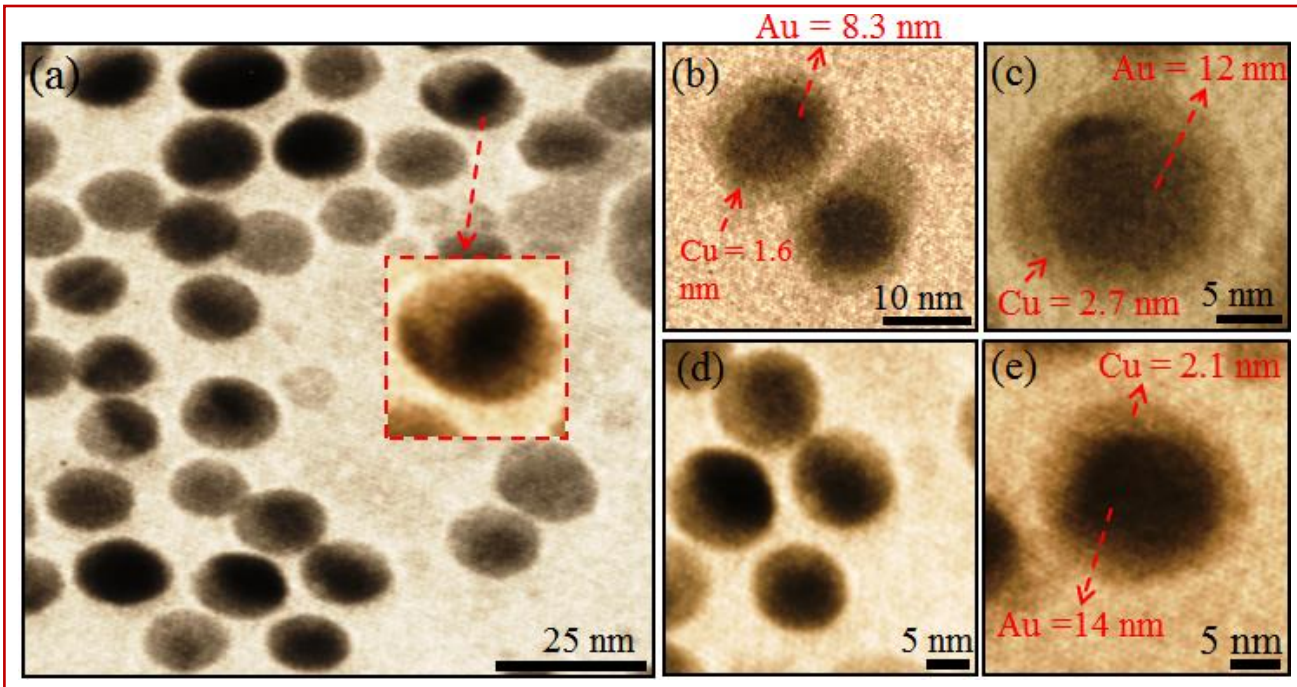

Fig. 5.6. TEM images of Cu deposited Au nanospheres.

Therefore, instead of the formation of uniform Ag shell, an irregular eccentric Ag NP was formed in the Cu NS. TEM images clearly show that in most particles (Fig. 5.4a-c), the darker Ag NPs are located in the non-uniform eccentric position to the lighter Cu NS (size = ~35-40 nm), having thickness of ~5-10 nm. In case of reverse nanostructure, the bare Ag NS of diameter (15-20 nm) was served as a seed for Cu deposition on its surface. The addition of Cu^{2+} ions on the surface of Ag NS in the presence of ascorbic acid led to the homogenous coating of the Cu-shell of thickness ~2.8-3.5 nm as shown in Fig. 5.5a,b. This gave rise to the formation of

Ag@Cu NCs (size = ~25 nm) in the form core@shell structural configuration, where the darker particle is recognized as Ag and the brighter particle is Cu due to the different electron density of Ag and Cu. The thickness of Cu-shell increased to ~5.2 nm with the higher addition of Cu^{2+} ions leading to the overall increase in size (~28-30 nm) of core@shell NCs as seen in Fig. 5.5c. Similarly, the Au@Cu NCs was formed, where a uniform coating of the Cu-shell of thickness ~1.5-2.7 nm was deposited on the surface of Au NS (~12-15 nm) which acts as the core for its deposition (Fig. 5.6). The size observed from the TEM images was different from the hydrodynamic diameter by DLS due to the existence of the hydration layer on the surface of NPs.

5.3.4 Optical properties of Monometallic and Core@Shell Bimetallic-TiO_2 Nanocomposites

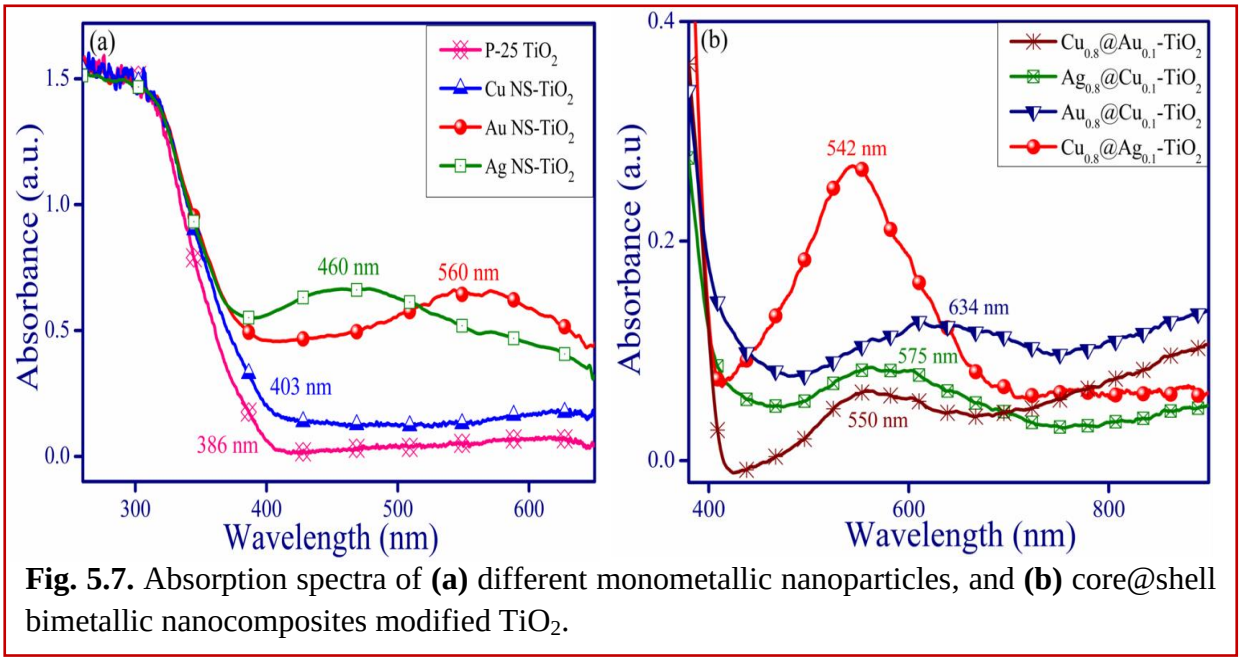

Fig. 5.7. Absorption spectra of **(a)** different monometallic nanoparticles, and **(b)** core@shell bimetallic nanocomposites modified TiO_2.

Fig. 5.7 shows the absorption spectra of different monometallic and core@shell BM NCs modified TiO_2 samples. The bare TiO_2 sample displayed an absorption onset at 386 nm due to the electronic transition from the 2p orbital of oxygen in the valence band (VB) to the 3d orbital of TiO_2 in CB. In contrast to TiO_2, the absorption onset was red-shifted to 403 nm in Cu NS modified TiO_2 due to the electronic transitions between the metal ion and the CB of TiO_2 [7,8,12-22]. However, Ag NS and Au NS loading on TiO_2 displayed a characteristic SP band at 460 nm and 560 nm, respectively, as observed in Fig. 5.7a. Similarly, the core@shell BM NCs modified TiO_2 showed characteristic absorption bands in the visible region at 542 nm and 550 nm for $Cu_{0.8}@Ag_{0.1}$-TiO_2 and $Cu_{0.8}@Au_{0.1}$-TiO_2 NCs, respectively (Fig. 5.7b). In case of

$Ag_{0.8}@Cu_{0.1}$-TiO_2 and $Au_{0.8}@Cu_{0.1}$-TiO_2 NCs, the red-shifted absorption bands were detected at 575 nm and 634 nm, respectively, (Fig. 5.7b) as compared to their respective monometallic NPs. Due to the coupling between the core@shell BM NCs and high reflective indexed TiO_2, the plasmon bands were red-shifted [66]. This red shifting in the absorption peaks of core@shell BM-TiO_2 NCs relative to monometallic-TiO_2 NCs and bare TiO_2 is a sign of decreasing band gap of TiO_2 [67].

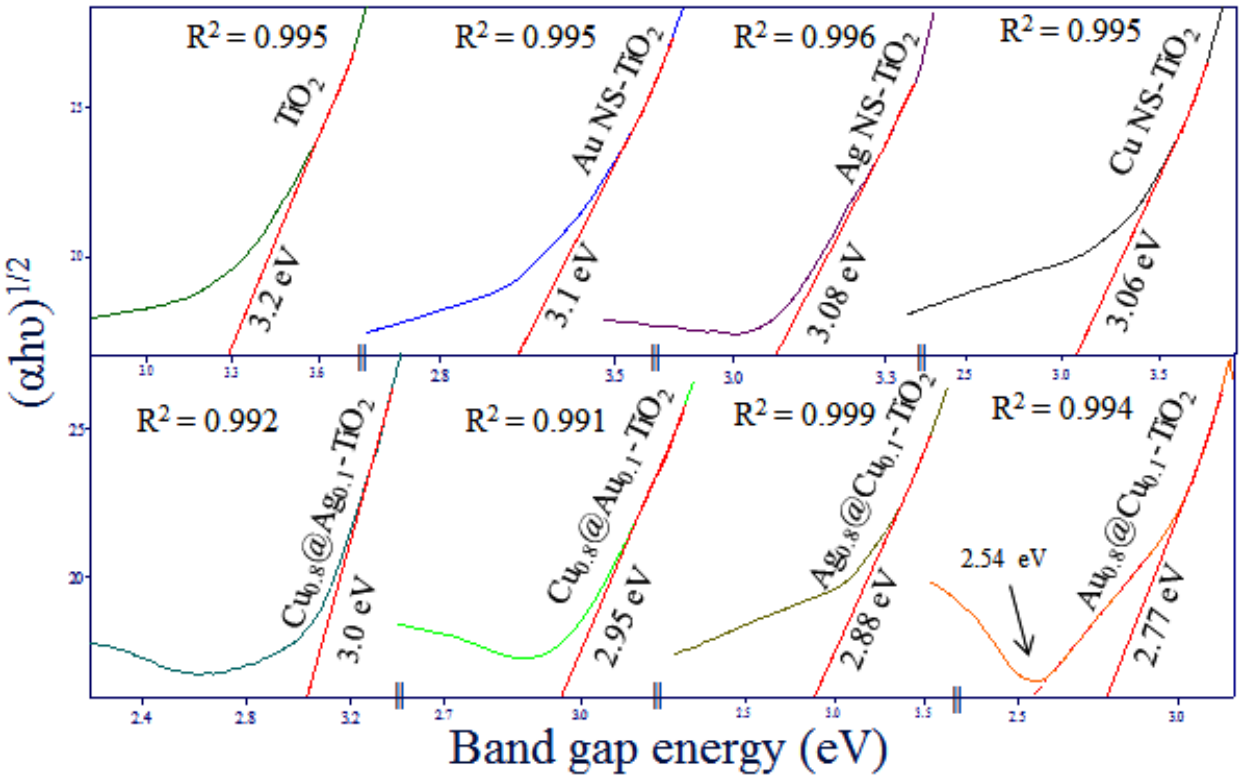

Fig. 5.8. Plot of $(\alpha h\nu)^{1/2}$ function versus the band gap energy of different monometallic and core@shell bimetallic modified TiO_2.

The band gap (E_g) of the various NCs was calculated using Tauc plot by extrapolating the linear area of the plot between $(\alpha h\nu)^2$ and $h\nu$, as shown in Fig. 5.8. The E_g helps in the determination of energy required to generate electron-hole (e^--h^+) pairs in the semiconductor to start a photocatalytic reaction. The calculated band gap, E_g was found to be 3.2 eV, 3.1 eV, 3.08 eV and 3.06 eV for TiO_2, Au NS-TiO_2, Ag NS-TiO_2 and Cu NS-TiO_2, respectively, as shown in Fig. 5.8. Whereas, the band gap was observed to be narrowed down in case of core@shell BM-TiO_2 NCs i.e., 3.0 eV, 2.95 eV, 2.88 eV and 2.77 eV for $Cu_{0.8}@Ag_{0.1}$-TiO_2, $Cu_{0.8}@Au_{0.1}$-TiO_2, $Ag_{0.8}@Cu_{0.1}$-TiO_2 and $Au_{0.8}@Cu_{0.1}$-TiO_2 NCs, respectively, in accordance with the red-shifting

in their absorbance peaks. Interestingly, in $Au_{0.8}@Cu_{0.1}$-TiO_2 NCs, the double band gap (2.77 eV and 2.54 eV) was observed probably due to two different compositions giving rise to two different transitions. Therefore, the absorption-shifts and hence, the band gap reduction in metal-TiO_2 can be controlled by varying the morphology of TiO_2 surface [68,69]. The comparative band gaps of various NCs relative to bare TiO_2 are shown in the form of histogram, Fig. 5.9. In addition, the EDX elemental mapping for the different monometallic and core@shell BM NCs modified TiO_2 clearly evidenced the presence of respective elements as shown in Fig. 5.10 and are summarized in Table 5.2.

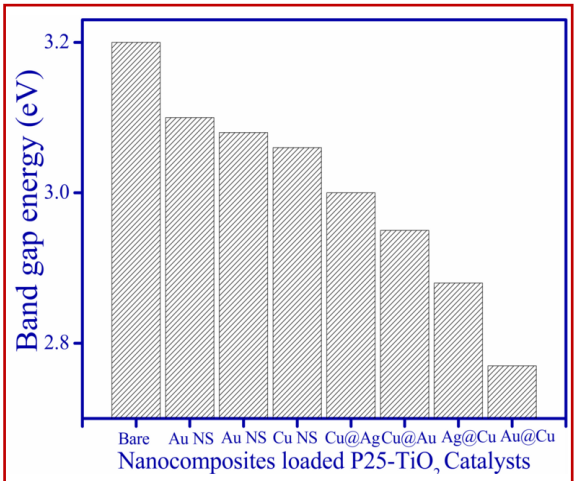

Fig. 5.9. Variation in band gap energy of different monometallic and core@shell bimetallic modified TiO_2.

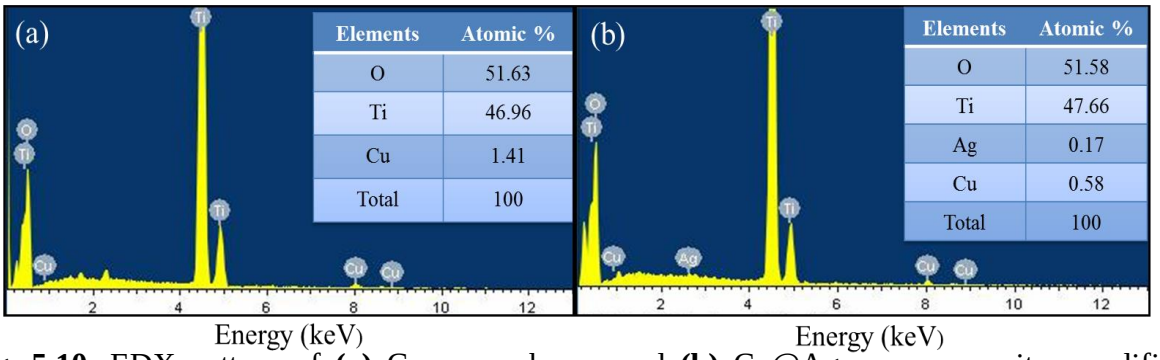

Fig. 5.10. EDX pattern of **(a)** Cu nanospheres, and **(b)** Cu@Ag nanocomposites modified TiO_2.

5.3.5 Photoluminescence Studies

The photoluminescence (PL) emission is primarily owed to the recombination of photoexcited e^- and photogenerated h^+ in the semiconductor and thus, it is a suitable method to determine the efficiency of trapping, migration, and transfer of charge carriers. Fig. 5.11a shows that the TiO_2 exhibited an emission band at 385 nm on excitation at 300 nm due to the band-edge photoluminescence. After modifying the TiO_2 with monometallic NPs (Cu, Ag and Au NS), the PL intensity tends to quench due to the prevention of e^--h^+ recombination, where Ag NS led to a larger decrease in PL intensity followed by Cu and Au NS (Fig. 5.11a). However, the core@shell

BM NCs displayed a maximum quenching relative to their corresponding monometallic-TiO_2 counterparts in the order of $Ag_{0.8}@Cu_{0.1}$-TiO_2 > $Cu_{0.8}@Ag_{0.1}$-TiO_2 > $Cu_{0.8}@Au_{0.1}$-TiO_2 > $Au_{0.8}@Cu_{0.1}$-TiO_2. This could be because of the proficient shuttling of photogenerated charge carriers from TiO_2 surface to BM alloy, creating a Schottky barrier at the interface of BM NCs and TiO_2 as an effective e^- trap and thereby, quenched the PL emission. These outcomes were similar to the previous results reported by Remita et al. [66] where BM Au-Cu modified TiO_2 was more perfect in electron trapping in comparison to monometallic Au or Cu NPs on TiO_2.

Table 5.2. Table summarizing the atomic % of elements obtained by EDX in different monometallic nanoparticles and core@shell bimetallic nanocomposites modified TiO_2.

Nanocomposites	O	Ti	Cu	Ag	Au
Ag NS-TiO_2	48.36	51.28	-	0.36	-
Ag@Cu-TiO_2	58.04	41.08	0.12	0.75	-
Au NS-TiO_2	42.42	57.16	-	-	0.42
Au@Cu-TiO_2	55.26	43.98	0.15	-	1.02
Cu@Au-TiO_2	50.37	48.45	0.71	-	0.06

5.3.6 Time Resolved Spectroscopy

Time resolved fluorescence decay studies were carried out to investigate the charge dynamics, which is associated with the e^- movement. The average lifetime, τ_{av} of photogenerated e^-/h^+ pairs were calculated to be 1.04 ns, 1.1 ns, 1.5 ns, 1.8 ns, 2.2 ns, 2.5 ns, 2.8 ns, 3.0 ns for TiO_2, Au NS-TiO_2, Cu NS-TiO_2, Ag NS-TiO_2, $Cu_{0.8}@Au_{0.1}$-TiO_2, $Au_{0.8}@Cu_{0.1}$-TiO_2 $Cu_{0.8}@Ag_{0.1}$-TiO_2 and $Ag_{0.8}@Cu_{0.1}$-TiO_2, respectively as shown in Fig. 5.11b. Thus, the lifetime of charge carriers was prolonged for TiO_2 modified with BM NCs and, thereby, increased the relaxation time of charge species of TiO_2 relative to monometallic NPs modified TiO_2. Also, Remita et al. [67] reported that the acceleration of charge carriers was faster for Au-Cu-TiO_2 NCs in contrast to single Au and Cu NPs.

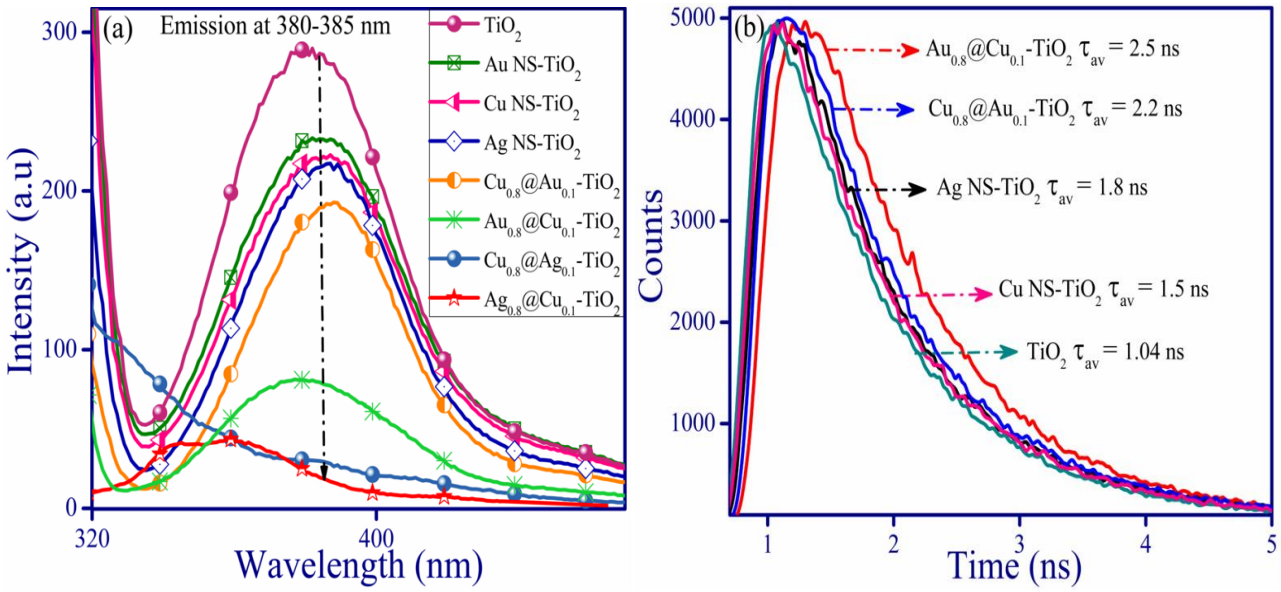

Fig. 5.11. (a) Emission spectra, and **(b)** Time resolved decay curve of monometallic nanoparticles and core@shell bimetallic nanocomposites modified TiO_2.

5.3.7 Photocatalytic Activity

The relative photocatalytic activity of monometallic as well as core@shell BM-TiO_2 NCs has been investigated for the reduction of 3-nitroacetophenone (NAP) to 3-aminoacetophenone (AAP) and 1-chloro-3-nitrobenzene (CNB) to 1-chloro-3-aminobenzene (CAB) under visible light.

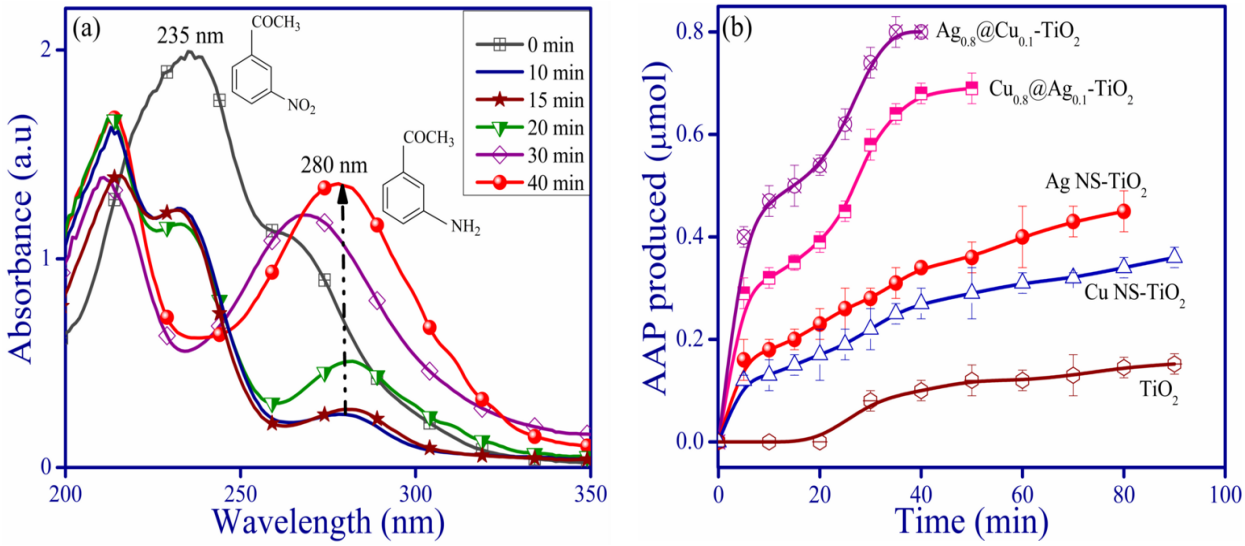

Fig. 5.12. (a) Changes in absorption spectra during the photoreduction of 3-nitroacetophenone (0.2 mM), and **(b)** time course graph showing the amount of 3-aminoacetophenone produced from the photoreduction of 3-nitroacetophenone (0.2 mM) by Cu and Ag nanoparticles and their core@shell bimetallic nanocomposites under visible light.

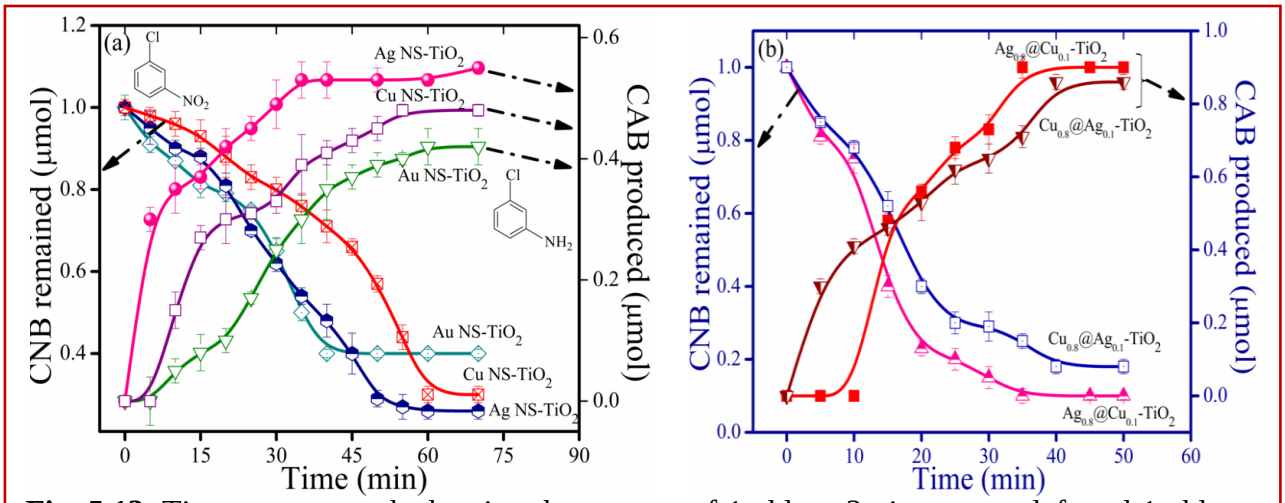

Fig. 5.13. Time course graph showing the amount of 1-chloro-3-nitroenzene left and 1-chloro-3-aminobenzene produced by **(a)** Cu, Ag and Au nanoparticles, and **(b)** core@shell Cu-Ag bimetallic nanocomposites under visible light.

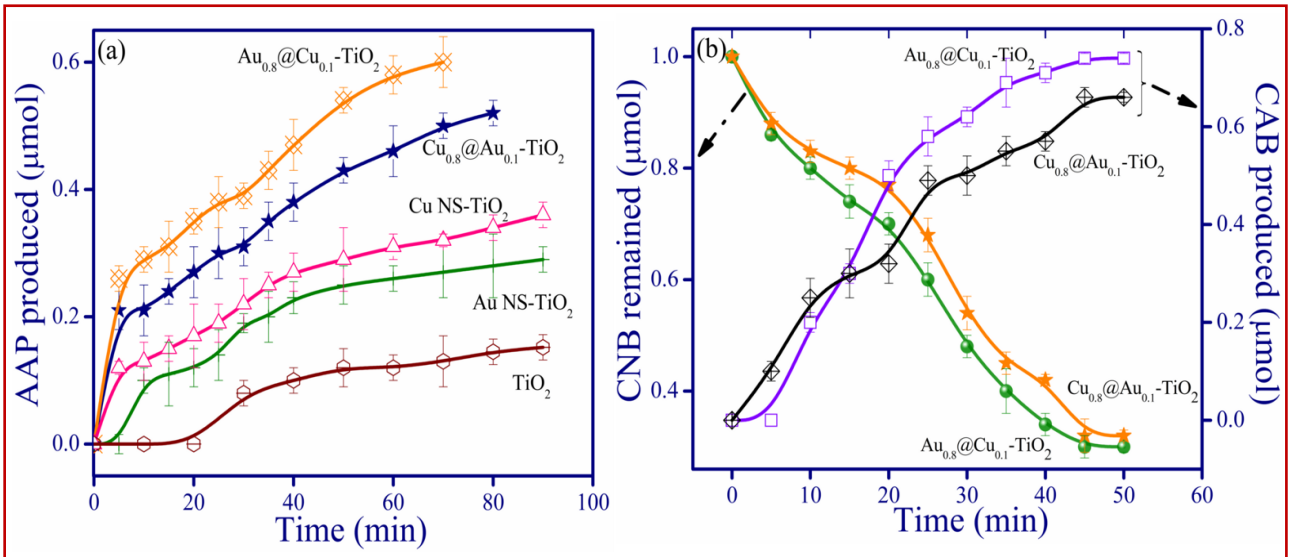

Fig. 5.14. Time course graph showing the amount of **(a)** 3-aminoacetophenone produced from the photoreduction of 3-nitroacetophenone, and **(b)** 1-chloro-3-nitroenzene left and 1-chloro-3-aminobenzene produced by Cu and Au nanoparticles and their core@shell bimetallic nanocomposites under visible light.

(a) Cu@Ag-TiO_2 and Ag@Cu-TiO_2 Nanocomposites

Fig. 5.12a displays the absorption graph for the reduction of NAP to AAP by using Ag NS-TiO_2 as a photo-catalyst. It was observed that the intensity of the absorption band of NAP at 235 nm decreased with the emergence of new peak at 280 nm, corresponding to AAP formation, whose intensity gradually increased with time. Fig. 5.12b corresponds to the time course graph

displaying the concentration of AAP formation from the reduction of NAP using Cu NS-TiO_2, Ag NS-TiO_2 and their core@shell BM-TiO_2 NCs. It displays that the amount of product increased linearly with reaction time, where the $Ag_{0.8}$@$Cu_{0.1}$-TiO_2 and $Cu_{0.8}$@$Ag_{0.1}$-TiO_2 exhibited higher yield of AAP, 80% and 69%, respectively, within 45-60 min reduction time, in contrast to their monometallic Cu NS-TiO_2 (36%) and Ag NS-TiO_2 (45%) NCs within 80-90 min. The photocatalytic reduction of CNB also displayed the decrease in concentration of CNB with a corresponding increase in CAB by reaction time (Fig. 5.13). In case of monometallic-TiO_2 NCs (Fig. 5.13a), the Ag NS-TiO_2 (CNB left = 26%) showed the higher yield of CAB 55%, followed by Cu NS-TiO_2 (CNB left = 30%) having a yield of CAB, 48%. However, by using $Ag_{0.8}$@$Cu_{0.1}$-TiO_2 (CNB left = 10%) $Cu_{0.8}$@$Ag_{0.1}$-TiO_2 (CNB left = 18%), the reduction process was highly improved, giving yield of 90% and 86% CAB, respectively (Fig. 5.13b).

(b) Cu@Au-TiO_2 and Au@Cu-TiO_2 Nanocomposites

In case of other photocatalysts, the $Cu_{0.8}$@$Au_{0.1}$-TiO_2 and $Au_{0.8}$@$Cu_{0.1}$-TiO_2 also showed higher yields of 60% and 52% AAP from the reduction of NAP than Au NS-TiO_2 (29%) Cu NS-TiO_2 (36%) as shown in Fig. 5.14a. Similarly, the photo-reduction of CNB to CAB was observed in a trend of $Au_{0.8}$@$Cu_{0.1}$-TiO_2 > $Cu_{0.8}$@$Au_{0.1}$-TiO_2 > Cu NS-TiO_2> Au NS-TiO_2 having yields of CAB 74%, 66%, 48%, 42%, respectively (Fig. 5.14b).

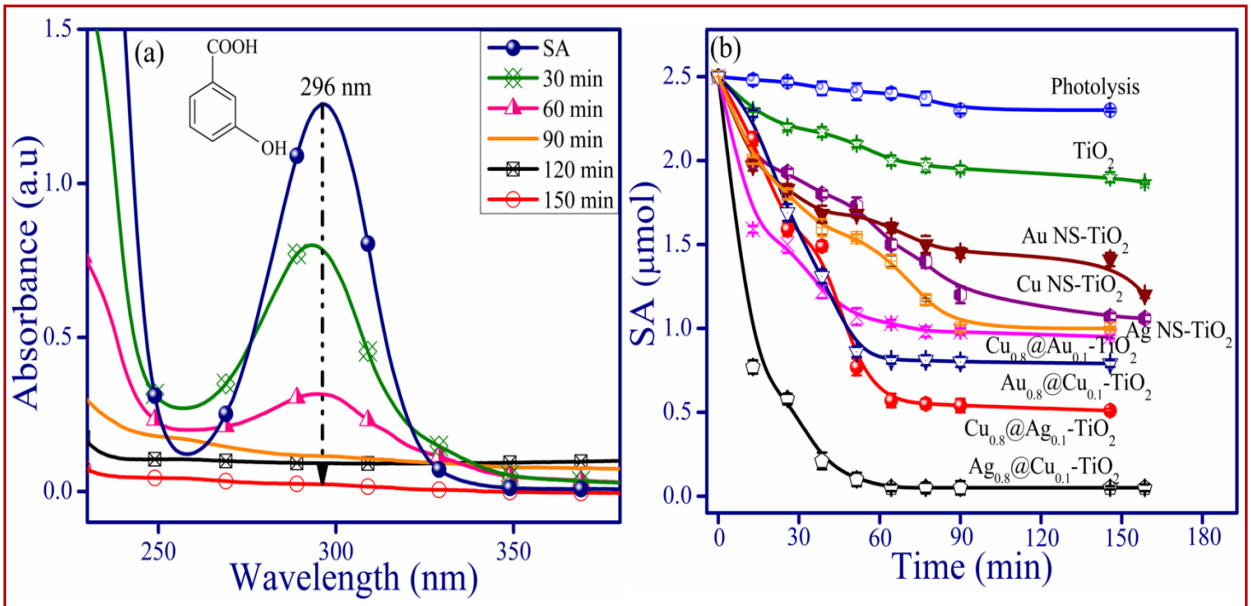

Fig. 5.15. (a) Changes in absorption spectra during degradation of salicylic acid (0.5 mM), and **(b)** time course graph showing the extent of photodegradation by different monometallic and core@shell bimetallic nanocomposites under visible light.

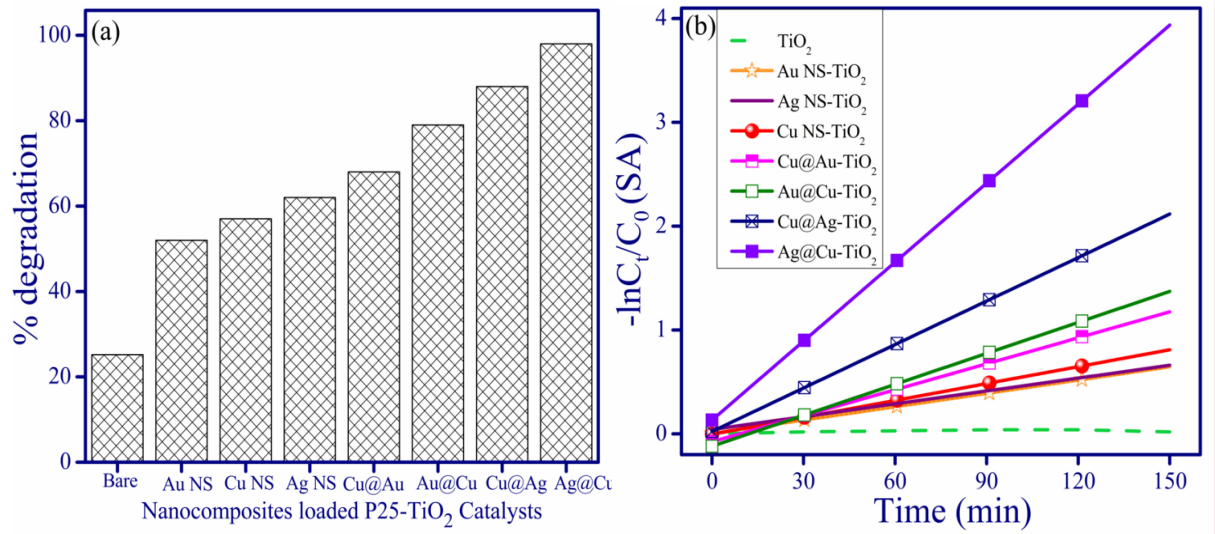

Fig. 5.16. (a) Percentage degradation of salicylic acid (0.5 mM), and **(b)** plot of $-\ln C_t/C_0$ versus time by different monometallic and core@shell bimetallic nanocomposites under visible light.

(c) Oxidation of Salicylic acid

The activity of various monometallic and core@shell BM-TiO_2 NCs was also tested for the oxidation of salicylic acid (SA), where Fig. 5.15a shows the decrease in absorption peak at 296 nm corresponding to the degradation of SA under visible light. The plot for their extent of degradation using above prepared catalysts versus time has been displayed in Fig. 5.15b. The stability of SA substrate was firstly tested under the visible light in the absence of any catalyst which confirmed its non-degradable nature. In addition, there was a negligible loss in the concentration of substrate during the dark reaction by TiO_2 and modified TiO_2 NCs that might be due to adsorption. A linear decrease in the concentration of SA was detected at various time intervals using different catalysts (Fig. 5.15b), indicating different extent of degradation. Fig. 5.16a corresponds to the comparative histogram showing the percentage degradation of SA by: TiO_2 (25%) < Au NS-TiO_2 (57%) < Cu NS-TiO_2 (52%) < Ag NS-TiO_2 (62%) < $Cu_{0.8}$@$Au_{0.1}$-TiO_2 (68%) < $Au_{0.8}$@$Cu_{0.1}$-TiO_2 (79%) < $Cu_{0.8}$@$Ag_{0.1}$-TiO_2 (88%) < $Ag_{0.8}$@$Cu_{0.1}$-TiO_2 (98%). The photo-degradation process follows pseudo first-order kinetics (Fig. 5.16b) where, the rate constant (k) was calculated (Fig. 5.17) and observed to be highest for $Ag_{0.8}$@$Cu_{0.1}$-TiO_2 (2.6×10^{-2} min^{-1}) followed by $Cu_{0.8}$@$Ag_{0.1}$-TiO_2 (1.6×10^{-2} min^{-1}), $Au_{0.8}$@$Cu_{0.1}$-TiO_2 (0.97×10^{-2} min^{-1}), $Cu_{0.8}$@$Au_{0.1}$-TiO_2 (0.65×10^{-2} min^{-1}) as compared to Ag NS-TiO_2 (0.41×10^{-2} min^{-1}), Cu NS-TiO_2

(0.34×10^{-2} min^{-1}), Au NS-TiO_2 (0.29×10^{-2} min^{-1}) and TiO_2 (0.13×10^{-2} min^{-1}) during SA photo-degradation.

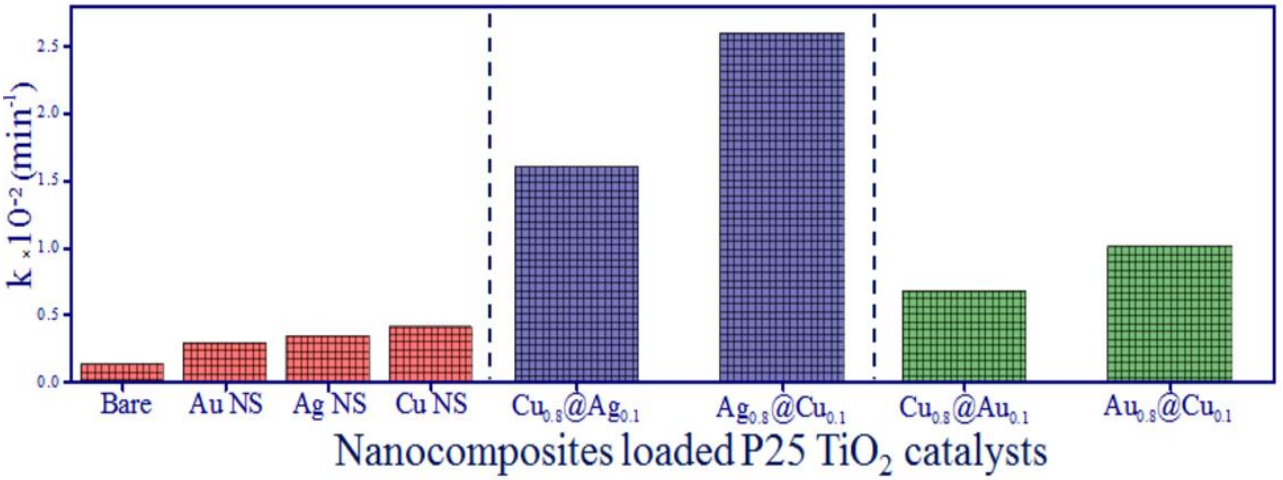

Fig. 5.17. Comparative Rate constant, k for the photodegradation of salicylic acid (0.5 mM) by different monometallic and core@Shell bimetallic nanocomposites under visible light.

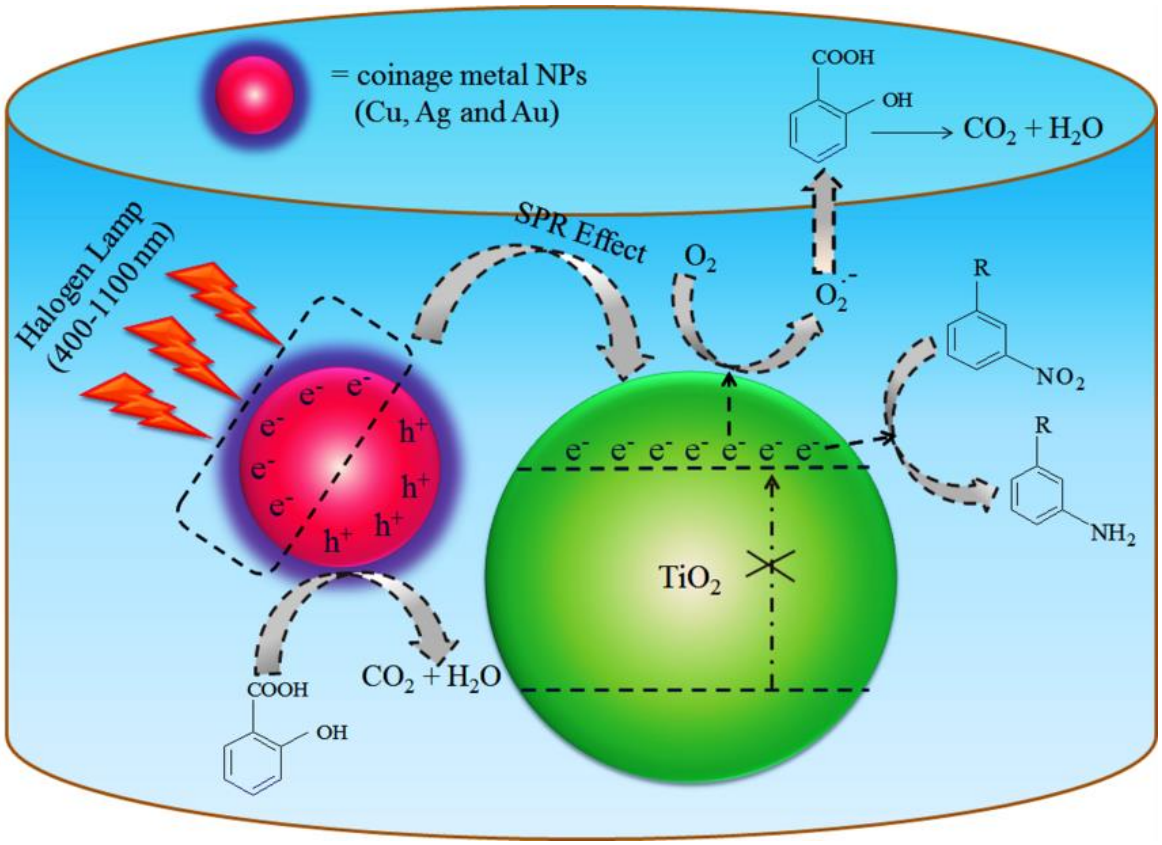

Scheme 5.1. Mechanism showing the surface plasmon resonance effect of coinage metal nanoparticles for TiO_2 photocatalysis under visible light.

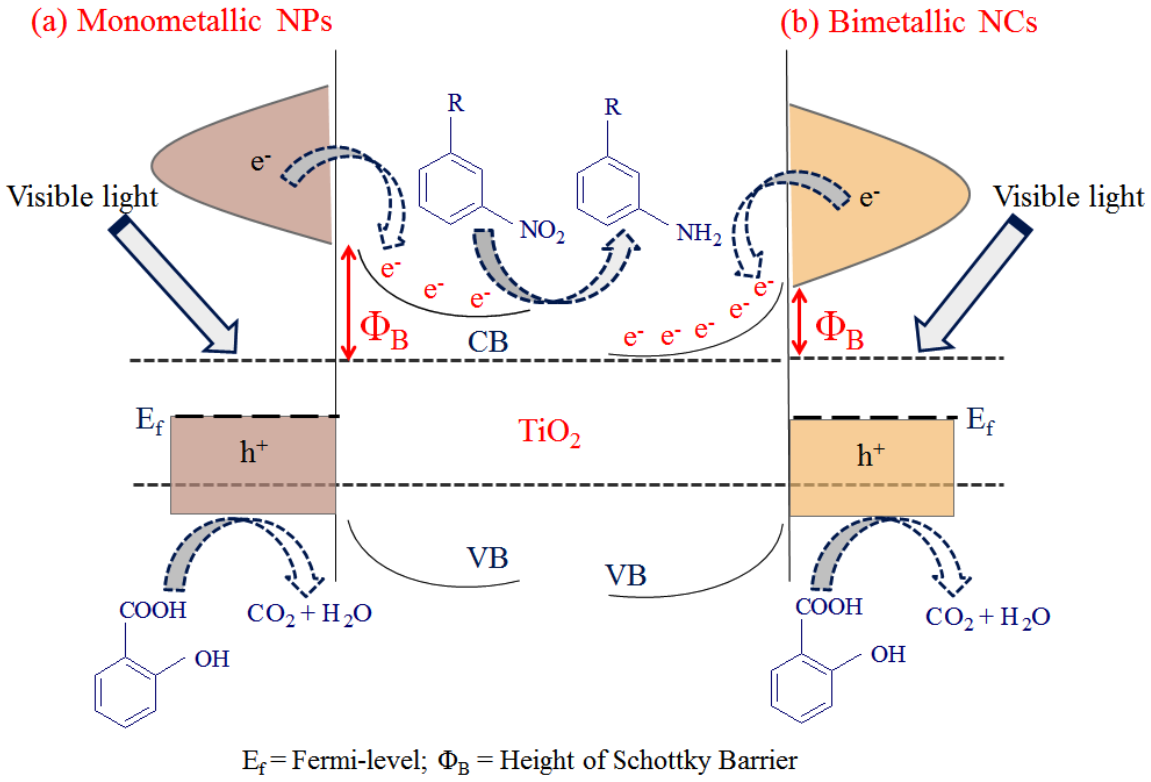

Scheme 5.2. Plausible mechanism for electron transfer from photoactivated (a) monometallic nanoparticles, and (b) bimetallic nanocomposites to TiO_2 for photocatalysis under visible light.

All the above results indicated that the TiO_2 modified with core@shell BM NCs showed the higher levels of photoactivity than the composites with both metals individually and bare TiO_2 under visible light. The enhanced photocatalytic activity in BM followed by monometallic-TiO_2 NCs comparative to bare TiO_2 under visible light can be explained by mechanism as displayed in Scheme 5.1. The coinage metal NPs loaded on TiO_2 absorb visible light due to the collective oscillation of surface free electrons in resonance with light, known as localized surface plasmon resonance [70]. This results in the transfer of e^- from the surface of metal NPs into the CB of TiO_2 [23-27]. Therefore, the noble particles become e^- deficient and hence, oxidizes isopropanol (hole scavenger) to acetone and return to their original metallic state, while e^- in the CB of TiO_2 [71] helps in the reducing the NAP and CNB substrates to their respective amines in the presence of inert atmosphere. In case of oxidation reactions, the transfer of e^- from the metal surface to TiO_2 CB led to the formation of positive charge on a metal surface (Scheme 5.1). While the transferred e^- in TiO_2 CB is consumed for the reduction of adsorbed oxygen to superoxide radicals [72]. Both the positive charges on metal surfaces and superoxide radicals are

Table 5.3. Various physical and chemical parameters of different monometallic nanoparticles and core@shell bimetallic nanocomposites modified TiO_2.

Catalysts	Absorbance (nm)	Band gap (eV)	e^--h^+ recombination time (ns)	Work function (eV)
TiO_2	-	3.2	1.04	-
Cu NS-TiO_2	-	3.1	1.5	4.7
Ag NS-TiO_2	460	3.08	1.8	4.3
Au NS-TiO_2	560	3.06	1.1	5.37
$Cu_{0.8}$@$Ag_{0.1}$-TiO_2	542	3.0	2.8	4.1
$Ag_{0.8}$@$Cu_{0.1}$-TiO_2	575	2.95	3.0	3.8
$Cu_{0.8}$@$Au_{0.1}$-TiO_2	550	2.88	2.5	4.6
$Au_{0.8}$@$Cu_{0.1}$-TiO_2	634	2.77	2.2	4.2

considered as strong oxidants and helps in the degradation SA to organic intermediates and consequently to water and CO_2. From the above mechanism, it can be concluded that the rate determining step for the photocatalysis is the transfer of photoexcited e^- from metal NPs to TiO_2. The photoactivated e^- has to overcome the Schottky barrier (Φ_B) formed at the metal-TiO_2 interface and therefore, the height of Φ_B strongly affects the efficiency of e^- transfer (Scheme 5.2). It is reported that the work function of the metal tends to decrease by alloying with other metal element having a lower work function [52,53,72]. As a result, the photoactivated core@shell BM-TiO_2 NCs transfers their e^- to TiO_2 more efficiently than their monometallics due to the decrease in Schottky barrier height (Φ_B) at the hetero-junction by alloying [72]. Hence, the transfer of photoexcited e^- from metal NPs to TiO_2 is an important factor in controlling the photocatalytic activity. Based on the different catalytic activities, the different BM-TiO_2 nanocatalysts can be ordered as: $Ag_{0.8}$@$Cu_{0.1}$-TiO_2 > $Cu_{0.8}$@$Ag_{0.1}$-TiO_2 > $Au_{0.8}$@$Cu_{0.1}$-TiO_2 > $Cu_{0.8}$@$Au_{0.1}$-TiO_2 NCs which can be attributed to their calculated work functions as follows:

$$W_{alloy}\,(eV) = (1-x) \times W_{core} + x \times W_{shell} \qquad (5.1)$$

where, 1-x = composition of core (0.8)

x = composition of shell (0.1)

W_{Core} = work function of the core

W_{Shell} = work function of the shell

Therefore, the various calculated work functions from the above equation and other parameters of different NCs are summarized in Table 5.3 and in agreement with the observed catalytic performances.

5.4 Conclusions

In summary, the comparative effect of coinage monometallic and their core@shell BM NCs on TiO_2 photocatalysis under the visible light illumination have been investigated. The synergistic effect of BM NCs might have a profound influence on TiO_2 photocatalysis and as a result, Cu@Ag-TiO_2, Ag@Cu-TiO_2, Cu@Au-TiO_2 and Au@Cu-TiO_2 exhibited efficient redox reactions than their monometallic counterparts because of the smooth e^- transfer from photoactivated NPs to TiO_2. Besides this, the BM-TiO_2 NCs shows a significant red-shift in the absorbance spectra, indicating that e^--h^+ pairs can be generated, even when the particle is irradiated with visible light. As a result, the optical band gaps of the modified TiO_2 NCs are reduced from 3.2 eV to 2.8 eV substantially. Therefore, the efficient charge separation at BM-TiO_2 NCs may contribute to the design of highly active photocatalysts driven by visible or sunlight.

5.5 References

[1] M. Bellardita, M. Addamo, A. D. Paola and L. Palmisano, *Chem. Phys.*, 2007, **339**, 94–103.

[2] M. Jakob, H. Levanon and P. V. Kamat, *Nano Lett.*, 2003, **3**, 353–358.

[3] A. Wood, M. Giersig and P. Mulvaney, *J. Phys. Chem. B*, 2001, **105**, 8810–8815.

[4] V. Subramanian, E. E. Wolf and P. V. Kamat, *J. Am. Chem. Soc.*, 2004, **126**, 4943–4950.

[5] A. Takai and P. V. Kamat, *ACS Nano*, 2011, **5**, 7369–7376.

[6] H. Choi, W. T. Chen and P. V. Kamat, *ACS Nano*, 2012, **6**, 4418–4427.

[7] P. Wang, B. Huang, Y. Dai and M. H. Whangbo, *Phys. Chem. Chem. Phys.*, 2012, **14**, 9813–9825.

[8] Z. Zheng, B. Huang, X. Qin, X. Zhang, Y. Dai and M. H. Whangbo, *J. Mater. Chem.*, 2011, **21**, 9079–9087.

[9] R. Kaur and B. Pal, *J. Mol. Catal. A: Chem.*, 2012, **355**, 39–43.

[10] C. F. Bohren and D. R. Huffman, *Absorption and Scattering of Light by Small Particles; Wiley: New York*, 1983.

[11] U. Kreibig and M. Vollmer, *Optical Properties of Metal Clusters; Springer: Berlin*, 1995.

[12] S. T. Kochuveedu, Y. H. Jang and D. H. Kim, *Chem. Soc. Rev.*, 2013, **42**, 8467–8493.

[13] M. M. Khan, S. A. Ansari, J. Lee and M. H. Cho, *J. Ind. Eng. Chem.*, 2013, **19**, 1845–1850.

[14] S. Sarina, E. R. Waclawik and H. Zhu, *Green Chem.*, 2013, **15**, 1814–1833.

[15] S. F. Chen, J. P. Li, K. Qian, W. P. Xu, Y. Lu, W. X. Huang and S. H. Yu, *Nano Res.*, 2010, **3**, 244–255.

[16] S. Linic, P. Christopher and D. B. Ingram, *Nat. Mater.*, 2011, **10**, 911–921.

[17] J. C. Scaiano and K. Stamplecoskie, *J. Phys. Chem. Lett.*, 2013, **4**, 1177–1187.

[18] W. T. Chen, Y. J. Hsu and P. V. Kamat, *J. Phys. Chem. Lett.*, 2012, **3**, 2493–2499.

[19] X. Zhou, G. Liu, J. Yu and W. Fan, *J. Mater. Chem.*, 2012, **22**, 21337–21354.

[20] A. Pearson, S. Bhosale, S. K. Bhargava and V. Bansal, *Appl. Mater. Interfaces*, 2013, **5**, 7007–7013.

[21] Y. Ishii, Y. Kanamori, T. Kawashita, I. Mukhopadhyay and S. Kawasaki, *J. Phys. Chem. Solids*, 2010, **71**, 511–514.

[22] H. Y. Zhu, X. B. Ke, X. Z. Yang, S. Sarina and H. W. Liu, *Angew. Chem., Int. Ed.*, 2010, **49**, 9657–9661.

[23] X. Zhang, Y. L. Chen, R. S. Liu and D. P. Tsai, *Rep. Prog. Phys.*, 2013, **76**, 046401.

[24] S. K. Cushing, J. Li, F. Meng, T. R. Senty, S. Suri, M. Zhi, M. Li, A. D. Bristow and N. Wu, *J. Am. Chem. Soc.*, 2012, **134**, 15033−15041.

[25] A. Primo, A. Corma and H. Garcia, *Phys. Chem. Chem. Phys.*, 2011, **13**, 886−910.

[26] S. Linic, P. Christopher and D. B. Ingram, *Nat. Mater.*, 2011, **10**, 911−921.

[27] H. Zhu, X. Chen, Z. Zheng, X. Ke, E. Jaatinen, J. Zhao, C. Guo, T. Xie and D. Wang, *Chem. Commun.*, 2009, 7524−7526.

[28] Y. Tian and T. Tatsuma, *J. Am. Chem. Soc.*, 2005, **127**, 7632−7637.

[29] Y. Tian and T. Tatsuma, *Chem. Commun.*, 2004, 1810−1811.

[30] A. Furube, L. Du, K. Hara, R. Katoh and M. Tachiya, *J. Am. Chem. Soc.*, 2007, **129**,

14852−14853.

[31] A. Z. Jurek, E. Kowalska, J. W. Sobczak, W. Lisowski, B. Ohtani, and A. Zaleska, *Appl. Catal. B*, 2011, **101**, 504–514.

[32] Y. Horiguchi, T. Kanda, K. Torigoe, H. Sakai and M. Abe, *Langmuir*, 2014, **30**, 922–928.

[33] N. Li, X. Zhang, S. Yuan, X. Zhang, Y. Yuan and X. Li, *Phys. Chem. Chem. Phys.*, 2015, **17**, 12023–12030.

[34] X. Y. Zhang, S. L. Yuan, Y. Z. Yuan and X. Li, *Optoelectron. Lett.*, 2015, **11**, 1–4.

[35] D. Tsukamoto, A. Shiro, Y. Shiraishi, Y. Sugano, S. Ichikawa, S. Tanaka and T. Hirai, *ACS Catal.*, 2012, **2**, 599–603.

[36] N. Toshima and K. Hirakawa, *Appl. Surf. Sci.*, 1997, **121**, 534–537,

[37] D. Wang, A. Villa, F. Porta, L. Pratia and D. Su, *J. Phys. Chem. C*, 2008, **112**, 8617–8622.

[38] A. Lehoux, L. Ramos, P. Beaunier, D. B. Uribe, P. Dieudonne, F. Audonnet, A. Etcheberry, M. J. Yacaman and H. Remita, *Adv. Funct. Mater.*, 2012, **22**, 4900–4908.

[39] A. K. Singh and Q. Xu, *ChemCatChem*, 2013, **5**, 652–676.

[40] R. P. Doherty, J. M. Krafft, C. Methivier, S. Casale, H. Remita, C. Louis and C. Thomas, *J. Catal.*, 2012, **287**, 102–113.

[41] A. Hugon, L. Delannoy, J. M. Krafft and C. Louis, *J. Phys. Chem. C*, 2010, **114**, 10823–10835.

[42] M. M. Esfahani, M. Mostafavi, B. Keita, L. Nadjo, P. Kooyman and H. Remita, *Gold Bull.*, 2010, **43**, 49–56.

[43] A. Sandoval, A. Aguilar, C. Louis, A. Traverse and R. Zanella, *J. Catal.*, 2011, **281**, 40–49.

[44] T. Redjala, H. Remita, G. Apostolescu, M. Mostafavi, C. Thomazeau and D. Uzio, *Gas Oil Sci. Technol.*, 2006, **61**, 789–797.

[45] F. Ksar, L. Ramos, B. Keita, L. Nadjo, P. Beaunier and H. Remita, *Chem. Mater.*, 2009, **21**, 3677–3683.

[46] B. Luo, X. Li, X. Li, L. Xue, S. Li and X. Li, *CrystEngComm.*, 2013, **15**, 5654–5659.

[47] T. Montini, V. Gombac, L. Sordelli, J. J. Delgado, X. Chen, G. Adami and P. Fornasiero, *ChemCatChem.*, 2011, **3**, 574–577.

[48] A. K. Schaper, H. Hou, A. Greiner, R. Schneider and F. Philips, *Appl. Phys. A*, 2004, **78**, 73–77.

[49] S. K. Mehta, R. Kaur and G. R. Chaudhary, *Colloids Surf. A*, 2012, **403**, 103–109.

[50] Z. Chen, D. Mochizuki, M. M. Maitani and Y. Wada, *Nanotechnology*, 2013, **24**, 265602.

[51] Y. Sohn, D. Pradhan, L. Zhao and K. T. Leung, *Electrochem. Solid-State Lett.*, 2012, **15**, K35–K39.

[52] I. Pasti and S. Mentus, *Mater. Chem. Phys.*, 2009, **116**, 94–101.

[53] R. Ishii, K. Matsumura, A. Sakai and T. Sakata, *Appl. Surf. Sci.*, 2001, **169**, 658–661.

[54] Y. Wang, P. Chen and M. Liu, *Nanotechnology*, 2006, **17**, 6000–6006.

[55] N. R. Jana, L. Gearheart and C. J. Murphy, *Langmuir*, 2001, **17**, 6782–6786.

[56] G. Kawamura, Y. Yang, and M. Nogami, *J. Phys. Chem. C*, 2008, **112**, 10632–10636.

[57] B. R. Gonzalez, A. Burrows, M. Watanabe, C. J. Kiely and L. M. L. Marzan, *J. Mater. Chem.*, 2005, **15**, 1755–1759.

[58] M. Liu and P. G. Sionnest, *J. Phys. Chem. B*, 2004, **108**, 5882–5888.

[59] A. F. A. Paneque, B. R. Gonzalez, I. P. Santos and L. M. L. Marzan, *J. Phys. Chem. C*, 2012, **117**, 2474–2479.

[60] A. K. Patra, A. Dutta and A. Bhaumik, *Catal. Comm.*, 2010, **11**, 651–655.

[61] A. Muzikansky, P. Nanikashvili, J. Grinblat and D. Zitoun, *J. Phys. Chem. C*, 2013, **117**, 3093–3100.

[62] J. P. Lee, D. Chen, X. Li, S. Yoo, L. A. Bottomley, M. A. El-Sayed, S. Park and M. Liu. *Nanoscale*, 2013, **5**, 11620–11624.

[63] S. Liu, Z. Sun, Q. Liu, L. Wu, Y. Huang, T. Yao, J. Zhang, T. Hu, M. Ge, F. Hu, Z. Xie, G. Pan and S. Wei, *ACS Nano*, 2014, **8**, 1886–1892.

[64] Y. Yoshida, K. Uto, M. Hattori and M. Tsuji, *CrystEngComm.*, 2014, **16**, 5672–5680.

[65] A. Monga and B. Pal, *New J. Chem.*, 2015, **39**, 304–313.

[66] Z. Hai, N. E. Kolli, J. Chen and H. Remita, *New J. Chem.*, 2014, **38**, 5279–5286.

[67] M. M. Khan, S. A. Ansari, D. Pradhan, M. O. Ansari, J. Lee and M. H. Cho, *J. Mater. Chem. A*, 2014, **2**, 637–644.

[68] M. Sahu and P. Biswas, *Nanoscale Res. Lett.*, 2011, **6**, 1–14.

[69] B. Choudhury, M. Dey and A. Choudhury, *Int. Nano Lett.*, 2013, **3**, 1–8.

[70] A. Primo, A. Corma and H. Garcia, *Phys. Chem. Chem. Phys.*, 2011, **13**, 886–910

[71] A. Tanaka, Y. Nishino, S. Sakaguchi, T. Yoshikawa, K. Imamura, K. Hashimoto and H. Kominami, *Chem. Commun.*, 2013, **49**, 2551–2553.

[72] Y. Shiraishi, H. Sakamoto, Y. Sugano, S. Ichikawa and T. Hirai, *ACS Nano*, 2013, **7**, 9287–9297.

Chapter 6

Influence of oxidative etching of Au nanostructures by $KMnO_4$ on its surface morphology, electro-kinetic properties and improved catalytic activity

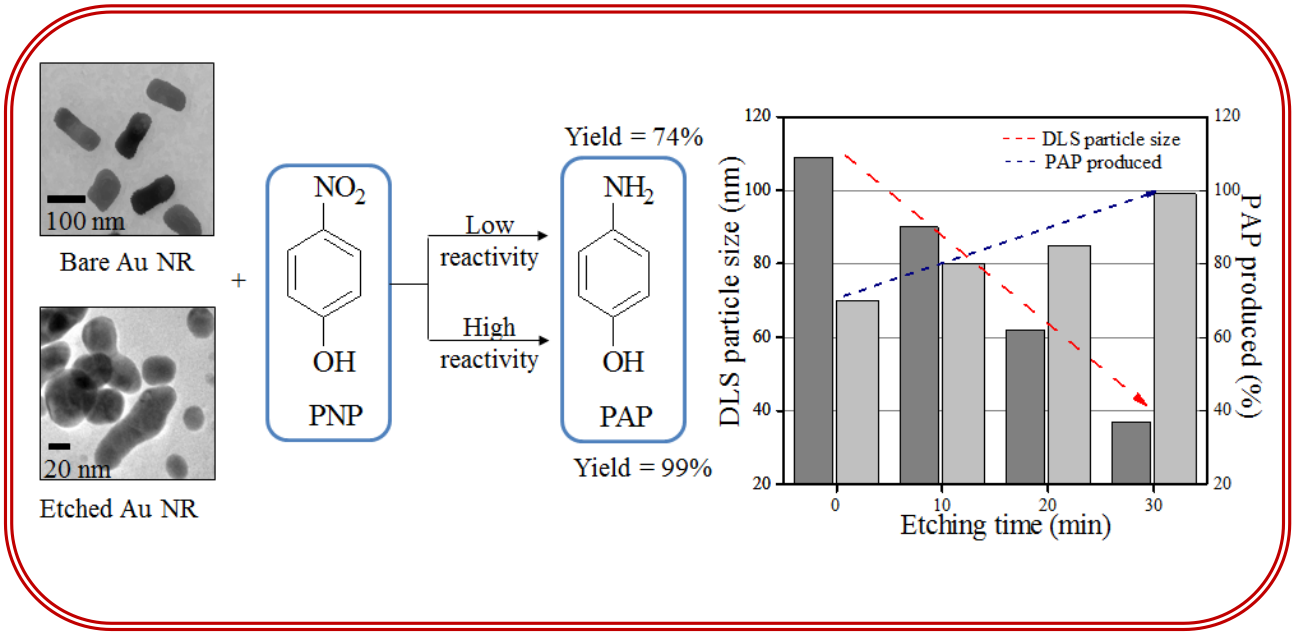

6.1 Introduction

The optoelectronics and physiochemical properties of Au nanoparticles (Au NPs) are proved to be very sensitive to their surface morphology [1-4]. Hence, the ability to tailor the mono-dispersed particles could alter the optical and catalytic properties [5-10] depending on the shape and size of the particles. The morphology of Au NPs can be altered by regulating the experimental parameters [11-14] such as surfactant to water ratio, capping agents, reducing agents, concentration of the metal salts, time and temperature during their fabrication. Several groups have attempted to produce various sizes and shapes of Au NPs using various chemical [11-14], biological [15-17] and physical methods [18-20]. For example, plant extracts such as Inonotus obliquus [15], Commelina nudiflora [16], Moringa oleifera [17], etc. have been reported to produce different shapes of Au NPs i.e., spherical, triangular, hexagonal and rods. The surface atoms of Au NPs sometimes tend to become saturated with the surrounding gas or absorbed ionic species and, thereby, blocking or poisoning the active catalytic sites. Therefore, the catalyst can be renewed and reused by an oxidative etching process using a suitable oxidant, without hampering their surface activity. It may result in dangling bonds, imbalancing of the forces and thus, generates chemically unsaturated, fresh surface and thermodynamically high-energy active anisotropic Au NPs [9,21], which is otherwise difficult to prepare by conventional synthetic methods. For example, the galvanic replacement reaction has been employed for generating noble-metal nanostructures in the form of nanocages or nanoboxes [22], but this special technique requires various experimental steps and high refluxing temperature. Therefore, alternate strategy has been reported to generate anisotropic shapes using external stimuli such as thermal/ or laser heating [23-25] and chemical methods [11,26-31]. In addition, electrochemical oxidation to Au crystals has also been reported [32,33]. Laser irradiation and thermal reshaping [21] processes are employed for the direct surface deformation [22], but these systems involve an expensive source of laser and comparatively higher temperature, respectively. In this respect, corrosive oxidative etching of as-prepared Au NPs have been found to be an unusual method to generate asymmetric Au nanocrystal possessing surface active facets [34], truncated sharp edges and corners [35], etc. This process may give rise to the formation of such NPs that may have fresh active surface atoms and high surface area, which exhibit enhanced catalytic activity depending on their morphology.

The oxidative dissolution is feasible using the oxidants that have the higher redox potential than Au NPs and a higher capability to gain electrons (e^-). Many etchants such as persulfate ($S_2O_8^{2-}$; E^0 = 2.0 V) [11], hydrogen peroxide (H_2O_2; E^0 = 1.78 V) [31] and coordination reagent, cyanide (CN^-) [11], hydrochloric acid (HCl; E^0 = 1.36 V) [26] and Pb^{2+} [36], etc. have been used in tailoring the Au NPs surface structure. Recently, Ag^+ ions have been used for lateral etching of Au nanorods, which gave rise to dumbbell like nanorods [37]. A variety of geometries from Ag octahedron were obtained by using NH_4OH/H_2O_2, with PVP as the capping agent [38]. Fan et al. [39] reported a versatile method for the selective etching of edges and facets of various shaped Au nanocrystals using surface-free-energy-distribution modifier. Besides this, Cu^{2+} ions are proposed to oxidize the Au nanorods to shorter rods in synergistic effect with dissolved O_2 [40], CTAB [41], H_2O_2 [42], KI [43] and Fe^{3+} [44]. A redox reaction undergoes between the surface sites of Au NPs and an oxidant leading to the dissolution of Au surface atoms resulting in the formation of NPs having narrow size distributions. However, many of these oxidants are harmful, toxic and difficult to manage, though $KMnO_4$ is an easily available, inexpensive reagent in the laboratory that has easy handling, mild toxicity and high oxidation power. It possesses an electrochemical potential of E^0 = 1.51 V, which is still higher than E^0 = 0.96 V of Au^{3+}/Au^0 and may aid in a better way in altering the Au NPs surface morphology. Though, previous literature [11,26-31] has mainly reported the optical properties and morphological changes in Au NPs by various oxidants (H_2O_2, CN^-, etc.) but none has reported the impact of NPs etched by $KMnO_4$. So, the present work aims to determine the surface electro-kinetics of Au NPs, as the oxidative etching of Au^0 results in its gradual dissolution to Au^{3+} and, thereby, altering the surface charge of Au NPs, measured in the form of zeta potential, ξ [45,46]. This change in geometric facets and the electronic charge residing over the Au NP surface could influence the absorption of reacting substrates and, thereby, improving its catalytic effects. Therefore, the oxidative dissolution of Au nanospheres (Au NS) and Au nanorods (Au NR) by aqueous $KMnO_4$ has been carried out for the formation of various anisotropic shapes to investigate their surface electro-kinetics and catalytic properties.

6.2 Experimental

6.2.1 Materials

Cetyltrimethylammoniumbromide (CTAB, $C_{19}H_{42}BrN$) and Silver nitrate ($AgNO_3$) were purchased from Sigma Aldrich and Fischer Scientific, India, respectively. Chloroauric acid ($HAuCl_4.3H_2O$), ascorbic acid ($C_6H_8O_6$), sodium borohydride ($NaBH_4$), potassium permanganate ($KMnO_4$), *p*-nitrobenzoic acid ($C_7H_5NO_4$) and *p*-nitrophenol ($C_6H_5NO_2$) were obtained from Loba Chemie, India. All the chemicals were used without any further purification and de-ionized water was obtained using a Milli-*Q*, Millipore ultra-filtration system with a measured conductivity of above 35 mho cm^{-1} at 25 °C.

6.2.2 Preparation of Au Nanospheres and Au Nanorods

The Au NS and Au NR were prepared by the reported [12,47] seed-mediated method. The seed solution of Au was prepared by reducing an aqueous mixture (10 mL) comprising CTAB (7.5 mL, 100 mM) and $HAuCl_4.3H_2O$ (250 µL, 10 mM) by $NaBH_4$ solution (600 µL, 10 mM). Then, these prepared Au seeds (ca. 5 mL) were added into the growth solution (50 mL) containing $HAuCl_4.3H_2O$ (2.5×10^{-4} M), CTAB (0.08 M) and ascorbic acid (250 µL, 100 mM) giving the wine red color to the Au NS solution. Whereas for the preparation of Au NR, 220 µL of above prepared seed solution was added into the growth solution (50 mL) comprising of $HAuCl_4.3H_2O$ (2 mL, 10 mM), CTAB (47.2 mL, 100 mM), $AgNO_3$ (300 µL, 10 mM) and ascorbic acid (320 µL, 100 mM). The appearance of the deep blue colored solution indicated the formation of Au NR. The as-synthesized different Au NPs were then repeatedly washed with de-ionized water under centrifugation at 8500 rpm for 5-10 min and re-dispersed in water.

6.2.3 Etching of Au Nanospheres and Au Nanorods

The oxidative etching of Au NS and Au NR was carried out by adding different volumes of $KMnO_4$ (20-120 µL, 100 mM) into 1 mL of NPs solution diluted in 1 mL of de-ionized water with simultaneous stirring. Then, the surface plasmon change in Au NPs was measured after each addition of $KMnO_4$ at regular intervals of time. The etched NPs were then washed with deionized water using centrifugation (8000 rpm for 5 min) and re-dispersed in water.

6.2.4 Characterization

The as-prepared etched Au NPs were characterized by UV-Vis spectrophotometer (Analytica Jena specord 205), Transmission electron microscopy, TEM (Hitachi 7500, 2Å, 120 KV) and an energy dispersive X-ray (EDX) analysis. The hydrodynamic diameter of Au NPs before and after the etching process was determined by taking 2-3 mL solution of Au NPs containing $KMnO_4$ (100 µL, 100 mM) in a cuvette at different intervals of etching time using a Brookhaven 90 plus

Particle Size Analyzer. The zeta potential (ζ) values were measured on Brookhaven zeta plus by taking 1.5-2 mL solution in a cuvette into which the palladium electrode attached to a support was dipped.

6.2.5 Electrochemical Properties

The cyclic voltammetry (CV) experiment was carried out with DY2300 potentiostat (Digi-Ivy) which comprises a platinum wire, Ag/AgCl and platinum as the counter, reference and working electrode, respectively, immersed in etched Au NS solution. This experiment for the redox probes Au^0/Au^{3+} was performed in 0.5 M H_2SO_4 electrolyte between the ranges of -0.2 V to 1.5 V at a scan rate 0.1 VS^{-1}. The potentiometric titration for the electrode potential of Au^0/Au^{3+} determination was performed with an Equiptronics Eq-602 potentiometer comprising a calomel and platinum electrode as the reference and working electrode, respectively, immersed in the solution (2 mL) of Au NS and Au NR. Then, the Au NPs solution was titrated with $KMnO_4$ solution (20-150 µL, 100 mM) and corresponding EMF values were noted after each addition.

6.2.6 Catalytic Activity

The catalytic performances of different etched Au NPs compared to bare unetched Au NPs were tested for the reduction of (5 mL, 0.2 mM) *p*-nitrophenol (PNP) and *p*-nitrobenzoic acid (PNB) containing ice-cold $NaBH_4$ solution (100 µL, 0.01 M) and calculated amounts of Au NPs (6.1×10^{15} atoms). The reaction samples were analyzed by UV-Vis spectrophotometer by measuring the absorption maxima ($\lambda_{max.}$ of PNP ~ 400 nm and PNB ~ 260 nm) at regular intervals of time and further, the quantification of the products was done by HPLC.

6.3 Results and Discussion

6.3.1 Optical Properties

The bare Au NS exhibited the characteristic surface plasmon (SP) band at 536 nm, which was blue-shifted to 530 nm and 527 nm (Fig. 6.1a) with the gradual decrease in the peak intensity during 20-30 min of $KMnO_4$ etching. It was accompanied by a color variation from wine-red to orange as displayed in the inset of Fig. 6.1a. This is in agreement with the report [48], where the magnitude of absorption of the Au NPs was seen to decrease due to their transformation into quantum-sized NPs by cysteine. In case of Au NR, the longitudinal surface plasmon (LSP) band (679 nm) showed a blue-shift to 663 nm and 645 nm during 10-20 min of etching, while the transverse surface plasmon (TSP) band remained at 533 nm, with a decrease in intensity of both

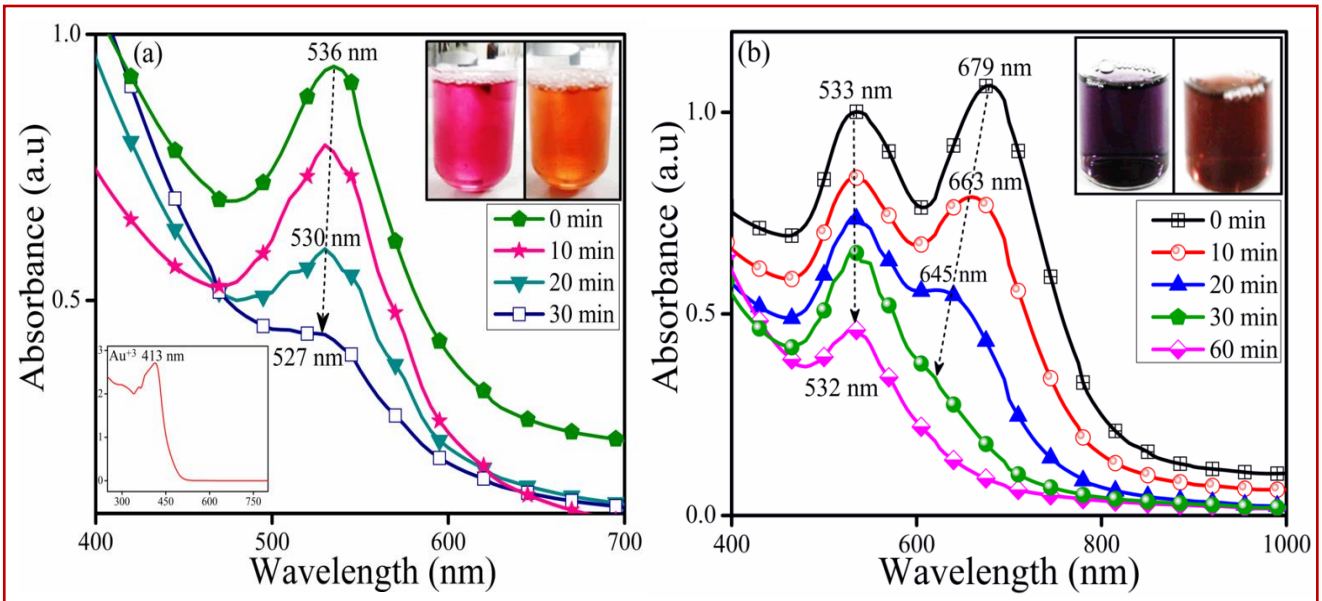

Fig. 6.1. Surface plasmon band change during the etching of **(a)** Au nanospheres, and **(b)** Au nanorods with $KMnO_4$ (100 µL, 100 mM) and inset shows the color change of Au nanoparticles before and after etching.

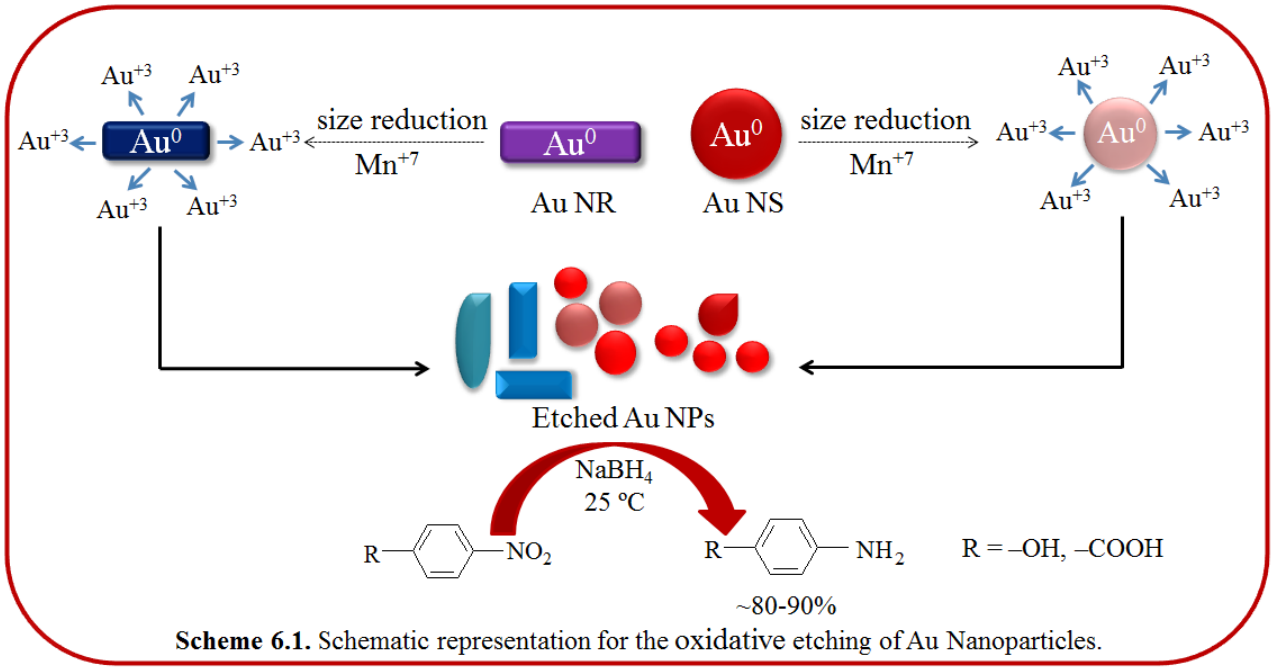

Scheme 6.1. Schematic representation for the oxidative etching of Au Nanoparticles.

the absorption bands as seen in Fig. 6.1b. This appearance of a blue shifted longitudinal band suggested that the dissolution started from the long ends of Au NR [11]. Further up to 40 min of etching, the LSP and TSP absorption bands of Au NR merged at λ_{max} = 532 nm of reduced intensity along with a notable color change from violet to red (Fig. 6.1b-*inset*). This result was similar to the reported LSP and TSP merger of Au NR at λ_{max} = 529 nm upon oxidation with

H_2O_2 [31]. These SP band variations indicated the morphological changes in Au NPs, as the plasmon bands are highly dependent on the shape, size and concentration of the NPs. However, the absorption peak of these etched Au NPs (Fig. 6.1) were different from the Au^{3+} (~413 nm, Fig. 6.1a-*inset*) suggesting that the Au NPs were not entirely oxidized to Au^{3+}. As the reduction potential of $KMnO_4$ (E^0 = 1.51 V) is higher than the Au^{3+}/Au^0 (E^0 = 0.96 V), therefore, a redox reaction occurs between the surface of Au NPs and an oxidant, resulting in the gradual layer by layer removal of Au surface atoms through its oxidative etching to Au^{3+} as illustrated in Scheme 6.1. This whole process leads to the morphological transformation of Au NPs having narrow size distribution. For example, the formation of spherical Au nanocrystals was reported through the aging of polyhedral Au nanostructures with Au^{3+} [27].

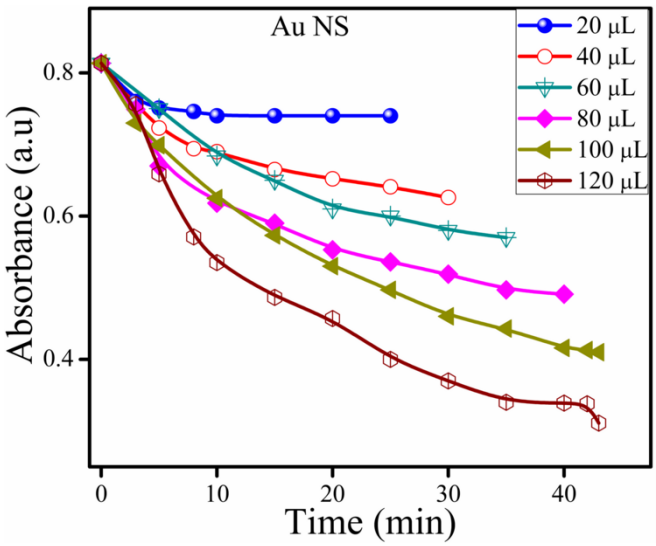

Fig. 6.2. Time course graph showing the effect of different amount of $KMnO_4$ on the absorbance of Au nanospheres.

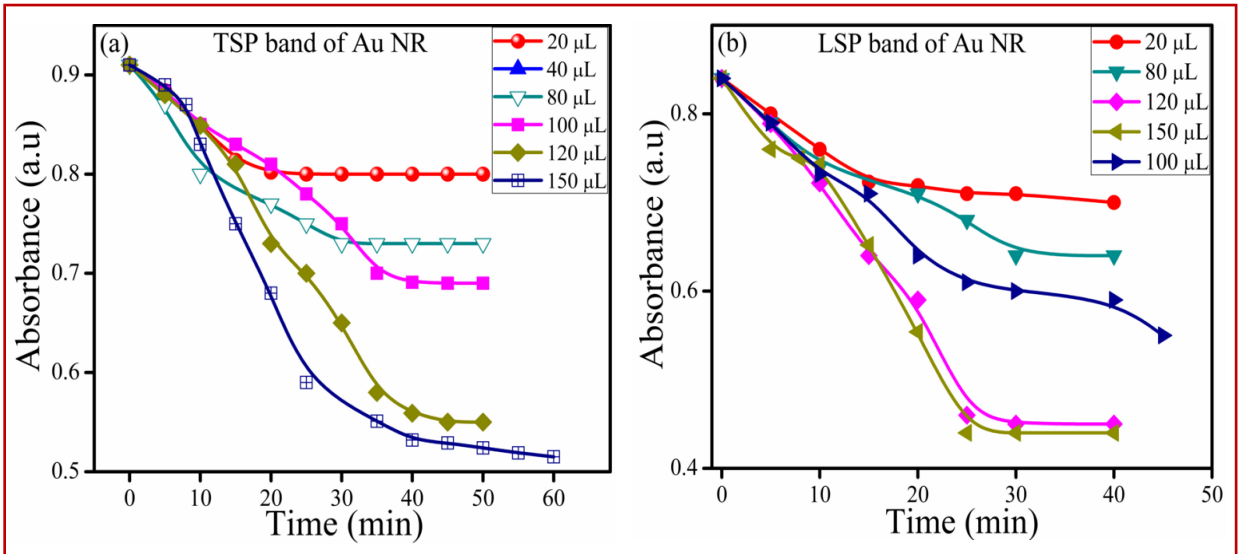

Fig. 6.3. Time course graph showing the effect of different amount of $KMnO_4$ on the absorbance of **(a)** transverse surface plasmon band, and **(b)** longitudinal surface plasmon band of Au nanorods.

The absorption intensity corresponding to the TSP band of Au NS (Fig. 6.2) and TSP (Fig. 6.3a) and LSP (Fig. 6.3b) bands of Au NR decreased exponentially with the gradual addition of $KMnO_4$, resembling first order reaction ($C_t = C_o e^{-kt}$) kinetics for the Au NPs dissolution. The rate of etching increased with the addition of $KMnO_4$ (20-150 µL) due to the gradual removal of Au atoms, however, it slowed down beyond 100-150 µL $KMnO_4$ usage. The rate of decrease in LSP band intensity was observed to be faster than the TSP band of Au NR due to the progressive shortening of rod length.

6.3.2 Dynamic Light Scattering and Morphological Studies

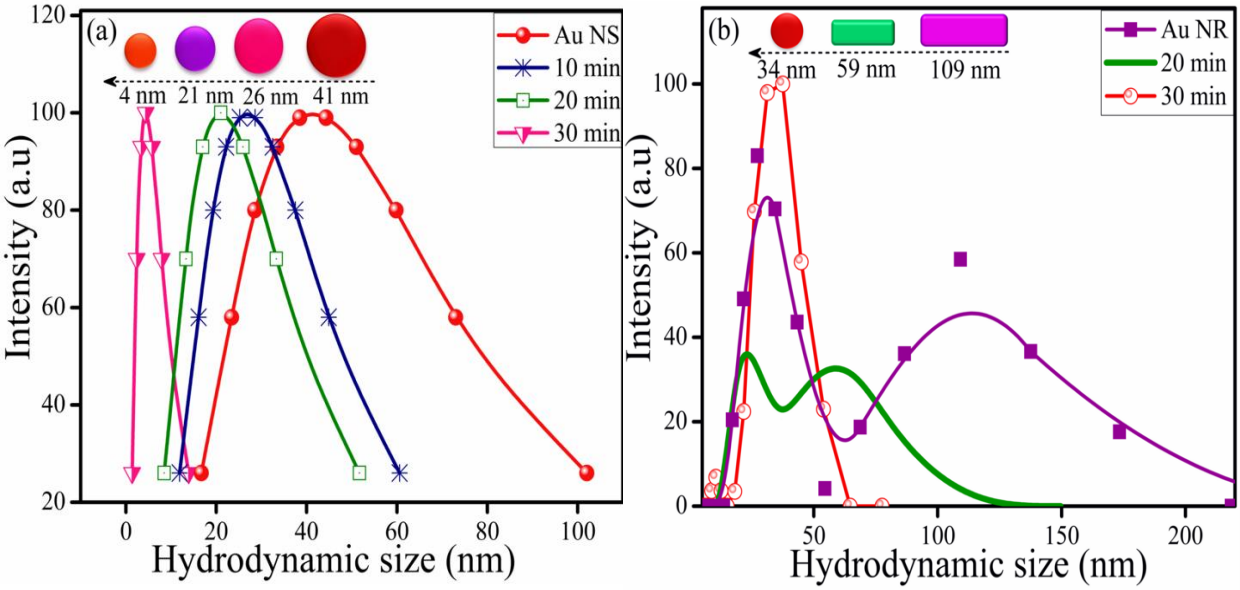

Fig. 6.4. Effect of $KMnO_4$ oxidative etching on DLS particle size distribution of **(a)** Au nanospheres, and **(b)** Au nanorods as a function of time.

The observed blue-shifts in the SP bands after $KMnO_4$ etching as noted in Fig. 6.1 can be attributed to the narrowing of size of Au NPs, which can be evidenced by dynamic light scattering (DLS) particle size distribution. It revealed that the average hydrodynamic diameter of Au NS (~41 nm) reduced to ~26 nm, ~20 nm and gradually to ~4 nm during 10-30 min of $KMnO_4$ etching (Fig. 6.4a) indicating the progressive decrease in size due to the etching of Au NS by $KMnO_4$. In case of Au NR, the bimodal particle distribution was observed, which showed a broader range of particle diameter of ~109 nm (aspect ratio ~3-3.5) that decreased to ~59 nm (Fig. 6.4b) after 20 min of etching. This fact indicated that the Au NR was transformed to shorter dimensions due to the gradual oxidative removal of Au atoms from the surface of Au NPs. The bare and etched Au NR showed another size distribution at ~27 nm and ~23 nm, respectively,

which signifies the rotational diffusion coefficient of the non-spherical nanorods as reported elsewhere [49-51]. Further, after 30 min of the etching process in Au NR, the DLS analysis showed a monomodal size distribution having an average diameter of ~37 nm, similar to Au NS, thereby confirming the conversion of rods into spherical particles.

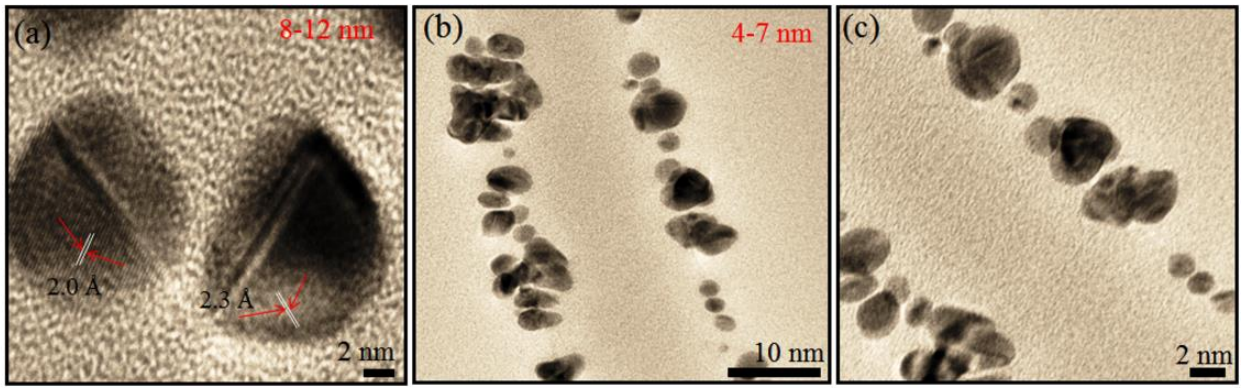

Fig. 6.5. TEM images of Au nanospheres after oxidative etching by $KMnO_4$.

TEM analysis further revealed the decrease in size of well-dispersed Au NS (~15 nm) to particle size ~8-12 nm having kinked structure (Fig. 6.5) after $KMnO_4$ etching. The Au NS was changed into anisotropic truncated nanostructures due to the haphazard and localized oxidative dissolution of the Au NS surface as can be clearly seen in Fig. 6.5a. The fringe spacings are measured to be 2.0 Å and 2.3 Å (Fig. 6.5a), which well corresponded with the (200) and (111) planes of the FCC Au (2.039 Å and 2.355 Å, JCPDS card no. 04-07484, respectively). Further, etching of Au NS led to their transformation into many deformed and distorted particles of size ~4-7 nm (Fig. 6.5b-c) with rough surfaces. On the other hand, the starting bare Au NR exhibiting an aspect ratio of ~3-3.5 (Fig. 6.6a) showed the reduction in length from ~25 nm to ~15-17 nm (aspect ratio ~2.6) due to the gradual etching of Au atoms at the extremity of rods as observed in Fig. 6.6b. The etching of Au NR also led to the formation of spheroids of size ~13-17 nm (~70-80%) and ~22-28 nm (~20-30%). An intermediate stage exhibited the clubbing of different anisotropic NPs together (Fig. 6.6c) followed by a quick dissolution and then consequently, fragmented (Wang et al. [48]) into a large number of smaller, distorted spherical shape particles of size ~1-3 nm (80-90%) and ~9-10 nm (10-20%) as seen in Fig. 6.6d. These results were similar to the literature [11,27,31], where H_2O_2, $S_2O_8^{2-}$ and Au (III) aided in progressive shortening of Au NR and eventually their transformation into nanospheres of narrow size distribution. The elemental analysis of bare CTAB-capped Au NS (Fig. 6.7a) displayed the

presence of Au, 90.2 atomic % and traces of Br, 9.8 atomic % due to the CTAB surfactant used during their preparation. On the other hand, the washed $KMnO_4$ (Fig. 6.7b) etched Au was found to be composed of Au, 75 atomic % and some traces of Mn in 24 atomic % due to the presence of residual oxidant.

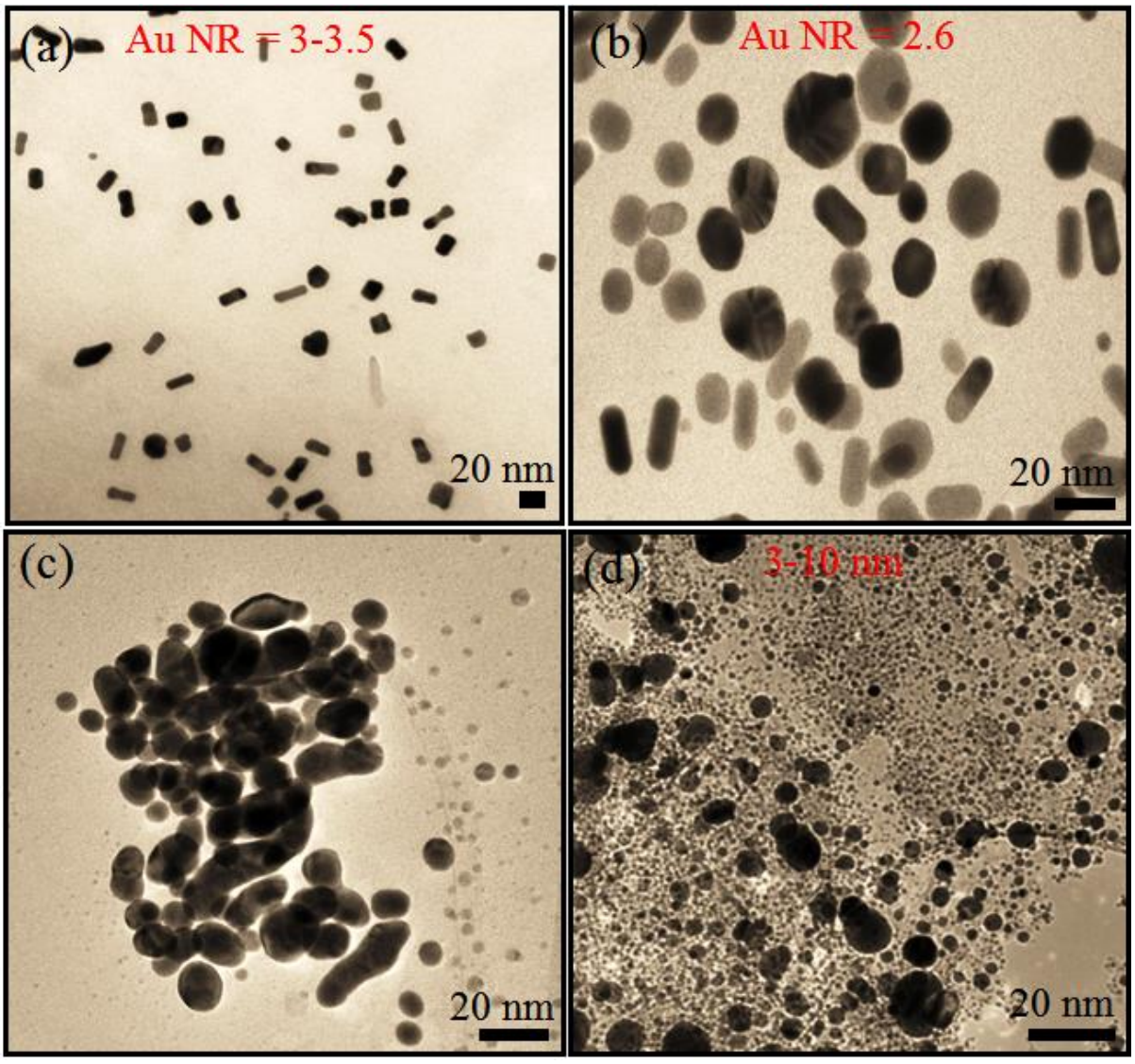

Fig. 6.6. TEM images of **(a)** bare Au nanorods before, and **(b-d)** after oxidative etching by $KMnO_4$.

6.3.3 Electrokinetic Parameters

It is assumed that the surface atoms of Au NPs i.e., Au^0 by oxidation with Mn^{+7} ions may produce Au^{3+} and Mn^{+2} ionic species in the solution and hence, developing an electrical double layer on the surface of etched Au NPs. Consequently, the net surface charge as well as the

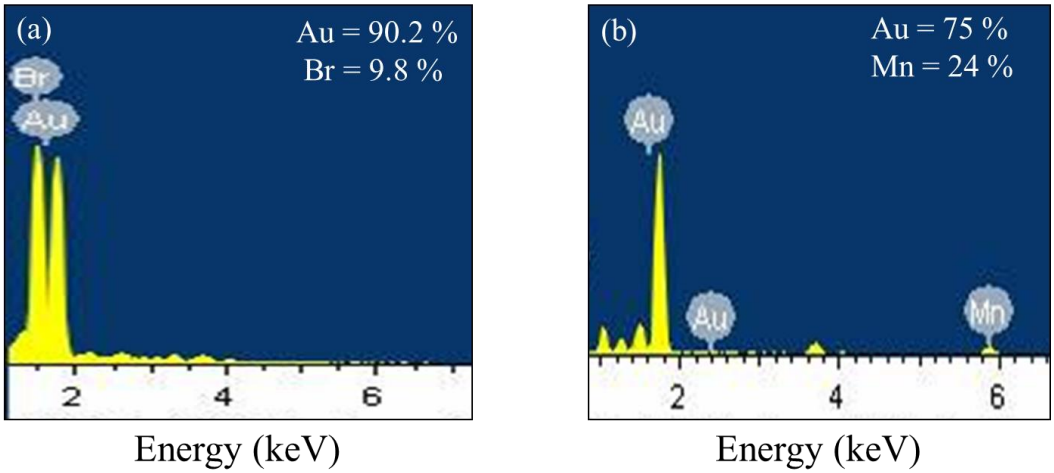

Fig. 6.7. EDX pattern of **(a)** bare Au nanospheres, and **(b)** $KMnO_4$ etched Au nanospheres.

conductance of the Au NPs solution was measured to be changed before and after the etching reaction. Therefore, the zeta potential (ζ) of bare Au NS (+ 37.8 ± 3.3 mV) was measured to increase to +44.08 ± 2.7 mV and +57.9 ± 4.1 mV during 10-30 min of $KMnO_4$ etching. This was corresponded with markedly higher conductance values (1107 to 1390 µS) due to these surfaces adsorbed ionic species as displayed in Fig. 6.8a. A similar trend was also observed during gradual etching of Au NR at various times (Fig. 6.8b), where ζ of bare Au NR +33.81 ± 4.4 mV was increased to +37.93 ± 3.3 mV and +47.35 ± 4.5 mV and conductance was significantly enhanced from 420 to 990 µS after 40 min of $KMnO_4$ etching. This high zeta potential values

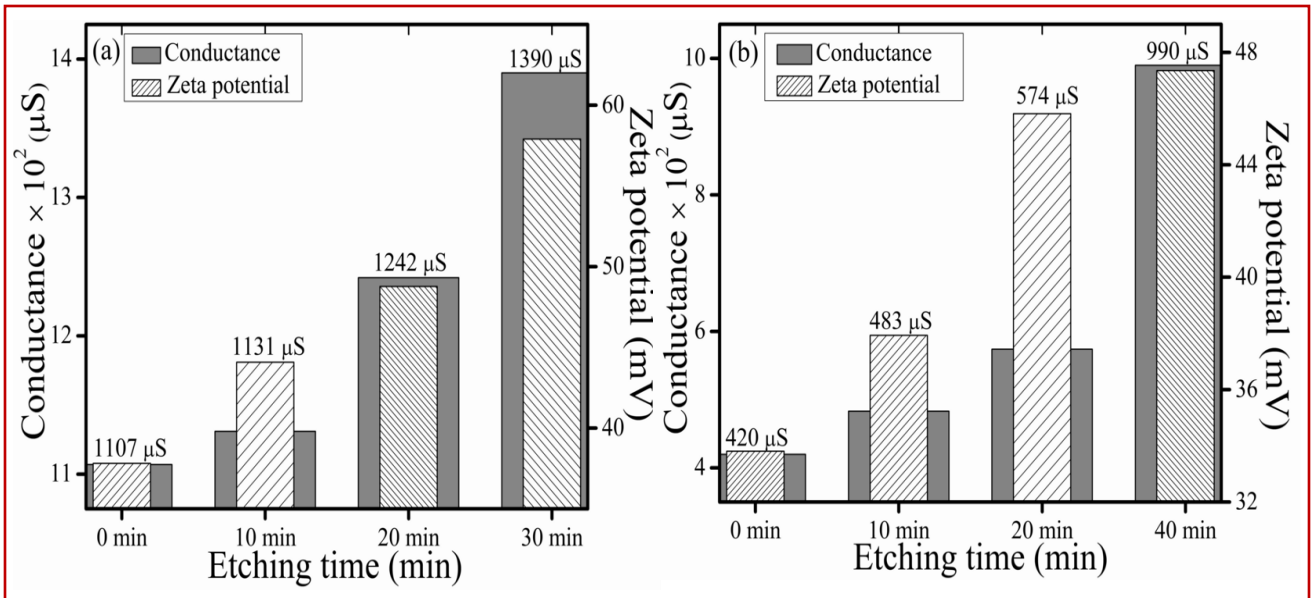

Fig. 6.8. Variation of zeta potential and conductance during oxidative etching of **(a)** Au nanospheres, and **(b)** Au nanorods by $KMnO_4$ (100 µL, 100 mM) at different intervals of time.

may lead to the suspension stability of etched Au NPs, which prevents the agglomeration of smaller Au NPs and thus, exhibiting an efficient optical and catalysis process [3,52].

6.3.4 Electrochemical Properties

The electrochemical study of etched Au NPs was carried out by cyclic voltammetry (CV) in order to confirm the Au^0/Au^{3+} redox couple formation. The bare $KMnO_4$ exhibited a small peak at 0.83 V, while no characteristic peak was found for bare Au NS confirming the absence of a redox probe couple Au^0/Au^{3+}. However, after 10 min of $KMnO_4$ oxidative etching of the Au NS, an anodic peak at -0.90 V (Fig. 6.9) was observed in good accordance with the standard electrode potential value of Au^0/Au^{3+} (E^0 = -0.96 V) supporting the Au^{3+} formation. Another intense peak at -1.1 V was possibly due to the Mn^{+2}/Mn^{+7} redox couple in close proximity to its standard value (-1.5 V). The anodic peak of Au^0/Au^{3+} gradually exhibited a negative shift [53] due to the decrease in size of the NPs with etching time (10-30 min) as supported by various experimental and theoretical results [54,55].

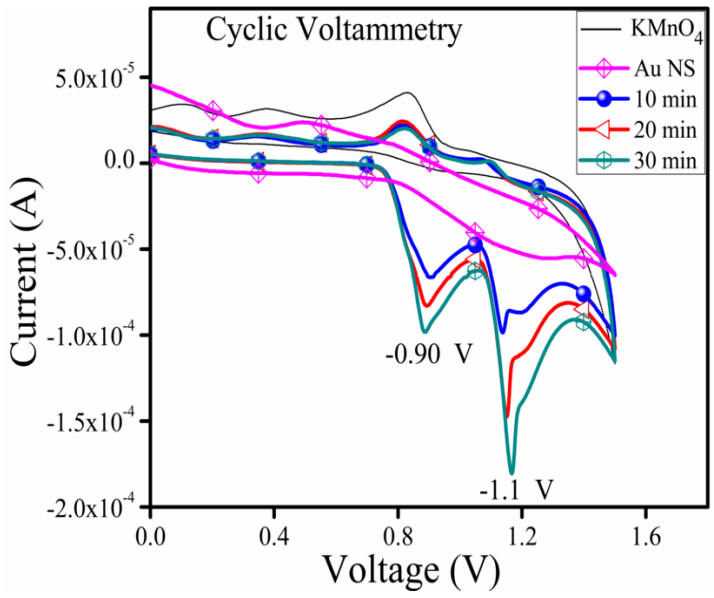

Fig. 6.9. Cyclic Voltammetry studies of $KMnO_4$ etched Au nanospheres in 0.5 M H_2SO_4 electrolyte.

The potentiometric titration of a certain amount of Au NS and Au NR with aqueous $KMnO_4$ exhibited S-shaped curve as shown in Fig. 6.10. On adding $KMnO_4$ to Au NPs solution, the amount of Au^0 gradually decreased with simultaneous increase in Au^{3+} concentrations, resulting in a slight increase in the EMF of the cell. After certain addition of $KMnO_4$ (beyond 120 µL), a sudden increase in the EMF of the cell was observed due to a complete oxidation of all Au^0 atoms into Au^{3+} ions. The calculated electrode potential, $E^0_{(Au^{3+}/Au^0)}$= 0.79 V and 0.75 V (calculated below) at half wave potential for Au NS and Au NR, respectively, differs slightly from its standard value (0.96 V) possibly because of the presence of K^+ and Mn^{+7}/Mn^{+2} species. Hence, the electrochemical studies support the morphological conversion of Au NPs through its oxidative dissolution to Au^{3+} as demonstrated by the above results.

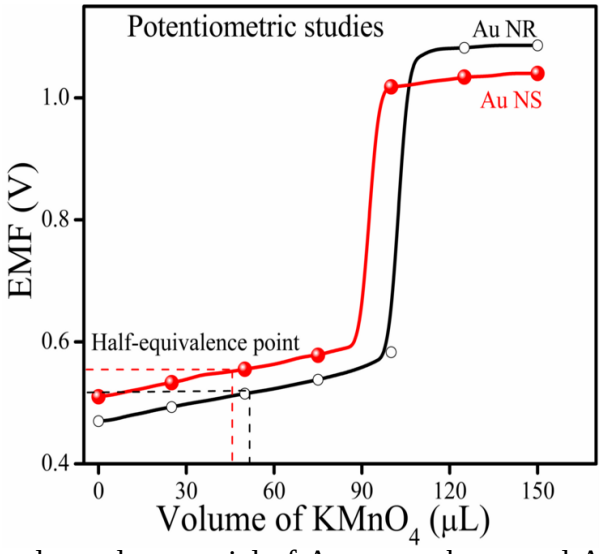

Fig. 6.10. Change in electrode potential of Au nanospheres and Au nanorods as a function of different amount of $KMnO_4$.

$$E_{(\text{half equivalence})} = E^0_{(Au^{+3}/Au^0)} - 0.242 \quad (6.1)$$

$$E^0_{(Au^{+3}/Au^0)} = E_{(\text{half equivalence})} + 0.242 \quad (6.2)$$

$$E^0_{(Au^{+3}/Au^0)} = 0.55\ V + 0.242 = 0.79\ V \quad \text{(Au NS)} \quad (6.3)$$

$$E^0_{(Au^{+3}/Au^0)} = 0.51\ V + 0.242 = 0.75\ V \quad \text{(Au NR)} \quad (6.4)$$

6.3.5 Catalytic Activity

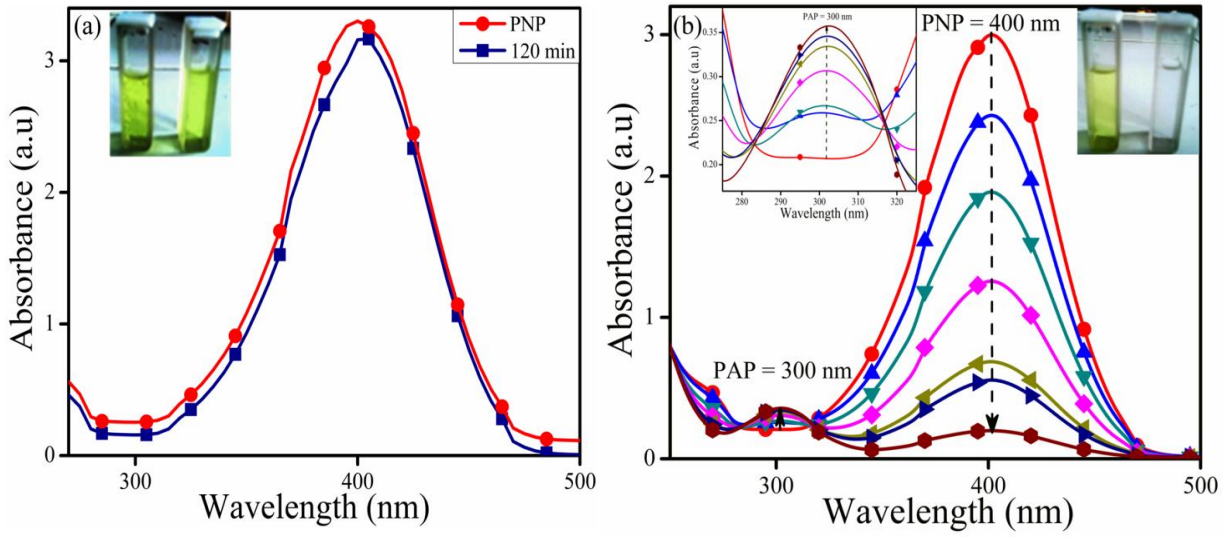

Fig. 6.11. Changes in absorption spectra of **(a)** *p*-nitrophenol (PNP) reduction by $NaBH_4$ in the **(a)** absence of nanoparticles, and **(b)** in the presence of Au nanopheres and inset show the enlarged view of formation of *p*-aminophenol (PAP).

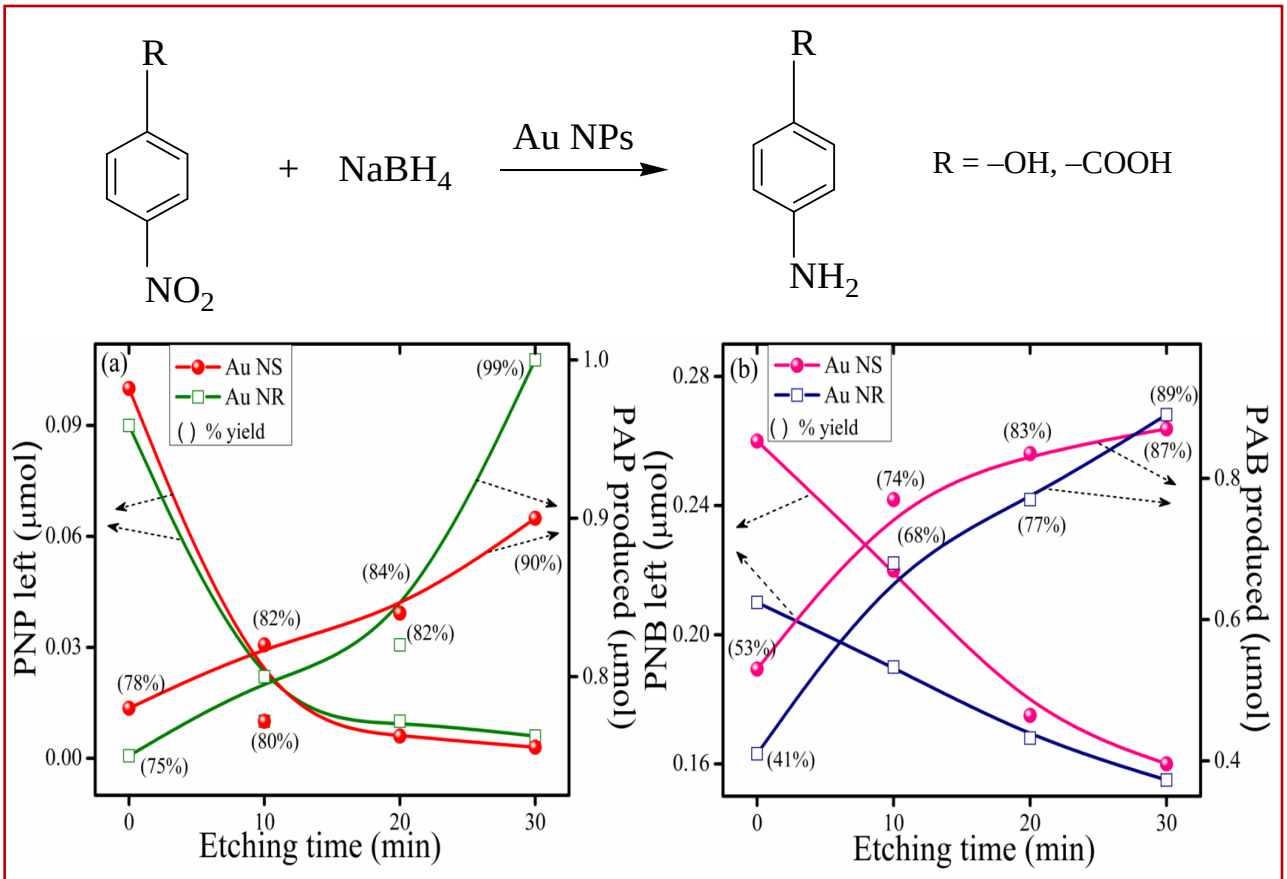

Fig. 6.12. Catalytic activity of Au nanospheres and Au nanorods at different time of $KMnO_4$ etching showing the reduction of **(a)** *p*-nitrophenol to *p*-aminophenol, and **(b)** *p*-nitrobenzoic acid to *p*-aminobenzoic acid.

The anisotropic etched Au nanostructures and bare unetched Au NPs have been utilized to account the comparative catalytic reduction of *p*-nitrophenol (PNP) and *p*-nitrobenzoic acid (PNB) to *p*-aminophenol (PAP) and *p*-aminobenzoic acid (PAB), respectively, by $NaBH_4$. The reduction of PNP to PAP by $NaBH_4$ in the absence of catalyst displayed no change in absorption maxima (400 nm) and color of PNP (Fig. 6.11a) up to 120-150 min. However, the absorption band intensity of PNP at 400 nm was gradually decreased with the emergence of new peak at 300 nm, corresponding to the PAP formation (Fig. 6.11b) with the addition of Au NS to the reaction medium. Therefore, the existence of metal NPs as a catalyst is very necessary for the commencement of the reduction reaction as the yellowish-green color of PNP was also disappeared (inset, Fig. 6.11b). Fig. 6.12 displayed that the etched Au NPs formed at different time of oxidative etching with $KMnO_4$ showed improved reduction reactions than the bare unetched Au NPs as a function of dimensions, high surface to volume ratio, or surface exposed

Table 6.1. Calculations of surface area to volume ratio of Au nanospheres.

S.No.	Diameter (nm)	Radius (nm)	Volume of sphere, $4/3\ \pi r^3$ (nm^3)	Surface Area of spheres, $4\pi r^2$ (nm^2)	Surface/Volume Ratio (nm^{-1})
			Etched NS (a)		
1.	10	5	523.3	314	0.6
			Etched NS (b)		
2.	7.5	3.7	212	171.9	0.81
3.	5	2.5	65.4	78.5	1.2
			Etched NS (c)		
4.	4.2	2.1	38.7	55.3	1.4

planes of Au nanocatalysts. The bare Au NS and Au NR displayed almost similar catalytic activity for the reduction PNP to PAP (yield = ~75-78%), however, a large difference in catalytic efficiency was observed after surface etching with $KMnO_4$ as shown in Fig. 6.12a. The PAP yield was highly enhanced to ~80-99% during the PNP reduction by Au NPs formed at different times of etching which took a significantly lesser time (20 min) than bare Au NPs (30-37 min). Similarly, the reduction of PNB exhibited higher yield of PAB (~68-89%) in comparison to bare unetched Au NPs (~41-53%) as seen in Fig. 6.12b. The superior catalytic activity of etched NPs can be explained due to their fragmentation into a large number of smaller size NPs (~3-4 nm) per-unit volume having a larger surface to volume ratio (Au NS = ca. 1.4 nm^{-1} and Au NR = 4.6 nm^{-1}) relative to bare unetched Au NS and Au NR with lesser surface to volume ratio 0.6 nm^{-1} and 0.47 nm^{-1}, respectively, (Table 6.1 and 6.2). This might result in the effective adsorption of reactant substrates on the surface of etched Au NS and Au NR [56] and, thereby, significantly enhanced (almost doubles) the catalytic activity. A similar result was also reported [8] for the reduction of *p*-nitroaniline, where Au NS exhibited a higher rate of reaction due to their higher surface area than that of the Au nanoprisms and Au NR. Besides, the rough surfaces of NPs and fresh-surface exposed atoms, achieved during the etching process shows more valency-unsaturated surface atoms which serve as active bonding sites [9,57] for superior catalytic performances. Thus, the surface morphology of Au nanostructures can be appropriately altered by the oxidative dissolution of Au surface atoms using $KMnO_4$ as an oxidant for improved catalysis and selectivity for many synthetic organic reactions.

Table 6.2. Calculations of surface area to volume ratio of Au nanorods.

S.No.	Length (nm)	Width (nm)	Radius (nm)	Volume of cylinder, $\pi r^2 h$ (nm^3)	Surface area, $2\pi r^2+2\pi rh$ (nm^2)	Surface/Volume Ratio (nm^{-1})
			Au NR (a)			
1.	21	7.1	5.25	1820.9	866.6	0.47
2.	25	7.1	5.25	9173.9	1046.7	0.11
			Etched Au NR (b)			
3.	15.5	6.6	3.3	531.3	390.3	0.73
4.	17.7	6.6	3.3	607.2	368	0.6
	Diameter (nm)		**Radius (nm)**	**Volume of sphere, $4/3\ \pi r^3$ (nm^3)**	**Surface Area of sphere, $4\pi r^2$ (nm^2)**	**Surface/Volume Ratio (nm^{-1})**
			Etched Au NR (c)			
5.	10.9		5.45	678.3	373	0.55
6.	13		6.58	1192.7	543.8	0.45
			Etched Au NR (d)			
7.	9.3		4.6	407.5	265.7	0.65
8.	3.9		1.95	31.04	47.7	1.53
9.	2.6		1.3	9.1	21.2	2.3
10.	1.3		0.65	1.14	5.3	4.65

6.4 Conclusions

In summary, the oxidative etching of Au NPs by a common oxidizing reagent, $KMnO_4$, is an effective post-synthesis tool for the morphological transformation and fragmentation into a large number of smaller size reactive Au nanocatalysts. This process has the advantage that the single starting NPs can be repeatedly used to obtain Au NPs of different sizes, possessing fresh active surface atoms using $KMnO_4$ as an oxidant. Therefore, anisotropic Au NPs with rough and asymmetric surfaces having high surface to volume ratio can be prepared at ease for optimum catalytic activity.

6.5 References

[1] C. Burda, X. Chen, R. Narayanan and M. A. El-Sayed, *Chem. Rev.*, 2005, **105**, 1025–1102.

[2] S. Eustis and M. A. El-Sayed, *Chem. Soc. Rev.*, 2006, **35**, 209–217.

[3] R. Kaur and B. Pal, *J. Mol. Catal. A: Chem.*, 2012, **355**, 39–43.

[4] R. Singh and B. Pal, *J. Mol. Catal. A: Chem.*, 2013, **378**, 246–254.

[5] I. Lee and F. Zaera, *J. Catal.*, 2010, **269**, 359–366.

[6] R. Narayanan and M. A. El-Sayed, *Nano lett.*, 2004, **4**, 1343–1348.

[7] R. Narayanan and M. A. El-Sayed, *J. Am. Chem. Soc.*, 2004, **126**, 7194–7195.

[8] S. Kundu, S. Lau and H. Liang, *J. Phys. Chem. C*, 2009, **113**, 5150–5156.

[9] M. A. Mahmoud, R. Narayanan and M. A. El-Sayed, *Acc. Chem. Res.*, 2013**, 46,** 1795–1805.

[10] J. Y. Kim, K. J. Ihn and J. S. Na, *J. Ind. Eng. Chem.*, 2011, **17**, 248–253.

[11] N. R. Jana, L. Gearheart, S. O. Obare and C. J. Murphy, *Langmuir*, 2002, **18**, 922–927.

[12] N. R. Jana, L. Gearheart and C. J. Murphy, *Langmuir*, 2001, **17**, 6782–6786.

[13] N. R. Jana, L. Gearheart and C. J. Murphy, *Adv. Mater.*, 2001, **13**, 1389–1393.

[14] N. R. Jana, L. Gearheart and C. J. Murphy, *J. Phys. Chem. B*, 2001, **105**, 4065–4067.

[15] K. D. Lee, P. C. Nagajyothi, T. V. M. Sreekanth and S. Park, *J. Ind. Eng. Chem.*, 2015, **26**, 67–72.

[16] P. Kuppusamy, M. M. Yusoff, S. J. A. Ichwan, N. R. Parine, G. P. Maniam and N. Govindan, *J. Ind. Eng. Chem.*, 2015, **27**, 59–67.

[17] K. Anand, R. M. Gengan, A. Phulukdaree and A. Chuturgoon, *J. Ind. Eng. Chem.*, 2015, **21**, 1105–1111.

[18] P. Murawala, A. Tirmale, A. Shiras and B. L. V. Prasad, *Mater. Sci. Eng. C*, 2014, **34**, 158–167.

[19] W. Guo, Y. Pi, H. Song and W. Tang, *J. Colloids Surf. A*, 2012, **415**, 105–111.

[20] K. S. Chen, T. S. Hung, H. M. Wu, J. Y. Wu, M. T. Lin and C. K. Feng, *Thin Solid Films*, 2010, **518**, 7557–7562.

[21] R. Narayanan, C. Tabor and M. A. El-Sayed, *Top Catal.*, 2008, **48**, 60–74.

[22] J. Zeng, Q. Zhang, J. Chen and Y. Xia, *Nano Lett.*, 2010, **10**, 30–35.

[23] M. B. Mohamed, K. Z. Ismail, S. Link and M. A. El-Sayed, *J. Phys. Chem. B*, 1998, **102**, 9370–9374.

[24] S. Link, C. Burda, B. Nikoobakht and M. A. El-Sayed, *J. Phys. Chem. B*, 2000, **104**, 6152–6163.

[25] S. S. Chang, C. W. Shih, C. D. Chen, W. C. Lai and C. R. C. Wang, *Langmuir*, 1999, **15**, 701–709.

[26] C. K. Tsung, X. Kou, Q. Shi, J. Zhang, M. H. Yeung, J. Wang and G. D. Stucky, *J. Am. Chem. Soc.*, 2006, **128**, 5352–5353.

[27] J. R. Fernandez, J. P. Juste, P. Mulvaney and L. M. L. Marzan, *J. Phys. Chem. B*, 2005, **109**, 14257–14261.

[28] A. Rai, A. Singh, A. Ahmad and M. Sastry, *Langmuir*, 2006, **22**, 736–741.

[29] Z. L. Wang, R. P. Gao, B. Nikoobakht and M. A. El-Sayed, *J. Phys. Chem. B*, 2000, **104**, 5417–5420.

[30] T. S. Sreeprasad, A. K. Samal and T. Pradeep, *Langmuir*, 2007, **23**, 9463–9471.

[31] G. Chandrasekara, K. Mougina, H. Haidaraa, L. Vidala and E. Gnecco, *Appl. Surf. Sci.*, 2011, **257**, 4175–4179.

[32] J. Shao, E. A. Josephs, C. Lee, A. Lopez and T. Ye, *ACS Nano*, 2013, **7**, 5421–5429.

[33] S. Ye, C. Ishibashi and K. Uosaki, *Langmuir*, 1998, **15**, 807–812.

[34] C. M. Cobley, M. Rycenga, F. Zhou, Z. Y. Li and Y. Xia, *Angew. Chem., Int. Ed.*, 2009, **48**, 4824–4827.

[35] J. An, B. Tang, X. Zheng, J. Zhou, F. Dong, S. Xu, Y. Wang, B. Zhao and W. Xu, *J. Phys. Chem. C*, 2008, **112**, 15176–15182.

[36] D. Dai, D. Xu, X. Cheng and Y. He, *Anal. Methods*, 2014, **6**, 4507–4511.

[37] F. Xie, W. Ye, H. Y. Sun, S. Kou and X. Guo, *Langmuir*, 2015, **31**, 6823–6828

[38] M. J. Mulvihill, X. Y. Ling, J. Henzie and P. Yang, *J. Am. Chem. Soc.*, 2009, **132**, 268–274.

[39] N. Fan, Y. Yang, W. Wang, L. Zhang, W. Chen, C. Zou and S. Huang, *ACS Nano*, 2012, **6**, 4072–4082.

[40] T. Wen , H. Zhang, X. Tang , W. Chu, W. Liu, Y. Ji, Z. Hu, S. Hou, X. Hu and X. Wu, *J. Phys. Chem. C*, 2013, **117**, 25769–25777.

[41] Q. Zhu, J. Wu, J. Zhao and W. Ni, *Langmuir*, 2015, **31**, 4072–4077.

[42] G. Weng, J. Li, J. Zhu and J. Zhao, *J. Nanopart. Res.*, 2014, **16**, 2728.

[43] J. Wang, Y. F. Li and C. Z. Huang, *J. Phys. Chem. C*, 2008, **112**, 11691–11695

[44] R. Zou, X. Guo, J. Yang, D. Li, F. Peng, L. Zhang, H. Wang and H. Yu, *CrystEngComm.*, 2009, **11**, 2797–2803.

[45] B. Mukherjee and J. W. Weaver, *Environ. Sci. Technol.*, 2010, **44**, 3332–3338.

[46] T. Kim, K. Lee, M. Gong and S. W. Joo, *Langmuir*, 2005, **21**, 9524–9528.

[47] M. Eguchi, D. Mitsui, H. L. Wu, R. Sato and T. Teranishi, *Langmuir*, 2012, **28**, 9021–9026.

[48] T. Wang, X. Hu and S. Dong, *Chem. Commun.*, 2008, 4625–4627.

[49] J. R. Fernandez, J. P. Juste, L. M. L. Marzan and P. R. Lang, *J. Phys. Chem. C*, 2007, **111**, 5020–5025.

[50] B. N. Khlebtsov and N. G. Khlebtsov, *Colloid J.*, 2011, **73**, 118–127.

[51] H. Liu, N. P. Pierre and Q. Huo, *Gold Bull.*, 2012, **45**, 187–195.

[52] I. S. Grover, S. Singh and B. Pal, *Appl. Surf. Sci.*, 2013, **280**, 366–372.

[53] P. R. Chandran, M. Naseer, N. Udupa and N. Sandhyarani, *Nanotechnology*, 2012, **23**, 1–8.

[54] W. J. J. Plieth, *Phys. Chem.*, 1982, **86**, 3166–3170.

[55] O. S. Ivanova and F. P. Zamborini, *Anal. Chem.*, 2010, **82**, 5844–5850.

[56] N. Gupta and B. Pal, *J. Colloid Interface Sci.*, 2012, **368**, 250–256.

[57] R. Narayanan and M. A. El-Sayed, *J. Am. Chem. Soc.*, 2004, **126**, 7194–7195.

Conclusions and Future Outlook

Chapter 1 provides an introductory note on the importance of coinage metal nanoparticles (NPs) of different size and shape in catalysis. It gives an idea how the development of bimetallic (BM) nanocomposites (NCs) overcame their monometallic counterparts in diverse applications. This growing interest towards the coinage bimetallic NCs have been discussed due to electronic and ensemble effect which are responsible for the various unique properties especially in catalysis. A concise overview of the various studies carried out earlier in this work and the research gap found during their literature surveys are also presented. A short description of methodology and characterization techniques for the determination of optoelectronic, structural, photophysical and catalytic properties are also illustrated.

Chapter 2 and 3 summarizes the effect of the chemical nature of coinage metal core, shell-thickness and the shape (nanospheres and nanorods) of BM NCs on the optical properties, surface electro-kinetics and catalytic activities relative to their monometallic counterparts. The Ag and Au shell-thicknesses on Au and Ag cores, respectively, can be easily tuned by controlling the concentration of starting precursor solutions. Since the chemical properties of Au and Ag are different, therefore, resulted in the formation of different morphologies i.e., Au@Ag and hollow Ag-Au alloy shells during Ag deposition on Au core and vice-versa, respectively. These BM NCs exhibited improved catalytic activity than their respective monometallic NPs due to the electronic charge transfer at the interface of two metals resulting in net electron density change on the surface of resultant BM NPs promoting the catalytic reactions proficiently. The catalytic activity of core@shell BM NCs dramatically decreases after a certain shell-thickness attributed to the weaker electronic effect between the distant core and shell. Among the various BM NCs, hollow Ag-Au shells are concluded to be the best catalyst for the reduction process as they offer more activity sites for the reactant substrates in addition to the synergistic effect of two metals. However, by changing the morphology of Au@Ag BM NCs from spheres to rods displayed the selective formation of 3-nitroaniline from the reduction of 1,3-dinitrobenzene relative to 1,3-phenylenediamine ascribed to their surface area, without using any toxic solvents and harsh experimental conditions. Hence, these coinage BM NCs can be utilized for tuning the

selectivity and yield of the product as a function of metal compositions, shape and morphology for the different organic reaction.

Chapter 4 explores that the galvanic displacement reaction can be controlled through the modification of the Ag NPs surface, which acts as a versatile template for the Au deposition. Therefore, the surfactants like PVP, CTAB and Triton X-100 passivizing the Ag NPs surface played an important role in controlling the morphology of resulting Ag-Au BM NCs. This led to the formation of diverse morphologies i.e., hollow, solid and porous structures of Ag-Au BM NCs, which exhibited unique optical and surface properties, intense color variation and catalytic activity relative to the monometallic Ag NPs. This was ascribed to the difference in rate of reaction between the surfactants passivizing the Ag NPs surface and incoming Au^{3+} ions and subsequently, changing the galvanic Au deposition rate. Hence, this surface-directed synthetic strategy can be favorably used to tailor NPs morphology and, thereby, the catalytic performances for various organic syntheses.

Chapter 5 emphasizes that the TiO_2 photocatalyst loaded with Cu-M (M = Ag, Au) core@shell BM NCs promotes efficient reduction and oxidation reactions than their monometallic counterparts (Cu, Ag, Au-TiO_2,) under the visible light. This is ascribed to the decreased height of Schottky barrier at the BM-TiO2 interface, resulted from the decreased work function of monometallic NPs by Cu alloying. Among the different BM-TiO_2, Cu@Ag-TiO_2, Ag@Cu-TiO_2, showed the best photoactivity relative to Cu@Ag-TiO_2 and Ag@Cu-TiO_2 because of their lower calculated work function (3.8-4.1 eV) than the Cu@Au-TiO_2 and Au@Cu-TiO_2 (4.2-4.6 eV) and thereby, smooth e^- transfer from photoactivated NPs to TiO_2. Therefore, it has been revealed that the nature of metal also displays a great role in the heterogeneous photocatalysis systems. Hence, the knowledge of such photocatalytic systems could be beneficial in designing highly active photocatalysts.

Chapter 6 explores the cost-effective single step technique for the synthesis of multi size and shaped Au nanostructures through the oxidative dissolution of Au nanospheres and Au nanorods using $KMnO_4$. This process involves the gradual removal of Au surface atoms followed by its oxidative dissolution to Au^{3+} and as a result, led to the formation of anisotropic particles having

narrow size distribution without by means of any synthetic route. These etched Au NPs possess higher surface to volume ratio and valency unsaturated fresh surface atoms that greatly enhances the interaction of reacting substrates and, thereby, exhibits superior catalytic activity relative to bare Au NPs prior to etching. Hence, these prepared anisotropic Au NPs can be a promising catalyst in extensive areas of industrially important organic or biochemical systems.

Future Outlook

BM NCs, a new class of nanomaterials, have great potential in catalysis; however, there is tremendous scope in biomedicines, SERS, nanoelectronic devices, magnetic properties of ferromagnetic NCs and sensing applications, etc. With the aim of improvement of preparation, stability, activity, selectivity and recycling properties, the BM nanomaterials can be obtained with different anisotropic shapes, size, metal ratio and their effect on the semiconductors. The application of semiconductor modified BM NCs is an attractive research objective which not only exhibit the better catalytic activity than the monometallic modified semiconductors, but also extends the light absorption of wide band-gap semiconductor to the wide range visible light. It is also likely that the BM NCs can be used for the synthesis of fine chemicals, i.e., cross coupling reactions, etc. in which the high degree of selectivity is required. In the present thesis, the BM NCs is based on the noble metals and therefore, sometimes the high cost and the rare availability of the noble metals makes the development difficult. Hence, the combination of relatively cheap elements with the noble metal into one composite affords more opportunities to make more effective and economic catalyst. In contrast to BM NCs, the trimetallic and multimetallic NCs may possess an even greater degree of reactivity and selectivity as more parameters are available for regulation. However, there are very limited reports, but it is becoming a very hot topic of interest from last few years.

List of Publications

1. **Anila Monga** and Bonamali Pal, "Improved Catalytic Activity and Surface Electro-kinetics of Bimetallic Au-Ag Core-Shell Nanocomposites," published in ***New Journal of Chemistry*** 39 (2015) 304–313.
2. **Anila Monga** and Bonamali Pal, "Preparation and Characterization of Different Shapes of Au-Ag Bimetallic Nanocomposites for Enhanced Physicochemical Properties," published in ***Colloids and Surfaces A: Physicochemical and Engineering Aspects*** 481 (2015) 158–166.
3. **Anila Monga** and Bonamali Pal, "Morphological and Physicochemical Properties of Ag-Au Binary Nanocomposites prepared using Different Surfactant Capped Ag Nanoparticles," published in ***RSC Advances*** 5 (2015) 39954–39963.
4. **Anila Monga** and Bonamali Pal, "Influence of Oxidative Etching of Au Nanostructures by $KMnO_4$ on its Surface Morphology, Electro-kinetic Properties and Improved Catalytic Activity," published in ***Journal of Industrial and Engineering Chemistry*** 31 (2015) 223–230.
5. **Anila Monga** and Bonamali Pal, "Enhanced Stability, Conductance, and Catalytic Activity of Gold Nanoparticles via Oxidative Dissolution by $KMnO_4$," published in ***Particulate Science and Technology*** 33 (2015) 159–165.
6. **Anila Monga** and Bonamali Pal, "Comparative Co-catalytic Effect of Monometallic and Bimetallic Core-Shell Nanocomposites on Titania Photocatalysis by Visible Light," under preparation.

Other publications:

1. **Anila Monga** and Bonamali Pal, "Sensitivity of the Multiple Functional Moieties of Amino Acids for the Self-assembly of Au nanoparticles on Different Physicochemical Properties," published in ***Journal of Cluster Science*** 25 (2014) 1085–1098.

Paper/Posters presented in Conferences

1. **Anila Monga** and Bonamali Pal, "Effect of Shapes of Au Nanoparticles on TiO_2 in the Photocatalytic Degradation of Methylene Blue," presented in National Conference on New Frontiers in Chemistry (NFIC-2013) held at Punjabi University, Patiala on 15-16th February, 2013.
2. **Anila Monga** and Bonamali Pal, "Shape-dependent Catalytic Activity of Gold Nanostructures for Nitrobenzene Reduction," presented in International Conference on Emerging Technologies-Micro to Nano (ETMN-2013) held at BITS Pilani, Goa Campus, on 23-24th February, 2013.
3. **Anila Monga** and Bonamali Pal, "Interparticle Coupling Effect on Optoelectronic, Electro-kinetic properties and Catalytic Activity of Au Nanoparticles," presented in National Conference on Innovative Molecules for Sustainable Future (NCIMSF-2013) held at Thapar University, Patiala on 24-26th October, 2013.
4. **Anila Monga** and Bonamali Pal, "Enhanced Stability, Conductance and Catalytic Activity of Gold Nanoparticles via Oxidative Dissolution by $KMnO_4$," presented in International Conference on Powder, Granule and Bulk Solids: Innovations and Applications (PGBSIA-2013) held at Thapar University, Patiala on 28-30th November, 2013.
5. **Anila Monga** and Bonamali Pal, "Hollow Ag-Au Bimetallic nanoparticles: Fabrication, Structure, Optical and Physicochemical Properties," presented in International Conference on Nanotechnology in the Service of Health, Environment and Society, (Nanoscitech-2014) at Panjab University, Chandigarh on 13-15th February, 2014.
6. **Anila Monga** and Bonamali Pal, "Titania-supported Au-Ag Core-Shell Bimetallic Catalysts of Different Shapes for Photocatalytic Degradation under Visible Light," presented in National conference on New Frontiers in Chemical Sciences (NFCS-2014) at Khalsa College, Patiala on 15th November, 2014.
7. **Anila Monga** and Bonamali Pal, "Effect of Capping Agents on the Morphology, Opto-electronics and Physico-chemical Properties of Ag-Au Bimetallic Nanocomposites," presented in International Conference on Recent Advances in Nanoscience and

Nanotechnology (ICRAN-2014) at Jawaharlal Nehru University, New Delhi on 15-16th December, 2014.

8. **Anila Monga** and Bonamali Pal, "Morphological study of Ag-Au bimetallic nanostructures prepared from various surfactants capped Ag nanoparticles for improved catalytic activity," presented in National Seminar on Synergistic Aspects of Chemical and Other Sciences (SACOS-2015) held at Punjabi University, Patiala on 15-16th February, 2015.

NJC

PAPER

Cite this: *New J. Chem.*, 2015, **39**, 304

Improved catalytic activity and surface electro-kinetics of bimetallic Au–Ag core–shell nanocomposites†

Anila Monga and Bonamali Pal*

Received (in Montpellier, France) 22nd August 2014,
Accepted 11th October 2014

DOI: 10.1039/c4nj01419g

www.rsc.org/njc

This paper demonstrates the preparation of core–shell nanocomposites (NCs) of Au_{core}–Ag_{shell} (Au@Ag) and Ag_{core}–Au_{shell} (Ag@Au) for measuring their catalytic activity and electro-kinetic properties relative to their respective monometallic counterparts. A significant blue-shift (530 → 408 nm) and a red-shift (420 → 550 nm) of the surface plasmon band for Au@Ag and Ag@Au NCs, respectively, were observed due to increased size of binary composites depending on the nature of the core and shell material. The thickness of the deposited Ag shells varied from ~3–10 nm on the Au core leading to the formation of Au@Ag NCs. On the other hand, the Ag core served as a sacrificial template, where Ag@Au NCs were converted to hollow Ag–Au alloy shells (~15 nm) because of the galvanic reaction between them due to the difference in their redox potential. An increased zeta potential was found for resulting Au@Ag (+57.8 mV) and hollow Ag–Au alloy shell (−20.13 mV) NCs in comparison to monometallic Au (−6.13 mV) and Ag nanospheres (−5.74 mV) due to surface passivation with aqueous $AgNO_3$ and $AuCl_4^-$ solution, respectively. These bimetallic NCs exhibited ~2 times higher catalytic activity than the monometallic nanoparticles depending on the shell thickness and the core of the respective metals for the nitrobenzene and 1,3-dinitrobenzene reduction.

1. Introduction

The bimetallic nanocomposites (NCs) composed of two different metals are more significant than monometallic ones due to their improved electronic and optical properties, superior catalytic activity, high selectivity and stability emanating from bi-functional or synergistic effects.[1–4] The unique properties of bimetallic NCs over monometallic counterparts can be attributed to the reasons where;[5] (i) each metal element in bimetallic NCs promotes different elementary reaction steps leading to a bi-functional mechanism; (ii) the electronic or the ligand effect,[6,7] where the addition of a second metal alters the electronic properties of the functioning sites of the first metal by electron transfer between the two different metals; (iii) an ensemble or a geometric effect[8] in which the coordination of atoms of a second metal to an atom of the first metal on the surface provides new geometries of active sites. In the past, much progress has been made for synthesis of NCs following a range of synthetic strategies, including co-reduction, galvanic replacement, thermal decomposition, seeded growth, photochemical, successive reduction, microwave, template, and electrochemical deposition methods.[3,9–16] They can adopt either core–shell or alloy structures depending upon the synthetic approach employed.[17,18] The core–shell NCs are attractive owing to the ability to increase the functionality and stability of NPs by monitoring the nature of the core and shell thickness. Moreover, the lattice mismatch between the core and the shell material may induce the interfacial strain, which has been shown to enhance catalytic rates in dual-metal systems. For example, the Au–Pt core–shell exhibited enhanced electrocatalysis for oxygen reduction reaction.[19] The Au–Pd core–shell heterostructures served as effective catalysts for catalyzing a Suzuki-coupling reaction.[20]

Among bimetallic systems, the coinage metal (Au–Ag) nanostructures have been extensively explored due to their facile synthesis techniques, tunable surface plasmon (SP) bands in the visible region, similar (FCC) crystal structures and lattice constants (a = 0.479 nm; Au and 0.486 nm; Ag) where Ag shells can be epitaxially formed in Au cores or *vice versa*. Many NCs of Au–Ag, Au–Cu, Ag–Cu, Au–Pd, Cu–Au, Cu–Pd, *etc.*[13,14,21–26] of different morphology have been reported. Xia *et al.* recently synthesized Au@Ag core–shell nanocubes with controllable shell thicknesses.[27] The Au@Ag core–shell NCs of different shapes, *e.g.*, octahedron, cube, decahedron, rod, wire, and icosahedrons,

School of Chemistry and Biochemistry, Thapar University, Patiala-147004, Punjab, India. E-mail: bpal@thapar.edu; Fax: +91-175-236-4498; Tel: +91-175-239-3128

† Electronic supplementary information (ESI) available: UV-vis absorption spectra, EDS spectra, HRTEM and SAED patterns of Au@Ag and Ag@Au NCs, calculation of the atomic ratio of Au/Ag, autocorrelation spectra for DLS particle size distribution, and UV-vis absorption spectra, HPLC and GC analysis for the reduction of NB and 1,3-DNB. See DOI: 10.1039/c4nj01419g

Colloids and Surfaces A: Physicochem. Eng. Aspects 481 (2015) 158–166

Contents lists available at ScienceDirect

Colloids and Surfaces A: Physicochemical and Engineering Aspects

journal homepage: www.elsevier.com/locate/colsurfa

Preparation and characterization of different shapes of Au–Ag bimetallic nanocomposites for enhanced physicochemical properties

Anila Monga, Bonamali Pal*

School of Chemistry and Biochemistry, Thapar University, Patiala 147004, Punjab, India

HIGHLIGHTS

- Shape dependent physicochemical properties of Au_{core}–Ag_{shell} nanocomposites.
- Au_{core}–Ag_{shell} morphology exhibits superior catalytic activity than monometallics.
- Dinitrobenzene reduction products varied depending on core shape and shell thickness.
- Ag layer deposition over Au nanorod reversed the selectivity of reduction products.

GRAPHICAL ABSTRACT

The Au nanorod$_{core}$–Ag_{shell} exhibited the selective formation of 3-nitroaniline for the reduction of 1,3-dinitrobenzene as compared to 1,3-phenylenediamine in case of Au and Ag nanorods. This demonstrates the essential role of synergistic effect of Au–Ag interface on the catalytic activity and selectivity of bimetallic nanocatalyst.

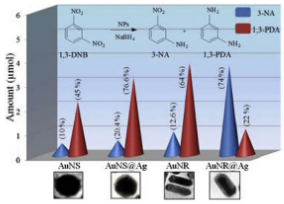

ARTICLE INFO

Article history:
Received 13 January 2015
Received in revised form 20 April 2015
Accepted 28 April 2015
Available online 11 May 2015

Keywords:
Au@Ag core–shell morphology
Au core shape
Shell thickness
Homogeneous catalysis
Nanocomposites

ABSTRACT

This paper reports the preparation and characterization of bimetallic Au_{core}–Ag_{shell} nanocomposites consisting, Ag shell of varied thickness (2–20 nm) and Au nanospheres and Au nanorods as cores for the selective catalytic reduction of nitro-organics. A significant blue-shift in the surface plasmon band, 529 nm of Au nanospheres, and 700 and 538 nm for Au nanorods to 400 nm, and 522 and 412 nm, respectively, was found with an increased thickness of Ag shell that led to a notable color change. The measured zeta potential of Au nanospheres (+26 mV) and Au nanorods (+22.4 mV) were also considerably increased due to the surface passivation with an Ag-shell over Au particles. It revealed that the catalytic reduction of 1,3-dinitrobenzene by the anisotropic Au nanorod$_{core}$–Ag_{shell} bimetallic nanocomposites produced a highly selective formation of 3-nitroaniline (74%) relative to 1,3-phenylenediamine by bare Au nanorod (64%), Au nanospheres (45%) and Au nanosphere$_{core}$–Ag_{shell} nanocomposites (76%). Whereas 53–60% aniline was obtained from the reduction of nitrobenzene by Au_{core}–Ag_{shell} compared to 34–41% yield by bare Au nanostructures. Thus, it was derived that the surface structural properties for the selective catalytic reduction of nitro-organics could be significantly tuned by varying the shape of the Au-core and Ag-shell thickness.

1. Introduction

Bimetallic alloys and core–shell nanocomposites (NCs) composed of two different metal nanoparticles (NPs) have received considerable attention [1–4] as compared to their respective monometallic NPs due to superior physicochemical, optical and

* Corresponding author. Tel.: +91 175 2393491; fax: +91 175 2364498.
E-mail address: bpal@thapar.edu (B. Pal).

http://dx.doi.org/10.1016/j.colsurfa.2015.04.051
0927-7757/

RSC Advances

PAPER

Cite this: *RSC Adv.*, 2015, **5**, 39954

Morphological and physicochemical properties of Ag–Au binary nanocomposites prepared using different surfactant capped Ag nanoparticles†

Anila Monga and Bonamali Pal*

Received 23rd December 2014
Accepted 27th April 2015

DOI: 10.1039/c4ra16940a

www.rsc.org/advances

This paper demonstrates the influence of surfactants of different chemical nature passivizing Ag nanoparticles (Ag NPs) on the morphology and physicochemical properties of Ag–Au bimetallic nanostructures. The Ag NPs were synthesized using polyvinylpyrrolidone (PVP), cetyltrimethylammoniumbromide (CTAB) and Triton X-100 (TX), followed by the deposition of Au on their surface. TEM analysis revealed the formation of hollow Ag–Au shells (~15 nm) and mixed solid Ag–Au alloys (~20–25 nm) using PVP and CTAB–Ag NPs, respectively, as their reaction templates. In contrast, porous-hollow aggregates of Ag–Au nanostructures (~16–22 nm) evolved during the reaction between Au^{3+} and TX–Ag NPs due to the difference in reaction rates between the Au^{3+} ions and various surfactant capped Ag NPs. As a result, these diverse morphologies of bimetallic nanostructures exhibited a significant variation in surface plasmon (SP) band, color, hydrodynamic size and zeta potential as compared to their monometallic Ag NPs. For example, a SP band of PVP–Ag NPs (488 nm) gradually red-shifted to 550 nm with the addition of Au^{3+} with notable color change from green to characteristic blue color indicating the composition change from Ag to Au rich. Therefore, the catalytic activity of various Ag–Au bimetallic nanostructures were found to be ~2 times higher than the monometallic Ag NPs for the reduction of different nitro-aromatic compounds, attributed to the electronic effect at the Ag–Au interface and their morphology.

1. Introduction

Coinage metal (Au, Ag and Cu) nanoparticles (NPs) are of great interest due to their fascinating optical, electronic and catalytic properties in various types of chemical transformations,[1–4] such as hydrogenation of nitro-aromatic compounds, oxidation, carbon–carbon bond formation, *etc.* In comparison to Ag and Cu, Au NPs have been extensively studied because of their facile synthesis, homogeneity, high resistance to oxidation and tunable surface plasmon (SP) band in the visible region.[5–7] The Ag NPs also have the exceptional extinction coefficient than any metal that lead to its use as sensing agent and for antimicrobial treatment.[5,8–10] However, monometallic Ag NPs have been found to be of limited practical use because of its severe susceptibility to oxidation,[11,12] which makes the optical and catalytic results for these particles non-reproducible. An extensive number of capping agents such as polymers, ligands, dendrimers and surfactants have been used to enhance NPs suspension stability to prevent their aggregation through electrostatic repulsion, steric repulsion or both.[13] The mechanism and functional groups involved in colloid stabilization differs with the chemical structure of capping agents, which may lead to varying particle size and stability.[14] But these stabilizing agents block or hinder the true optical and catalytic properties to a certain extent.

Therefore, another helpful attempt has been employed to coat Ag NPs with a layer of Au which imparts chemical stability and protects the Ag core against oxidation due to the electron transfer[12,15,16] between two metallic elements. This gives rise to the formation of bimetallic nanocomposites (NCs) which exhibit unique superior activity, high selectivity, and stability, interesting electronic, optical, chemical, and biological properties as compared to their monometallic counterparts. This can be attributed to,[17–21] (i) the electronic effect, in which the electronic charge transfer takes place between two metal elements leading to a change in the electron density on the resultant bimetallic structures; (ii) synergistic effect, in which each metal element in bimetallic NCs promote different elementary reaction steps. For example, the polyelectrolyte multilayer supported Au–Ag core–shell ($k = 0.18\ min^{-1}$) NCs showed higher catalytic activity[22] for the reduction of *p*-nitrophenol to *p*-aminophenol by $NaBH_4$ than the corresponding monometallic Au ($k = 0.019\ min^{-1}$) and Ag ($k = 0.069\ min^{-1}$)

School of Chemistry and Biochemistry, Thapar University, Patiala-147004, Punjab, India. E-mail: bpal@thapar.edu; Fax: +91-175-236-4498; Tel: +91-175-239-3491

† Electronic supplementary information (ESI) available: Calculations of Ag–Au atomic ratio, electrokinetic parameters of monometallic CTAB–Ag NPs, TX–Ag NPs and their respective Ag–Au bimetallic NCs, TEM images of different Ag–Au bimetallic NCs, UV-Vis absorption spectra for the reduction of chloronitrobenzene to chloroaminobenzene, time course graph showing catalytic activity of monometallic TX–Ag NPs and their Ag–Au bimetallic NCs and HPLC chromatograms. See DOI: 10.1039/c4ra16940a

Journal of Industrial and Engineering Chemistry 31 (2015) 223–230

Contents lists available at ScienceDirect

Journal of Industrial and Engineering Chemistry

journal homepage: www.elsevier.com/locate/jiec

Influence of Oxidative Etching of Au Nanostructures by $KMnO_4$ on its Surface Morphology, Electro-kinetic Properties and Improved Catalytic Activity

Anila Monga, Bonamali Pal *

School of Chemistry and Biochemistry, Thapar University, Patiala 147004, Punjab, India

ARTICLE INFO

Article history:
Received 11 January 2015
Received in revised form 14 June 2015
Accepted 27 June 2015
Available online 4 July 2015

Keywords:
oxidative dissolution
$KMnO_4$ etching
asymmetric Au nanostructures
electrochemical properties
electro-kinetic parameters
catalytic reduction

ABSTRACT

This paper reports the impact of oxidative etching of Au nanospheres and nanorods by $KMnO_4$ on their surface morphology, electro-kinetic properties and catalytic activity. A significant blue-shift of the surface plasmon bands for Au nanospheres (536 to 527 nm) and Au nanorods (679 to 532 nm) were observed, due to their size and shape alterations after oxidative dissolution. TEM analysis also revealed the formation of various irregular Au nano-morphologies such as spheres (~4-7 nm), low aspect ratio rods (2.6) and spheroids (~13 nm) of narrow size distribution after $KMnO_4$ etching. As a result, the hydrodynamic diameter of Au nanospheres (~41 nm) and Au nanorods (~109 nm) were reduced to ~4 nm and ~34 nm, respectively. The oxidative dissolution of Au^0 by $KMnO_4$ occurred via its oxidation to Au^{3+} ions as confirmed by the measured electrode potential, $E^0_{(Au^0/Au^{3+})}$ = -0.90 V by cyclic voltammetry with significant increase in the zeta potential and conductance values. The etched Au nanoparticles being smaller in size and of higher surface to volume ratio resulted in ~ 2 fold higher catalytic activities for the reduction of *p*-nitrophenol and *p*-nitrobenzoic acid as compared to bare unetched Au nanostructures.

1. Introduction

The optoelectronics and physiochemical properties of Au nanoparticles (AuNP) are proved to be very sensitive to their surface morphology, size and shape [1–4]. Hence, the ability to tailor the mono-dispersed particles could alter the optical and catalytic properties [5–10] depending on the particle size and shape. The morphology of AuNP can be tuned by regulating the experimental parameters [11–14] such as surfactant to water ratio, concentration of the metal precursor, reducing agents, capping agents, and temperature and time during their synthesis. Several groups have attempted to produce various sizes and shapes of AuNP using various chemical [11–14], biological [15–17] and physical methods [18–20]. For example, plant extracts such as Inonotus obliquus [15], Commelina nudiflora [16], Moringa oleifera [17], etc. have been reported to produce different shapes i.e., spherical, triangular, hexagonal and rods of AuNP. Sometimes the surface atoms of AuNP tend to become saturated with the surrounding gas or absorbed ionic species and thereby blocking or poisoning the active catalytic sites. The catalyst can be renewed and reused by an oxidative etching process using a suitable oxidant, without hampering their surface activity. It may result in dangling bonds, imbalancing of the forces and thus generates chemically unsaturated, fresh surface and thermodynamically high-energy active anisotropic AuNP [9,21] surfaces, which is otherwise difficult to prepare by conventional synthetic methods. For example, the galvanic replacement reaction has been employed for generating noble-metal nanostructures in the form of nanocages or nanoboxes [22], but this special technique requires various experimental steps and high refluxing temperature. Therefore, alternate strategy has been reported to generate anisotropic shapes using external stimuli such as thermal/or laser heating [23–25] and chemical methods [11,26–31]. In addition, electrochemical oxidation to Au crystals has also been reported [32,33]. Laser irradiation is utilized for direct surface deformation [22], but this experimental setup requires a costly laser source, while thermal reshaping [21] needs comparatively higher temperature. In this respect, corrosive oxidative etching of as-prepared AuNP have been found to be an unusual method to generate asymmetric Au nanocrystal possessing surface active facets [34],

* Corresponding author. Tel.: +91 175 2393128; fax: +91 175 2364498.
E-mail address: bpal@thapar.edu (B. Pal).

http://dx.doi.org/10.1016/j.jiec.2015.06.027
1226-086X/

Particulate Science and Technology, 33: 159–165

ISSN: 0272-6351 print/1548-0046 online
DOI: 10.1080/02726351.2014.947660

Taylor & Francis
Taylor & Francis Group

Enhanced Stability, Conductance, and Catalytic Activity of Gold Nanoparticles via Oxidative Dissolution by $KMnO_4$

ANILA MONGA and BONAMALI PAL

School of Chemistry and Biochemistry, Thapar University, Patiala, India

The present paper reports the oxidative etching of Au nanospheres by an oxidant, $KMnO_4$, which resulted in the formation of new particles of different reduced sizes from single starting nanoparticles. The significant blue-shifting (536 → 527 nm) of the surface plasmon band for Au nanospheres was observed due to their size alterations after oxidative dissolution of Au^0 to Au^{+3}. This was supported by the cyclic voltammetry studies, which revealed an anodic peak at −0.90 V in agreement with the standard electrode potential of Au^0/Au^{+3} (−0.96 V). Dynamic light scattering (DLS) analysis showed that the hydrodynamic diameter of Au nanospheres (~41 nm) was decreased from ~26 to 4 nm as a function of $KMnO_4$ concentration, as further evidenced by TEM. This oxidation-driven process resulted in colloids with higher zeta potential, conductance, and enhanced catalytic activity (~2 times) than their bare nanoparticles for the reduction of *p*-nitrophenol to *p*-aminophenol attributed to the higher surface area-to-volume ratio.

Keywords: Au nanospheres, catalytic activity, hydrodynamic size, $KMnO_4$, oxidative etching, zeta potential

1. Introduction

The physicochemical properties of Au nanoparticles (AuNPs) like optical, physical, electronic, and catalytic properties are found to be highly dependent on their size and shape (Burda et al. 2005; Eustis and El Sayed 2006; Kundu et al. 2009; Mahmoud et al. 2013; Yen et al. 2009). Hence, the ability to control the morphology of AuNPs is an important goal to the material researchers. By suitably controlling the experimental parameters such as concentration of the metal precursor, reducing agents, stabilizers, and reaction conditions (temperature, time) during the synthesis of AuNPs, the size and shape of NPs can be tuned (Jana et al. 2001, 2001a, 2001b; Jana et al. 2002). So far, postsynthetic size reduction or shape transformation of AuNPs has also been demonstrated by the application of thermal (Mohamed et al. 1998), laser heating (Link et al. 2000), and chemical (Rodriguez-Fernandez et al. 2005; Rai et al. 2006; Tsung et al. 2006) methods after the synthesis of NPs. Laser irradiation is utilized for direct surface deformation (Mohamed et al. 1998), but the experimental setup requires a costly laser source, while thermal reshaping (Link et al. 2000) needs comparatively higher temperature. Among chemical methods, oxidative etching has been found to be a powerful tool to control the morphology, which activates the specific facets of a nanocrystal (Cobley et al. 2009) and truncates sharp edges and corners (An et al. 2008). It is achievable by the oxidant having higher reduction potential than AuNPs and hence has a tendency to gain electrons. Many oxidants like hydrogen peroxide, H_2O_2; $E^0 = 1.78$ V (Chandrasekar et al. 2011), persulfate, $S_2O_8^{2-}$; $E^0 = 2.0$ V, cyanide CN^- (Jana et al. 2002), hydrochloric acid, HCl; $E^0 = 1.36$ V (Tsung et al. 2006), etc., have been used in tailoring the shape and size of AuNPs. The redox reaction takes place between the oxidant and AuNP surface sites resulting in oxidative dissolution of Au atoms, producing AuNPs of narrow size distribution (Zheng et al. 2014). However, these oxidants are toxic, hazardous, and difficult to handle, though $KMnO_4$ is an alternate easily available cheap reagent in the laboratory having mild toxicity, high oxidizing ability, and easy handling. It has intermediate electrochemical potential ($E^0 = 1.51$ V) as compared to other oxidants, but still higher than that of Au^{3+}/Au^0($E^0 = 0.96$ V), which can serve as an effective etchant for altering the surface morphology of AuNPs in a controlled manner.

The oxidative etching of metal NPs during the course of morphological transformation leads to the dissolution of Au^0 to Au^{+3} and thus, can alter the surface charge that could be measured in terms of variation of zeta potential (ξ) (Kim et al. 2005; Mukherjee and Weaver 2010) responsible for the stability of the colloidal system. This results in dangling of bonds, creating an imbalance of the forces on the fresh surface, which gives rise to a new equilibrium and hence new properties (Mahmoud et al. 2013; Narayanan et al. 2008). It has a wide range of applications in catalysis as the catalytic activity depends upon the surface atoms located on the corners, edges of NPs and hence expands the function

Address correspondence to: Bonamali Pal, School of Chemistry and Biochemistry, Thapar University, Patiala 147004, India. E-mail: bpal@thapar.edu

Color versions of one or more of the figures in the article can be found online at www.tandfonline.com/upst.

J Clust Sci (2014) 25:1085–1098
DOI 10.1007/s10876-014-0691-7

ORIGINAL PAPER

Sensitivity of the Multiple Functional Moieties of Amino Acids for the Self-Assembly of Au Nanoparticles on Different Physicochemical Properties

Anila Monga · Bonamali Pal

Received: 24 August 2013 / Published online: 23 January 2014

Abstract This paper investigates the extent of the self-assembly process of Au nanoparticles, depending on the nature of structural and functional moieties of various amino acids (L-cystine, glutathione, L-cysteine and *N*-acetyl cysteine) and their influence on the plasmon sensitivity and electrokinetic parameters in correlation with the catalysis of *p*-nitrophenol reduction. DLS particle size analysis revealed that the hydrodynamic size 10–20 nm of Au nanospheres was increased to 135–550 nm, 100–460 nm and 130–240 nm after the addition of L-cystine, L-cysteine and glutathione, respectively, in contrast to no significant change of particle size (15–60 nm) after *N*-acetyl cysteine addition. This difference in the extent of aggregation as a function of structures of amino acids is further evidenced by lengthy tubular arrays formation by glutathione as compared to branched chain like morphology obtained by L-cystine through TEM. FTIR studies further confirmed the binding of amino acids to Au nanospheres via –SH followed by linking of adjacent nanoparticles through H-bonding. Due to the conformational diversity of amino acids, the surface adsorbed –SH, $–COO^-$ and $–NH_3^+$ species over assembled Au nanoparticles led to the alteration of zeta potential and conductance, thus affected the catalysis for the reduction of *p*-nitrophenol as compared to unmodified Au nanoparticles.

Keywords Self-assemble Au nanospheres · Amino acid modified Au nanoparticles · Electrokinetic parameters · Catalytic activity

Electronic supplementary material The online version of this article (doi:10.1007/s10876-014-0691-7) contains supplementary material, which is available to authorized users.

A. Monga · B. Pal (✉)
School of Chemistry and Biochemistry, Thapar University, Patiala 147004, Punjab, India
e-mail: bpal@thapar.edu